Winter 11-12-2012

Proceeding of International Conference on Electrical Engineering and Information Technology EEIT-2012

Prof. Dr.Srikanta Patnaik

Editorial

The Electrical, Electronics and Information Technology deals with recent developments and practices adopted in various projects in different Engineering disciplines and specializations i.e. Rock Dredging, Concrete Technology, Grid Computing, Electrical Propulsion and the Stationary Plasma Thruster, Turbo Charging, Ultra Filtration, Nano Filtration and Reverse Osmosis, FACTS Devices, Sensors, Advanced Materials for Aircraft and Helicopters, Data Communication and Network Protocol, Satellite Communication Systems, Optoelectronic Devices, Wireless Communication, Applications of CFD Techniques in Aero-propulsive Characterization of Missiles, Hazardous Waste Management, Liquid Fueled SCRAMJET Combustors, Armor Materials and Designs, Heat Transfer in Nuclear Reactors, Defense Electronics Systems, World Class Manufacturing, Value Engineering & Engineering Ethics. Traditionally, Computing studies occupy two partitions i.e. Sciences and Engineering, separated by a line roughly at the computer architecture level. A more effective organization for Computer Science and Engineering requires an intrinsically interdisciplinary framework that combines academic and systems-oriented computing perspectives. Researchers have been developing such a framework, which reaggregates Computer Science and Engineering, then repartitions the resulting single field into analysis and synthesis components. The framework is based on the notion that Science is foremost about dissecting and understanding, and engineering is mostly about envisioning and building. The computer had a great effect on Communication. We must examine the idea of modeling in a computer and with the aid of a computer. For modeling, we believe that Computer is the basic Infrastructure to centralize communication. Any communication between people about the same concept is a common revelatory experience about informational models of that concept. Each model is a conceptual structure of abstractions formulated initially in the mind of one, and while communicating if it is different from those in the mind of other, there is no common model and no communication. Researchers are working on applying their wireless and mobile research to transportation, health care, education, collaboration and environmental sustainability. Projects already underway include safe and efficient road transportation, autonomous driving, wireless medical implants, mobile video delivery, multiparty wireless videoconferencing and energy harvesting.

The Conference sometimes is conducted in collaboration with other Institutions. IRNet encourage and invite proposals from Institutes within India and abroad to join hands to promote research in various areas of discipline. These conferences have not only promoted the International exchange and cooperation, but have also won favorable comments from National and International participants, thus enabled IRNet to reach out to a global network within three years time. The conference is first of its kind and gets granted with lot of blessings. The conference designed to stimulate the young minds including Research Scholars, Academicians, and Practitioners to contribute their ideas, thoughts and nobility in these disciplines of Engineering.

I sincerely thank all the authors for their valuable contribution to this conference. I am indebted towards the reviewers and Board of Editors for their generous gifts of time, energy and effort. It's my pleasure to welcome all the participants, delegates and organizer to this international conference on behalf of IRNet family members.

Convener:

Mr. Bikash Chandra Rout
IIMT, IRNet
Interscience Campus,
Bhubaneswar, Odisha, India

SECURE MULTIPATH ROUTING FOR DATA CONFIDENTIALITY IN MOBILE AD HOC NETWORKS

SANDHYA.P[1] & JULIA PUNITHA MALAR DHAS[2]

[1]Noorul Islam University,Kanyakumari,Tamil Nadu.
[2]Dept. of Computer Science, Noorul Islam University,Kanyakumari

Abstract-In mobile ad hoc networks (MANET), the traditional way of communication performed by the nodes by choosing the geographical location causes complexity. Also the existence of malicious nodes in the transmission path may drop the data packet or influence the routing messages. In order to overcome these issues, in this paper, we propose a secure multipath routing for improving data confidentiality in MANET. Initially multiple paths are established among source and destination for data transmission. In the established paths, the monitoring nodes are chosen based on the parameters such as available bandwidth and residual energy using swarm intelligence. These monitoring nodes involve in malicious nodes detection and informing the source on attack. When the source wants to transmit the data to the destination, it eliminates the path with malicious nodes and bypasses the data through other alternate path. Then a secure key management technique is deployed to defend against the malicious attack. By simulation results, we show that the proposed approach enhances the data confidentiality as well as minimizes the overhead.

I. INTRODUCTION

A. Mobile Ad Hoc Networks (MANET)

A self-configuring network consisting of mobile hosts inclusive of wireless communication devices in termed as MANET. Often, there may be random changes in the network topology as nodes are mobile. This network can either be a standalone or linked to the Internet. The nodes should be capable of transmitting traffic since the communicating nodes may perhaps be outside the transmission range. [1] Some of the significant features that distinguish MANET from other networks are infrastructure-less, dynamic topology, low and unpredictable bandwidth, and limited amount of resources, device security and physical security as well as short range connectivity. [2] The applications of MANET are sensor networks, military operations, disaster recovery, medical support, e-commerce, vehicular traffic and accident guidance, ad-hoc communication, conferences, multi-user games, robotic pets, biological detection, mobile workspace, rescue operations, cellular network and in other vital applications. [1]

B. Attacks in MANET

The MANETs are more susceptible to security attacks rather than wired networks. Due to the facts such as restricted protection of every individual node, uneven behavior of connectivity, deficit of certification authority, centralized monitoring or administration, security is complicated aspect to be maintained in these networks. In such a wireless network, attacks can enter from all possible direction and focus at any node. Hence each node is priorly ready for facing attacks straightly or in a roundabout way. In particular, an attack from a compromised node inside the network is destructive and difficult to get identified. [3]

MANETs are exposed to both passive and active attacks. During active attacks, the adversary does replication, alteration and removal of swapped data. While in passive attacks results in eavesdropping of data. In particular, the attacks in such a network can result in congestion, spreading wrong routing information, avoiding regular functioning of services or complete shutdown. [3] [4]

Some of the active attacks are described as follows

- *Wormhole Attack*

The reception of data packet at malicious node at one location followed by the tunnel the same packet to other location in the network and again re-transmission of these packets into the network is defined as wormhole attack. This attack has a possibility to get established via wired link among two colluding attackers or through a single long-range wireless link.

- *Black hole Attack*

The technique by which the attacker utilizes the routing protocol to publicize itself that it possess shortest path to the node is said to be black hole attack. When the malicious nodes enter the communicating path of the nodes, it has the possibility to access the packets passing through them. It further causes packet drops resulting in denial of service (DoS) attack.

- *Byzantine Attack*

A single compromised intermediate node or group of compromised nodes works together and performs routing loop generation, packet transmission over non-optimal paths and selective packet dropping resulting in routing service degradation. This kind of attack comes under byzantine failures and it is difficult to detect such failures.

- *Information Disclosure*

The confidential information is likely to get leaked to unauthorized nodes in the network owing to the compromised node. The confidential information includes the information concerned with network topology, geographic location of nodes or optimal routes to authorized nodes in the network.

- *Resource Consumption Attack*

The process by which the attacker consumes resource of other nodes existing in the network is termed as resource consumption attack. The resources includes battery power, bandwidth etc which are actually available in limited quantity in the network. The attacker appears as redundant route requests, recurrent generation of beacon packets or transmission of stale packets to nodes.

Snooping is attack which is concerned with passive attack and it is explained below.

- *Snooping*

The illegal access made to other person's data is termed as snooping. Some of the example of the snooping includes viewing e-mail emerging on another's computer screen or observing the content typed over other system. The complicated snoopers utilize software programs for monitoring remote activity on a computer or network devices. [5]

C. Security Requirement in MANET

MANET security contains some requirements which on accomplishing changes into secure environment. Their needs are difficult to get satisfied devoid of negotiating the unique features of MANET. The security needs of MANET are as follows. [2]

1.Authentication

The legal access to the network can be secured using authentication technique. When nodes want to communicate with each other, the identity of node has to be fulfilled. Without incorporating this requirement, other requirements are difficult to get incorporated as it is more complex task.

2.Authorization and accounting

In order to access shared resources, the nodes in the network must possess suitable permissions. Also the nodes should not permit other devices to access their private information. Besides, the authorization policies are associated with mechanisms of tracking resource utilization recognizing bottlenecks, charging users for services for networks statistical information etc.

3.Privacy and confidentiality

The data stored on the nodes, exchanged data and location information of the devices has to be protected in most scenarios. The term privacy defines the protection of identity and/or location of the node. The term confidentiality is attained using encryption technique such that proper key systems are utilized.

4.Availability and survivability

The network has to provide services on requirement in spite of break-ins which is termed as network availability. The ability of the network to offer services in any scenario and comes back to normal state is termed as survivability.

E.Data integrity

It is necessary for the user to guarantee that the data is devoid of tampering in circumstances that includes banking, military operations and equipment controls. This is referred to as data integrity.

F.Non-Repudiation

A node has to be responsible to its actions and should not deny its responsibility which is referred to as non-repudiation. This is attained using digital signatures that link the data.

D. Problem Identification

In the existing system the nodes communicated by selecting a geographical location, thus creating some perimeter surrounding them and exploiting the resultant area as the destination address. Even though all the destinations within the specified area are reached using this technique, it obscures operation since the specified area may be blank. This forces the source to either enlarge the perimeter or try a different area together. The existing threshold cryptographic technique does not provide authorization and access control service. The routing performance in a cooperative manner is not explained in detail also initiates to develop an improved system.

In MANET, the malicious node may drop the data packets or influence the routing messages. Also the malicious flooding attack causes congestion in the entire network. In order to overcome these issues, in this paper we propose an effective defense technique for enhancing security in MANET.

II. RELATED WORKS

Quansheng Guan et al [6] have proposed a joint authentication and topology control scheme in MANET. Their technique adaptively tunes the network configuration to optimize the effective throughput and the efficiency of authentication protocols with cooperative communications. They employed a discrete stochastic approximation approach in the proposed scheme to handle the imperfect channel knowledge and the dynamically changing topology.

Ayyaswamy Kathirvel et al [7] proposed an umpiring system to offer security for routing and data forwarding operations in mobile ad hoc networks. This umpiring system has three models that include single umpiring system, double umpiring system, and triple umpiring system. In their system, every node in the path performs packet forwarding and umpiring from source to destination. Instead of applying cryptographic technique, they utilize flagging technique. Through this method, when the umpiring node detects any misbehavior, those guilty nodes are flagged.

R. Murugan et al [8] have proposed a key distribution and authentication system for mobile ad hoc network. Their approach combines identity-based and threshold cryptography for offering flexibility and efficient key distribution. Further the ability for an arbitrary pair of devices to exchange a key in a secure fashion is guaranteed. This process is irrespective to the MANETs size which is varied due to the nodes mobility and also offers end-to-end authentication.

Md.MashudRanaetal[9] have proposed an enhanced DSR protocol for routing packets between hosts in an ad hoc network. Their protocol uses acknowledgement, and trust value calculation technique in addition with dynamic source routing which adapts quickly to routing changes when host movement is frequent. Moreover the technique ensures security against spoofing and route modification attacks. Since their protocol requires route request message to be sent twice, there is degradation in the time required for a message to reach destination. This causes tradeoff between security and speed of message transmission.

S.M. Sarwarul Islam Rizvi et al [10] have proposed a security scheme for protecting mobile agents and agent server in ad hoc network using threshold cryptography technique. Their technique offers solution to the problems concerned with central certificate authority and trusted third party in PKI by distributing trust among several network nodes. It also offers security services that include confidentiality, integrity and authenticity. The method that offers authorization and access control service is not provided in this approach.

Karim El Defrawy et al [11] have proposed an on-demand location based anonymous MANET routing protocol (PRISM). Their protocol relies on group signatures to authenticate nodes, ensure integrity of routing messages while preventing node tracking. It utilizes group signature schemes and location based forwarding mechanism. As this scheme discloses less of the topology, it is more privacy friendly.

III. SECURE MULTIPATH ROUTING TECHNIQUE

A. Overview

In this paper, we propose a secure multipath routing for data confidentiality in MANET. Initially, multiple paths are established among source and destination for data transmission. In the established paths, the nodes with maximum available bandwidth and residual energy are chosen as monitoring nodes using swarm intelligence. These monitoring nodes help in detecting the malicious nodes and it informs the source in case of detecting an attack. When the source wants to transmit the data to the destination, it eliminates the path with malicious nodes and bypasses the data through other alternate path. Then a secure key management technique is deployed that offers data privacy not only at intermediate malicious nodes but also at destination.

B. Estimation of metrics

1. Estimation of Available Bandwidth

Let AB represent the available bandwidth

Let LC_i be the link capacity related to one-hop neighbor i

Let CR be the collective rates assigned to all ingress and egress flows.

The link capacity is measured as the sum of the CR_{ij} and AB_i which is expressed as follows

$$LC_i = CR_{ij} + AB_i \quad (1)$$

Following the measurement of link capacity, the available bandwidth is defined using Eq (2)

$$AB_j \triangleq \max \{0, LC_j - CR^{ij}\} \quad (2)$$

[12]

2. Estimation of Residual Energy

The residual energy (RE) is computed by every node in the network by monitoring its energy consumption for transmission and reception process every t seconds.

Let E_d represent the energy dissipated during transmission and reception.

Let d be the distance among the nodes.

Let E_{tx} be the energy consumed by the node during packet transmission.

Let E_{rx} be the energy consumed by the node during packet reception.

The energy consumed to transmit a data packet of size z units to distance d is computed using following equation (3)

$$E_{tx}(z, d) = (E_d * z) + (E_{tx} * z * d^2) \quad (3)$$

The energy consumed to receive a data packet of size z units is computed using following equation (4)

$$E_{rx}(z) = E_d * z \quad (4)$$

The total energy consumed while transmitting data packet is computed using Eq. (6)

$$E_t = E_{tx} + E_{rx} \quad (5)$$

After the transmission and reception of packet of z units, the residual energy of the node i is computed as follows

$$RE_i = RE_{ini} - E_t \quad (6)$$

where RE_{ini} is the Initial energy of the node. [13]

C. Proposed technique

Our proposed technique mainly concentrates on improving the data confidentiality in the network. It involves three phases namely.

Phase -1: Multipath Route Discovery

Phase -2: Attack Detection

Phase -3: Security Mechanism

Phase -1 Multipath Route Discovery

The steps involved in the multipath route discovery are as follows

Let S and D represent the source and destination respectively

Let R_{rq} be route request message

Let R_{rp} be the route reply message

Let DP represent the data packet.

Let RR be the route reserve where the nodes stores its routing information.

Let N_i represent the intermediate nodes. (where i=1, 2, 3 ,…,n)

Let ACK represent the acknowledgement.

1) When S wants to transmit DP to D, it initially verifies its RR for the availability of appropriate route to D.

2) If RR(S) = empty

Then

$$S \xrightarrow{R_{rq}} N_i$$

End if

The Step (2) implies that when the route reserve of the source does not contain any route to destination, the route discovery process is initiated by the source through a broadcasting of route request message.

The format of R_{rq} message is shown in table 1

TABLE I

Format of Route request message			
Source ID	Sequence Number	Destination ID	Previous hop node ID

3) N_i upon receiving R_{rq} updates it routing table with the source ID, sequence number, destination ID, and previous hop node ID and it examines its destination ID.

If $N_i \neq D$

Then

N_i rebroadcasts R_{rq} to its neighboring nodes.

Else

$$N_i \xrightarrow{R_{rp}} S$$

End if

If N_i corresponds to the intended D, it sends R_{rp} to S. Otherwise it re-broadcasts the R_{rq} to its neighbors. This process is repeated till R_{rq} reaches D.

4) If N_i receives two R_{rq} with similar request ID, then the first request packet is given priority and other packet is discarded.

5) When D receives R_{rq}, it unicasts R_{rp} packet for each received R_{rq} in the reverse path towards S.

$$D \xrightarrow{R_{rp}} S$$

6) Each N_i that receives R_{rp} updates its routing table and then unicasts this R_{rp} in the reverse-path using the earlier-stored previous-hop node information.

7) The step 5 is repeated till R_{rp} reaches S.

8) S then utilizes the multiple routes chosen from the information received from R_{rp} for data transmission.

Fig 1 demonstrates the route discovery mechanism. When S wants to transmit the data packet, it initially broadcasts the route request message to it neighboring nodes N_1, N_4, and N_6. These nodes upon receiving request verify whether they are intended destination. As they are not intended destination, N_1, N_4 and N_6 rebroadcasts the request to its neighbors {N_2, N_4}, {N_2, N_5 and N_7} and {N_4, N_7} respectively. As N_2 receives the request from N_1 as well as N_4, it chooses the request received first and discards the other request. Every intermediate node performs this similar action till the request packet reaches D. When D receives each route request packet unicasts reply packet in the reverse path towards S. S then chooses the multipath say {S-N_1-N_2-N_3-D},{ S-N_4-N_5-D } and { S-N_6-N_7-N_8-D }obtained from information of reply packets for data transmission.

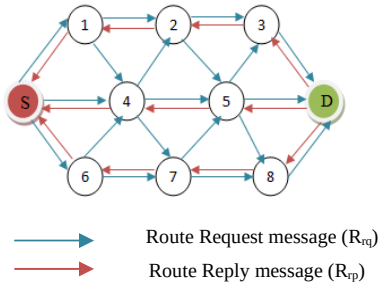

Fig 1 Route Discovery Mechanism

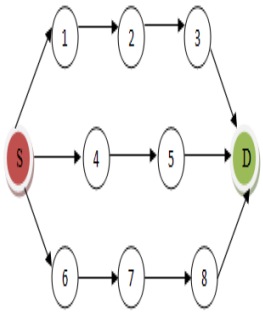

Fig 2 Multipath Route Establishment

Phase -2: Detection of Malicious Nodes

The detection of malicious nodes involves two steps. The first step involves the selection of monitoring nodes (MoN)

based on the parameters such as residual energy and bandwidth using swarm intelligence based ant colony optimization. The second step involves the detection of malicious nodes utilizing the monitoring nodes.

Step 1 Monitoring node selection

Let FA be the forward ant agent

Let BA be the backward ant agent

FA is launched by S and it visits each N_i along each path with the mobility which is estimated based on the probabilistic decision rule (shown in Eq.7).

$$P_v(N_i, S) = \begin{cases} \dfrac{[p_1(N_i,S)]^{\alpha}.[p_2(N_i,S)]^{\beta}}{\sum_{N_i \in N_{rx}} [p_1(N_i,S)]^{\alpha}.[p_2(N_i,S)]^{\beta}} & \text{, if } v \notin E(N_i) \\ 0, otherwise \end{cases} \quad (7)$$

where $p_1(N_i, S)$ represent pheromone value

p_2 (N_i, S_o) represent the heuristic value related to bandwidth.

N_{rx} represents the receiver node.

E (N_i) represents the routing table for N_i.

α and β are the parameters that control the relative weight of the pheromone and heuristic value respectively.

FA upon reaching each N_i gathers the nodes status that (Estimated in section 3.2.1 and 3.2.2) and stores in its pheromone table (Shown in table 1).

The format of pheromone table is given in table 2

TABLE II

Format of Pheromone Table			
Source Node ID	Destination ID	Available Bandwidth(AB)	Residual Energy(RE)

FA upon reaching D transfers the collected status of all the nodes into BA which is generated in D. BA traverses the similar path travelled by FA but in the opposite direction. It then updates the pheromone table with the available bandwidth and residual energy of the corresponding N_i. When BA reaches S, it transfers the status of all the nodes. S chooses the nodes with maximum available bandwidth and residual energy as monitoring nodes. Fig 3 illustrates the selection of monitoring nodes. N_2, N_4 and N_8 with maximum available bandwidth and residual energy are chosen as MoN.

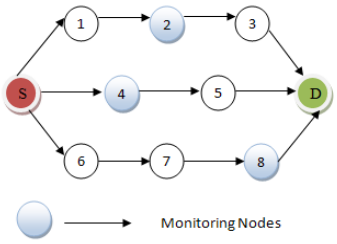

Fig 3 Selection of monitoring nodes

Step 2 Malicious Node Detection

The selected MoNs continuously monitors its adjacent nodes within the transmission range and gathers the nodes status.

If ($AB_i < AB_{th}$) & ($RE_i < RE_{th}$)

Then

The node is marked as malicious

MoN $\xrightarrow{warning\_message}$ S

End if

When S wants to transmit the data packet to D, it discards the path with malicious nodes and transmits the data packet through the alternate available paths in the direction of D. This process is illustrated in fig 4.

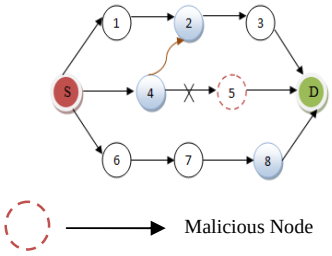

Fig 4 Malicious Node detection

The MoN (N_4) detects N_5 to be malicious node and sends the warning message to S. S while transmitting data packet discards the path {S - N_4- N_5 – D} and utilizes the alternate path {S - N_4- N_2-N_3-D}.

Phase-3 Security Mechanism

When S receives the warning message, it initiates a key management scheme for securing the data transmission in the network.

S chooses a secret number (f), a large co-prime (u, v) and generates a common key (K_S) which is shown below.

$$K_S = u^f \bmod v \quad (8)$$

Similarly, D chooses a secret number (g) and generates a common key (K_D) which is shown below.

$$K_D = u^g \bmod v \quad (9)$$

Both S and D possess common shared key which is generated as follows

$$K_{sh} = u^{fg} \bmod v$$

S in prior to transmitting the data, splits the data into n packets, and encrypts it with K_S, source and destination IDs. Subsequently, the intermediate node IDs are attached to the data packets without encryption. This permits N_i to extract the source and destination IDs.

Each time N_i receives a DP, it simply forwards this packet to the next hop node. Without the need of knowing source and destination address, all the packets will arrive to D.

When all the n packets are received, D uses K_{sh} to extract the source and destination address in each packet and compares it with its destination address.

If packet is for the node

Then

It decrypts it using K_{sh}.

Else

The packet is dropped and also cannot try to decrypt the packet.

End if

This technique offers data privacy not only at intermediate malicious nodes but also at destination.

IV. SIMULATION RESULTS

A. Simulation Parameters

We use NS2 [14] to simulate our proposed Secure Multipath Routing for Data Confidentiality (SMRDC) protocol. In this simulation, the channel capacity of mobile hosts is set to the value of 2 Mbps. We use the distributed coordination function (DCF) of IEEE 802.11 for wireless LANs as the MAC layer protocol. It has the functionality to notify the network layer about link breakage. In our simulation, the number of nodes is varied as 25, 50, 75 and 100. The mobile nodes move in a 750 meter x 750 meter square region for 50 seconds simulation time. We assume each node moves independently with the same average speed. All nodes have the same transmission range of 250 meters. In our simulation, number of attackers varied as 1,2,3,4 and 5. Random Way Point mobility model is used. The simulated traffic is Constant Bit Rate (CBR).

Our simulation settings and parameters are summarized in table 3.

Table 3: Simulation parameters

No. of Nodes	25,50,75 & 100
Area	750 X 750
MAC	802.11
Radio Range	250m
Simulation Time	50 sec
Traffic Source	CBR
Routing Protocol	SMRDC
Packet Size	512 Bytes
Mobility Model	Random Way Point
Speed	5 m/s

Pause time	1 seconds
No. Of Attackers	1, 2, 3, 4 and 5.
Initial Energy	10.1 J
Initial Sending Power	0.660
Initial Receiving Power	0.395

B. Performance Metrics

We evaluate performance of the new protocol mainly according to the following parameters. We compare the DSDV routing protocol with our proposed SMRDC protocol.

Average Packet Delivery Ratio: It is the ratio of the number of packets received successfully and the total number of packets transmitted.

Average end-to-end delay: The end-to-end-delay is averaged over all surviving data packets from the sources to the destinations.

Energy Consumption: It is the amount of energy consumed by nodes during the data transmission.

Throughput: It is the number of packets successfully received by the receiver.

Packet Drop: It is the number of packets dropped during the data transmission

The simulation results are presented in the next section.

C. Results & Analysis

A. Based on Nodes

Initially we vary the number of nodes as 25, 50, 75 and 100.

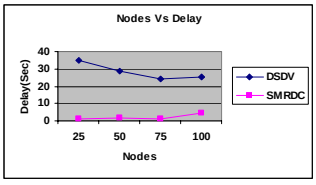

Fig 5: Nodes Vs Delay

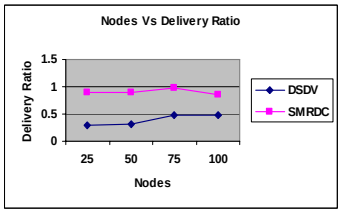

Fig 6: Nodes VS Delivery Ratio

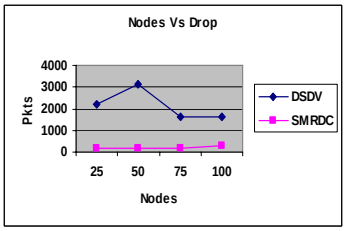

Fig 7: Nodes Vs Drop

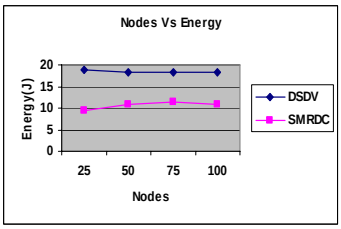

Fig 8: Nodes Vs Energy

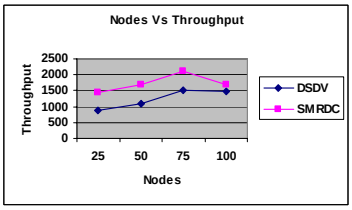

Fig 9: Nodes Vs Throughput

From figure 5, we can see that the average end-to-end delay of our proposed SMRDC protocol is less than the existing DSDV protocol.

From figure 6, we can see that the delivery ratio of our proposed SMRDC is higher than the existing DSDV protocol.

From figure 7, we can see that the packet drop of our proposed SMRDC is less than the existing DSDV protocol.

From figure 8, we can see that the energy consumption of our proposed SMRDC is less than the existing DSDV protocol

From figure 9, we can see that the throughput of our proposed SMRDC is higher than the existing DSDV protocol.

B. Based on Attackers

In our second experiment we vary the number of attackers as 1,2,3,4 and 5.

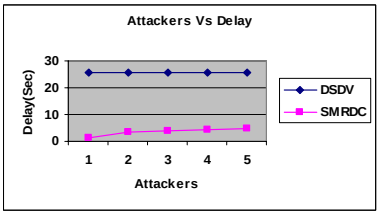

Fig 10: Attackers Vs Delay

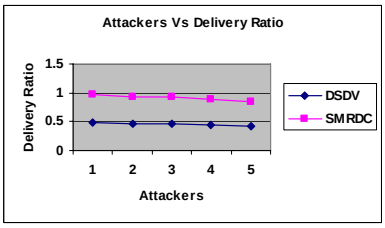

Fig 11: Attackers Vs Delivery Ratio

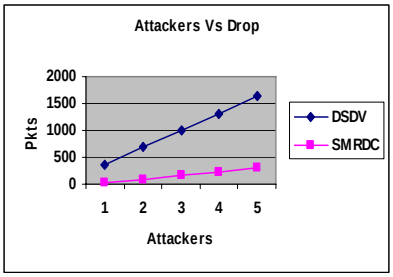

Fig 12: Attackers Vs Drop

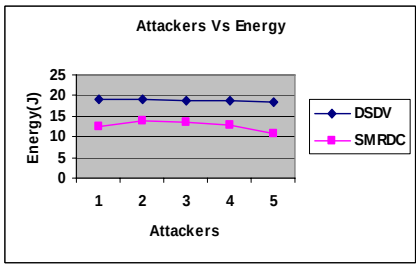

Fig 13: Attackers Vs Energy

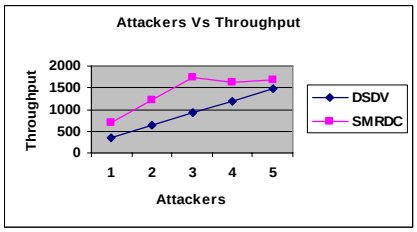

Fig 14: Attackers Vs Throughput

From figure 10, we can see that the average end-to-end delay of our proposed SMRDC protocol is less than the existing DSDV protocol.

From figure 11, we can see that the delivery ratio of our proposed SMRDC is higher than the existing DSDV protocol.

From figure 12, we can see that the packet drop of our proposed SMRDC is less than the existing DSDV protocol.

From figure 13, we can see that the energy consumption of our proposed SMRDC is less than the existing DSDV protocol

From figure 14, we can see that the throughput of our proposed SMRDC is higher than the existing DSDV protocol.

V. CONCLUSION

In this paper, we have proposed a secure multipath routing for improving data confidentiality in MANET. Initially multiple paths are established among source and destination for data transmission. In the established paths, the monitoring nodes are chosen based on the parameters such as available bandwidth and residual energy using swarm intelligence based ant colony optimization. These monitoring nodes involve in malicious nodes detection and informing the source on attack. When the source wants to transmit the data to the destination, it eliminates the path with malicious nodes and bypasses the data through other alternate path. Then a secure key management technique is deployed to defend against the malicious attack. This technique offers data privacy not only at intermediate malicious nodes but also at destination. By simulation results, we have shown that the proposed approach enhances the data confidentiality as well as minimizes the overhead.

REFERENCES

[1] Rutvij Jhaveri, Kruti Dangarwala and Neha Bhanot, *"Security and Service Discovery Issues in Mobile Ad-hoc Networks"*, International Journal of Networking, Volume 1, Issue 1, pp-01-03, 2011.

[2] Jameela Al-Jaroodi, *"Routing Security in Open/Dynamic Mobile Ad Hoc Networks"*, International Arab Journal of Information Technology, Vol 4, No 1, 2007.

[3] Sureyya Mutlu and Guray Yilmaz, *" A Distributed Cooperative Trust Based Intrusion Detection Framework for MANETs"*, The Seventh International Conference on Networking and Services(ICNS), pp 292 to 298, 2011

[4] N.Shanthi, Dr.L.Ganesan, and Dr.K.Ramar, *" Study of different attacks on multicast mobile ad hoc networks"*, Journal of Theoretical and Applied Information Technology, 2005-2009

[5] A. K. Rai, R. R. Tewari and S. K. Upadhyay "*Different Types of Attacks on Integrated MANET-Internet Communication*", International Journal of Computer Science and Security (IJCSS) Volume (4): Issue (3) 265 pp 245-74.

[6] Quansheng Guan, F. Richard Yu, Shengming Jiang and Victor C.M. Leung, *" A Joint Design for Topology and Security in MANETs with Cooperative Communications"*, Proceedings, IEEE, ICC, 2011.

[7] Ayyaswamy Kathirvel, Rengaramanujam Srinivasan, *" A System of Umpires for Security of Wireless Mobile Ad Hoc Network"*, International Arab Journal of e-Technology, Vol. 1, No. 4, June 2010.

[8] R. Murugan and A. Shanmugam, *" Key Distribution System for MANET with Minimum Prior Trust Relationship"*, International Journal of Recent Trends in Engineering, Vol. 1, No. 2, May 2009.

[9] Md. Mashud Rana, Alimuzzaman Khan, Syeda Suhana Rahman, *" Routing Security in Mobile Ad Hoc Networks: An Extension of DSR"*, Journal of Emerging Trends in Engineering and Applied Sciences (JETEAS), pp 155-159, 2011.

[10] S.M. Sarwarul Islam Rizvi, Zinat Sultana, Bo Sun, Md. Washiqul Islam, *" Security of Mobile Agent in Ad hoc Network using Threshold Cryptography*", World Academy of Science, Engineering and Technology, 2010.

[11] Karim El Defrawy, and Gene Tsudik, *" Privacy-Preserving Location-Based On-Demand Routing in MANETs*, IEEE Journal on selected areas in communications, vol 29, no 10, 2011.

[12] Vishnu Kumar Sharma and Dr. Sarita Singh Bhadauria, *" Agent based Bandwidth Reservation Routing Technique in Mobile Ad Hoc Networks"*, International Journal of Advanced Computer Science and Applications(IJACSA), Vol. 2, No. 12, 2011

[13] Dilip Kumar S.M, and Vijaya Kumar B.P., " EAAC: Energy-Aware Admission Control Scheme for Ad Hoc Networks", World Academy of Science, Engineering and Technology, 2009.

[14] Network Simulator : : http:///www.isi.edu/nsnam/ns

STF CODING OF MIMO-OFDM SYSTEMS WITH PRE-DFT PROCESSING

A SRI RANGA RAJU[1] & KRISHNA MOHAN MOORATHOTA[2]

[1,2]Department of ECE, S.V.P Engineering College, Visakhapatnam

Abstract—Subcarrier based space processing was conventionally employed in Orthogonal Frequency Division Multiplexing (OFDM) systems under Multiple-Input and Multiple-Output (MIMO) channels to achieve optimal performance. At the receiver of such systems, multiple Discrete Fourier Transform (DFT) blocks, each corresponding to one receive antenna, are required to be used. This induces considerable complexity. In this paper, we propose a pre-DFT processing scheme for the receiver of MIMO-OFDM systems with space-time-frequency coding. With the proposed scheme, the number of DFT blocks at the receiver can be any number from one to the number of receive antennas, thus enabling effective complexity and performance tradeoff. Using the pre-DFT processing scheme, the number of input signals to the space-time-frequency decoder can be reduced compared with the subcarrier based space processing. Therefore, a high dimensional MIMO system can be shrunk into an equivalently low dimension one. Due to the dimension reduction, both the complexity of the decoder and the complexity of channel estimation can be reduced. In general, the weighting coefficients calculation for the pre-DFT processing scheme should be relevant to the specific space-time-frequency code employed. In this paper, we propose a simple universal weighting coefficients calculation algorithm that can be used to achieve excellent performance for most practical space-time-frequency coding schemes. This makes the design of the pre-DFT processing scheme independent of the optimization of the space-time-frequency coding, which is desirable for multiplatform systems.

Index Terms—*Orthogonal frequency division multiplexing (OFDM), multiple-input and multiple-output (MIMO), Spacetime-frequency code.*

I. INTRODUCTION

For high data rate wideband wireless communications, Orthogonal Frequency Division Multiplexing (OFDM) can be used with Multiple-Input and Multiple-Output (MIMO) technology to achieve superior performance. In conventional MIMO-OFDM systems, subcarrier based space processing [1]-[9] was employed to achieve optimal performance. However, it requires multiple discrete Fourier transform/inverse DFT (DFT/IDFT) blocks, each corresponding to one receive/transmit antenna. Even though DFT/IDFT can be efficiently implemented using fast Fourier transform/inverse FFT (FFT/IFFT), its complexity is still a major concern for OFDM implementation [10]. In addition, the use of multiple antennas requires the basedband signal processing components to handle multiple input signals, thus inducing considerable complexity for the decoder and the channel estimator at the receiver. To reduce the complexity of such systems, several schemes [10]-[15] were proposed in the literature.

For an OFDM system with multiple transmit antennas, the schemes mentioned above [13]-[15], explicitly or implicitly, assume that the channel state information (CSI) is known at the transmitter. In mobile communications, where the channel can vary rapidly, it is difficult to maintain the CSI at the transmitter up-to-date without substantial system overhead [16]. Space-time-frequency codes [1]-[9] were proposed for OFDM systems to fully take advantage of the frequency diversity and spatial diversity presented in frequency selective fading channels without the requirement of the availability of CSI at the transmitter. For such a system, traditional subcarrier based space processing induces considerable complexity due to the reasons mentioned before.

In this paper, we propose to use pre-DFT processing to reduce the receiver complexity of MIMO-OFDM systems with space-time-frequency coding. In our proposed scheme, the received signals at the receiver are first weighted and then combined before the DFT processing. Owing to the pre-DFT processing, the number of DFT blocks required at the receiver can be reduced, and a high dimensional MIMO system can be shrunk into an equivalently low dimension one. Both enable effective complexity reduction.

One important issue in the proposed pre-DFT processing scheme for MIMO-OFDM systems with space-time-frequency coding is the calculation of the weighting coefficients before the DFT processing. In general, the weighting coefficients calculation are specific to the space-time-frequency coding scheme. In this paper, we propose a universal weighting coefficients calculation algorithm that can be applied in most practical space-time-frequency codes such as those proposed in [1]-[4], [6], [8] and [9]. This makes the design of the pre-DFT processing scheme independent of the optimization of the space-time-frequency coding, which is desirable for multiplatform systems.

In general, the weighting coefficients before the DFT processing can be calculated assuming that the CSIs are explicitly available. In this paper, we will show that the weighting coefficients can also be obtained using the signal space method [10], [11] without the explicit knowledge of the CSIs. This helps to reduce the complexity of channel estimation required by the space-time-frequency decoding since the number of equivalent channel branches required to be estimated in the proposed scheme can be reduced from the number of receive antennas to the number of DFT blocks.

This paper is organized as follows. In Section II, the proposed scheme for MIMO-OFDM systems is described. The calculation of weighting coefficients with/without explicit CSIs is introduced in Section III and IV, respectively. Some discussions about the proposed pre-DFT processing scheme are given in Section V. Simulation results are then presented in Sections VI. Finally, Section VII concludes our work. Throughout this paper, the following notations will be used.$(\cdot)^*$, $(\cdot)^T$, and $(\cdot)^H$ in the superscripts denote conjugate, transpose and Hermitian transpose, respectively. Likewise, diag(x) denotes a diagonal matrix **x** with on its diagonal; rank(·) denotes the rank of (·) ; E(·) denotes the expectation of(·); trace(·) denotes the trace of matrix(·); and $\lambda_i(\cdot)$ denotes the ith largest eigenvalue of matrix (·).

II. SYSTEM MODEL

We investigate a MIMO-OFDM system with N subcarriers as shown in Fig. 1. In the system, there are F transmit antennas and M receive antennas. At the tth OFDM symbol period, the output of the space-time-frequency encoder is assumed to be as follows:

$$C^{(t)} = c_{0,1}^{(t)}, \dots, c_{N-1,1}^{(t)}, \dots, c_{0,F}^{(t)} \dots c_{N-1,F}^{(t)}$$

$$T = 0,1, \dots, T-1 \qquad (1)$$

where $c_{n,f}^{(t)}$ $_{n,f}$ is the coded information symbol at the nth subcarrier of the tth OFDM symbol period transmitted from the fth transmit antenna, and T is the number of OFDM symbols in a space-time-frequency codeword. When T = 1, the spacetime-frequency code reduces to a space-frequency code.

After the IDFT processing, at the tth OFDM symbol period, the lth sample at the fth transmit antenna is given by

$$s_{t,l}^{(f)} = \frac{1}{N}\sum_{n=0}^{N-1} c_{n,f}^{(t)} e^{j2\pi ln/N},$$
$$-N_g \le l \le N, f = 1, \dots, F, t = 0, \dots, T-1 \qquad (2)$$

where N_g is the length of the cyclic prefix, and we assume that (N_g + 1) < N to keep high transmission efficiency. In the following, we assume that the channel does not vary over the period of one space-time-frequency codeword (i.e., the period of T OFDM symbols). Furthermore, we assume that the channel impulse responses (CIRs) decay to zero during the cyclic extension, or L ≤ (N_g + 1) < N where L is the maximum length of the CIRs. At the mth receive antenna, the lth sample at the tth OFDM symbol period is then given by

$$r_{t,l}^{(m)} = \sum_{f=1}^{F} h_l^{(m,f)} * s_{t,l}^{(f)} + z_{t,l}^{(m)}$$
$$-N_g \le l < N, m = 1, \dots, M, t = 0, \dots, T-1 \qquad (3)$$

where * denotes the convolution product, $h_l^{(m,f)}$ denotes the CIR between the fth transmit antenna and the mth receive antenna, and $z_{t,l}^{(m)}$ denotes the additive white Gaussian noise (AWGN) component at the mth receive antenna.

At the receiver, before the DFT processing, the M data streams from the output of the M receive antennas are weighted and then combined to form Q branches. After the guard interval removal, the weighted and combined signals are then applied to the DFT processors. Note that there are Q branches, and hence the number of DFT blocks required at the receiver is Q. As a result, compared to the conventional receiver structure [1]-[9], where M DFT blocks are used, the number of DFT blocks employed at the receiver can be reduced when pre-DFT processing is used.

For the qth branch, the output of the DFT processor at the tth OFDM symbol period is given by

$$v_{n,q}^{(t)} = \sum_{f=1}^{F}\sum_{m=1}^{M} \omega_{m,q} H_n^{(m,f)} c_{n,f}^{(t)} \sum_{m=1}^{M} \omega_{m,q} \hat{z}_{t,n}^{(m)} \qquad (4)$$

$$H_n^{(m,f)} = \sum_{t=0}^{L-1} h_l^{(m,f)} e^{-j2\pi ln/N} \qquad (5)$$

$$\hat{z}_{t,n}^{(m)} = \sum_{t=0}^{N-1} z_{t,l}^{(m)} e^{-j2\pi ln/N} \qquad (6)$$

and $\omega_{m,q}$ is the weighting coefficient for the mth receive antenna at the qth branch. In order to keep the noise white and its variance at different branch the same, we assume that the weighting coefficients are normalized (i.e.,$\Omega^H\Omega = I_Q$, where Ω is an M × Q matrix with the (m, q)th entry given by $\omega_{m,q}$, and I_Q is a Q × Q identify matrix).

III. WEIGHTING COEFFICIENTS CALCULATION WITH EXPLICIT CSI

In this section, we will present a way to calculate the weighting coefficients for the proposed pre-DFT

processing scheme. When the ML decoder is employed, the pair-wise error probability (PEP) can be used to denote system performance,
which is further determined by the pair-wise codeword distance [11]. The pair-wise codeword distance $d^2(C, E \mid H)$ between a favored coded sequence

$$E = \left[E^{(0)}, E^{(1)}, \dots, E^{(T-1)}\right]^T$$

where

$$E^{(t)} = \left[e_{0,1}^{(t)}, \dots, e_{N-1,1}^{(t)}, \dots, e_{0,F}^{(t)}, \dots, e_{N-1,F}^{(t)}\right]$$

$(\forall t \in [0, T-1])$ and the transmitted code sequence

$$C = \left[C^{(0)}, C^{(1)}, \dots, C^{(T-1)}\right]^T$$

where $C^{(t)(\forall t \in [0,T-1])}$ is defined in (1), is given by

$$C^{(t)}(\forall t \in [0, T-1])$$

$$d^2(C, E \mid H) = \sum_{t=0}^{T-1} \sum_{q=1}^{Q} \sum_{n=0}^{N-1} \sum_{m=1}^{M} \sum_{m'=1}^{M} \omega_{m,q} \omega_{m,q}^* \sum_{f=1}^{F} \sum_{f'=1}^{F} H_n^{(m,f)} \left(H_n^{m',f'}\right)^* \left(c_{n,f}^{(t)} - e_{n,f}^{(t)}\right)\left(c_{n,f'}^{(t)} - e_{n,f'}^{(t)}\right)^* \quad (7)$$

According to [11], minimizing the pair-wise error probability is equivalent to maximizing the pair-wise codeword distance given by (7). A close observation of (7) indicates that the optimal weighting coefficients are related to the specific codeword pair. To make the weighting coefficients and the codeword pair independent, we average (7) over all codewords pair ensemble ı . As a result, we get

$$\overline{d^2(C, E \mid H)} = \sum_{q=1}^{Q} \sum_{m=1}^{M} \sum_{m'=1}^{M} \omega_{m,q} \omega_{m,q}^* \sum_{n=0}^{N-1} \sum_{f=1}^{F} \sum_{f'=1}^{F} H_n^{(m,f)} \left(H_n^{(m',f')}\right)^* \sum_{t=0}^{T-1} \left(c_{n,f}^{(t)} - e_{n,f}^{(t)}\right)\left(c_{n,f'}^{(t)} e_{n,f'}^{(t)}\right)^* \quad (8)$$

where the overbar stands for the average over all the codewords pair ensemble.

In order to rewrite (8) into a matrix form, let C_n be an F X T matrix with the (f, t)th entry given by $c_{n,f}^{(t)}$, E_n be an matrix with the (f, t)th entry given by $e_{n,f}^{(t)}$, and H_n(n = 0, . . . , N-1) be an M X F with the (m, f)th entry given by $H_n^{(m,f)}$. With these definitions, (8) can be written into

$$\overline{d^2(C, E \mid H)} = trace(\Omega^T \Phi \Omega^* \quad (9)$$

where

$$\Phi = \sum_{n=0}^{N-1} H_n k_n H_n^H \quad (10)$$

with

$$k_n = \overline{(C_n - E_n)(C_n - E_n)^H} \quad (11)$$

Let the eigenvalues of Φ be λ_q(q = 1,…,M) with $\lambda_1 \geq \lambda_2 \geq \cdots \geq \lambda_M$ and $\omega_q(q = 1, \dots, Q)$be the ith column of Ω. It is well known that $\omega_q(q = 1, \dots, Q)$ when are the conjugate of the eigenvectors of Φ corresponding to the eigenvalues λ_q(q = 1,…,M), the maximum of $\overline{d^2(C, E \mid H)}$ is achieved and is given by [22]

$$\left(\overline{d^2(C, E \mid H)}\right)_{max} = \sum_{q=1}^{Q} \lambda_g(\Phi) \quad (12)$$

In general, to obtain Φ in (14), we need both knowledge of the CSIs and the space-time-frequency code since k_n is dependent on the specific space-time-frequency code. However, since the channel information is not available at the transmitter, the space time-frequency coding scheme should not favor or bias a particular sub-carrier or a particular transmit antenna. As a result, in the following, it will be shown that for most practical space-time-frequency codes, it is reasonable to assume that Φ is in the following form:

$$\Phi = k \sum_{n=0}^{N-1} H_n H_n^H \quad (13)$$

where k is a constant that is independent of n. As a result, the weighting coefficients (i.e., $\omega_q(q = 1, \dots, Q)$), which are the conjugate of the eigenvectors of Φ, are independent of the specific space-time-frequency coding scheme. For the space-time-frequency codes proposed in [8] and [9],for example, as shown in Appendix A, k_n can be expressed as follows:

$$k_n = k_1 . diag\left(\beta_{\tau(n)}\right) \quad (14)$$

where k_1 is a constant number independent of n, $\beta_{\tau(n)}$ = [0, · · · , 0, 1, 0, · · ·, 0] is an F − dimensional standard basis vector with 1 in its $\tau(n)$th component and 0 elsewhere, and $\tau(n)$is determined by the space-frequency coding scheme. Using (14), as shown in Appendix A, Φ can be proved to be in the form of (13) with $k = k_1/F$.

For space-time-frequency codes where the orthogonal space time block code (STBC) [17], [18] is employed (e.g., the codes proposed in [1]-[4]) as an

inner code. Using the orthogonal property of STBC, we can easily prove that

$$k_n = diag\left(\overline{2\left|c_{n,1}^{(0)} - e_{n,1}^{(0)}\right|^2}, \ldots, \overline{2\left|c_{n,F}^{(0)} - e_{n,F}^{(0)}\right|^2}\right) \quad (15)$$

It is reasonable to assume that the signals at the input of the inner encoder have the same distribution for different subcarriers and different transmit antennas, especially when an interleaver is employed between the outer encoder and the inner encoder. As a result, k_n can be written as

$$k_n = k\, I_F \quad (16)$$

Therefore, (10) can also be simplified into (13) for these codes. For a general space-time-frequency code such as that proposed in [6], simulation results in Section VI will also show that excellent performance can be achieved by using the weighting coefficients calculated based on Φ given by (13).

IV. WEIGHTING COEFFICIENTS CALCULATION WITHOUT EXPLICIT CSI

In the following, we propose a way to obtain the weighting coefficients (i.e., the eigenvectors of Φ) without explicit CSI. This is especially important for differential modulation, where the CSI is not supposed to be explicitly known at the receiver. For coherent modulation, when CSI is not explicitly required for the weighting coefficients calculation, the complexity of channel estimation2 can be reduced since the number of equivalent channel branches required to be estimated is now reduced from the number of receive antennas to the number of DFT branches.

Note that the covariance matrix of the received signal vector $r_{t,l} = \left[r_{t,l}^{(1)}, r_{t,l}^{(2)}, \ldots, r_{t,l}^{(M)}\right]^T$ can be given by

$$R = E\left[r_{t,l} r_{t,l}^H\right] \quad (17)$$

The (m, m')th element of R is given by

$$\rho_{m,m'} = E\left[r_{t,l}^{(m)}\left(r_{t,l}^{m'}\right)^*\right] = \sum_{f=1}^{F}\sum_{f'=1}^{F}\sum_{v=l-L+1}^{l}\sum_{v'=l-L+1}^{l} h_{l-v}^{(m,f)}\left(h_{l-v'}^{(m,f')}\right)^* E\left(s_{t,v}^{(f)}\left(s_{t,v'}^{(f')}\right)^*\right) + N_0\delta(m - m') \quad (18)$$

Similar to the SIMO case proposed in [10], when a large number of subcarriers are used, it is reasonable to assume that the transmitted signals are white, that is

$$E\left(s_{t,v}^{(f)}\left(s_{t,v'}^{(f')}\right)^*\right) = E_s\delta(f - f')\delta(v - v') \quad (19)$$

where E_s is the average energy of the coded symbol. Hence, by substituting (19) into (18) and after some manipulations, $\rho_{m,m'}$ can be proven to be given by

$$\rho_{m,m'} = \frac{E_s}{N}\left(\sum_{f=1}^{F}\sum_{n=0}^{N-1} H_n^{(m,f)}\left(H_n^{(m',f')}\right)^*\right) + N_0\delta(m - m') \quad (20)$$

where N_0 is the variance of the noise. Using (13), we then have

$$\rho_{m,m'} = \frac{E_s}{Nk}\Phi_{m,m'} + N_0\delta(m - m') \quad (21)$$

where $\Phi_{m,m'}$ is the (m, m')th entry of Φ.

From (21), it can be easily seen that the eigenvectors of Φ are the same as those of R. As a result, we can obtain the weighting coefficients directly from R without explicit knowledge of CSI.

V. COMPLEXITY CONSIDERATION

The proposed MIMO-OFDM system consists of pre-DFT weighting and combining, weighting coefficients calculation, DFT-processing, channel estimation, and ML decoding. By weighting and combining before the DFT processing, the number of branches to be handled by the ML decoder is reduced from M to Q. As a result, compared with the subcarrier based processing [1]-[9], the complexity of ML decoding can be reduced.

As for the complexity coming from the DFT processing, the pre-DFT weighting and combining, the ratio of the number of multiplications needed between the proposed scheme and the subcarrier based scheme is as follows:

$$\eta = \frac{\mathrm{QN}\log_2 N + QMN}{\mathrm{MN}\log_2 N} = \frac{Q}{M}\left(\frac{\log_2 N + M}{\log_2 N}\right) \quad (22)$$

From (22), it can be seen that, when $\log_2 N \gg M$, η is close to Q/M. From (12), it is easy to see that the number of DFT blocks at the receiver, Q, is determined by the rank of Φ. After some manipulations, we have

$$rank(\Phi) \le min\left(rank\left(\tilde{R}^{1/2}\right), M, FL\right). \quad (23)$$

where

$$\tilde{R}^{1/2} = \left[R_0^{1/2}, R_1^{1/2}, \ldots, R_{L-1}^{1/2}\right]. \quad (24)$$

while $\mathrm{R_l} = \mathrm{R_l^{1/2}}\mathrm{R_l^{1/2}}$ are the receive correlation matrix as defined in [19]. From (23), we can see that

Φ is singular when$\widetilde{R}^{1/2}$ is not of full row rank or FL is smaller than M. In this case, the number of DFT blocks required can be smaller than the number of receive antennas to achieve optimal performance. On the other hand, when Φ is nonsingular, it is still possible to achieve good performance with a limit number of DFT blocks due to the small contribution of the small eigenvalue to the average pair-wise codeword distance $\left(d^2(C, E \mid H)\right)$

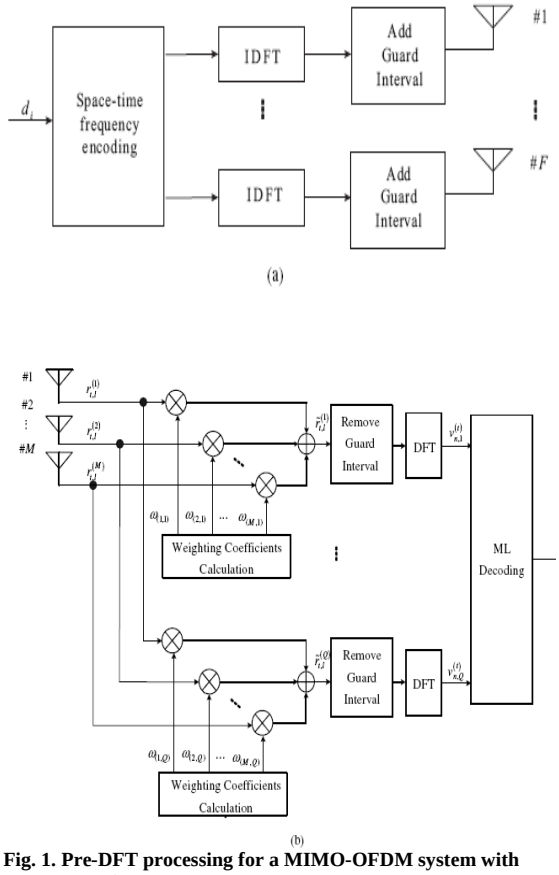

Fig. 1. Pre-DFT processing for a MIMO-OFDM system with space-time-frequency coding: (a) transmitter; (b) receiver.

VI. SIMULATION RESULTS

In the considered MIMO-OFDM system, the number of subcarriers in an OFDM symbol is 64 (N = 64) and the length of the guard interval is 12 (N_g = 12). In the simulations, we assume that there are four receive antennas at the receiver and two or four transmit antennas at the transmitter. Further, we assume that the channel is quasi-static and perfect channel information is available at the receiver. Without special notation, the optimal lines in the figures are obtained using ML decoders based on subcarrier space processing as the corresponding references. Further, E_b/N_0 in all figures is a shorthand for E_b/N_0 per receive antenna.

A. Performance of space-time-frequency codes proposed in [1] with pre-DFT processing

In this part, we consider the code proposed in [1], where full diversity order provided by the fading channel can be achieved with low trellis complexity. As in [1], we use the optimal rate 2/3 TCM codes [21] designed for flat fading channels. For simplicity, only the 4-state 8PSK TCM code is used and the parity check matrix is (6 4 7) in octal form.

When the two-ray equal gain Rayleigh fading channel
model is employed, the bit error rate (BER) performance of the proposed scheme is shown in Fig. 2. It can be observed that, with the increase of the number of DFT blocks at the receiver, better performance can be achieved. When the number of DFT blocks is increased from one to two, significant performance gain (e.g., 5.01 dB when $P_e = 10^{-4}$) can be achieved. When the number of DFT blocks is three or four, the performance is close to optimal.

When the weighting coefficients are obtained based on
the signal space method as discussed in Section IV, the performance of the proposed scheme over two-ray equal gain Rayleigh fading channel is also shown in Fig. 2. In the simulations, P is set to 64. From Fig. 2, we can see that the performance of the proposed scheme using the signal space method is almost the same as that with complete CSI.

B. Performance of space-time-frequency codes proposed in [8] and [6] with pre-DFT processing

The space-time-frequency code proposed in [8] can achieve full diversity without any rate reduction. In our simulations, the codeword of the space-frequency code **C** is given by Eqn. (3.1) in [8], and QRD-M algorithm is employed as the space-time-frequency decoder [23]. The performance of the proposed scheme over a six-ray exponential decay quasi-static Rayleigh fading channel is shown in Fig. 3. In Fig.4, the general space-time-frequency code proposed in [6] is employed with 16-state trellis and QPSK modulation [21]. It can be seen from Fig. 3 and Fig. 4 that similar results can be obtained as those in Part A irrespective for channel type and system configuration. As a result, the weighting coefficients obtained in Section III can also be applied here.

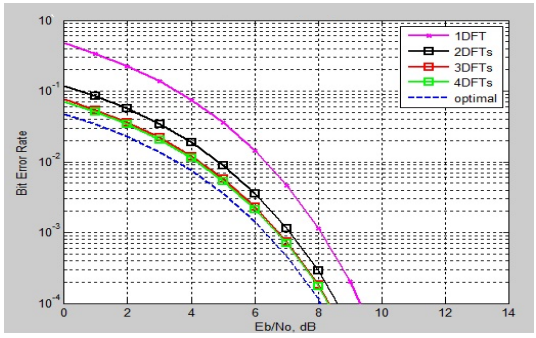

Figure 2.1 BER performance of the proposed scheme with the space-time-frequency code over a two-ray equal gain Rayleigh fading channel.

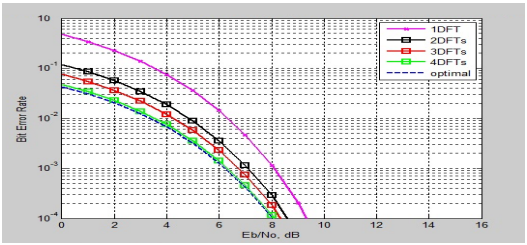

Figure 2.2 BER performance of the proposed scheme with the space-time-frequency code over a two-ray equal gain Rayleigh fading channel

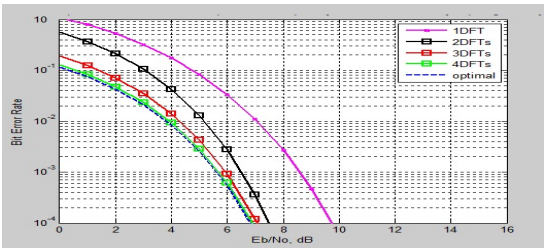

Figure 2.3 BER performance of the proposed scheme with the space-time-frequency code over a six-ray exponential decay Rayleigh fading channel

VII. CONCLUSION

In this paper, a pre-DFT processing scheme was proposed for a MIMO-OFDM system with space-time-frequency coding. With the proposed scheme, system complexity and performance can be effectively traded off. A simple weighting coefficients calculation algorithm was also derived. Theoretical analysis and simulation results have shown that the algorithm can be applied for most existing practical space-time-frequency codes. Using the proposed scheme, we have also shown that it is possible to use a very limited number of DFT blocks to achieve near optimal system performance.

REFERENCES

[1] Y. Gong and K. B. Letaief, "An efficient space-frequency coded OFDM system for broadband wireless communications," *IEEE Trans. Commun.*, vol. 51, no. 11, pp. 2019-2029, Nov. 2003.

[2] D. R. V. Jagannadha Rao, V. Shashidhar, Z. A. Khan, and B. S. Rajan, "Low complexity, full-diversity space-time-frequency block codes for MIMO-OFDM," in *Proc. IEEE Global Telecommun. Conf.*, vol. 1, Nov. 29- Dec. 3, 2004, pp. 204-208.

[3] Z. Liu, Y. Xin, and G. B.Giannakis, "Space-time-frequency coded OFDM over frequency-selective fading channels," *IEEE Trans. Signal Processing*, vol. 50, no. 10, pp. 2465-2476, Oct. 2002.

[4] A. Stamoulis and N. Al-Dhahir, "Impact of space-time block codes on 802.11 network throughput," *IEEE Trans. Wireless Commun.*, vol. 2, no. 5, pp. 1029-1039, Sept. 2003.

[5] B. Lu, X. Wang, and K. R. Narayanan, "LDPC-based space-time coded OFDM systems over correlated fading channels: performance analysis and receiver design," *IEEE Trans. Commun.*, vol. 50, no. 1, pp. 74-88, Jan. 2002.

[6] D. Agrawal, V. Tarokh, A. Naguib, and N. Seshadri, "Space-time coded OFDM for high data-rate wireless communication over wideband channels," in *Proc. IEEE Veh. Technol. Conf.*, vol. 3, May 18-21, 1998, pp. 2232-2236.

[7] H. Bolcskei, M. Borgmann, and A. J. Paulraj, "Space-frequency coded MIMO-OFDM with variable multiplexing-diversity tradeoff," in *Proc. IEEE Int. Conf. Commun.*, vol. 4, May. 11-15, 2003, pp. 2837-2841.

[8] W. Su, Z. Safar, and K. J. R. Liu, "Full-rate full-diversity space-frequency codes with optimum coding advantage," *IEEE Trans. Inf. Theory*, vol. 51, no. 1, pp. 229-249, Jan. 2005.

[9] L. Shao and S. Roy, "Rate-one space-frequency block codes with maximum diversity gain for MIMO-OFDM," *IEEE Trans. Wireless Commun.*, vol. 4, no. 4, pp. 1674-1687, July 2005.

[10] M. Okada and S. Komaki, "Pre-DFT combining space diversity assisted COFDM," *IEEE Trans. Veh. Technol.*, vol. 50, no. 2, pp. 487-496, Mar. 2001.

[11] D. Huang and K. B. Letaief, "Pre-DFT processing using eigen-analysis for coded OFDM with multiple receive antennas," *IEEE Trans. Commun.*, vol. 52, no. 11, pp. 2019-2027, Nov. 2004

[12] S. Hara, M. Budsabathon, and Y. Hara, "A pre-FFT OFDM adaptive antenna array with eigenvector combining," in *Proc. IEEE Int. Conf. Commun.*, vol. 4, June 2004, pp. 2412-2416.

[13] D. Huang and K. B. Letaief, "Symbol-based space diversity for coded OFDM systems," *IEEE Trans. Wireless Commun.*, vol. 3, no. 1, pp. 117- 127, Jan. 2004.

[14] S. Li, D. Huang, K. B. Letaief, and Z. Zhou, "Joint time-frequencybeamforming for MIMO-OFDM systems," in *Proc. IEEE GlobalTelecommun. Conf.*, Nov. 2005, pp. 3927-3931.

[15] J. Yang and Y. Li, "Low complexity OFDM MIMO system based on channel correlations," in *Proc. IEEE Global Telecommun. Conf.*, vol. 2, Dec. 2003, pp. 591-595.

[16] J. C. Roh and B. D. Rao, "Multiple antenna channels with partial channel state information at the transmitter," *IEEE Trans. Wireless Commun.*, vol. 3, no. 2, pp. 677-688, Mar. 2004.

[17] V. Tarokh, H. Jafarkhani, and A. R. Calderbank, "Space-time block codes from orthogonal designs," *IEEE Trans. Inf. Theory*, vol. 45, no. 5, pp. 1456-1467, July 1999.

[18] S. M. Alamouti, "A simple transmit diversity technique for wireless communications," *IEEE J. Sel. Areas Commun.*, vol. 16, no. 8, pp. 1451-1458, Oct. 1998.

[19] H. Bolcskei, M. Borgmann, and A. J. Paulraj, "Impact of the propagation environment on the performance of space-frequency coded MIMOOFDM," *IEEE J. Sel. Areas Commun.*, vol. 21, no. 3, pp. 427-439, Apr. 2003.

[20] A. Edelman, Eigenvalues and condition number of random matrics, PhD. Thesis, M. I. T. Press, Cambridge, MA, USA, May 1989.

[21] H. Jamali and T. Le-Ngoc, *Coded Modulation Techniques for Fading Channels*. Boston, MA: Kluwer, 1994.

[22] R. A. Horn and C. R. Johnson, *Matrix Analysis*. Cambridge Univ. Press,1985.

[23] W. H. Chin, "QRD based tree search data detection for MIMO communication systems," in *Proc. IEEE Veh. Technol. Conf.*, vol. 3, May 30-June 1, 2005, pp. 1624–1627.

OBSERVER BASED SENSORLESS CONTROL OF BRUSHLESS DC MOTOR WITH DIRECT TORQUE CONTROL

SREETHUMOL M V[1] & DINESH PAI A[2]

[1,2]Dept. of Electrical Engineering, Rajiv Gandhi Institute of Technology Kottayam, Kerala, India

Abstract — In this paper, a back EMF observer based position sensorless control scheme for Brushless DC (BLDC) motor with trapezoidal back EMF is presented. The drive is operated under Direct Torque Control scheme in the constant torque region. A sensorless operation is achieved through the back EMF observer using voltages and currents in stationary reference frame. The speed which is estimated using back EMF observer is used for the estimation of electromagnetic torque. Here the inverter DC-link voltage and two line currents are only measured for control and thus suitable for low cost application. The effectiveness of the proposed scheme is verified through extensive simulation. Simulation results indicate improved speed performance of BLDC motor.

Keywords *- Brushless DC (BLDC) motor, Direct Torque Control (DTC), Dynamic torque response, Position Sensorless Cotrol, Observer, Back EMF observer.*

I. INTRODUCTION

Permanent Magnet Brushless DC (BLDC) motors with trapezoidal back EMF became very popular because of its several distinct advantages such as high efficiency, high power density, high torque to volume ratio and simplicity in control [1]. They are used in many applications ranging from servos to traction drives. BLDC motors often employ concentrated windings [2], since these results in the end windings to short. The BLDC motors are generally fed from a quasi rectangular current and have trapezoidal back EMF in order to reduce the torque ripple and thus maximize the efficiency and torque capability. The BLDC drives require discrete position sensors which enhances the cost. This paper focus on sensorless control of the BLDC motors for high performance applications.

The Direct Torque Control (DTC) was originally developed for induction motor drives that directly control the electromagnetic torque and the flux [3]. It is less sensitive to parameter variations and much simpler to implement. The DTC scheme has been extended to BLDC motor drives for the high performance application [4]-[6].

In [7], a torque control scheme for BLDC motor at low speeds and maximum efficiency based on the *d–q–0* reference frame. It includes the phase back-EMF waveforms in natural *a–b–c* reference frame are transformed to the *d–q–0* reference frame. The electromagnetic torque estimation in [7] is based on the product of the instantaneous back EMF and current. The torque pulsations due to the commutation are reduced while using the pre-stored phase back EMF values which are obtained using mid-precision position sensor. The torque estimation, however, depends on parameters such as dc-link voltage and phase inductance. Moreover, sophisticated PWM method is required to drive the BLDC motor. Further, two phase conduction method is to be used rather than a three-phase one which may create problem in high speed applications.

In [8], the electromagnetic torque is estimated in dq-reference frame and modified 2×2 line-line park's transformation is used. The flux is controlled using the d-axis current, which is kept at zero. Rather than a sensorless speed drive a position sensorless drive for DTC is developed, where the electrical rotor position is estimated using winding inductance and stationary reference frame stator flux linkages and currents.

This study presents an observer based sensorless speed control with direct torque control (DTC) of BLDC motor. This method provides advantages such as fast torque response compared to that of vector control, simplicity in control and position sensorless drive. Here the coordinate transformations are done using line to line park transformation that forms a 2×2 matrix instead of the conventional 2×3 matrix [8]. The electromagnetic torque is estimated using the dq - axis back EMF's, currents and electrical rotor speed. For the sensorless drive the speed is estimated using back EMF observer. Simulation results are presented to illustrate the effectiveness of the observer based sensorless speed control of BLDC drive operated under DTC scheme.

The paper is organized as follows. In sect. II, the mathematical model of BLDC motor is described. In sect. III the DTC of BLDC is discussed. Sect. IV deals with the back EMF observer for the electrical rotor speed. The simulation results and its analysis are given in sect.V.

II. BLDC MOTOR MODEL

The equivalent circuit of BLDC motor with trapezoidal back EMF with the PWM inverter is modeled as in Fig. 1. The following assumptions are made while modeling.

1) The motor is unsaturated
2) The air gap length is constant
3) The stator windings are symmetrical and the resistances and inductances of the motor winding are constant
4) The armature reaction is negligible
5) Iron losses are negligible

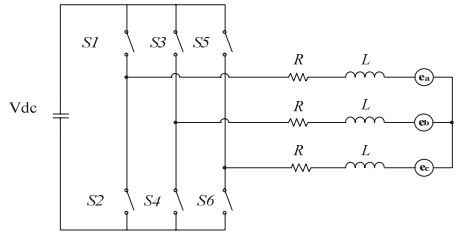

Fig.1. Equivalent circuit of BLDC motor with PWM inverter

The voltage of BLDC motor in abc - frame is given as

$$\left.\begin{aligned} v_a &= Ri_a + L\frac{di_a}{dt} + e_a \\ v_b &= Ri_b + L\frac{di_b}{dt} + e_b \\ v_c &= Ri_c + L\frac{di_c}{dt} + e_c \end{aligned}\right\} \quad (1)$$

Where, v_a, v_b, v_c are the phase voltages, i_a, i_b, i_c are the phase currents, e_a, e_b, e_c are the back EMF's which are assumed to be trapezoidal, R is the phase resistance and L is the phase inductance.

The electromagnetic torque equation is given by

$$\frac{dw_m}{dt} = \frac{T_{em} - T_L - Bw_m}{J} \quad (2)$$

where, T_L is the load torque, B is the coefficient of friction, J is the motor inertia constant, w_m is the mechanical angular speed and T_{em} is the electromagnetic torque which is expressed in terms of back EMF's and stator currents as

$$T_{em} = \frac{e_a i_a + e_b i_b + e_c i_c}{w_m} \quad (3)$$

III. DTC SCHEME FOR BLDC DRIVE

Two two-level hysteresis controllers are used for the torque and flux error as shown in Fig.2. The actual flux and electromagnetic torque are compared with the corresponding estimated values. Thus the key factor in the DTC of BLDC drive is the electromagnetic torque estimation. The torque is estimated in the dq-reference frame. The electromagnetic torque T_{em} estimation for a balanced system in $d-q$ reference frame is given as follows:

$$T_{em} = \frac{3P}{4w_{re}}\left(e_{qs}i_{qs} + e_{ds}i_{ds}\right) \quad (4)$$

Where P is the number of poles, w_{re} is the electrical rotor speed, e_{ds}, e_{qs}, i_{ds} and i_{qs} are the $d-q$ axis back EMF's and currents respectively. Here, the speed term in the denominator creates problem at zero and near zero speed.

The DTC of BLDC drive is implemented based on the stator flux linkage observers. The stator flux linkage vector can be estimated from the stationary αβ - reference frame stator voltages and currents which are directly measured.

The stationary reference frame flux linkages can be expressed as follows,

$$\left.\begin{aligned} \psi_{s\alpha} &= \int (V_{s\alpha} - R_s i_{s\alpha})dt \\ \psi_{s\beta} &= \int (V_{s\beta} - R_s i_{s\beta})dt \end{aligned}\right\} \quad (5)$$

In this work, the DC link voltage is measured, and the abc - frame voltages are estimated form the DC link voltage and is transformed into αβ - coordinates by modified line-line Clark transformation [10]. Also, only two line currents are measured, from which the ba-ca frame currents are found and is transformed in to αβ - coordinates and dq - coordinates using modified line-line Clark and Park's transformation respectively. From this the αβ - coordinate voltages and currents, the flux linkages in αβ - frame are estimated.

$$\left.\begin{aligned} \psi_{s\alpha} &= V_{s\alpha}t - R_s\int i_{s\alpha}dt + \psi_{s\alpha}(0) \\ \psi_{s\beta} &= V_{s\beta}t - R_s\int i_{s\beta}dt + \psi_{s\beta}(0) \end{aligned}\right\} \quad (6)$$

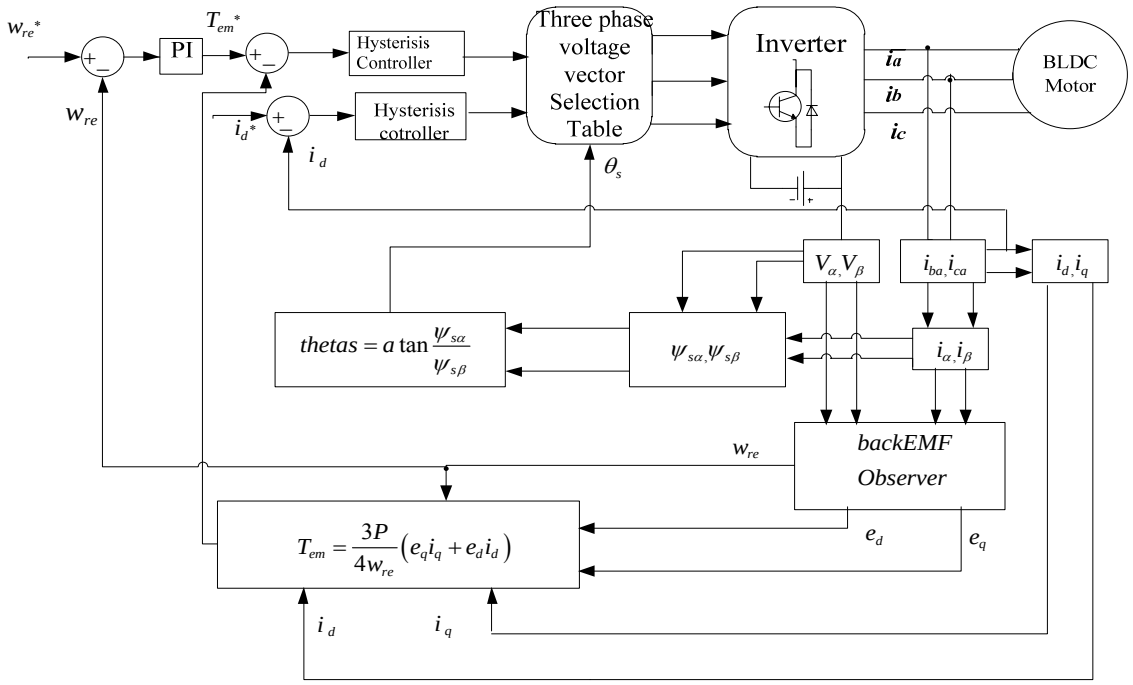

Fig.2 Block schematic of DTC based speed control of BLDC motor Drive

Where $V_{s\alpha}$, $V_{s\beta}$, $i_{s\alpha}$, $i_{s\beta}$ are the stationary reference frame voltages and currents. $\psi_{s\alpha}(0)$ and $\psi_{s\beta}(0)$ are the initial stator flux linkage at the instant of first switching. The approximate initial starting flux values at initial zero position is $\psi_{s\alpha}(0) = 0$ and $\psi_{s\beta}(0) = -2K_{LL}\pi/(3\sqrt{3})$. Where K_{LL} is the line to line back EMF constant.

Here instead of $|\psi_s|$, its amplitude is indirectly controlled by d-axis current in constant torque region, the i_d is controlled as zero.

The voltage vector block in Fig.2 receives the input signals ψ, τ and the angular position θ_s and generates the appropriate control voltage vector for the inverter by a look up table, and the angular position θ_s where the flux vector is located is given as:

$$\theta_s = a\tan\frac{\psi_{s\beta}}{\psi_{s\alpha}} \qquad (7)$$

The switching table for controlling both the amplitude and direction of rotation of stator flux is given in Table I. All the possibilities can be tabulated into a switching table. The output of the torque hysteresis comparator is denoted as τ, the output of the flux hysteresis comparator as ψ and the flux linkage sector is denoted as θ. The torque hysteresis comparator is a two level comparator; τ =0 means that the actual value of the torque is above the reference and out of the hysteresis limit and τ =1 means that the actual value is below the reference and out of the hysteresis limit. The flux hysteresis comparator is also a two level comparator where ψ=1 means that the actual value of the flux linkage is below the reference and out of the hysteresis limit and ψ =0 means that the actual value of the flux linkage is above the reference and out of the hysteresis limit.

TABLE I

SWITCH SELECTION TABLE FOR BLDC MOTOR DRIVE

φ	T	θ					
		θ(1)	θ(2)	θ(3)	θ(4)	θ(5)	θ(6)
φ=1	T=1	V2(110)	V3(010)	V4(011)	V5(001)	V6(101)	V1(100)
	T=-1	V6(101)	V1(100)	V2(110)	V3(010)	V4(011)	V5(001)
φ=-1	T=1	V3(010)	V4(011)	V5(001)	V6(101)	V1(100)	V2(110)
	T=-1	V5(001)	V6(101)	V1(100)	V2(110)	V3(010)	V4(011)

It is suggested that non zero vectors to be used with a PMSM or BLDC drive. Instead, a non zero vector which decreases the absolute value of the torque is used. The argument is that the application of a zero vector would make the change in torque subject to the rotor mechanical time constant which may be rather long compared to the electrical time constants of the system. This results in a slow change of the torque.

It is defined ψ and τ to be the outputs of the hysteresis controllers for flux and torque, respectively, and θ(1)-θ(6) as the sector numbers to

be used in defining the stator flux linkage positions. In Table I, if ψ =1, then the actual flux linkage is smaller than the reference value. On the other hand, if ψ =0, then the actual flux linkage is greater than the reference value. The same is true for the torque.

The torque reference is generated from the speed error between the actual and estimated speed. Here the estimated using the back EMF observer. Also the electrical rotor position which is used in the 2×2 line-line Park's transformation.is obtained by integrating the electrical rotor speed.

IV. BACK EMF OBSERVER

A back EMF observer for the system is designed based on the state space model of the system. Thus the state equation of a BLDC motor in stationary reference frame can be obtained from (1) is given as:

$$\left.\begin{aligned} \dot{i_\alpha} &= \frac{1}{L}v_\alpha - \frac{R}{L}i_\alpha - \frac{1}{L}e_\alpha \\ \dot{i_\beta} &= \frac{1}{L}v_\beta - \frac{R}{L}i_\beta - \frac{1}{L}e_\beta \end{aligned}\right\} \quad (8)$$

where v_α v_β , i_α i_β , and e_α e_β are the $\alpha\beta$ - axis voltages, currents and back EMF's respectively.

The state space model for the system is given as follows

$$\left.\begin{aligned} \dot{\mathrm{x}} &= \mathrm{Ax} + \mathrm{Bu} \\ \mathrm{y} &= \mathrm{Cx} \end{aligned}\right\} \quad (9)$$

Where $\mathrm{x} = \left[i_\alpha, i_\beta, e_\alpha, e_\beta\right]^T$ is the state matrix, $\mathrm{u} = \left[v_\alpha, v_\beta\right]^T$ is the input matrix, $\mathrm{y} = \left[i_\alpha, i_\beta\right]^T$ is the output matrix. Here,

$$A = \begin{bmatrix} -R/L & 0 & -1/L & 0 \\ 0 & -R/L & 0 & -1/L \\ 0 & 0 & 0 & 0 \\ 0 & 0 & 0 & 0 \end{bmatrix},$$

$$B = \begin{bmatrix} 1/L & 0 \\ 0 & 1/L \\ 0 & 0 \\ 0 & 0 \end{bmatrix},\ C = \begin{bmatrix} 1 & 0 & 0 & 0 \\ 0 & 1 & 0 & 0 \end{bmatrix}$$

where R and L are the resistance and inductance of the motor whose values are given in Table II.

The system is observable and it is possible to design the observer as follows:

$$\dot{\mathrm{x}} = \mathrm{Ax} + \mathrm{Bu} + \mathrm{K}(y - \hat{y}) \quad (10)$$

Where K is the observer gain matrix, and is obtained from the pole placement technique. And the observer gain K is given as

$$\mathrm{K} = \begin{bmatrix} k_1 & 0 & k_3 & 0 \\ 0 & k_2 & 0 & k_4 \end{bmatrix}^T$$

where k_1, k_2, k_3 and k_4 are the positive constants

Here the back EMF in the stationary frame is the immeasurable quantity. And it is estimated from the actual and estimated value of the output, i.e. the stationary reference currents. Thus the equation for the back EMF is described as follows

$$\hat{e} = \mathrm{K}_i(y - \hat{y}) \quad (11)$$

Equation (11) gives the dynamics of the back EMF signal. Thus the estimated back EMF is obtained by integrating (11) and is given as follows

$$\hat{e} = \int \mathrm{K}_i(y - \hat{y})dt \quad (12)$$

In order to improve the accuracy a proportional term is added to (11), and hence the back EMF is given as

$$\hat{e} = \mathrm{K}_p(y - \hat{y}) + \int \mathrm{K}_i(y - \hat{y})dt \quad (13)$$

where K_p is the gain matrix with positive constant.

Using the equation (13), the back EMF's in αβ - frame is obtained , and the $\hat{E}$ the amplitude of back EMF is given by

$$\hat{E} = \sqrt{{e_\alpha}^2 + {e_\beta}^2} \quad (14)$$

From the knowledge of this back EMF the speed can be calculated using the relation,

$$E = PK_e\omega \quad (15)$$

Since for a Brushless DC motor with a trapezoidal back EMF waveform, the back EMF is

proportional to the electrical rotor speed. Here in the above relation, P is the number of pole pairs, K_e is the back EMF constant of the motor, E is the amplitude of every phase back EMF.

V. SIMULATION RESULTS

The drive system shown in Fig.2 has been simulated in MATLAB/Simulink. Table II shows the ratings and parameters of the BLDC motor considered. The sampling interval is selected as 10μs. The magnitudes for the torque and flux hysteresis bands are selected as 0.01 Nm and 0.01Wb respectively. The switch selection table for the inverter given in Table I is employed for the DTC scheme. In the designed back EMF observer, the gains are obtained as: $K_1=K_2=13.82$, $K_3=K_4=-1$ and the proportional gain $K_5=K_6=-4$.

Fig.3 shows the speed and torque response when a load of 2.2 Nm is applied at 0.25sec. Initially the motor run at no load with a speed of 500 rad/s. When the load is suddenly increased the q-axis current amplitude also increases and fast torque response is achieved. The estimated torque follows the desired torque satisfactorily. When the load torque changes abruptly, there is a dip in the speed response. However the motor tracks the reference speed of 500 rad/s within 0.0125sec. The ripple seen in the torque and current can be minimized by properly selecting the torque hysteresis band size.

In Fig.4, the d-axis current fluctuates around at its reference value which is set at zero value. In order to provide the required motor torque, the q-axis current changes to 5 A when load is applied at 0.25sec. To provide a smooth electromagnetic torque, the q-axis current fluctuates around the dc offset value.

The actual and the estimated electrical rotor position are shown in Fig.5. The electrical rotor position and speed are estimated using the back EMF Observer. The estimated rotor position tracks the actual rotor position. Fig.6. shows the actual and estimated electrical speed of the drive.

TABLE II
BLDC MOTOR PARAMETERS

1 HP, 310 V, 4 pole, 50Hz		
Rated speed	4600	(rpm)
Rated current	4.52	(A)
Rated torque	2.2	(Nm)
Winding inductance	3.285	(mH)
Winding resistance	1.535	(Ω)
Rotor inertia constant	$1.8e^{-4}$	(Kg m^2)
Frictional co-efficient	0.001	(Nm/rad/s)

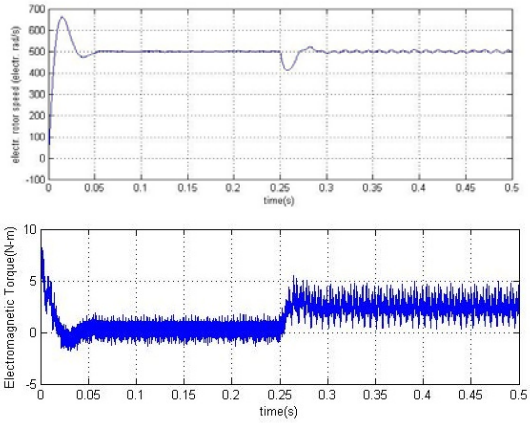

Fig.3. Estimated speed and electromagnetic torque when 2.2Nm load torque is applied at 0.25sec

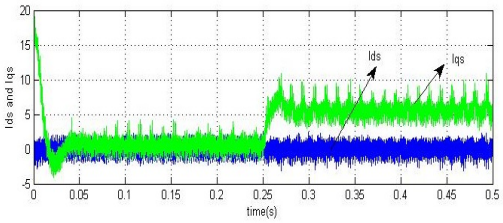

Fig.4. Steady state and transient behavior of the d-axis and q-axis stator currents under 2.2Nm load torque at 0.25sec.

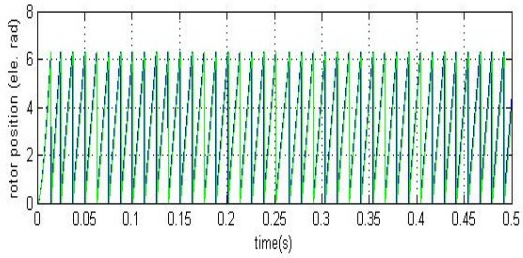

Fig.5. Actual and estimated rotor position

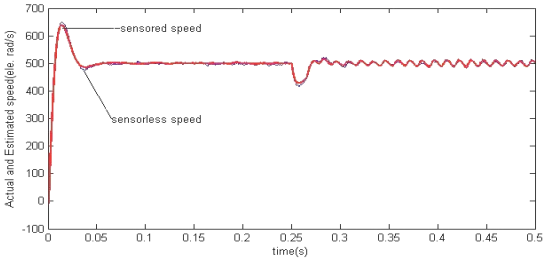

Fig.6. sensored and sensorless speed response

Fig. 7. Shows the $\alpha\beta$ - axis stator flux linkage locus under the zero and loaded condition of the motor. Here the speed is controlled and hence a better circular flux trajectory is obtained. The amplitude of the stator flux linkage is the amplitude of the flux linkage of the permanent magnet itself, and it is indirectly controlled at its optimum value by

means of d-axis current. Fig.8. shows the flux sector of the drive.

VI. CONCLUSION

An observer based sensorless speed control of BLDC motor drive, operated under DTC scheme is discussed in this paper. In this scheme, the electromagnetic torque is estimated in the rotating dq - reference frame. The electrical rotor speed required in the torque estimation is obtained using the back EMF observer. From the simulation results, it has been shown that this scheme can used for high performance applications. The drive system is sensitive to resistance changes and hence parameter adaptation can be adopted for further improvements in the performance. SVPWM technique can also be combined with this scheme to reduce the current and torque ripples while keeping the robustness in the torque control.

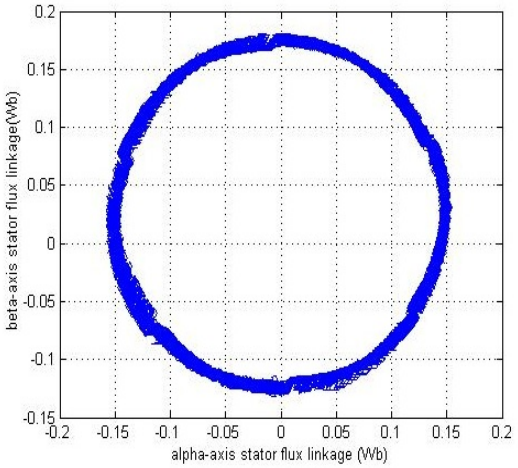

Fig.7. $\alpha\beta$ - axis flux linkage trajectory BLDC Drive

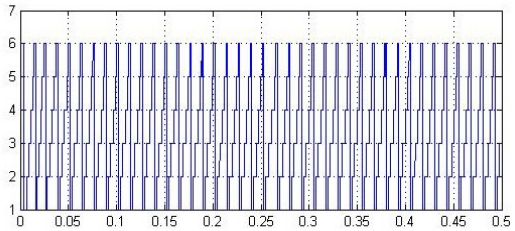

Fig.8. Stator Flux Sector

REFERENCES

[1] T. Kenjo and S. Nagamori, *Permanent-Magnet and Brushless DC Motors*. Oxford, U.K.: Clarendon, 1985.

[2] T. S. Low, T. H. Lee, K. J. Tseng, and K. S. Lock, "Servo performance of a BLDC drive with instantaneous torque control," *IEEE Trans. Ind. Appl.*, vol. 28, no. 2, pp. 455–462, Mar./Apr. 1992.

[3] I. Takahashi and T. Noguchi, "A new quick-response and high-efficiency control strategies of an induction motor," *IEEE Trans. Ind. Appl.*, vol. 22, no. 5, pp. 820–827, Sep./Oct. 1986.

[4] L.Zhong, M. F. Rahman, W. Y. Hu, and K. W. Lim, "Analysis of direct torque control in permanent magnet synchronous motor drives," *IEEE Trans. Power Electron.*, vol. 12, no. 3, pp. 528–536, May 1997.

[5] P. J. Sung,W. P. Han, L. H. Man, and F. Harashima, "A new approach for minimum-torque-ripple maximum-efficiency control of BLDC motor," *IEEE Trans. Ind. Electron.*, vol. 47, no. 1, pp. 109–114, Feb. 2000.

[6] S. J. Kang and S. K. Sul, "Direct torque control of brushless dc motor with non-ideal trapezoidal back-EMF," *IEEE Trans. Power Electron.*, vol. 10, no. 6, pp. 796–802, Nov. 1995.

[7] P. J. Sung, W. P. Han, L. H. Man, and F. Harashima, "A new approach for minimum-torque-ripple maximum-efficiency control of BLDC motor," *IEEE Trans. Ind. Electron.*, vol. 47, no. 1, pp. 109–114, Feb. 2000.

[8] S. B. Ozturk and H. A. Toliyat, " Direct torque and indirect flux control of brushless dc motor ," *IEEE Tran. Mechatronics, vol.16, No.2,, pp. 351–360,* Apr. 9–11, 2011.

SCAVENGING ENERGY FROM WASTE HEAT USING A NOVEL ZCS BUCK CONVERTER

ANITHA P.[1]& K. R. VARMAH[2]

[1,2]Department of Electrical & Electronics Engg., Rajagiri School of Engg. & Tech., Kakkanad, Ernakulam, India

Abstract - Harvesting of Energy from environment friendly sources has emerged as a solution for global warming. Hence the idea of recovering energy from waste heat is much discussed recently. The main advantage of using thermoelectric module is that it has no moving parts and is capable of converting waste heat directly into electrical energy. The basic principle behind is the Seebeck effect. Power from TEG module cannot be used directly. Hence a DC-DC converter is an essential part of the system. This paper presents a high-efficiency Zero Current Switching (ZCS) Buck Converter. The switching losses in the high frequency power switching converters can be reduced considerably by introducing soft switching techniques. Conventional ZCS converters are operated with constant on-time control. Hence they suffer from disadvantages such as a wide switching frequency range for given wide input source, load current harmonics at unpredictable frequencies, difficulty in filter design & reduced efficiency. By inserting an auxiliary switch in series with a resonant capacitor, the proposed topology can obtain a novel ZCS buck DC-DC battery charger and significantly decrease the switching losses in active power switches. This helps to increase the efficiency of the entire system. The entire circuit is designed and modelled using the power electronic software PSIM©. The hardware is realized using MOSFET as the power switches and they are controlled digitally usingARM7 LPC 2138 microcontroller.

Index Terms*- Soft Switching, Thermo electric module, Zero Current Switching.*

I. INTRODUCTION

Because the growing concern over the environmental protection issues and due to the alarming hike in the price petroleum products, efforts to seek alternative energy sources are being carried out throughout the world. Energy harvesting is the process by which energy is generated from external sources (e.g., solar power, thermal energy, wind energy, and kinetic energy), captured, and stored. Main application of this is in wearable electronics, where energy harvesting devices can power or recharge cell phones, mobile computers, radio communication equipment, etc. The applications may be extended to include high power output devices (or arrays of such devices) placed at remote locations to serve as reliable power stations for large systems. Power densities available from such harvesting devices depend highly upon various factors. The output energy can be stored in a capacitor, super capacitor, or a battery. Capacitors are used when the application needs to provide huge energy spikes. Batteries leak less energy and are therefore used when the device needs to provide steady flow of energy. Hence a suitable battery charging system is an inevitable part of the system.

There are different schemes for energy harvesting and the thermo electric power generation is discussed here. A thermo electric module is a solid state energy conversion device. It converts thermal energy from a temperature gradient into electric energy and is usually called TE power generator (TEG). It can also be used for cooling as it can generate a temperature gradient across the module when the electric power source is added.

The output from the TEG module can be used to charge a rechargeable battery such as the one in mobile phones, laptops etc. This paper discusses the design, working and simulation of a suitable DC-DC converter which, by using ZCS technique reduce the switching losses.

The operation principle specifications and the electrical model of TEG module is explained in section II. The working of the proposed converter is given in section III. The design and simulation results are in section IV.

II. THERMO ELECTRIC GENERATOR

Thermo Electric Generators (TEGs) work on the basis of Seebeck Effect which explains how a thermal gradient formed between two dissimilar conductors can produce a voltage. The temperature gradient in a conducting material results in heat flow, this results in the diffusion of charge carriers. The flow of charge carriers between the hot and cold regions in turn creates the potential difference. The theorem put forward by Jean Charles Athanase Pettlier explains how a junction of two dissimilar conducting materials can act as either a heater or a cooler, depending upon the direction of current flow. These two effects lead to the development of TEGs. Hence a TEG essentially consists of the junction of two dissimilar materials and the presence of a thermal gradient. Large voltage outputs are possible by connecting many junctions electrically in series and thermally in parallel. Figure1. shows a typical TEG module.

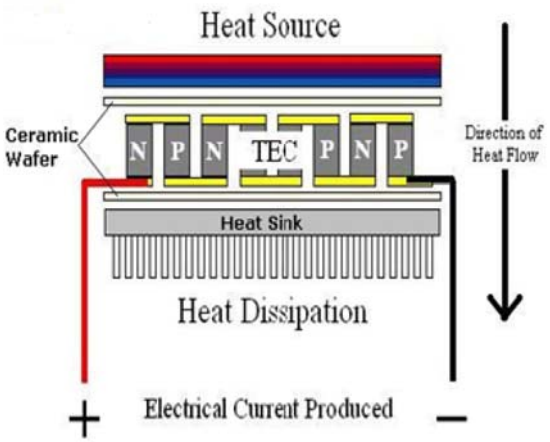

Figure 1. One typical TEG module in a waste heat harvest system.

There are four basic components in the system (1) a heat source - which can be an exhaust pipe or a heat exchanger (2) a TEG module – composed of a P-type and N-type semiconductor pellets connected together (3) a cold-side heat sink and (4) the electrical load. The system can also have a voltage regulation circuit, or a fan for the heat sink.

Thermoelectric materials are classified in terms of its figure of merit ($Z= \alpha^2T/ \rho k$) where α is Seebeck coefficient, ρ, the electrical resistivity, and k, the thermal conductivity. The larger the value of Z, the better is the thermo electric material. On the other hand, Z is a function of temperature. Hence, the value of Z of a specific thermo electric material becomes the maximum at a certain temperature. The selection of suitable thermo electric module should be done taking into account not only the large value of Z, but also their thermal stability and impact on environment. The recently developed modules consist of P and N doped bismuth telluride semiconductors sandwiched between two metalized ceramic plates. These ceramic plates are for adding rigidity and electrical insulation for the system. TEG's just don't work like regulated power supplies. For a given temperature gradient, output voltage varies directly as load resistance. This means there is no inherent output voltage regulation. The reason of this can be explained on the basis of the electrical equivalent of a TEG module. The electrical equivalent of a TEG module is as in Figure 2. TEG's have appreciable internal resistance. Hence as more current is drawn by the electrical load (as load resistance decreases), more of the available power is dissipated within it, and there is an appreciable voltage drop due to the internal resistance.

Due to this drawback, we may have to incorporate a regulator circuit along with the TEG module. It can be a series regulator, or a shunt regulator. But a DC-DC converter can provide a better regulation. There are applications, like micro power generation systems where the voltage level has to be stepped up or stepped down. This cannot be accomplished by a shunt or series regulator.

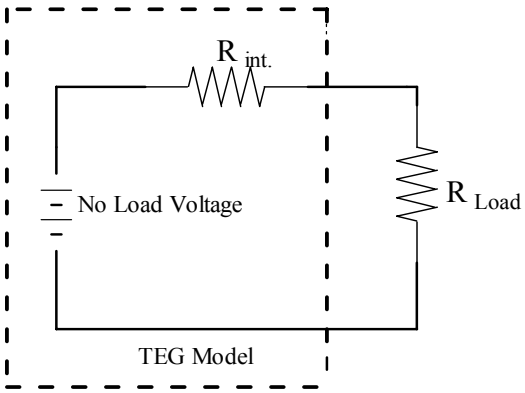

Figure 2. Electrical Model of a TEG System

The voltage output greatly depends on the nature of the thermo electric material used. The voltage output of a TEG module is given by the relation

$$V = \alpha \Delta T \qquad (1)$$

The Seebeck Coefficient α normally varies between 100 μV / K and 300 μV / K. The output voltage clearly depends on the temperature gradient. The voltage or current levels can be changed by connecting more number of modules either in series or in parallel. For example if the current level from a single device is adequate, but the voltage is insufficient, we usually place additional modules electrically in series. On the other hand, if the current is to be increased, we can have the modules connected in parallel. The optimum series parallel configuration for a given load depends on so many factors such as the expected range of temperature gradient, the desired voltage level, the maximum value of current that may be drawn at the rated voltage, whether a voltage regulation circuit is needed, physical conditions of the place where the system is to be operated, economic aspects etc.

By adding DC-DC converters, a better output voltage regulation can be ensured, but they add much towards increasing the cost of the entire system. Another difficulty faced is in the design of the converter so that the input impedance matches with the internal resistance of the TEG(s). This impedance matching is essential to ensure maximum power transfer from source to load.

III. RESONANT CONVERTERS

With the advancements in the field of power electronic devices, especially with the introduction of fast switching power semiconductor devices, DC to DC converters have gained momentum over conventional battery chargers with linear power

regulators. These converters were controlled using PWM techniques and were of small size, light weight, highly reliable, and were highly efficient in energy conversion. But they suffer from high switching stress and high switching power losses.

In order to overcome the aforementioned problems
soft switching techniques were introduced. Such topologies work basically on the principle of resonance and hence were named as resonant converters.

The most commonly used type of resonant converters is resonant switch converters, where the resonant property of the LC network is used to modify the switch voltage and current wave forms, so that it can be made on or off at a favourable condition. They can again be classified as zero voltage switching (ZVS) and zero current switching (ZCS) converters. This work deals with ZCS technique which eliminates the voltage and current overlap by forcing the switch current to zero before the switch voltage rises, making it more effective than ZVS in reducing switching losses, especially for slow switching power devices.

The ZCS technique can be added to ordinary buck converters, where the current produced by LC resonance flows through the switch causing it to turn on and off at zero current. A traditional L-type ZCS buck converter which can be used as battery charger is shown in Figure 3.

This converter circuit operates with constant on time control. Hence output voltage regulation is possible by controlling the off time of the switch. Consequently, this control system generates harmonics at unpredictable frequencies. This can be considered as the greatest drawback of the traditional circuits, as here the switches need to operate with a wide frequency range for a given wide input source and load voltage, thus making the filter design difficult. These shortcomings of the conventional ZCS buck converter are to be taken into consideration and a modification was made on this conventional topology.

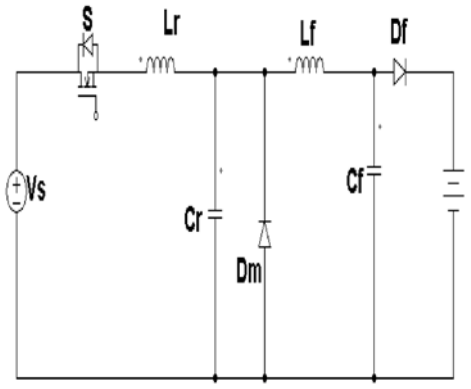

Figure 3. Conventional ZCS Buck converter

IV. MODIFIED CONVERTER

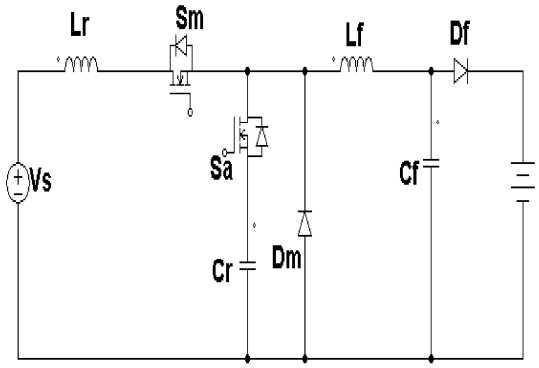

Figure 4. Modified ZCS Buck converter

The proposed topology is as shown in Figure 4.

Here an auxiliary switch S_a is in series with the resonant capacitor. The main power switches S_m and the auxiliary switches Sa have a common terminal and can be operated synchronously without any isolating devices, as shown in Fig. 3. In the novel ZCS battery charger, the auxiliary power switch S_a is off when the main power switch S_m is turned on. The resonance between resonant inductor and resonant capacitor occurs only when the auxiliary power switch S_a is turned on. The main power switch is turned off with ZCS. Thus the auxiliary power switch S_a holds the resonance for a period of time. So the novel ZCS topology can regulate the output by controlling the switching of the auxiliary switch.

V. DESIGN PROCEDURE

A TEG module with the following specifications was selected for design and simulation.

1. Hot side temperature - 300^0 C
2. Cold side temperature - 30^0 C
3. Open circuit voltage - 10.7 V
4. Matched load output voltage - 5.3 V
5. Matched load output current - 1.0 A
6. Matched load output power - 5.3 W
7. Internal resistance at 27^0 C - 2.7- 3.6 Ω

For the design of the proposed ZCS buck converter, the following performance parameters are defined.

1. Normalised voltage gain $M = V_0/V_s$
2. Normalised load $Q = R0/Z_0$
3. Average charging current $I_0 = V_0/R_0$
4. Normalised switching frequency $f_{ns} = fs/f_o$

The proposed converter finds application mainly as battery charger for rechargeable lead acid batteries. Let the battery specifications be 3.6 V, 1400m Ah. with a maximum current of 1.0 A and minimum of

0.6 A. Let the maximum and minimum values of voltages be 3.8 V and 2.75 V respectively.
The charger has the following parameters:-

- Input Voltage V_s = 5.3V
- Output voltage V_0 = 3.6 V
- Load current I_0 = 1.0 A
- Switching Frequency f_s = 105 K Hz

The output resistance is calculated as

$$R_0 = V_0 / I_0 = 3.6/1.0 = 3.6\ \Omega$$

The normalised voltage gain M can be found as

$$M = V_0/V_s = 3.6/5.3 = 0.7.$$

The characteristic impedance Z0 = R0/Q

Taking Q = 0.9, $Z_0 = Q * R_0 = 4\ \Omega$

Taking f n_s as 0 .5, the resonant frequency

$$f_0 = f_s/f_{ns} = 210\ \text{K Hz}.$$

Resonant inductance is calculated as

$$L_r = Z0/2\pi f_0 = 3.03\ \mu\text{H}$$

Resonant Capacitance

$$C_r = 1/2\pi f_0 Z_0 = .189\ \mu\text{F}$$

To limit the charging current ripple and the output voltage ripple, the circuit parameters for the low-pass filter of the ZCS battery charger are set as follows

- Filter inductance
  $L_f = 100 * L_r = 303\ \mu\text{H}$
- Filter capacitance
  $C_f = 100 * C_r = 18.9\ \mu\text{F}$

VI. SIMULATION RESULTS

The circuit was modelled and simulated using power electronic software PSIM©. Figure 5. shows electrical model of the TEG module selected.

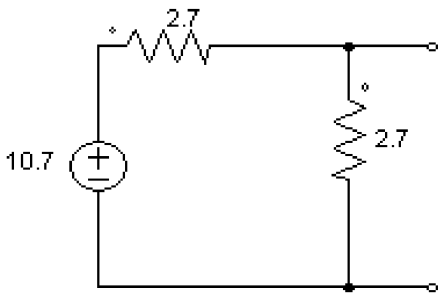

Figure 5. Electrical equivalent of the selected TEG module

The circuit model in PSIM© is as in Figure 6.

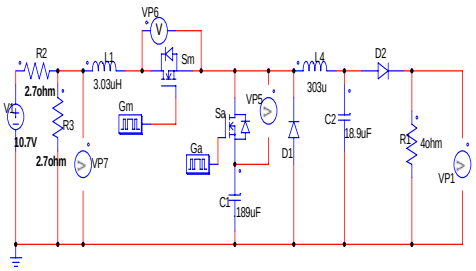

Figure 6. Simulation Model using PSIM

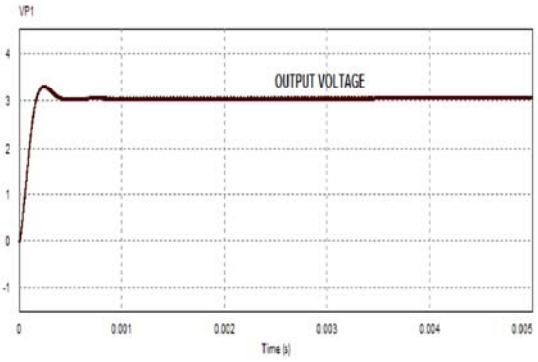

Figure 7. Variation of Output Voltage with Time

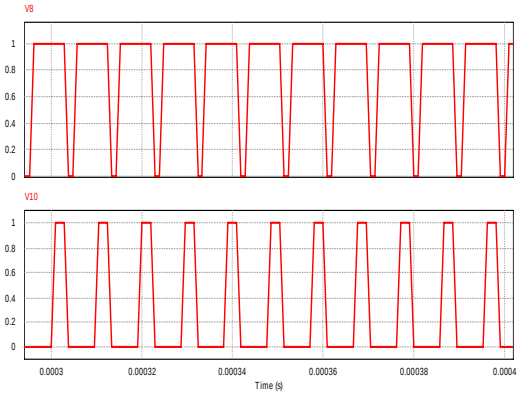

Figure 8. Gate Signals

The simulation result showing variation of output voltage with time is as in Figure 7. This output voltage corresponds to gate signals as in Figure 8. The main switch voltage and current waveforms were obtained as shown in Figure 9. It is clear that the switch is operated under ZCS. The auxiliary switch voltage and current waveforms are in Figure 10. The soft switching is evident in the figure.

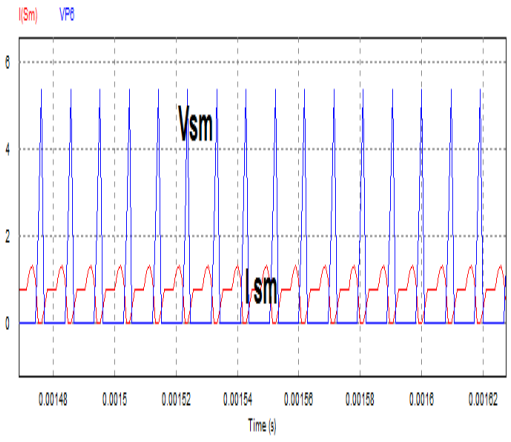

Figure 9. Main Switch Voltage and Current

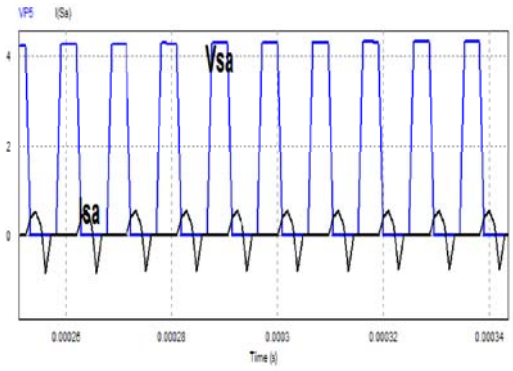

Figure 10. Auxiliary Switch Voltage and Current

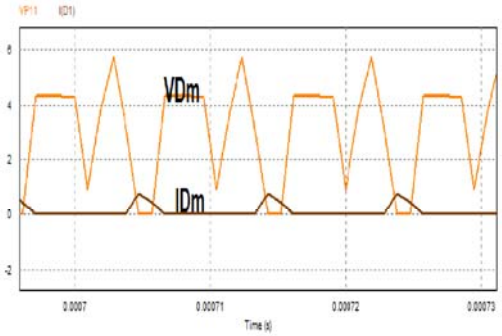

Figure 11. Auxiliary Switch Voltage and Current

Other main power electronic device used is the diode. The voltage and current waveforms across this component is shown in Figure 11. Hence it is evident that ZCS condition is satisfied for switches and the other components are also operated under soft switching. This helps to reduce both switching and conduction losses resulting in an increased efficiency.

The main feature of this modified ZCS converter is the easiness of control over the duration of resonance. By adjusting the gate signal to the auxiliary switch, the resonance period and hence the output voltage can be easily controlled. Hence the main power switch can be operated at fixed frequency and the problems with filter design can be avoided. This can also be verified through simulation.

The on time period of the auxiliary switch was increased by .02 microseconds and the gate signals at this condition were obtained as in Figure 12. below. With these gate signals the output voltage was obtained as shown in figure 13. The magnitude of voltage was observed to increase to 6 V. Similarly a reduction in on time of the auxiliary switch was found to provide a reduction in output voltage. Hence it was clearly observed from the simulation results that the output voltage regulation can be obtained by controlling the gate signals to the auxiliary switch alone. Thus the main power switch can be operated at constant switching frequency. This is the main feature of this new topology

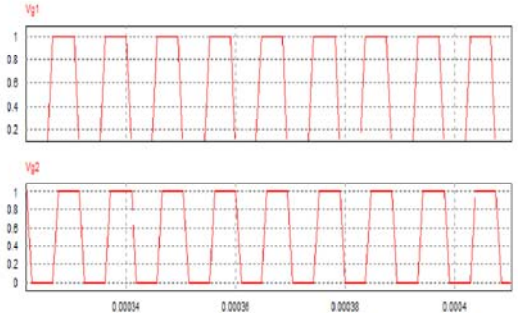

Figure 12. Changed Gate Voltages

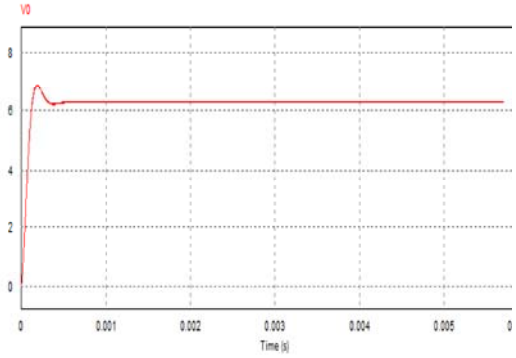

Figure 13. New Output Voltage

VII. CONCLUSION

A novel ZCS buck converter topology has been proposed in this paper. The input to the converter is provided from a TEG module. This can be incorporated along with the exhaust pipes of vehicles and the waste heat can be converted into electrical energy. The output of the converter can be used to charge rechargeable batteries such as those in mobile phones. Hence this new system helps to charge the mobile phones and laptops while travelling without utilizing electrical energy from conventional sources. Since resonant techniques such as ZCS is used the switching power losses is reduced and efficiency of power conversion is increased.

The hardware of this topology can be realized using MOSFETs as the switching devices. The switches can be digitally controlled using microcontrollers. The idea of introducing an auxiliary switch in order to control the resonant period can be incorporated with soft switching boost converters also, so that the output voltage of the TEG module can be stepped up to a suitable level to be used in DC motor drives. Once successfully implemented, this topology can bring revolutionary changes in the field of efficient energy utilization.

REFERENCES

[1] Ying-Chun Chuang, "High-efficiency ZCS buck converter for rechargeable batteries," IEEE Trans. Ind. Electron., Vol. 57, No. 7, pp. 2463-2472, July 2010.

[2] Y.C. Chuang and Y. L. Ke, "High-efficiency and low-stress ZVT–PWM dc to dc converter for battery charger," IEEE Trans. Ind. Electron, vol. 55, no. 8, pp. 3030–3037, Aug. 2008.

[3] Ned Mohan Tore M. Undeland, William P. Robbins, " Power Electronics Converters Applications and Design, Wiley, India, 2009, chapter 9.

[4] S. Zhou and G. A. Rincon-Mora, "A high efficiency, soft switching dc–dc converter with adaptive current-ripple control for portable applications," IEEE Trans. Circuits Syst. II, Exp *Brief*s, vol. 53, no. 4, pp. 319–323, Apr. 2006.

[5] Y.C. Chuang and Y.L. Ke, "A novel high-efficiency battery charger with a buck zero-voltage -switching resonant converter," IEEE Trans. Energy Convers., vol. 22, no. 4, pp. 848–854, Dec. 2007.

[6] J. J. Chen, F. C. Yang, C. C. Lai, Y. S. Hwang, and R. G. Lee, A high-efficiency multimode Li–ion battery charger with variable current source and controlling previous stage supply voltage," IEEE Trans. Ind. Electron. vol. 56, no.7, pp. 2469– 2478, Jul. 2009, Dec. 2007.

[7] J. Sallán, J. L. Villa, A. Llombart, and J. F. Sanz, "Optimal design of ICPT systems applied to electric vehicle battery charge," IEEE Trans. Ind. Electron., vol. 56, no. 6, pp. 2140–2149, Jun. 2009.

[8] Dong Cao, Fang Zheng Peng, "Multiphase Multilevel Modular DC–DC Converter for High-Current High-Gain TEG Application," IEEE Trans. Industry Applications, Vol. 47, no.3, May/June 2011.

[9] Seijiro Sano, Hiroyuki Mizukami, Hiromasa Kaibe, Development, of High-Efficiency Thermoelectric Power Generation System", Technical report.

[10] Molan Li, "Thermoelectric-Generator-Based DCDC Conversion Network for Automotive Applications", Master of Science Thesis, Stockholm, Sweden 2011.

SIMULATION OF A VIBRATION BASED GREEN ENERGY HARVESTING SYSTEM

K VINIDA[1], GINNES K JOHN[2] & DOMINIC MATHEW[3]

[1,2&3]Department of EEE, Rajagiri School of Engg. & Tech., Kerala, India.

Abstract —This paper presents the simulation of the mathematical model of an electromagnetic micro generator which converts vibration into electrical energy. The output of the micro generator is of the order of millivolts and is an ac voltage. It has to be converted to dc as well as stepped up into a higher voltage as required by an electronic load. This is achieved by a step up converter where a direct ac/dc conversion takes place. A closed loop control is incorporated so that the output is maintained even when the input voltage is changed.

Index Terms—*Boost Converter, Buck boost converter, Micro generators.*

I. INTRODUCTION

In the present scenario of global warming, self powered devices play a very important role. They can perform their operations without any external supply by scavenging energy from the environment. With the ever reducing power requirements of both analog and digital circuits, power scavenging approaches are becoming increasingly attractive. Fabrication of such power sources using MEMS (Micro Electro Mechanical Systems) technology is attractive in order to achieve small size and high precision.

The power requirement of electronic devices such as wireless sensors, medical implants etc. has been considerably reduced due to the developments of the highly efficient semiconductor devices. The power requirement of these electronic devices are of the order of a few milli watts which can be harvested from the ambient energy in the form of heat, light, vibration etc., by using various types of micro generators. The types of micro generators include electromagnetic, electrostatic, piezoelectric [4]–[6]. Usually batteries have been traditionally used as the energy source for such low power wireless applications. However, they are limited by their capacity and size. Moreover, they need to be recharged and replaced periodically.

Conversion of ambient mechanical vibration into electrical energy is a field of attraction for many researchers. An analytical model which predicts the performance of electromagnetic harvester based on the knowledge of acceleration is designed [4]. Using MEMS technology, a system incorporating electrostatic motion driven generator for low frequency motion is developed [5]. Buck boostconverter is incorporated for low voltage energy harvesting using vibration based piezoelectric generators are designed with MEMS technology [6]. A design incorporating a variable capacitor to power low power electronic devices is developed using MEMS technology [7]. An energy allocation algorithm with predictable energy inputs has been developed for the realization of networks composed of energy harvesting devices [10]. A model has been developed for converting radio frequency waves from air to electrical energy [11].

In this work, the micro electromagnetic generator which consists of a permanent magnet, copper coils and a spring as shown in Figure. 1, is taken as the energy source. In this micro generator, the base is attached to permanent magnet through a spring. The permanent magnet is kept in between the coils. Whenever the base is vibrated, the magnetic flux produced by the permanent magnet is cut by the coil thereby there is a rate of change of flux linkages. So a sinusoidal electromagnetic force is generated according to Faraday's laws of electromagnetic induction. The voltage generated by the micro generator depends upon the number of turns of coil and the magnetic structure.

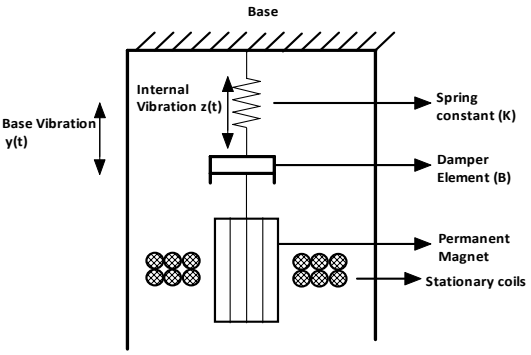

Figure. 1. Micro electromagnetic generator

Since the ac voltage generated by the micro electromagnetic generator is very small which is of the order of a few hundred milli volts, it needs a power electronic interface circuit to convert this low voltage into the minimum voltage required by an electronic circuit and to convert it into a DC voltage and also to store the electric power in the power storage elements.

The block diagram for low voltage energy harvesting is shown in Figure. 2. The ambient

vibration is converted into electrical energy by the MEMS transducer. The output of the transducer is an ac voltage with a low magnitude which has to be converted into a dc voltage and also to be stepped up to the required value to supply the low power electronics load. There are two stages involved in this conversion process. They are rectification and boosting processes [5]. The conventional power converters reported for energy harvesting circuits consist of a diode bridge rectifier and a dc/dc converter for stepping up the voltage as shown in Figure. 3.

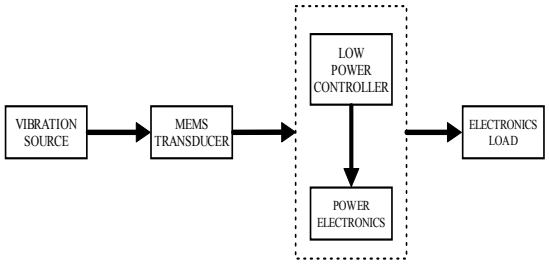

Figure. 2. Block diagram for low voltage energy harvesting.

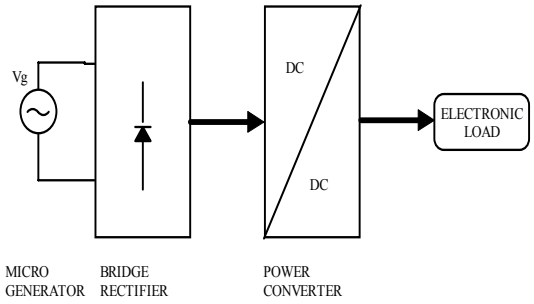

Figure. 3. Conventional power converter

The main disadvantage in this two stage topology is that since the output of micro generators is very low, rectification is not possible with the conventional diodes. The forward voltage drop in the diodes causes losses as input current is much higher than output current thereby the power conversion efficiency is decreased [2].

This leads to the development of direct AC/DC step up converter which converts the ac voltage with low magnitude generated by the micro electromagnetic generator into a dc voltage with a higher magnitude thereby avoiding diode bridge rectifier which results in a higher efficiency. The block diagram for low voltage energy harvesting with an ac/dc step up converter is shown in Figure. 4.

The proposed ac/dc step up converter consists of a boost converter which operates during the positive half cycle of the input voltage and a buck boost converter which operates during the negative half cycle of the input voltage. Both the converters are operated in the DCM (Discontinuous Conduction Mode) since the input current of buck boost converter is discontinuous under default circuit operation.

The advantages of operating converters in DCM are (a) the implementation of control scheme is easier and (b) switching losses of converter can be reduced.

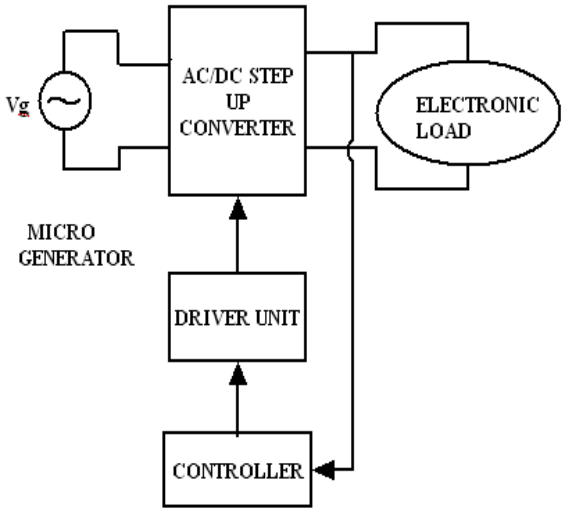

Figure. 4. Block diagram for low voltage energy harvesting with an ac/dc step up converter.

The rest of the work is organised as follows. The mathematical modeling of the micro generator is done in section II. A complete analysis of the ac/dc step up converter is presented in section III. The various operational modes are discussed in section III A. The relation between the switching frequency, duty cycle and various parameters of the circuit has been derived in section III B. The simulation circuit with closed loop control scheme and simulation results are presented in section III C.

II. MODELING OF MICROGENERATOR

The output of electromagnetic micro generator is 400mV. The input to the micro generator is sinusoidal vibration with an amplitude of 0.2m and with a frequency of 108 Hz. When the vibration is given to the base, the spring and permanent magnet experiences an internal vibration with respect to the housing. This will result in the rate of change of flux linkages thereby an emf is generated at the coil terminals. The base vibration is represented by *y(t)*. The internal vibration which is experienced by the permanent magnet, damper and the spring is represented by *z(t)*. The spring constant is represented by *K*, the damper element is represented by *B* and permanent magnet is represented by mass *m*. From Figure. 1, the mathematical modeling of micro generator can be done [1] as follows. The EMF E_i of the micro generator can be obtained as

$$E_i = n\frac{\partial\varphi}{\partial t} = n\frac{\partial\varphi}{\partial z}\frac{\partial z}{\partial t} = n\frac{\partial\varphi}{\partial z}z'$$

$$\therefore E_i = C_E z' \quad (1)$$

Where $C_E = n\frac{\partial\varphi}{\partial z}$ represents the electromechanical constant which depends upon the number of turns of the
coil and magnetic structure.

The mathematical model from Figure. 1 can be written as

$$my''(t) = mz''(t) + Bz'(t) + Kz(t) \quad (2)$$

$$y''(t) = z''(t) + \frac{B}{m}z'(t) + \frac{K}{m}z(t) \quad (3)$$

Here, the mechanical work is converted into electrical energy by damper. The electrical power P_e is obtained as

$$P_E = E_i \times i \quad (4)$$

The mechanical power P_m is given by rate of doing work.

$$P_m = \frac{dW}{dt} = F \times v \quad (5)$$

The damping force F_B is responsible for the energy conversion.

$$\therefore F_B \times v = E_i \times i \quad (6)$$

From equation (1)

$$F_B \times z' = C_E z' \times i = n\frac{\partial\varphi}{\partial z}z' \times i \quad (7)$$

$$F_B = n\frac{\partial\varphi}{\partial z} \times i \quad (8)$$

Since $F = ma$, from equation (8)

$$z'' = \left(n\frac{\partial\varphi}{\partial z} \times i\right) + m = (C_E/m) \times i \quad (9)$$

From equation (3), $\alpha 1$ is given by K/m, $\alpha 2$ is given by B/m and α3 is given by C_E/m. From equations (3), (7) & (9), the electromagnetic micro generator can be modeled as shown in Figure. 5.

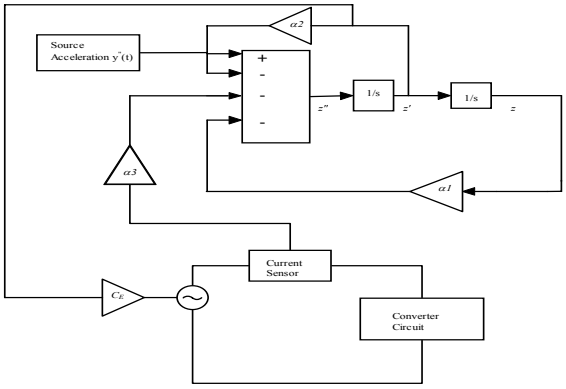

Figure. 5. Mathematical model of an electromagnetic micro generator

III. AC/DC STEP UP CONVERTER

The proposed converter shown in Figure. 6 consists of a boost converter connected in parallel with a buck boost converter. The boost converter consists of an inductor L1, switch S1, diode D1 and the buck boost converter consists of inductor L2, switch S2, diode D2. The output capacitor C is charged by the boost converter during the positive half cycle and by the buck boost converter during the negative half cycle of the sinusoidal input voltage obtained from the micro generator. Here the negative voltage gain of the buck boost converter is used to obtain the dc output voltage during the negative half cycle of the sinusoidal input voltage.

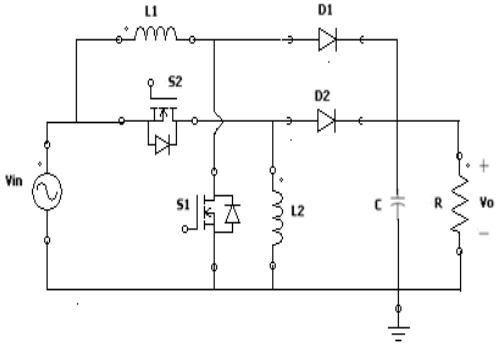

Figure. 6 [2]. Proposed AC/DC step up converter

A. Modes of operation of proposed converter

There are four modes of operation of the proposed converter [2]. Mode 1 and Mode 2 operate during positive half cycle of the input voltage and Mode 3 and Mode 4 operate during the negative half cycle of the sinusoidal input voltage.

Mode 1:

In this mode, since the input voltage is positive, the boost converter operates. When the gate pulse of boost converter is high, switch S1 is on, the inductor L1 stores its energy through the switch S1 as shown in Figure. 7. The inductor current increases from zero as shown in Figure. 8.

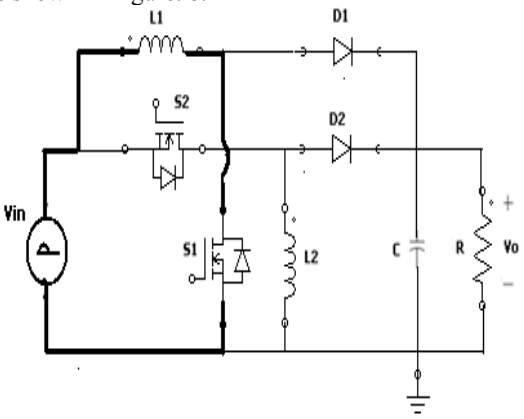

Figure. 7. Mode 1 [2] (Gate pulse of S1 high & Gate pulse of S2 low)

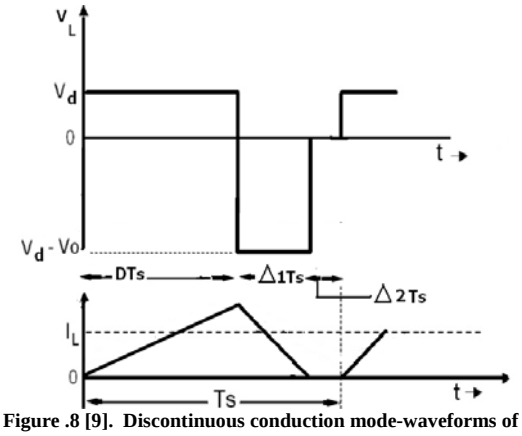

Figure .8 [9]. Discontinuous conduction mode-waveforms of a boost converter

Mode 2:

During positive half cycle, when the switch S1 is off, the diode D1 becomes forward biased and the inductor L1 supplies its energy along with the supply voltage to the load as shown in Figure. 9. The inductor current decreases and becomes zero as shown in Figure. 8.

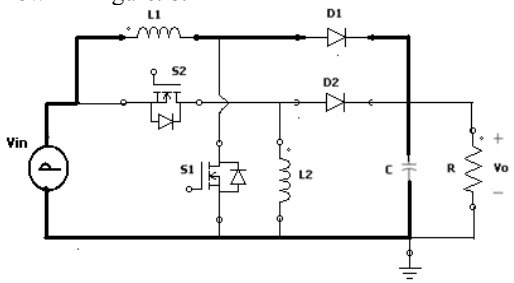

Figure. 9 [2]. Mode 2 (Gate pulse of S1 low & Gate pulse of S2 low)

Mode 3:

During the negative half cycle of the sinusoidal input voltage, buck boost converter operates. When the gate pulse of the buck boost converter is high, the switch S2 is on, the inductor L2 stores its energy as shown in Figure. 10. The inductor current increases as shown in Figure. 11. The capacitor discharges through the load.

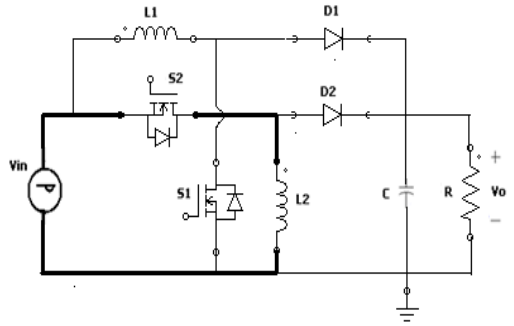

Figure. 10 [2]. Mode 3 (Gate pulse of S1 low & Gate pulse of S2 high)

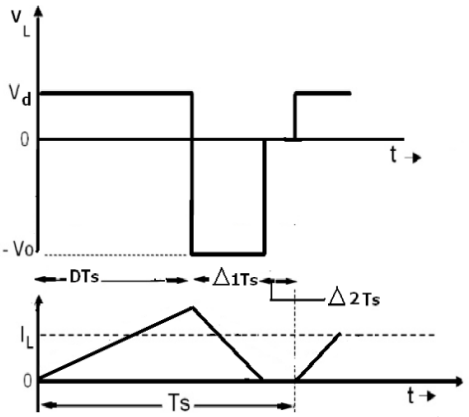

Figure. 11 [9]. Discontinuous conduction mode-waveforms of a buck boost converter

Mode 4:

During the negative half cycle, when the switch is off (as the gate pulse to the buck boost converter is low),

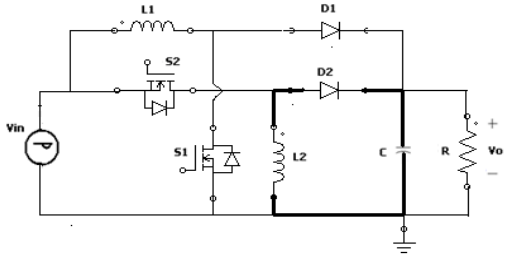

Figure. 12 [2]. Mode 4 (Gate pulse of S1 low & Gate pulse of S2 low)

the diode D2 becomes forward biased, the inductor supplies its energy through the load and also charges the capacitor C as shown in Figure. 12. The inductor current starts to decrease and it becomes zero and tends to become negative. Since the diode is an unidirectional element, it does not allow the inductor current to flow in the opposite direction.

B. Circuit design

The circuit is designed for supplying 55mW of power to the load with a peak to peak input voltage of 800mV which is the output of micro electromagnetic generator. The output voltage is selected to be 3.3V in order to supply the electronic load. The inductor values and the duty cycle of both the boost and buck boost converters are assumed to be equal. The switching frequency is selected as 50 kHz. For the boost converter with DCM, the inductor value can be calculated from equation (10)

$$\Delta I = \frac{V_{in} \times T_{on}}{L} \qquad (10)$$

Where ΔI is the ripple current for an input voltage of V_{in} and an output voltage $V_{out.}$ for a frequency f

where $\frac{1}{f} = T = T_{on} + T_{off}$ (11)

The inductor value is obtained as 4.7µH. The capacitor value is obtained from (12) as 68µF.

$$C \geq \frac{I_{pmax}\pi\left[1-\sqrt{\frac{V_{min}}{V_{max}}}\right]}{f\times\Delta V_0} \quad (12)$$

The output current is calculated from (13)

$$I_0 = \frac{P}{V_{min}} \quad (13)$$

The inductor value for buck boost converter is also chosen to be 4.7µH. The value of the resistor is obtained from (14).

$$R = \frac{V_{min}}{I_0} \quad (14)$$

C. Simulation circuits and Simulation results

The micro electromagnetic generator is modeled and simulated in Power Electronic software PSIM© as shown in Figure. 13. With the design values, the power circuit and the control circuit have also been simulated and satisfying results have been obtained.

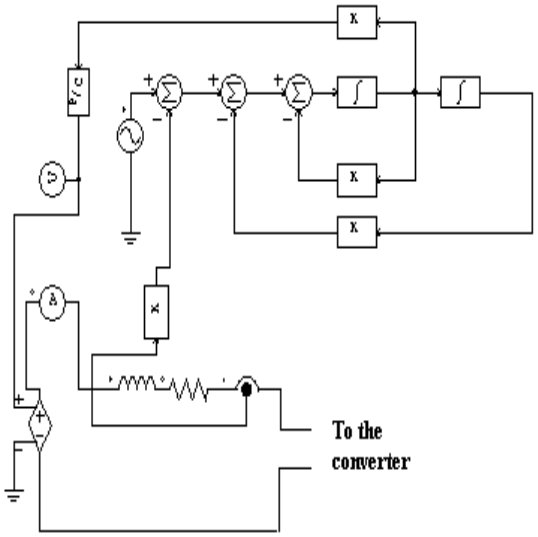

Figure. 13. Simulation circuit of mathematical model of the electromagnetic micro generator.

The values of $\alpha 1$, $\alpha 2$, $\alpha 3$& C_E have been calculated from parameters of electromagnetic micro generator [1]. The input source acceleration with a magnitude of 0.2m and a frequency of 108 Hz as shown in Figure. 14, is given as an input to the generator. It can produce a peak to peak output voltage of 800 mill volts as shown in Figure. 15.

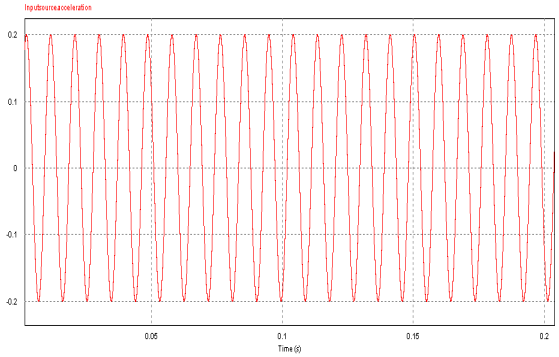

Figure. 14. Input source acceleration

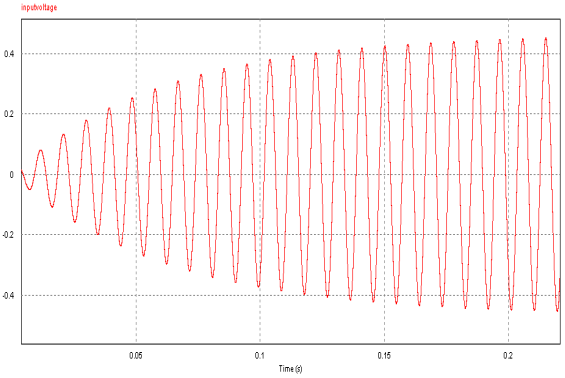

Figure. 15. Micro generator output voltage

The rms value of the micro generator output current was found to be 1.28A.

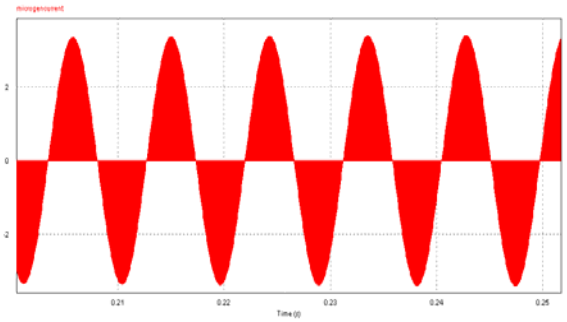

Figure. 16. Micro generator output current

The closed loop control has been implemented in the simulation. The simulation circuit of the converter part is shown in Figure. 17. The reference output voltage is set as 3.3V as required for an electronic load. The electronic load is modeled as a resistor.

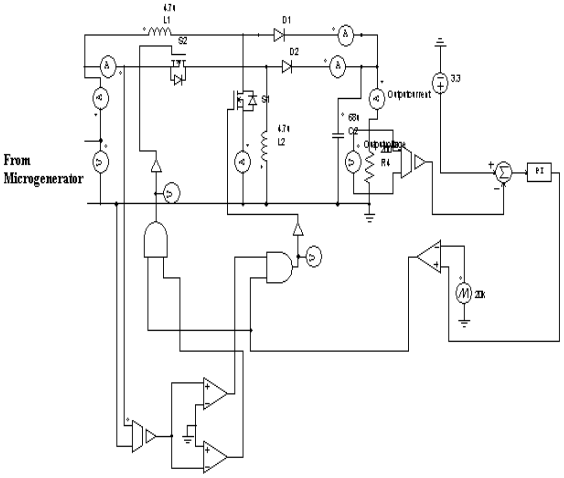

Figure. 17. Simulation circuit of the proposed converter

The discontinuous conduction of boost and buck boost converters can be clearly observed from Figure. 18 & Figure. 19. The feedback from the output is taken and is compared with the reference value and the error is fed to PI controller and the output of the PI controller is compared with the saw tooth waveform and PWM signals are obtained. The saw

tooth waveform and the PI controller output as shown in Figure. 20.

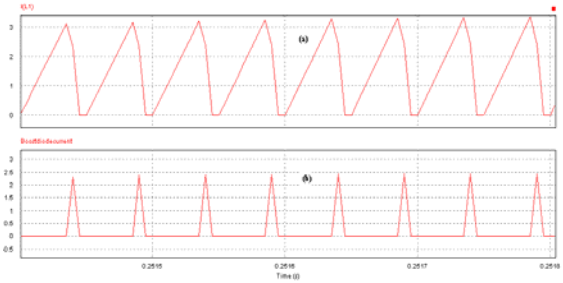

Figure. 18. (a) Variation of boost inductor current with time (b) Variation of boost diode current with time

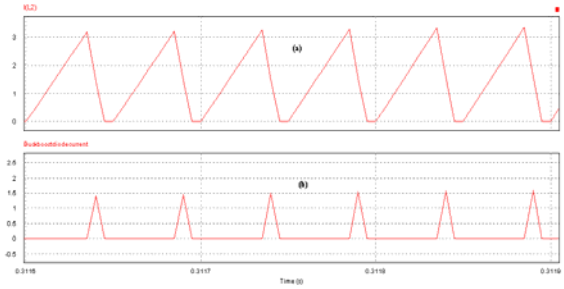

Figure. 19. (a) Variation of buck boost inductor current with time (b) Variation of buck boost diode current with time

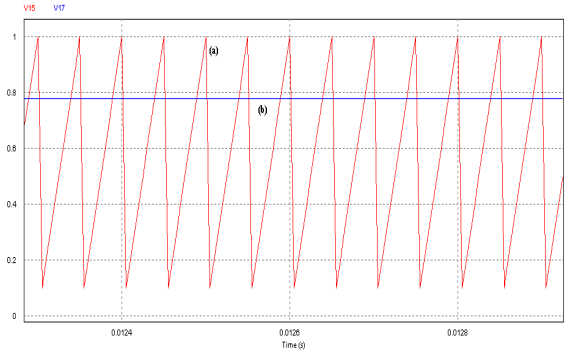

Figure. 20. (a) Saw Tooth Waveform (b) PI controller output

The gate pulses of boost and buck boost converter switches are shown in Figure. 21. The gate of the MOSFETs is switched on by the PWM output based on the output of the zero crossing detector.

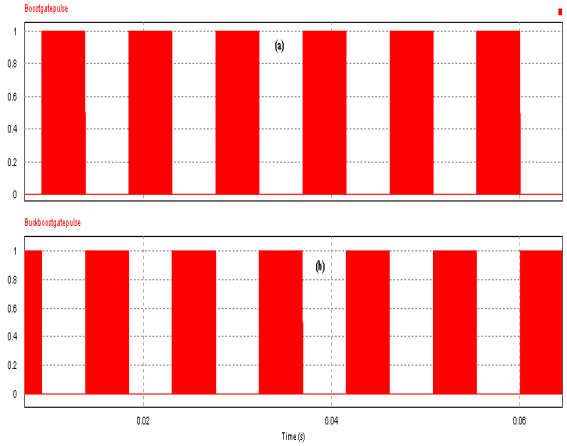

Figure. 21. (a) Boost gate pulses (b) Buck boost gate pulses

The input voltage of the converter is an ac voltage with a peak of 400mV and the output voltage is a regulated dc voltage which settles at 3.16V as shown in Figure. 22. (a). The output current also settles at 0.0158A as shown in Figure. 22. (b).

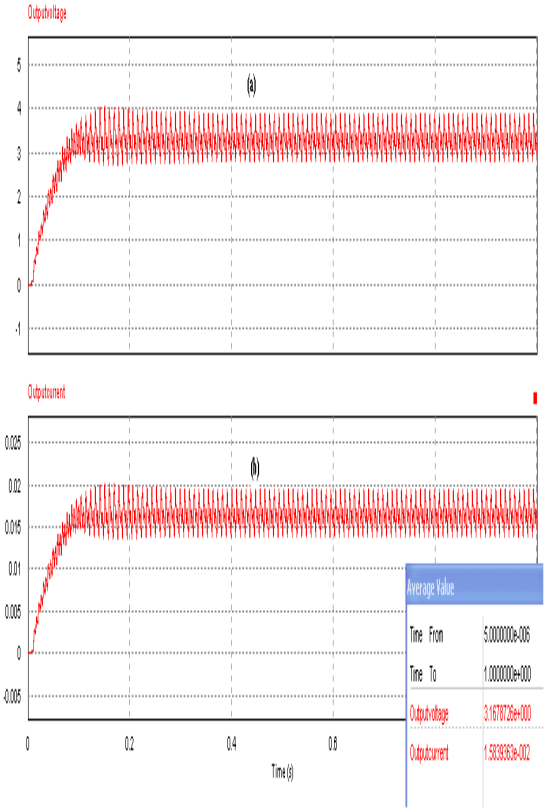

Figure. 22. (a) Variation of output voltage with time (b) Variation of output current with time

IV. CONCLUSION

The low voltage energy harvesting is achieved here since the input supply to this converter is from an electromechanical micro generator which scavenges the energy from ambient sources such as vibration. An ac/dc step up converter using boost and buck boost converters which operate during positive and negative half cycles respectively has been designed and simulated successfully. It has been found that when the peak input voltage is varied from 373mV to 446mV the average value of output voltage varies from 3.02V to 3.16V.

REFERENCES

[1] RohanDayal, SumanDwari, Leila Parsa,"A New Design for Vibration-Based Electromagnetic Energy Harvesting Systems Using Coil Inductance of Microgenerator" in IEEE Transactions on Industry Applications. Vol.47, No.2, March/April 2011.

[2] S. Dwari and L. Parsa, "A novel direct AC/DC converter for efficient low voltage energy harvesting," n IEEE

Transactions on Power Electronics, V0l. 25, No. 8, August 2010.

[3] S. Dwari, R. Dayal, and L. Parsa, "An efficient AC/DC converter for efficient low voltage energy harvesting," in Proc. IEEE Ind. Electron.Soc.Annu. Conf., Nov. 2008, pp. 484-488.

[4] Enrico Dallago, Marco Marchesi, and Giuseppe Venchi, "Analytical Model of a Vibrating Electromagnetic Harvester Considering Nonlinear Effects", in IEEE TransactionsOn Power Electronics' Vol.25, No. 8,August 2010.

[5] B. H. Stark, P. D. Mitcheson, M. Peng, T. C. Green, E. Yeatman, and A. S. Holmes, "Converter circuit design, semiconductor device selection and analysis of parasitics formicropower electrostatic generators," IEEE Trans. Power Electron., vol. 21, no. 1, pp. 27–37, Jan. 2006.

[6] E. Lefeuvre, D. Audigier, C. Richard, and D. Guyomar, "Buck-boost converter for sensorless power optimization of piezoelectric energy harvester,"IEEE Trans. Power Electron., vol. 22, no. 5, pp. 2018–2025, Sep.2007.

[7] Scott Meninger, Jose Oscar Mur-Miranda, Rajeevan Amirtharajah Anantha Chandrakasan and Jeffrey Lang "Vibration-to-electric energy conversion," IEEE Trans.Very Large Scale Integr. Syst., vol. 9, no. 1, pp. 64–76, Feb.2001.

[8] X. Cao,W.-J. Chiang,Y.-C.King, andY.-K. Lee, "Electromagnetic energy harvesting circuit with feedforward and feedback DC–DC PWM boost converter for vibration power generator system," IEEE Trans. PowerElectron., vol. 22, no. 2, pp. 679–685, Mar. 2007.

[9] Ned Mohan, Power Electronics, Converters, Applications and Design John Wiley &Sons Inc.

[10] Gorlatova, M., Wallwater, A., Zussman, G. "Networking low-power energy harvesting devices: Measurements and algorithms,"Mobile Computing, IEEE Transactions on Volume: PP , Issue: 99 2012.

[11] El-Anzeery, H.M.G.E.-D.M.; El-Bagouri, M.A.E.-A.S.; Guindi, R."Novel radio frequency energy harvesting model" Power Engineering and Optimization Conference (PEDCO) Melaka, Malaysia, 2012 Ieee International pp. 209 – 213,2012.

DIRECT CURRENT CONTROL BASED PWM RECTIFIER FOR THREE PHASE VOLTAGE SOURCE

R.NARESH[1], V.SRINIVAS[2] & K.NARESH[3]

[1,3]Bomma engg. college
[2]Nigama Engg. College Assoc.

Abstract- This paper is concerned with the design and simulation of a pulse width modulation (PWM)rectifier for three-phase Permanent Magnetic motor drive. Based on the mathematical model of PWM rectifier, the dual-close-loop engineering design with decoupled feed-forward control is applied in the 3- phase voltage source rectifier. The objective to be reached is to realize unity power factor at the input ac mains and regulate output voltage. The paper presents the MATLAB/SIMULINK simulation model.The results confirm the validity of the model and its control method.

***Keywords**: PWM rectifier, unity power factor, decoupled feed-forward control*

1. INTRODUCTION

Power electronics equipments become more widely used. Unfortunately, the standard diode/Thyristor bridge rectifiers at the input side cause several problems as: Low input power factor, high values of harmonic distortion of ac line currents, and harmonic pollution on the grid. In recent years, the research interest in the area of PWM rectifiers has grown rapidly [1] [2]. The PWM rectifier offers several advantages such as: control of DC bus voltage, bi-directional power flow, unity power factor, and sinusoidal line current. Many pulse-width modulation (PWM) techniques have been adopted for these rectification devices to improve the input power factor and shape the input current of the rectifier into sinusoidal waveform. The phase and amplitude control (PAC) seems to be the most simple structure and provides a good switching pattern, but the dc offset on input current of the rectifier during transient state deteriorates the control system stability. The current regulating fashion in synchronous frame has the advantages of fast dynamic current response, good accuracy, fixed switching frequency and less sensitive to parameter variations [3]. In actual implementations, the direct current control scheme is widely adopted. Various control strategies have been proposed to regulate the dc bus voltage while improving the quality of the input ac current in direct current control scheme [4]. The traditional control strategies establish two loops: a line current inner loop of power factor compensation and an output voltage outer loop for voltage regulation. In this paper, the design method and controller model based on direct current control are analyzed. This paper briefly reviews the principles and the topologies of 3-phase PWM rectifier, gives a dual- close-loop design method of system controller. The control strategy is proved feasibility by MATLAB/SIMULINK simulation with different loads.

2. THREE-PHASE RECTIFIER MODEL VOLTAGE SOURCE PWM

Figure 1 shows the circuit diagram of the three-phase voltage source rectifier structure. In order to set up math model, it is assumed that the AC voltage is a balanced three phase supply, the filter reactor is linear, IGBT is ideal switch and lossless [5]. Where ua , ub and uc are the phase voltages of three phase balanced voltage source, and ia , ib and ic are phase currents, vdc is the DC output voltage, R1 and L mean resistance and inductance of filter reactor, respectively, C is smoothing capacitor across the dc bus, RL is the DC side load, ura , urb , and urc , are the input voltages of rectifier, and iL is load current.

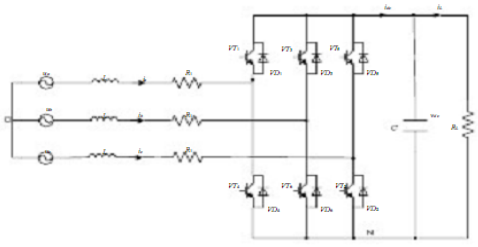

Figure 1. Circuit schematic of three-phase two-level boost-type rectifier

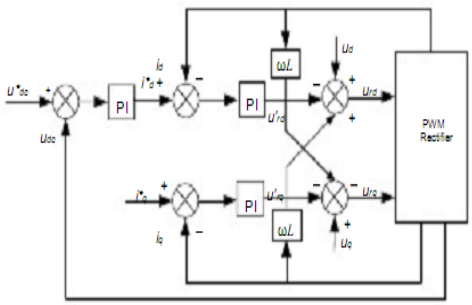

Figure 2. Control block diagram of d-q dual-close-loop controller of the rectifier

The following equations describe the dynamical behavior of the boost type rectifier in Park coordinated

$$\begin{cases} L\dfrac{di_d}{dt} = u_d - i_d R_1 + \omega L i_q - u_{rd} \\ L\dfrac{di_q}{dt} = u_q - i_q R_1 - \omega L i_d - u_{rq} \\ C\dfrac{dV_{dc}}{dt} = -\dfrac{V_{dc}}{R_r} + \dfrac{3}{2}(S_d i_d + S_q i_q) \end{cases} \quad (1)$$

Where, $u_{rd} = S_d V_{dc}$, $u_{rq} = S_q V_{dc}$, u_{rd}, u_{rq} and S_d, Sq are input voltage of rectifier, switch function in synchronous rotating ds-q coordinate, respectively. ud , uq and id , iq are voltage source, current in synchronous rotating d-q coordinate, respectively. is angular frequency.

2.1. Design of current

loop It is seen from (1) that mutual interference exists in the d-q current control loops. The voltage decouplers are therefore designed to decouple the current control loops and suitable feed forward control components of source voltages are also added to speed up current responses. The d–q current control loop of the rectifier in the proposed system is shown in Figure 2. Where the d – q voltage commands can be expressed as

$$\begin{cases} u_{rd} = -u'_{rd} + \omega L i_q + u_d \\ u_{rq} = -u'_{rq} + \omega L i_d + u_q \end{cases} \quad (2)$$

Let us take into account this assumption in (1) and get the following equations:

$$\begin{cases} L\dfrac{di_d}{dt} = -i_d R_1 + u'_{rd} \\ L\dfrac{di_q}{dt} = -i_q R_1 + u'_{rq} \end{cases} \quad (3)$$

The simple proportional-integral (PI) controllers are adopted in the current regulation, urd and urq are

$$\begin{cases} u_{rd} = -(K_{ip} + \dfrac{K_{iI}}{s})(i^*_d - i_d) + \omega L i_q + u_d \\ u_{rq} = -(K_{ip} + \dfrac{K_{iI}}{s})(i^*_q - i_q) + \omega L i_d + u_q \end{cases} \quad (4)$$

As sume that the d–q voltage commands are not saturated for linear operation of PWM modulation and the d–q current control loops have been fully decoupled. For d-axis current control loop, the structure can be simplified to Figure 3.

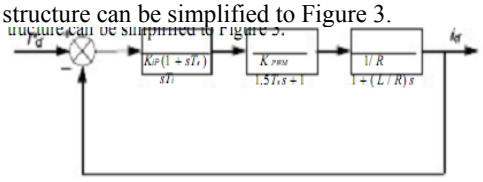

Figure 3. Equivalent control block diagram of the d–q current control loop

When the current responses speed is concerned, the current regulator can be designed as the typical model system. For pole-zero cancellation, take Ti = L / R . The open-loop current transfer function can be expressed as

$$W_i(s) = \frac{K_{iP} K_{PWM}}{RT_i s(1.5T_s + 1)} \quad (5)$$

According to Parameter adjusting method for typical model system, when damping ratio =0.707, we have the following equation

$$\frac{1.5T_s K_{iP} K_{PWM}}{RT_i} = \frac{1}{2} \quad (6)$$

The parameters of the PI controller should bechosen as

$$\begin{cases} K_{iP} = \dfrac{RT_i}{3T_S K_{PWM}} \\ K_{iI} = \dfrac{K_{iP}}{T_i} = \dfrac{R}{3T_s K_{PWM}} \end{cases} \quad (7)$$

2.2. Design of voltage loop

The transfer function of voltage regulator is

$$G(s) = K_{vP}\frac{1+T_v}{T_v s} \quad (8)$$

$$K_{vI} = \frac{K_{vP}}{T} \quad (9)$$

By Figure 4, the open transfer function of system can be expressed as

$$W_{ov}(s) = \frac{0.75K_{vP}(1+sT_v)}{CT_v s^2(4T_v s+1)} \quad (10)$$

Due to the main function of voltage control loop is to keep stability of output voltage, so the noise immunity must be taken into account in the course of design voltage loop. The proper choice to this end is to adopted typical û model system. So

$$\frac{0.75K_{vP}}{CT} = \frac{h_v + 1}{32h^2 T^2} \quad (11)$$

Where, $h_v = T_v / 4T_s$ is the frequency width in the voltage loop, take $h_v = 5$, then

$$T_v = 20T_s \quad (12)$$

Finally the result obtained is

$$\begin{cases} K_{vP} = \dfrac{C}{5T_s} \\ K_{vI} = \dfrac{K_{vP}}{20T_s} \end{cases} \quad (13)$$

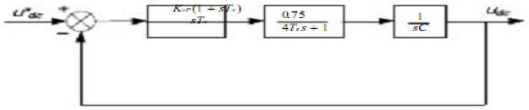

Figure 4. Equivalent control block diagram of the voltage control loop

3. SIMULATION RESULTS

The decoupled dual-close-loop controller has been simulated using MATLAB/SIMULINK to test the performance of VSC described by the proposed model. The whole system behavior is simulated as a discrete control system. The simulation model is shown in figure 5 and figure 6. The actual rectifier is shown at the top of the model in figure 5. In the circuits, the ac source is an ideal balanced three-phase voltage source with frequency of 50Hz. The phase to phase voltage is 380V. The line resistor of each phase is 0.0lΩ. The line inductance of each phase is 5mH. The output capacitor is 4700uF. In steady state, the dc voltage is set to be 500V. The switching frequency is 10kHz.

$$T_v = 20T_s \qquad (12)$$

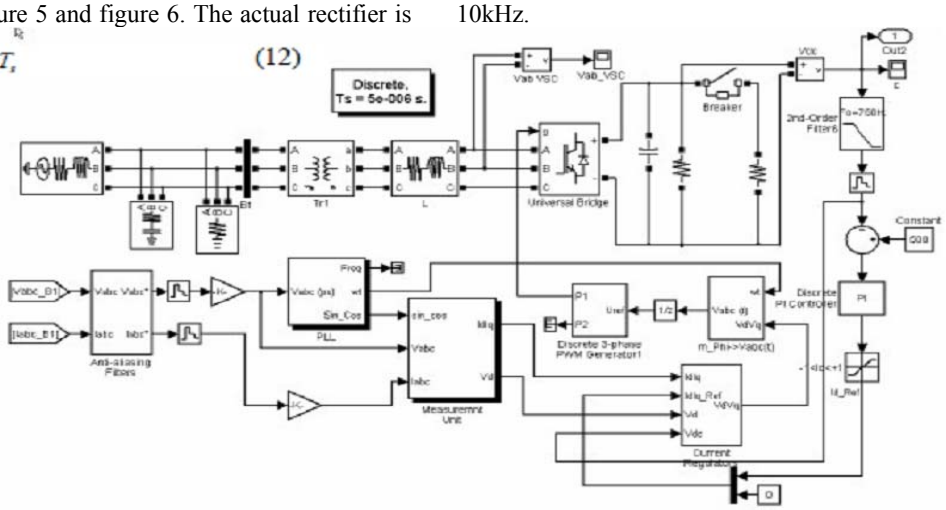

Figure 5.Three-phase voltage source PWM rectifier system mode

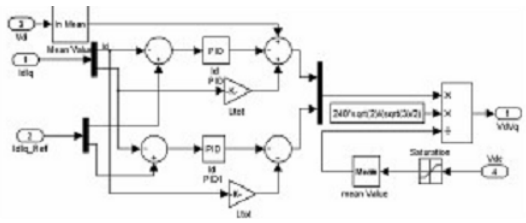

Figure 6.The current regulator unit

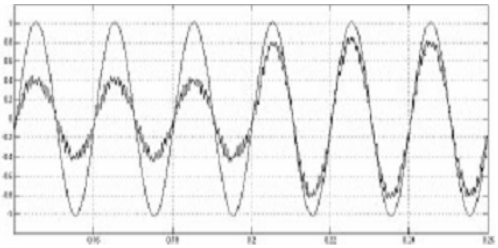

Figure 8 Simulation result for line current

The following two figures summarize the results of the simulation. The first figure shows the transient response of the output voltage during the load variation. The second figure shows transient response of input current for a step load change. At t=200 ms, a 10-kW load is switched-in. We can see that the dynamic response of the DC regulator to this sudden load variation (10 kW to 20 kW) is satisfactory. The DC voltage is back to 500 V within 1.5 cycles and the unity power factor on the AC side is maintained.

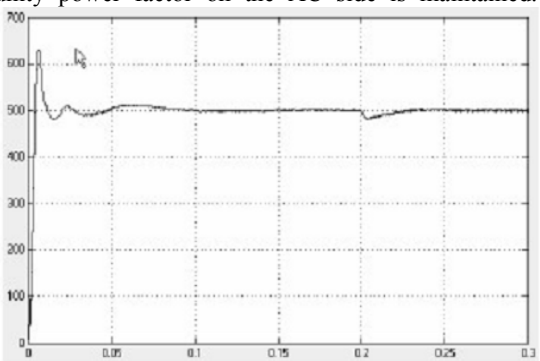

Figure 7 Simulation result for DC-Link voltage dynamics

4. CONCLUSION

In this paper, a major improvement is obtained inmodeling the rectifier. By using nonlinear input transformation, the conventional nonlinear models can be improved to linear models. This improvement makes the design of the controller become straightforward [6]. The controller can be designed analytically and independently with the operating point. Decoupled feed-forward controller for 3-phase voltage source rectifier is designed in the paper. Simulation result shows that very fast response can be achieved in both dc quantity and reactive power control. The solution proposed in this paper requires the sensing of input voltage, line current and output voltage. Generally speaking, industrial loads for this rectifier are variable loads, this being the main drawback to obtain simple controllers. Achieving robustness to load variations is not a simple control problem because whenever load varies, the amplitude of the line current must change to a new value to keep dc voltage regulation, but keeping the control objective over the line current shape. It is difficult to

treat this problem as a tracking problem without measuring the load since the line current reference depends on it. A robust controller for rectifier using the IDA approach and GSSA modeling is proposed in [7].It is said that the method transform the nonstandard tracking control problem into a regulation one. The same solution by the IDA-PBC is presented in Work [8].But it is worth to further study to prove the feasibility in actual implementations.

REFERENCES

[1] Ricardo Luiz Alves, and Ivo Barbi,"A New Hybrid HighPower Factor Three-Phase Unidirectional Rectifier",Industrial Electronics, 2006 IEEE International Symposiumon Volume 2, July 2006 pp.1046 – 1051.

[2] Ye, Y., Kazerani, M., Quintana, V.H., "A NovelModeling and Control Method for three-pahse PWMconverters", Power Electronics Specialists Conference, 2001.PESC. 2001 IEEE 32nd Annual Volume 1, 17-21 June 2001,pp.102 – 107

[3] Jninne-ChingLiao, Sheng-NianYeh, "A Novel Insantaneous Power Control Strategy and Analytic Model for Integrated Rectifier/Inverter Systems, IEEE Transactionon Power Electronics,2000 VOL. 15, NO. 6, pp.996- 1006.

[4] Mariusz Malinowski, Marian P. Kazmierkowski, Andrzej M. Trzynadlowski, "A Comparative Study of Control Techniques for PWM Rectifiers in AC Adjustable SpeedDrives",IEEE TRANSACTIONS ON POWER ELECTRONICS, VOL. 18, NO. 6, NOVEMBER 2003,pp.1390 – 1396.

[5] Wang Jiuhe, Yin Hongren, Zhang Jinlong, and Li Huade,"Study on Power Decoupling Control of Three Phase Voltage Source PWM Rectifiers", Power Electronics and Motion Control Conference, 2006

[6] Z. Yang, and L. Wu, "A new Passivity-Based Control Method and Simulation for DC/DC Converter", Proceedings of the 5th World Congress on Intelligent Control and Automation, Hangzhou, P. R. China, June 15-19, 2004, pp.5582-5585.

[7] Z. Yang, and L. Wu, "A new Passivity-Based Control Method and Simulation for DC/DC Converter", Proceedings of the 5th World Congress on Intelligent Control and Automation, Hangzhou, P. R. China, June 15-19, pp.5582-5585.

A COMPARISON OF MOSFET AND GTO BASED AC-AC VOLTAGE STABILIZER REGULATED BYBUCK-BOOST MODE

PRIYA JOSE[1], ANNA MATHEW[2] & K R VARMAH[3]

[1,2&3]Department of Electrical and Electronics Engineering, Rajagiri School of Engineering and Technology Kakkanad.

Abstract—Voltage stabilizer is an essential part of the electrical appliances due to power quality problems. They are designed for wide range of input fluctuations to maintain specified output voltage. For voltage regulation, conventional topology uses a multitappedtransformer with compensating transformer. The limitations of conventional topology are, low correction speed of voltage fluctuations, heavy and bulky system, high maintenance cost, high service cost and the limitation of available taps. In order to overcome the limitations of conventional topology, a new electronic AC-AC voltage stabilizer is proposed. In the new electronic AC-AC voltage stabilizer, the multitapped transformer used in the conventional topology is replaced with an H-bridge AC chopper.In the paper two topologies are proposed for a new electronic AC-AC voltage stabilizer by replacing the multitapped transformer. First topology uses eight switches whereas the second uses only four switches. Both topologies use an H-bridge chopper. In the eight switch H-bridge chopper GTOs are used as switches and in the four switch H-bridge chopper MOSFET is used for chopping. To eliminate harmonic distortion PWM switching are used for the switches. Comparing the two topologies, the four switch topology is seen more advantageous over eight switch topology for household applications. The circuit for MOSFET and GTO is modelled using the power electronics software PSIM©.

Index Terms— *Ac-Ac Regulator,Compensating transformer,PWM switching*

I. INTRODUCTION

Stabilizer is the Automatic Voltage regulator, which regulates the output power. It produces the output voltage as per customer demand for the appliance. Voltage stabilizers are an effective solution to voltage fluctuation problems. They are designed for wide range of input fluctuations to maintain specified output voltage. The output voltage waveform is completely distortion free and the regulation is unaffected by the load power factor.The power quality issues like sag, swell, interruptions, imbalance make variations in the supply voltage.Voltage stabilizer allows output voltage to remain at the desired level despite of the input voltage variations.In the conventional topology a multi tapped transformer and a compensating transformer is used. It is used for generating the control voltage [1], [2] for compensation. In this topology tap changers are used for changing the taps. These tap changer are
operated by a servo motor. The main objective of a tap-changer is to stabilise the amplitude of the output voltage. The major task of the controller in the tap-changer system is to minimize the fluctuation of voltage amplitude with respect to the reference voltage of the regulation bus. This bus could be far from the secondary of the transformer. The compensating transformer will isolate the control circuit from the power circuit. As the number of turns in the secondary side of the compensating transformer is more than the primary side, a fraction of load current will pass through the switching devices.The limitation of conventional topology is,Wear and tear due to the mechanical movement, requiresperiodic replacement of brushes,due to low correction speedthere will be voltage overshootand voltage dip,heavy and bulky, low response, Possibility of arcing, high maintenance cost, high service cost and the limitation of available taps.Some of the limitations of servo mechanism can be overcome by replacing tap changerswith relays [4], [5]. According to the difference in the input voltage and output voltage, a control voltage will generate and the control voltage will operate therelay. So proper tapping for generating the compensating voltage is selected by the relay. But the limitation of this mechanism is periodic maintenance due to relay failure, poor regulation, interrupts load current duringstep change.

Then a new topology is evolved with double stage conversion of AC-AC in buck mode and boost mode. In this topology either stepping up or stepping down is carried out.It requires freewheeling period, for that itneeds two more switch in each mode[8].So system will be more complex with six switches. Also a complex control strategy is needed. This paper introduces a twonew topology which is more efficient than above topologies. In the first topology replaces the multitapped transformer with four switches of MOSFET. So the action of these four switches generates the control voltage.In the second topology replaces the multitapped transformer with eight switches of GTO. So the action of these switches generates the control voltage.The new topologies has the advantages of no moving part, less maintenance, tight regulated output +/-1%, Fast correction speed, Low cost in higher KVA, high

efficiency, no arcing,and better accuracy with wide stabilizing voltage range due to the utilisation of PWM switching.By the new topology the control voltage can be varied continually, so that wide range of voltage control is possible.

II. PROPOSED AC-AC REGULATOR USING FOUR SWITCHES

The power circuit for AC-AC voltage stabilizer is shown in Fig. 1.The circuit is designed for a RL load. It has four switches; Power MOSFET is used as the switch. Each switch has four diodes for bidirectional flow. A compensator transformer is used for adding and subtracting a control voltage from the input voltage.

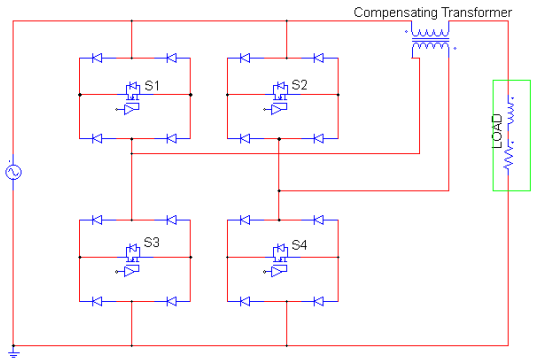

Fig. 1 AC-AC voltage Stabilizer

The regulator is capable of stepping up or stepping down the input voltage, depending on the selected switching devices. Four AC switches (S_1, S_2, S_3, and S_4) are arranged as an “H-bridge". Switching through $S_1$and S_4adds a control voltage to the input supply voltage. While switching through $S_2$and S_3subtracts a control voltage from the input supply voltage through the compensating transformer.

In the first half of the switching cycle S_1 and S_4 will operate, by which a control voltage is added to the input voltage, then the output voltage is boosted. For the next half cycle S_2 and S_3 will operate, so the control voltage is reduced from the input voltage. In effect the output voltage is reduced. The effect of above two is averaged in a switching cycle which will be the actual output voltage. If the operating period of S_2 and S_3 is more than S_1 and S_4 in a switching cycle,the actual output voltage will be less than the input voltage. If the operating period of S_1 and S_4 is more than S_2 and S_3 in a switching cycle,the actual output voltage will be more than the input voltage. Four modes of operation of the new topology is shown in Fig. (2), (3), (4), and (5).

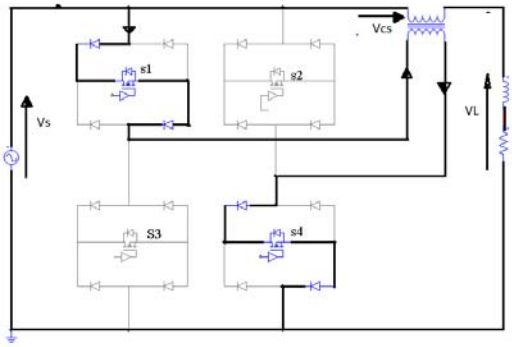

Fig 2.S_1& S_4 is active for positive half cycle

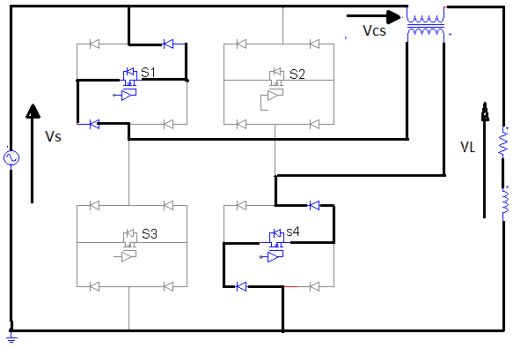

Fig 3.S_1& S_4 active for negative half cycle

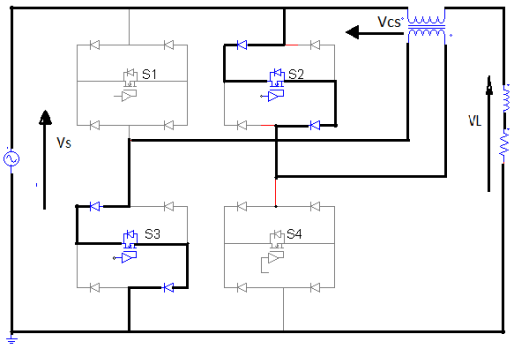

Fig 4 S_2 &S_3 active for positive half cycle

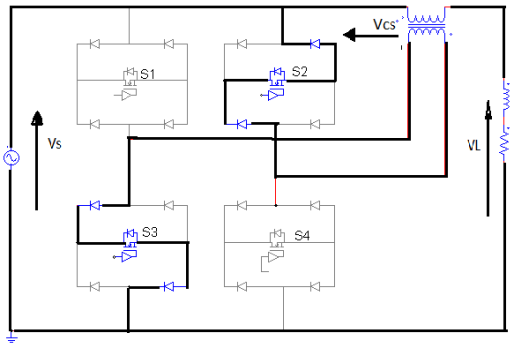

Fig 5.S_2& S_3 is active for negative halfcycle

III. PROPOSED AC-AC REGULATOR USING EIGHT SWITCHES

In the proposed regulator eight switches(GTOs) are used to form the H-bridge. Eight switches are arranged as four pairs.In each pair two GTOs are connected as antiparallel for bidirectional flow is shown in Figure 6.

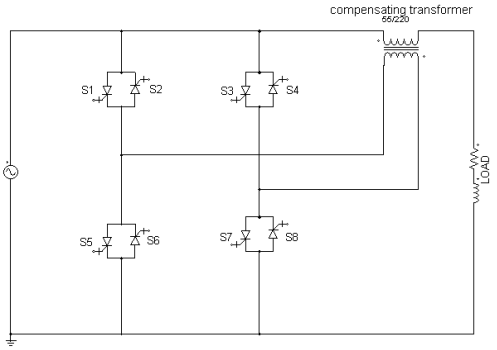

Fig 6.AC-AC regulator using GTO

During positive half cycle of input voltage switches S1 and S7 will operate for boosting the input voltage then switches S3 and S5 will operate for stepping down the input voltage. The above switching operation will continue alternatively till the end of the positive half cycle. Operating time of the switches will be calculated by the processor by sensing the input voltage. The mode of operation during positive half cycle is shown in Figure 7 and Figure 8. During negative half cycle of input voltage, switches S2 and S8 will operate for boosting the input voltage. Switches S4 and S6 will operate for stepping down the input voltage. The above switching operations will continue alternatively till the end of the negative half cycle. Operating time of the switches will be calculated by the processor after sensing the input voltage. The mode of operation during negative half cycle is shown in Figure 9 and Figure 10

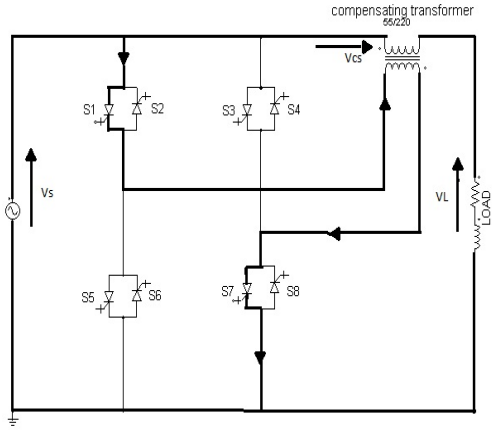

Fig 7.S_1& S_7 is active for positive half cycle

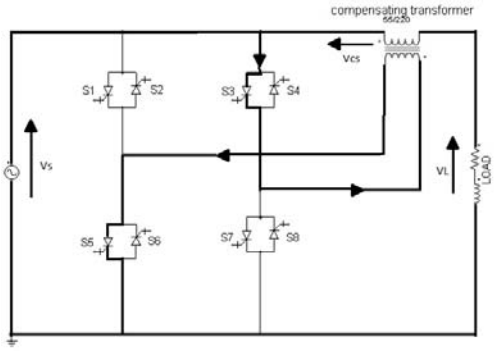

Fig 8.S_3& S_5 active for positive half cycle

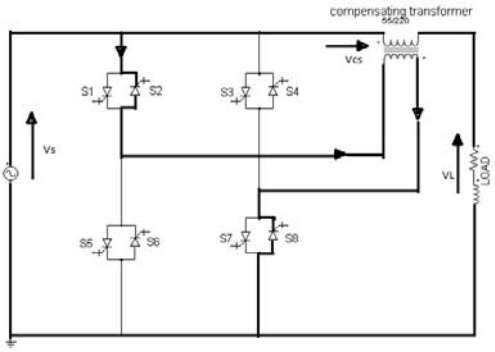

Fig 9S_2 &S_8 active for negative half cycle

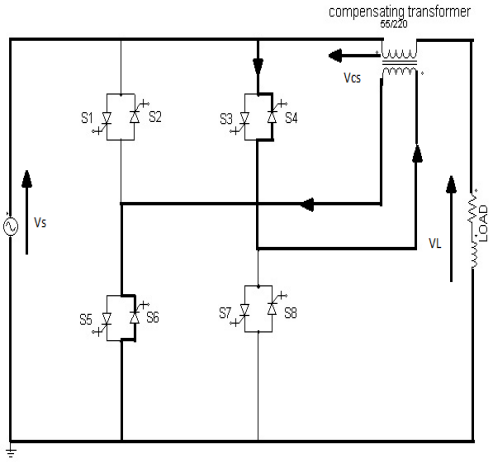

Fig 10. S_4& S_6 is active for negative half cycle

IV. CIRCUIT DESIGN

The proposed regulator circuit is shown in Fig.1.The input supply voltage can be expressed as Vs, and the output voltage at the load terminal can be expressed as V_L .The load voltage is the sum of the supply voltage (Vs) and the secondary voltage (V_{cs}) of the compensating transformer. The primary voltage of the compensating transformer is (V_{cp}). The duty ratio of the pwm switching pulse is expressed as D. The specification of the Ac-Ac voltage stabilizer is shown in Table Iand the switching sequence is shown in Table II.

TABLE I
SPECIFICATION OF AC-AC STABILIZER

Quantity	Value
Number of Phases	1
Rated Input Voltage	220V,(Peak)
Stabilized Output Voltage	220V,(Peak)
Percentage of Input Voltage Variation	79% - 131%
Output power	500VA
PWM Switching Frequency	50 KHz
Compensating transformer power	300VA

TABLE II
SWITCHING SEQUENCE

ACTIVE SWITCH	LOAD VOLTAGE	MODE
S_1& S_4	$V_L=V_S+V_{cs}$	BOOST
S_2&S_3	$V_L=V_S-V_{cs}$	BUCK

$$V_s(\omega t) = \sqrt{2V_s}\sin(\omega t)$$

In the boost converter mode

$$V_{cs}(\omega t) = D * \left(\frac{N_s}{N_P}\right) * V_{cp}(\omega t) \quad (1)$$

$$;0.5 \le D \le 1$$

Where $V_{cp}(\omega t) = V_s(\omega t)$ (2)

$$V_L(\omega t) = \left(\left(D * \left(\frac{N_S}{N_P}\right)\right) + 1\right) * V_S(\omega t) \quad (3)$$

$$; 0.5 \le D \le 1$$

In the buck converter mode

$$V_{cs}(\omega t) = D * \left(\frac{N_s}{N_P}\right) * V_{cp}(\omega t); 0 \le D \le 0.5 \quad (4)$$

Where $V_{cp}(\omega t) = -V_s(\omega t)$(5)

$$V_L(\omega t) = \left(1 - \left(D * \left(\frac{N_S}{N_P}\right)\right)\right) * V_S(\omega t) \quad (6)$$

The supply current $I_s$is the sum of load current I_L and transformer primary current $I_{cp.}$

$$I_s(\omega t) = I_L(\omega t) + I_{cp}(\omega t) \quad (7)$$

$$I_L(\omega t) = I_{cs}(\omega t) = \frac{V_L(\omega t)}{z} \quad (8)$$

$$I_{cp}(\omega t) = I_L(\omega t)\left(\frac{N_{cs}}{N_{cp}}\right) \quad (9)$$

RMS input supply power (P_s)=I_sV_s(10)

Output load power (P_L) =I_LV_L(11)

Compensating transformer power (P_c) =$I_{cs}V_{cs}$(12)

$P_c = I_L\left(\frac{N_{cs}}{N_{cp}}\right)V_S$(13)

Where load impedance is Z_L

$$Z_L = \sqrt{{X_L}^2 + {R_L}^2} \quad (14)$$

V. CONTROL CIRCUIT DESIGN

A. CLOSED LOOP CONTROL

In the closed loop mode if the input voltage is varied from required voltage, an error voltage will generate.That error voltage is passed through a PI. The PI will generate a signal which will compensate for the error voltage. The signal from the PI is compared with the saw tooth wave form. The amplitude of the saw tooth should be greater than the compensated error signal; otherwise no pulse will be generating at zero error from the comparator. The duty ratio of the PWM pulses from the comparator is varying to get stabilized output voltage. The control circuitis shown in Figure.11.

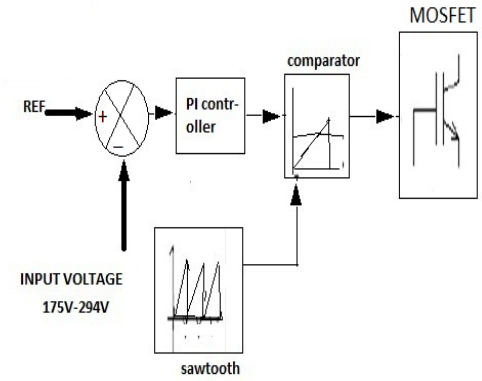

Fig 11.Control circuit

VI. SIMULATION RESULTS

The power circuit and the control circuit were simulated as per the design using PSIM software and satisfactoryresults were obtained. As shown in the simulation results the average output voltage remains within the limits of set value 220V even if input voltage fluctuates. The allowable input voltage variation is from 175V to 298V.The LC filter is introduced in the primary side of the compensating transformer to smoothen the control voltage.

TABLE III
SIMULATION PARAMETER

Resistor	100 Ω
Inductor	1 mH
LC Filter	100 mH, 5µF
Compensating Transformer	350VA,55/220

VII. SIMULATION RESULT OF AC-AC REGULATOR USING MOSFET

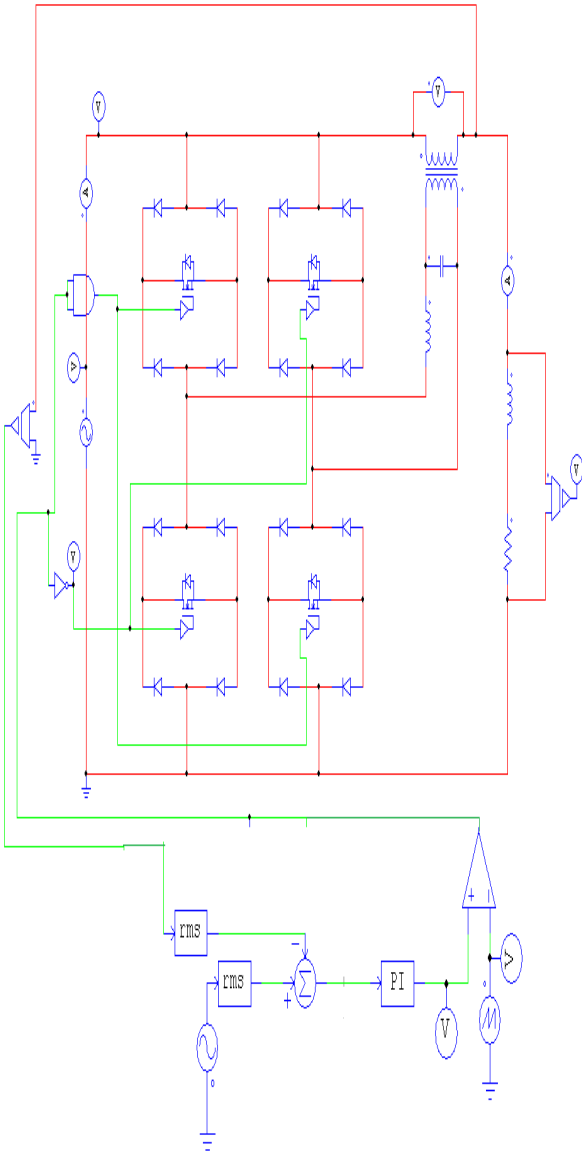

Fig.12.Closed loop control of four switch AC-AC regulator

The simulation result of closed loop control for 13% rise in input voltage is shown in Fig.13, Fig.14 and Fig15. Observing the wave form, we can see that 13% rise in input voltage is compensated by the control voltage of 30V.

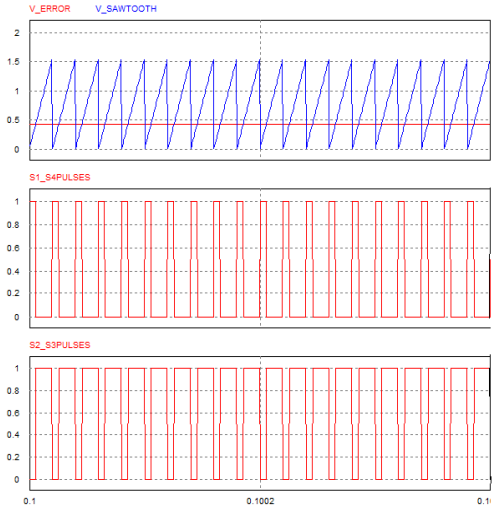

Fig.13.Switching pulse generation for 13% rise in input voltage

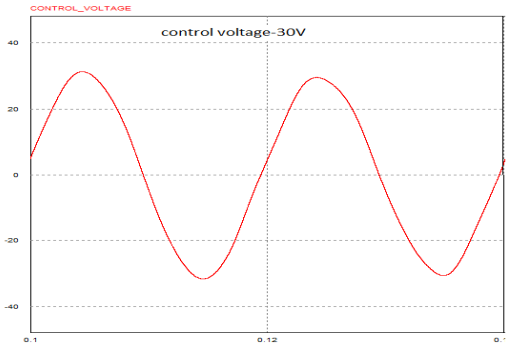

Fig.14.control voltage generated for 13% rise in input voltage

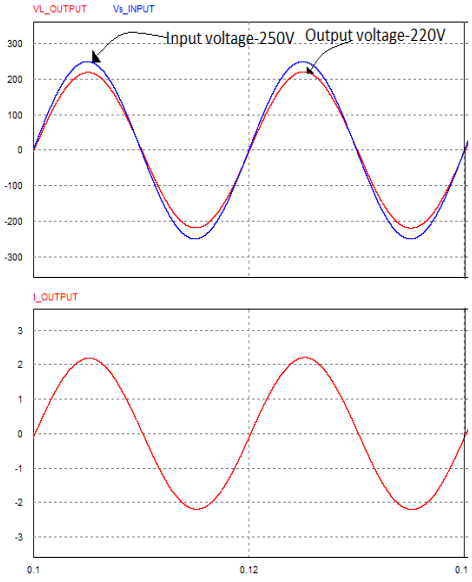

Fig.15. Comparison of input and output voltage ,output current for 13% rise in input voltage and 50 KHz switching frequency with LC filter in closed mode control

VIII. SIMULATION RESULT OF AC-AC REGULATOR USING GTO

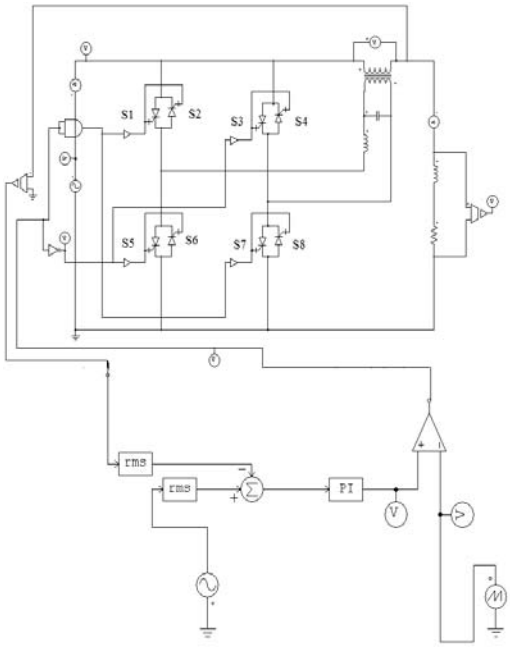

Fig.16.Closed loop control of GTO based AC-AC regulator

In the closed loop control, duty ratio of the PWM switching is automatically adjusted to generate the control voltage for compensating the input voltage variations from the reference voltage. The circuit for closed loop control is shown in Fig. 16. The simulation result of closed loop control for 13% rise in input voltage is shown in Fig. 17 and Fig.18.. Observing the wave form, we can see that 13% rise in input voltage is compensated by the control voltage of 30V.

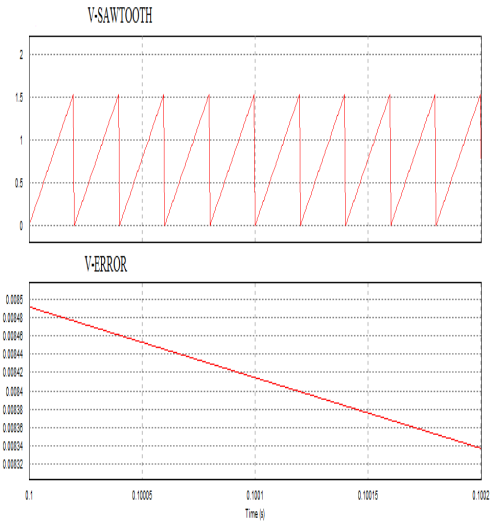

Fig 17.control voltage generated for 13% rise in input voltage

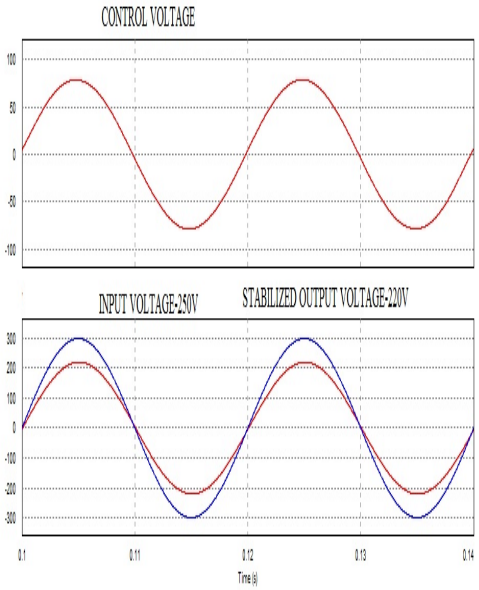

Fig .18Comparison of input and output voltage, output current for 13% rise in input voltage and 50 KHz switching frequency with LC filter in closed mode control

IX. COMPARISON BETWEEM MOSFET AND GTO TOPOLOGY

In the four switch topology four MOSFET switches are used with 16 diode in the power circuit. But in the eight switch topology only eight GTO switches are used. So the size of the latter topology will be smaller and compact than former one. GTO Gate requires tremendous amount of switching current that will be equal to the device current. High current gate drive is needed. GTO needs external devices to control turn-off and on pulses, whereas MOSFET doesn't need it. Gate of the GTO only needs a pulse for switching, whereas MOSFET needs a continuous supply of gate voltage. Higher on state voltage drop and power losses for GTO. The progress in semiconductor technology will undoubtedly lead to higher power rating,faster switching speed,and lower cost. Compared to GTO, MOSFET has faster switching speed and lower cost.

So from the comparative study ,it is concluding that for AC-AC voltage stabilizer four switch topology is more efficient than eight switch topology for low voltage applications. The eight switch topology can be used for high voltage and high current applications in switching frequency range of 10kHz. So from the comparative study, it is concluding that for AC-AC voltage stabilizer four switch topology is more efficient than eight switch topology. The progress in semiconductor technology will undoubtedly lead to higher power rating,faster switching speed,and lower cost. Compared to GTO, MOSFET has faster switching speed and lower cost. So from the comparative study, it is concluding that for AC-AC voltage stabilizer four switch topology is more

efficient than eight switch topology for low voltage applications. The eight switch topology can be used for high voltage and high current applications in switching frequency range of 10kHz.

X. CONCLUSION

An automatic voltage stabilizer keeps the output voltage constant, despite of the variations in the input voltage. A new electronic AC-AC stabilizer using H-bridge is proposed with two new topologies. First H-bridge topology uses eight GTO switches while the second topology uses four MOSFET switches. Comparative study between the two topologies highlights that, the topology that uses GTO switches can be used for high voltage and high current applications supporting industrial application while MOSFET based topology finds application in low voltage, household applications. A GTO based system is more costly than MOSFET based system. Advantage of the proposed H bridge topology based voltage stabilizer is that it has reduced cost and weight. Moreover these can support a wide range of voltage control.In the four switch topology, input voltage can be regulated from 176 to 294 Volt, while in eight switch topology, the input voltage regulation is from 174 to 298 Volt.Compensating transformer voltage opposes/aids the output voltage, and provides necessary buck/boost operation, to provide required voltage regulation.

REFERENCE

[1]. J. Faiz and B. Siahkolah, "*Differences Between Conventional andElectronic Tap-Changers And Modifications Of Controller*", IEEETrans. on Power Delivery, Vol. 21, No. 3, pp. 1342–1349, July 2006.

[2]. J. Faiz and B. Siahkolah, "*New Controller for an Electronic Tap Changer—Part II: Measurement Algorithm and Test Results*", IEEE Trans. on Power Delivery, Vol. 22, 1No. 3, pp. 230-237, Jan. 2007.

[3]. Hamdy Ahmed Ashour, "*A New Electronic Step-Up/Down Voltage Stabilizer Topology Based On H-Bridge AC Chopper*", 12th International Middle-East Power System Conference, pp. 600-604,2008.

[4]. J. V. Lopez, J. C. C. Rodriguez, S. M. Fernandez, S. M. Garcia andM. A. P. Garcia, "*Analysis Of Fast On Load Multi Tap-Changing Clamped-Hard-Switching AC Stabilizers*", IEEE Trans. on Power Delivery, Vol. 21, No. 2, pp. 852-861, April 2006.

[5]. R. Echavarria, A. Claudio and M. Cotorogea, "*Analysis, Design, and Implementation of a Fast On-Load Tap Changing Regulator*", IEEE Trans. on Power Electronics, Vol. 22, No. 2, pp. 527–534, March 2007.

[6]. Do-Hyun Jang and Gyu-Ha Choe, "*Step-Up/Down AC Voltage Regulator Using Transformer With Tap Changer And PWM AC Chopper*", IEEE Trans. on Industrial Electronics, Vol. 45, No. 6, pp.905–911, Dec. 1998.

[7]. J. C. Campo, J. Vaquero, M. A. Perez and S. Martinez, "*Dual-Tap Chopping Stabilizer With Mixed Semi-Natural Switching*", IEEE Trans. on Power Delivery, Vol. 20, No. 3, pp. 2315–2326, July 2005.

[8]M. R. Hajimoradi, A. Yazdian, H. Mokhtari."*Double Stage Switch Mode AC Voltage Regulator"2nd* power electronic drives and technologies conference, IEEE 2011.

STEGANOGRAPHY: A COMPARISON FOR ITS QUALITY

REEBA SEBASTIAN[1] & ROSAMMA SEBASTIAN[2]

[1,2]ECE Department, Amaljyothi College of Engineering, Kottayam,India

Abstract— Steganography is the art of hiding information in ways that prevent the detection of hidden messages. Steganography, derived from Greek, literally means "covered writing." It includes a vast array of secret communications methods that conceal the message's very existence. Steganography and cryptography are cousins in the spycraft family. Cryptography scrambles a message so it cannot be understood. Steganography hides the message so it cannot be seen. Steganography method used in this paper is based on biometrics. The biometric feature used to implement steganography is skin tone region of images . We propose using human skin tone detection in colour images which will provide an excellent secure location for data hiding. Skintone detection is performed using HSV (Hue, Saturation and Value) color space. Data embedding is performed using frequency domain approach - DWT (Discrete Wavelet Transform). Secret data is hidden in one of the high frequency sub-band and low frequency sub-band of DWT by tracing skin pixels in that sub-band. Different steps of data hiding are applied by cropping an image interactively. Cropping results into an enhanced security than hiding data
without cropping i.e. in whole image, so cropped region works as a key at decoding side. This study shows that by comparing steganography mechanism, in the sense that, we track skin tone objects in image, and hiding inside separately in both of the bands. And also satisfactory PSNR (Peak- Signal-to-Noise Ratio) is obtained in both cases.

Keywords*-Biometrics, Skin tone Detection, DWT, Cropping, PSNR*

I. INTRODUCTION

As the world becomes more industrialized, the risk of confidential data being stolen or modified are high,especially because the internet is available to the general public. Due to this accessibility, encryption is vital. So for this, here we are adopting the technique of steganography. Here we are hiding the data inside another image and can be retrieve it only by the one who knows the key. Embedding data, which is to be hidden, into an image requires two files. The first is the innocent-looking image that will hold the hidden information, called the cover image. The second file is the message—the information to be hidden. A message may be plain text, ciphertext, other images, or anything that can be embedded in an image. When combined, the cover image and the embedded message make a stegoimage. A stego-key (a type of password) may also be used to hide, then later decode, the message.

II. SKIN COLOUR TONE DETECTION

It is already proven that the best to detect skin will be easier in HSV color space.Any color image of RGB color space can be easily converted to HSV which is not that much sensitive to HVS (Human Visual System) .This takes advantage of biometrics features such as skin tone, instead of embedding data anywhere in image, data will be embedded in selected regions. Skintone detection is performed on input image using HSV (Hue, saturation, value) color space. The goal of skin color detection is to build decision rule that will discriminate between skin and non-skin pixels. A skin detector typically transforms a given pixel into an appropriate color space and then uses a skin classifier to label the pixel whether it is a skin or a non-skin pixel .

The skin detection algorithm produces a mask, which is simply a black and white image. The black pixel values are 0 (false) and the white pixel values are 1 (true). This mask of ones and zeros acts as a logic map for skin detection (i.e., if a pixel is 1 this pixel location is likely skin).The simplest way to decide whether a pixel is skin color or not is to explicitly define a boundary. RGB (Red, Green, Blue) matrix of the given color image can be converted into different color spaces to yield distinguishable regions of skin or near skin tone. Mainly two kinds of color spaces are available HSV (Hue, Saturation and Value) and YCbCr(Yellow, Chromatic Blue, Chromatic red) spaces. For this work HSV color space is chosen. It is experimentally found and theoretically proven that the distribution of human skin color constantly resides in a certain range within the color space . Yang and Waibel [3] are able to achieve skin tracking by dimensional reduction of the available color space.

In this work, skin detection is performed using HSV color space. For this convert RGB image into HSV color space. In HSV, responsible vales for skin detection are Hue & Saturation so extract the Hue and Saturation dimensions into separate new variables (H & S). For skin detection threshold should be chosen as [H1, S1] & [H2, S2]. A pixel is classified as skin pixel if the values [H, S] fall within the threshold. Threshold is predefined range associated with the target skin pixel values. Most of the researchers determined threshold as h_range = [0, 0.11] and s_range = [0.2, 0.7]. Sobottaka and Pitas [4] defined a face localization based on HSV. They

found that human flesh can be an approximation from a sector out of a hexagon with the constraints: Smin= 0.23, Smax =0.68, Hmin =0° and Hmax=50°.

III. DISCRETE WAVELET TRANSFORM

Cover image is transformed in frequency domain. This is performed by applying Haar-DWT, the simplest DWT on image leading to four sub-bands. Secret data embedding is performed in one of the frequency sub-band by tracing skin pixels in that band.Secret data is embedded in two of the four sub-bands separately. It can be embedded in low frequency sub-band and high frequency sub-bands.Finally we will compare the performance of hiding mechanisms in both of the two sub-bands.

IV. EMBEDDING PROCESS

Embedding steps are applied with Cropping. Before performing all steps cropping on input image is performed and then in only cropped region data hiding is performed, not in whole image. Cropped region works as a key at decoding side so cropping results into more security. Cropping provides enough security. Embedding process affects only certain regions of Interest (ROI) rather than the entire image. So utilizing objects within images can be more advantageous. This is also called as Object Oriented steganography .

V. ENCODING PROCESS

Suppose C is original 24-bit color cover image of M×N size. It is denoted as: C= {xij, yij, zij |1 ≤ i ≤ M, 1 ≤ j ≤ N, xij, yij, zij Є {0, 1,.., 255}} Let S is secret data. Here secret data considered is binary image of size a×b. Flowchart for this case is shown in Fig. 1 and different steps are discussed in detail. Let size of cropped image is Mc×Nc where Mc≤M and Nc≤N and Mc=Nc. i.e. Cropped region must be exact square as we have to apply DWT later on this region.

a) Step 1: Once image is loaded, apply skin tone detection on cover image. This will produce mask image that contains skin and non skin pixels. Skin tone detection is discussed in coming subsection.

b) Step 2: Ask user to perform cropping interactively on mask image (Mc×Nc). Then original image is also cropped of same area. Cropped area must be in an exact square form as we have to perform DWT later and cropped area should contain skin region such as face, hand etc since we will hide data in skin pixels of one of the sub-band of DWT. Here cropping is performed for security reasons. Cropped rectangle will act as key at receiving side. If it knows then only data retrieval is possible. Eavesdropper may try to perform DWT on whole image; in such a case attack will fail as we are applying DWT on specific cropped region only.

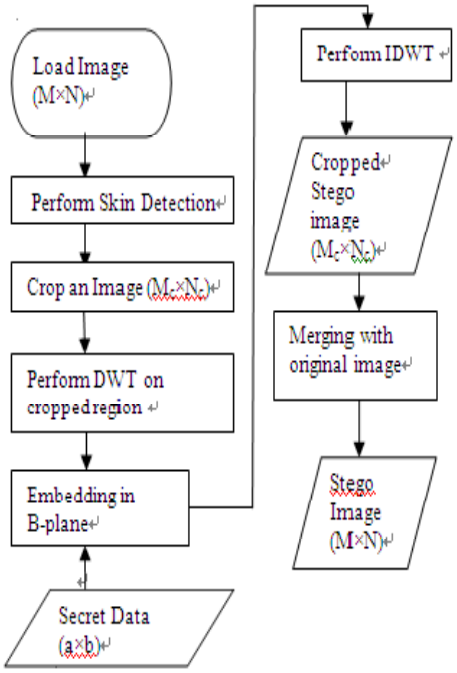

Figure 1. Flowchart of With Cropping case of Embedding Process

c) Step 3: Apply DWT to only cropped area (Mc×Nc) not whole image (M×N). This yields 4 sub-bands denoted as HLL,HHL,HLH,HHH . (All 4 sub-bands are of same size of Mc/2, Nc/2). Payload of image to hold secret data is determined based on number of skin pixels present in one of high frequency sub-band in which data will be hidden.

d) Step 4: Perform embedding of secret data in one of sub-band that we obtained earlier by tracing skin pixels in that sub-band. Other than the low frequency sub-band (LL) any high frequency sub-band can be selected for embedding as LL sub-band contains significant information.

e) Step 5: Perform IDWT to combine 4 sub-bands.

f) Step 6: A cropped stego image of size Mc×Nc is obtained in above step (step 5). This should be similar to original image after visual inspection but at this stage it is of size Mc× Nc, So we need to merge the cropped stego image with original image to get the stego image of size M×N. To perform merging we require coefficients of first and last pixels of cropped area in original image so that r calculated. Thus a stego image is ready for quality evaluation.

A. Skin colour tone detection using HSV.

The goal of skin color detection is to build decision rule that will discriminate between skin and non-skin pixels. A skin detector typically transforms a given pixel into an appropriate color space and then uses a skin classifier to label the pixel whether it is a skin or a non-skin pixel [9].

The skin detection algorithm produces a mask, which is simply a black and white image. The black pixel values are 0 (false) and the white pixel values are 1

(true). This mask of ones and zeros acts as a logic map for skin detection (i.e., if a pixel is 1 this pixel location is likely skin).The simplest way to decide whether a pixel is skin color or not is to explicitly define a boundary. RGB (Red, Green, Blue) matrix of the given color image can be converted into different color spaces to yield distinguishable regions of skin or near skin tone. Mainly two kinds of color spaces are available HSV (Hue, Saturation and Value) and YCbCr(Yellow, Chromatic Blue, Chromatic red) spaces. For this work HSV color space is chosen. It is experimentally found and theoretically proven that the distribution of human skin color constantly resides in a certain range within the color space [1]. Yang and Waibel [10] are able to achieve skin tracking by dimensional reduction of the available color space.

In this work, skin detection is performed using HSV color space. For this convert RGB image into HSV color space. In HSV, responsible values for skin detection are Hue & Saturation so extract the Hue and Saturation dimensions into separate new variables (H & S). For skin detection threshold should be chosen as [H1, S1] & [H2, S2]. A pixel is classified as skin pixel if the values [H, S] fall within the threshold. Threshold is predefined range associated with the target skin pixel values. Most of the researchers determined threshold as h_range = [0, 0.11] and s_range = [0.2, 0.7]. Sobottaka and Pitas [11] defined a face localization based on HSV. They found that human flesh can be an approximation from a sector out of a hexagon with the constraints: Smin= 0.23, Smax =0.68, Hmin =00 and Hmax=500.

B. Discrete wavelet transform and Haar-DWT

This is one of the frequency domain in which steganography can be implemented. In this work DWT is used as it performs better than the DCT. DCT is calculated on blocks of independent pixels, a coding error causes discontinuity between blocks resulting in annoying blocking artifact. This drawback of DCT is eliminated using DWT. DWT applies on entire image. DWT offers better energy compaction than DCT without any blocking artifact. DWT splits component into numerous frequency bands called sub bands known as

LL – Horizontally and vertically low pass
LH – Horizontally low pass and vertically high pass
HL - Horizontally high pass and vertically low pass
HH - Horizontally and vertically high pass

Since Human eyes are much more sensitive to the low frequency part (LL sub-band) we can hide secret message in other three parts without making any alteration in LL sub-band [5]. As other three sub-bands are high frequency sub-band they contain insignificant data. Hiding secret data in these sub-bands doesn't degrade image quality that much. In this work, we use simplest DWT, Haar-DWT, to transform images into frequency domain. sub-band they contain insignificant data. Hiding secret data in these sub-bands doesn't degrade image quality that much. In this work, we use simplest DWT, Haar-DWT, to transform

images into frequency domain.

C. Advantages of Haar Wavelet transform as follows:

- Best performance in terms of computation time.
- Computation speed is high.
- Simplicity.

It performs two steps, row and column transformation respectively. Entire row of an image matrix is taken, then do the averaging, differencing is done. After we treated entire row of an image matrix, then do the averaging and differencing process for the entire each column of images.

D. Decoding Process

All steps of Decoder are opposite to Encoder. 24 bit color stego image of size M×N is input to decoding process. Decoding process is explained below. Flowchart shows different steps . In this case we must need a value of cropped area to retrieve data. Suppose cropped area value is stored in 'rect' variable that is same as in encoder. So this 'rect' will act as a key at decoder side. Care must be taken to crop same size of square as per Encoder. By tracing skin pixels in HH and LL sub-band of DWT secret data is retrieved.

VI. CONCLUSION

In this study, we have hidden datas inside images. Images are differentiated with haar wavelet transform. We have resided datas inside both high frequency and low frequency bands. And after retrieving the original data, we have compared the PSNR values and MSE values for both high frequency and low frequency bands. The PSNR value is higher when hiding in low frequency sub-band.

VII. SIMULATION RESULTS

In this section we demonstrate simulation results for proposed scheme.This have been implemented using MATLAB 7.8. A 24 bit color image is employed as cover-image of size 356×356 . The secret images are of size 32×32.We use Peak signal to noise ratio (PSNR) to evaluate quality of stego image after embedding the secret message. The performance in terms of PSNR (in dB) is demonstrated for the method in the following subsections.

PSNR is defined as per Equation (4) and Equation (5).

$$PSNR = 10 \log10 (255\text{^}2/MSE), \quad (4)$$

$$\text{Where, } MSE = (1/ (M \times N)) \sum_{i=1}^{M} \sum_{j=1}^{N} (xij - yij)\text{^}2 \quad (5)$$

xij and yij represents pixel values of original cover image and stego image respectively. The PSNR value for hiding in high frequency band is 44.2151.The PSNR value for hiding in low frequency band is 39.4191.The calculated PSNR usually adopts dB value for quality judgement, the larger PSNR is, higher the image quality (which means there is a little difference between cover image and stego image).On the contrary smaller dB value means there is a more distortion.

ACKNOWLEDGMENT

First of all we sincerely thank the almighty for his choicest blessings for completing this work. We extend our thanks to all teachers and friends of Amal jyothi college of engineering, Kanjirappally.

REFERENCES

[1] A Secure Skin Tone based Steganography Using Wavelet Transform Anjali A. Shejul, Umesh L. Kulkarni, International Journal of Computer Theory and Engineering, Vol.3, No.1, February, 2011 1793-8201

[2] A. Cheddad, J. Condell, K. Curran and P. Mc Kevitt, "Biometric inspired digital image Steganography", in: Proceedings of the 15th Annual IEEE International Conference and Workshops on the Engg.of Computer-Based Systems (ECBS'08), Belfast, 2008, pp. 159-168.

[3] Yang, J., & Waibel, a. (1996). A real-time face tracker. Proceedings of the 3th IEEE Workshop on Applications of Computer Vision, Sarasota, Florida, 142-147

[4] Sobottka, K. and Pitas, I.:"Extraction of facial regionsand features using color and shape information." Proc. IEEE International Conference on Image Processing, pp. 483-486.(1996)

[5] Chen,P. Y.and Liao,E.C., :A new Algorithem for Haar Wavelet Transform," 2002 IEEE International Symposium on Intelligent Signal Processing and Communication System, pp.453-457(2002).

[6] A. Cheddad, J. Condell, K. Curran and P. Mc Kevitt, "Biometric inspired digital image Steganography", in: Proceedings of the 15th Annual IEEE International Conference and Workshops on the Engg.of Computer-Based Systems (ECBS'08), Belfast, 2008, pp. 159-168

COMPARATIVE STUDY OF CLUSTERING METHODS IN VLSI CIRCUIT PARTITIONING

R.MANIKANDAN[1] & P.SWAMINATHAN[2]

[1,2]School of Computing, SASTRA University, Thanjavur,India

Abstract— Partitioning is a vital part of VLSI physical design. The objective of paper is to address various clustering methods with emphasis on VLSI Circuit partitioning. Three major algorithms for VLSI Circuit partitioning are discussed: Two step clustering method, Hierarchical clustering method and K-Means clustering method. The performance of all the approaches is compared using bench mark data. Analysis of the investigation result proves that K-means model achieves greater performance than other models in recognizing sub-circuits with minimum amount of interconnection between them.

Keywords*-com Circuit Partitioning, K-Means Clustering, Hierarchical Clustering, Two Step Clustering.*

1. INTRODUCTION

VLSI Circuit partitioning is to divide the circuit into a number of sub-circuits with minimum interconnection between them. Circuit partitioning is a critical area of VLSI Physical design automation. In order to design complex logic circuits it is often necessary to sub-divide multi- million transistor design into manageable pieces. The presence of hierarchy gives rise to natural clusters of cells. Most of the widely used algorithms tend to ignore this fact and divide the net list in a balanced portioning ,thus frequently the resulting partitions are not optimal. This paper proposes a different clustering approach to solve VLSI Circuit partitioning problem. It is trained to learn useful sub-circuits with lowest amount of interconnection between them. Finally, three different data clustering methods namely two step clustering, Hierarchical clustering and K-Means clustering are considered for dividing the circuits into sub circuits. [2],[3],[4]

2. CLUSTERING METHODS

2.1 Two Step Cluster Method

Two step clusters is an algorithm mainly designed to analyze the large datasets. There are a number of features employed by the Two-step clustering methods which differentiate it from traditional clustering algorithms. The features include ability to handle very large datasets, ability to handle both continuous and categorical variables, and ability to automatically determine the optimum number of clusters. The Two-step clustering is based upon a sequential approach of creating clusters and then sub-clusters. The name Two-step clustering is already an indication that the method is based on a two-stage approach: Firstly, the algorithm undertakes a procedure that is very similar to the K-means algorithm. Secondly, the algorithm conducts a modified Hierarchical agglomerative clustering procedure by combining the objects sequentially to form homogenous clusters. This is done by building a so-called cluster feature tree whose "leaves" represent distinct objects in the dataset [1]

2.2 Hierarchical clustering method

Partitioning methods are based on specifying an initial number of groups, and iteratively reallocation objective among groups to convergence. In contract, hierarchical methods combine or divide existing groups, creating a hierarchical structure that reflects the order in which groups are merged or divided

In data mining, hierarchical clustering is a method of cluster analysis which seeks to build a hierarchy of clusters. Strategies for hierarchical clustering generally fall into two types:

Agglomerative: This is a "bottom up" approach: each observation starts in its own cluster, and pairs of clusters are merged as one moves up the hierarchy.

Divisive: This is a "top down" approach: all observations start in one cluster, and splits are performed recursively as one moves down the hierarchy.

In general, the merges and splits are determined in a greedy manner. The results of hierarchical clustering are usually presented in a dendrogram.

In the general case, the complexity of agglomerative clustering is $\mathcal{O}(n^3)$, which makes them too slow for large data sets. In our paper , we have used divisive clustering approach.

2.3 K-Means Clustering Method

K-Means is one of the simplest unsupervised learning algorithms that solve the well known clustering problem. The procedure follows a simple and easy way to classify a given data set through a certain number of clusters (assume k clusters). The main idea is to define k centroids, one for each

cluster. These centroids have to be selected carefully since their placement will always affect the end result. So, the better choice is to place them as far as possible. The algorithm is composed of following steps:

(1) Place k points into the space represented by the objects that are being clustered. These points represent initial group of centroids.
(2) Assign each object the group that has the closest centroid.
(3) When all objects have been assigned, recalculate the positions of the k centroids.
(4) Repeat steps 2 and 3 until the centroids no longer move. This produces a separation of the objects into groups of the objects into groups from which the metric to be minimized can be calculated.
The sensitiveness of the algorithm to the initial set of randomly chosen centroids can be reduced by running the algorithm multiple times. [2]

3. RESULTS AND OBSERVATION

The clustering algorithms are compared according to the following factors:

1 . The size of the data set
2. Quality of the clustering
3. Timing factor

For each factor, four tests are made, one for each algorithm. After analyzing the results of testing the clustering algorithms, K-Means algorithm is well suited for VLSI Circuit partitioning problem. The test results are given below. We have used C# and VB.NET software for implementing the three clustering algorithms.

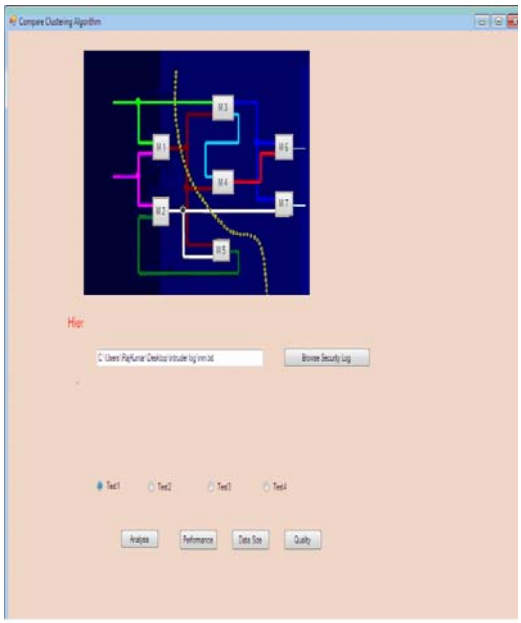

Fig-1 Comparing clustering Algorithms

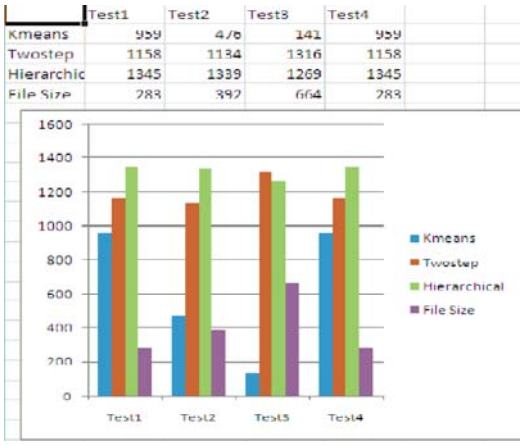

Fig-2 Data Analysis

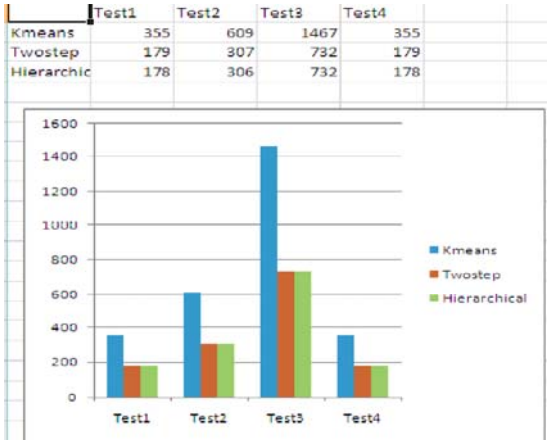

Fig-3 Quality Analysis

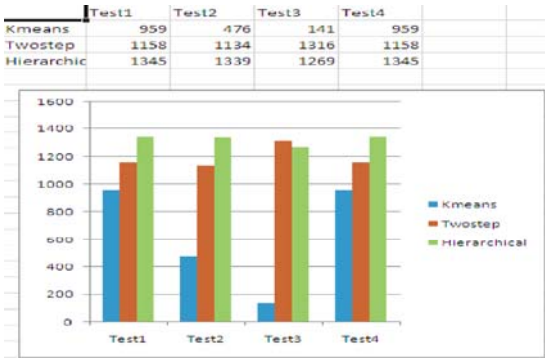

Fig-4 Timing Analysis

4. CONCLUSION

In this paper, We have discussed and evaluated the performance of algorithms like K-Means clustering , Hierarchical clustering and Two step clustering . By the evaluation, we conclude that K-Means algorithm gives better result, it takes less time for partitioning of VLSI Circuit . Quality analysis and data analysis point of view K-Means algorithm is well suited for VLSI Circuit partitioning .

REFERENCES

[1] Osama Abu abbas "Comparison between data clustering Algorithms" The Arab journal of Information Technology vol.5, No.3, July 2008, pp 320-325

[2] R.Manikandan "Improving Efficiency of Textual static web content mining using clustering Techniques", Journalof Theoretical and Applied Information Technology, vol.33, No.2, November 2011, pp 193 - 196

[3] R. Manikandan, Jaladhanki Sindura, M.D.L. SriRavali and P. Swaminathan, "Efficient Mathematical Model on VLSI Circuit Partitioning" Research Journal of AppliedSciences, Engineering and Technology 4(13):1978-1979,2012.

[4] M. Thiyagarajan and R. Manikandan, 2011 "Hypergraph and Coprocessor design for VLSI Partitioning Problems", Journal of Theoretical and Applied Information Technology Vol 26. No. 2,pp 107-111.

AN ENHANCED METHOD FOR FORENSIC DETECTION OF IMAGE MANIPULATION

ROSHNI ROY K.[1] & INDU REENA VARGHESE[2]

[1,2]Department of Electronics and Communication, Amaljyothy College of Engineering, Kerala, India.

Abstract—The widespread availability of internet and modern image editing softwares has made the manipulation of images very easy. This leads to an environment where the authenticity of digital images are often in doubt. An enhanced technique for detection of image tampering is proposed in this work. The proposed work is capable of detecting the composite manipulations done on an image based on two algorithms. In the first method, image is first compressed using Discrete Wavelet Transform (DWT), divided into blocks and is sorted using lexicographic sorting. Phase correlation between the image blocks is used as a similarity checking criterion. This method is suitable for detection of block wise tampering. The variations between the blocks can be used as hints of manipulation. In the additional method, the properties of an authentic camera output are characterized based on a system model. The linear part of post-camera processing done on an image is modeled as a tampering filter whose coefficients are estimated using blind deconvolution. These estimated coefficients are then used to identify tampering operations like sampling, filtering, rotation etc. performed on the image.

Keywords- *Authenticity; Discrete Wavelet Transform; phase correlation; image tampering; blind deconvolution.*

I. INTRODUCTION

The recent developments in the field of image processing have made it very easy for the forgers to manipulate the images. Any manipulation on an image brings about variations in the image artifacts only within a specific range so that the manipulated image may appear visually convincing. The forensic researchers have developed a lot many forensic algorithms to detect digital forgeries. Most work on tampering detection methods identify tampering by studying the properties of a manipulated image in terms of the distortions it undergoes and also requires an exhaustive search over all the numerous kinds of post-processing operations to detect tampering.

Earlier, watermarking techniques were used to detect image manipulations and forgeries. But it requires pre processing of images before sending. The experts in forgery can render several forms of image tampering such as double JPEG compression, cut-and-paste image forgery, and image origin falsification undetectable through existing tamper detection methods.

An advanced method of tamper detection is proposed in this work. Digital image forgeries such as resampling, JPEG compression with different quality factors, addition of noise, rotation, filtering, copy-move forgery, image compositing and a lot many tampering operations can be detected based on the two supporting algorithms.

A wavelet based approach is presented which uses wavelet transform for compression of tampered image. The variation between the blocks within an image can be checked for identifying the block wise manipulations on an image. The dimension of the doubted image is reduced using Discrete Wavelet Transform after which the image is divided into overlapping blocks of fixed size. Lexicographic sorting is applied on this image and the variation between the blocks is identified based on the phase correlation.

A novel technique based on blind deconvolution is proposed in addition, to identify previously unseen manipulations. We consider that the raw image from a camera is untampered and characterize its properties based on a ground model. The post processing operations done on an image brings about a combination of linear and non linear parts in an image. The linear part is related to the tampering operations. The coefficients of the linear part are estimated based on a blind deconvolution. The similarity between the coefficients of the test input and the reference image is calculated which is compared with a chosen threshold value. A similarity index which is greater than the threshold shows that the image is authentic.

II. PROPOSED ALGORITHM

A. Detection Based on phase correlation

The detection of reference and matching blocks on the lowest level of wavelet transform compressed image is done here. The RGB to gray scale conversion is performed whose DWT is calculated. Overlapping block pixels are converted into a matrix and blocks with maximum contrast are selected. The row wise sorting of the matrix is performed, phase correlation between rows is calculated and the candidate block co-ordinates are mapped into a new matrix.

The Discrete Wavelet transform of the image does not change the information content present in the signal. The Discrete Wavelet Transform is applied to reduce the size of the image at each level. The image is decomposed into four sub images (approximation, vertical, horizontal and diagonal components) of the

image at each of the levels. The sub image corresponding to the coarse level coefficients or the approximation image is used for further decomposition. The approximation coefficients are represented as AA. These sub images can be combined for the restoration of the actual decomposed image.

Figure 1. DWT of an image

The above figure shows the DWT applied on an image up to level 3. If the number of levels used for decomposition is 'A', then the matching is performed on the coarse level coefficients of the image at level 'A' which is denoted as AAA. The images used for matching of overlapping blocks at each iteration are AAA, AAA -1,….. AA 1..The image at the lowest resolution is AAA and is used for matching of blocks .These matched blocks are carried to the next higher level and the last match is performed on the actual image itself.

Phase correlation ρ, is used for template matching which is inverse Fourier transform of the ratio between two images blocks (F) shown below:

$$F = (f(\text{block1}) \times \text{conj}(f(\text{block 2}))) / (\|f(\text{block 1}) \times \text{conj}(f(\text{block 2}))\|) \quad (1)$$

where 'f' is the Fourier transform, and 'conj' represents the complex conjugate.

B. Detection based on blind iterations

Using the test image, we construct the imaging model and estimate the color interpolation coefficients and parameters using component forensic methodologies described in an earlier work which helps in finding the actual output of the camera and the coefficients of the tampering block. The percentage of difference between these tamper filter coefficients and delta function gives an idea on the amount of tampering.

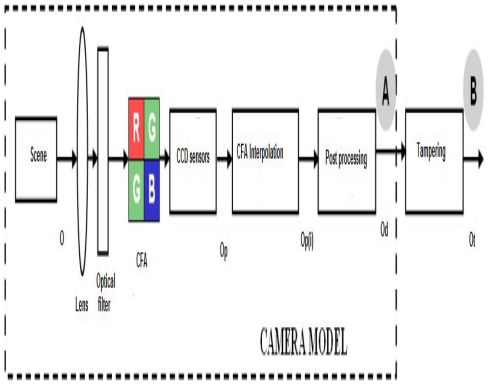

Figure 2. Representation of the model of the camera system

Let O be the real-world scene to be captured by the camera and let p be the Color Filter Array(CFA) pattern matrix. The CFA sampling converts the real-world scene O into Op. After this, the pixel values corresponding to the points where Op(x, y, c) = 0 are interpolated using its neighboring pixel values to obtain Op(i). After interpolation, post processing operations like JPEG compression is done on the image and the final output is Od.

Component forensics can be used to reverse-engineer the imaging process and determine the important camera components parameters like CFA and color interpolation. The image pixel at location (x, y) is classified into any of the three regions based on the gradient features in a local neighborhood. They are X1, X2, X3. The region X1 contains those parts of the image with a significant horizontal edge for which (Hx,y) – (Vx,y)>T . X2 contains those parts with (Vx,y) – (Hx,y) >T and the remaining smooth parts of the image are in region X3. Here T is a threshold; (Hx,y) is the horizontal gradient and (Vx,y) is the vertical gradient at the location (x,y) respectively. A set of linear equations can be generated for all the pixels in each region Xi(i = 1,2, 3) based on the final output Od. The interpolation coefficients α(Xi) is obtained by solving these equations which is used in finding the interpolation error. This is used in estimating the actual CFA pattern.

Let O be the test input and Ote be the camera output estimate. Ote can be found by filtering the corresponding color of O with the coefficients of the inverse filter u. By imposing the camera constraints on Ote, Ote" can be found.

$$\text{Ote''}(x, y, c) = \sum_{m,n} \alpha(Xi)(m, n, c)\,\text{Ote}(x- m, y- n, c) \quad \text{for all } \{x, y\} \square Xi; \text{ and } 1<= c<= 3$$
$$= \text{Ote}(x,y,c) \quad \text{otherwise} \quad (2)$$

The tampering filter coefficients are found by

separately minimizing the cost function Z^c in each color channel. The cost function is given as:

$$Z^c(u) = \sum_{x,y} (Ote''(x, y, c) - Ote(x, y, c))^2 + \eta \left(\sum_{a,b} u(a,b,c) - 1\right)^2 \quad (3)$$

We make an assumption, $\sum_{m,n} u(m, n, c) = a$ constant K for c = 1,2,3. If the original image and its tampered version have similar brightness levels, the value of K will be 1. η is to adjust the weights of the relative individual costs .So, the cost function Z^c in the cth color component aims at minimizing the overall interpolation error and the deviation of the filter coefficient sum from 1.

A recursive algorithm is used to solve the cost minimization problem and to estimate the coefficients of the tampering block. This is shown in the Fig 2.

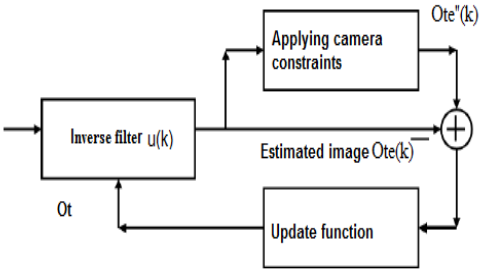

Figure 3. Estimation of coefficients of the tampering block

By passing the test image Ot through the estimate of the inverse blurring filter u(k), estimate of the original image Ote(k) can be found. Ote"(k) is obtained by imposing the camera constraints as in the previous case. Then the interpolation error is found. The inverse filter coefficients should be updated according to (7).

We have,

$$u(k+1) = u(k) + s_k g_k \quad (4)$$

where, s_k is the step size.

$$g_k = -\nabla Z(u(k)) \quad \text{if } k = 0$$

$$= -\nabla Z(u(k)) + \beta_{k-1} s_{k-1} \quad \text{otherwise} \quad (5)$$

$$\beta_{k-1} = (< \nabla Z(u(k)) - \nabla Z(u(k-1)), \nabla Z(u(k))>) / (\text{norm}(\nabla Z(u(k-1)))) \quad (6)$$

Also, $Z=\sum_c Z^c$ where $1 \leq c \leq 3$. It is seen that the optimization problem is convex and converges to a unique solution.

III. SIMULATION RESULTS

For the database, several images were downloaded from internet and collected images from Canon A75 and Fujifilm S3000 to generate a database of 40 different images. Different tampering operations were performed on these images which tampering using Adobe Photoshop cloning tool, resampling, JPEG compression with different quality factors, rotating with 1-20 degrees and median filtering.

A. Phase correlation approach

The images were compressed by DWT and applied the phase correlation based checking.The sizes of the blocks were chosen based on the image size. The detection results on the US currency note image is represented in Fig.4

(a) (b) (c)

Figure 4. Forgery detection result (a) original image (b) tampered image (c)detection result with 15% noise.

The detection results for manipulation by duplication of regions are represented in Fig.5

(a) (b) (c)

Figure 5.Forgery detection result (a) original image (b) tampered image having more than one duplicated result (c) result of detection.

B. Blind Deconvolution Approach

The application of blind iterations on each image resulted in the computation of tampered block coefficients. If we plot the cost function C on green channel against the number of iterations in Fig.6, is it seen that C converges in around iterations.

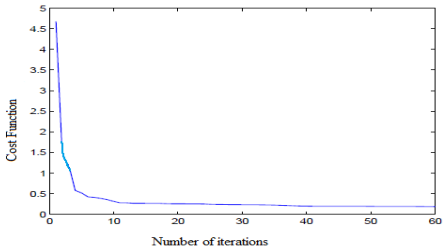

Figure 6: Cost function convergence

A thresholding scheme can be used to check the authenticity of images. If we have the test input, the frequency domain coefficients of the tampering filter (Ht) is found out and it is compared with the spectral response Hr of a reference authentic image .The measurement of their similarity is done based on their corresponding normalized values.

$$S(\theta t, \theta r) = \sum_{x,y} | \theta t(x,y) - \partial t | * | \theta r(x,y) - \partial r | \quad (7)$$

Here, S denotes the similarity score, θt and θr are the normalized values of Ht and Hr respectively. ∂t is the mean of θt and ∂r is the mean of θr. If S is greater than a chosen threshold, it means that the image is authentic.

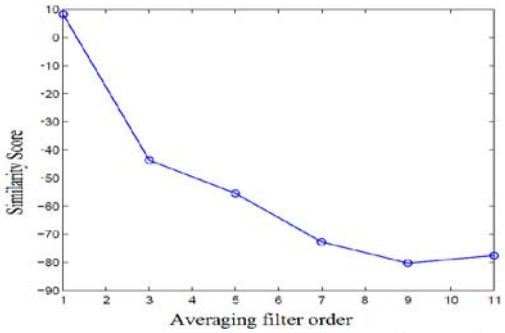

Figure 7.Similarity scores between coefficients of the tampered image and the reference image for spatial averaging.

In Fig.7, we see that when the similarity scores obtained from comparison of filtered image's coefficient are plotted against filter order, the similarity scores reduce with increase in the magnitude of the distortion.

IV. CONCLUSION

Algorithms for the detection of forgery using wavelet transforms and blind iterations were proposed. The computational complexity of the first method is lower, and detection is possible even if the forger has added noise and changed the JPEG quality levels. But the detection of duplicated regions with rotation through angles and scaled regions is impossible. In the detection of tamper based on the blind deconvolution, the images captured by the camera are considered as authentic and further manipulations done on it would make it inauthentic. The properties of a raw image are characterized based on the system model. The linear part of the post camera processing is modeled using a tampering filter whose coefficients are estimated based on the blind deconvolution. These coefficients are used for identification of the tampering. This method is best suited for identification of manipulation s like filtering, compression, rotation etc.

ACKNOWLEDGEMENT

The author thank the Management and the Principal of Amaljyothy College of Engineering, Kanjirappally for providing excellent computing facilities and encouragement.

REFERENCES

[1] Saiqa Khan, Arun Kulkarni, "An Efficient Method for Detection of Copy-Move Forgery Using Discrete Wavelet Transform," International Journal of Computer Science and Engineering, Vol.2, No. 5, pp: 1801-1806, Aug 2010.

[2] Saiqa Khan, Arun Kulkarni, "Reduced Time Complexity for Detection of Copy-Move Forgery Using Discrete Wavelet Transform" International Journal of Computer Science Applications, Vol. 6, No. 7, pp: 31-36, Sep 2010.

[3] Kakar, Pravin,Sudha, N., Ser, W., "Exposing digital image forgeries by detecting discrepancies in motion blur". IEEE transactions on multimedia, 2011.

[4] Granty, R.E.J."Survey on passive methods of image tampering detection" International Conference on Communication and Computational Intelligence (INCOCCI), 2010.

[5] Yingda Lv, Xuanjing Shen, Haipeng Chen, "An improved image blind identification based on inconsistency in light source direction", The journal of supercomputing ,Volume 58, Issue 1, pp 50-67, October 2011.

[6] Sarah A. Summers, Sarah C. Wahl "Multimedia Security ForensicsAuthentication of Digital Images"ForensicResearch http://cs.uccs.edu/~cs525/studentproj/proj52006/sasummer/doc/cs525projsummersWahl.doc

[7] D.Kundur and D. Hatzinakos, "A Novel Blind Deconvolution Scheme for Image Restoration using Recursive Filtering," *IEEE Trans. on Signal Processing*, vol. 46, no. 2, pp. 375-390, Feb 1998.

[8] G. R. Ayers and J. C. Dainty, "Iterative Blind Deconvolution Method and its Applications," *Optics Letters*, vol. 13, no. 7, pp. 547–549, 1988.

[9] Myna.A.N. , M.G.Venkateshmurthy , C.G.Patil "Detection of Region Duplication Forgery In Digital Images Using Wavelets and Log-polar Mapping", in Proc. of International Conference on Computational Intelligence and Multimedia Applications, Volume 3, 13-15 ,pp.371 – 377, July 2-6, 2007.

[10] A. Swaminathan, M. Wu, and K. J. Ray Liu, "Component Forensics of Digital Cameras: A Non-Intrusive Approach," Proc. of Conference on Information Sciences and Systems, Princeton, NJ, Mar 2006.

Information Sciences and Systems, Princeton, NJ, Mar 2006.

[11] A. C. Popescu and H. Farid, "Exposing Digital Forgeries in Color Filter Array Interpolated Images," IEEE Transactions on Signal Processing, vol. 53, no. 10, pp. 3948–3959, Oct 2005.

[12] H. Farid and S. Lyu, "Higher-Order Wavelet Statistics and their Applicationto Digital Forensics," IEEE Workshop on Statistical Analysis in Computer Vision, Madison, WI, 2003.

[13] J. Lukas and J. Fridrich, "Estimation of Primary Quantization Matrix in Double Compressed JPEG Images," Proc. of DFRWS, Aug 2003.

[14] J. Adams, "Interaction between Color Plane Interpolation and other Image Processing Functions in Electronic Photography," SPIE Camerasand Sys. for Electronic Photography & Scientific Imaging, Feb 1995.

[15] A. C. Popescu and H. Farid, "Statistical Tools for Digital Forensics," 6thIntl. Work. on Info. Hiding & LNCS, vol. 3200, pp. 128–147, May 2004.

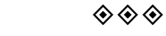

MOTION HISTOGRAM DATA HIDING WITH HISTOGRAM PRESERVING PROPERTY

JISHA ANU JOSE[1] & GEEVARGHESE TITUS[2]

[1,2] Department of ECE, Amal Jyothi College of Engineering, Kerala, India

Abstract - This paper deals with data hiding in uncompressed video. Unlike using motion vector for data hiding which gives only a coarse representation of the actual motion. We target the motion at the pixel level. The frame difference is used to construct a motion histogram and the cover sequence for hiding data is obtained from the histogram. The secret message bitstream is embedded into this sequence by finding suitable candidate vector. The method is implemented and tested for hiding text messages in an uncompressed video and the results are evaluated. The proposed method is less complex and histogram distortion was found to be very less.

Keywords - *Data Hiding, Pixel Change Ratio Map(PCRM), Motion Histogram, Steganography.*

I. INTRODUCTION

Steganography is a technique used to hide a secret message within a cover media in such a way that others cannot detect the presence of the hidden message. For performing steganography, we need a cover media, stego function, stego- key and the secret message to be hidden. The cover media can be a plaintext, still image, video and audio. Performing data hiding in video was studied in wide variety of literatures. In [5], data hiding is performed using the motion vector of the video by considering macroblocks of the frames. But it is seen that the motion vector computed over macroblock of size 16X16 gives only a coarse representation of the actual motion. It is therefore desirable to consider motion at the pixel level to get much more fine motion estimation.

In the literature [1], author proposed a simple and efficient method to extract motion features at pixel level by using frame differencing. Based on the difference frame, they developed the motion histogram. The paper focused on using motion histogram for video retrieval, video clustering and video classification, but has not studied motion histogram steganography. In literature [2], author uses a histogram preserving algorithm for data hiding in images. The method will maximize the payload while preserving the histogram and constrains the steganographic distortion at the desired level.

In this paper, we combined histogram data hiding method used for still images and the motion histogram of the video to perform the steganography. This approach is based on using the motion histogram for generating the cover sequence which is decomposed into a series of binary sequences. One among the several candidate vectors is selected to represent the secret message and the cover sequence is replaced by the selected candidate vector. The method was found to be less complex compared to the motion vector schemes.

II. MOTION HISTOGRAM

Video is formed from a sequence of frames. Digital video is a very promising host candidate that can carry a large amount of data (payload). Pixel change ratio map (PCRM) indicates moving regions in a particular video sequence. The histogram of PCRM is called the Motion Histogram.

The algorithm to generate the PCRM is motivated by the fact that the human visual system perceives motion if the intensity of motion is high and the motion continues for a reasonably long duration. We accumulate the changes in pixel intensity over all the frames in a video sequence to generate PCRM for that segment. We initialise PCRM having size that of the frame to zero. If the frame size is MxN, then PCRM is a matrix of size MxN initialised to zero. First obtain frames from the video and convert it into gray. Determine the absolute difference between the frames so as to get the difference frames. For a frame i, the difference frame is determined as

$$DI_i = |P_{i+1} - P_i| + |P_i - P_{i-1}|. \quad (1)$$

After obtaining the difference frame for all the frame sequence of the video, check each pixel in the difference frame. If the pixel value is greater than 10, increment the corresponding location value in PCRM by 1. Repeat the process for all the difference frames and thus obtain a complete PCRM. The comparison of DI_i with a threshold is to undo the effect of any noise associated with the camera.

Plot the PCRM to get the motion histogram and determine the peak of the histogram ie, the number of times a pixel value of the difference frame is greater than 10 and that count is repeated maximum in the PCRM. This count value and one increment of the count value in the histogram is grouped to form a bin. If the count that is repeated maximum is x, then a bin is formed such as $[x,x+1]$. Then visit all the pixel locations in PCRM and group those pixels that fall in the selected bin to form a sequence. Now represent

every *x* 's as 0 and *(x+1)* 's as 1 in the sequence. This new sequence of 0's and 1's form the binary cover sequence for steganography.

III. STEGANOGRAPHIC METHOD

A. *Data Hiding Method:*

In this method, a number of candidate stego vectors representing a block of secret bits are produced and a criteria for lowering steganographic distortion. The secret message may be a string and is converted into binary sequence. We divide the secret message sequence into a series of bit blocks, each of which contains *k* bits, where

$k=\frac{length\ of\ cover\ sequence}{length\ of\ message\ sequence}$=*transmission rate.*

Generate a matrix G= [Q I_8] of size 8X (k+8), which consist of two parts. Q is the stego key of size 8X k and I_8 is 8X8 identity matrix. For each secret bit block s= [s_1 s_2 .... s_k] we generate 2^8 different types of binary vectors with length (k+8) using modulo-2 calculation

V_t=[s_1 s_2.... s_k 0 0 .....0]+[b(t,1) b(t,2) ....b(t,8)]. G

Where t=0, 1,...,(2^8-1). (2)

The first term is made of k secret bits and eight zeros and the second term is a binary version of an integer t within [0,1,....,(2^8-1)], obtained as

b (t,u)= $\left\lfloor t/2^{u-1} \right\rfloor$ mod 2 (3)

where u=1,2,...,8

The binary vectors, V_t is used to generate candidate vectors.

Steps of embedding

1. Find the number of cover bits that have flipped from 0 to 1 and lets denote it S_0. Also find the number of cover bits that have flipped from 1 to 0 and denote it S_1.
2. Determine rate of 0's in the cover sequence and name it as α. Usually it has a value of 0≤ α ≤0.5.
3. To generate the candidate vectors, calculate decimal value of each V_t using the equation,

$$v_t=\sum_{K=1}^{k+8} V_t(K).2^{K-1} \quad (4)$$

4. Assign Y=2^{k+8} and *x*= v_t and let C_t be a vector with initialised length zero.
5. Calculate T=max[1, round(Y. α)]
6. If *x*≤ T-1, append a 0 to the end of C_t and update value of Y as Y=T. Otherwise, append a 1 to the end of C_t and update value of Y as Y=Y-T and *x*=(*x*-T).
7. If Y>1, repeat step 3, else terminate the process. The steps 3-7 generates 2^8 candidate vectors of length l_t.
8. For each C_t, compare it with l_t cover sequences and find

   $n_{t,0}$= number of positions where C_t=1 and cover sequence=0.

   $n_{t,1}$= number of positions where C_t=1 and cover sequence=1.
9. For each C_t determine

   $r_t= n_{t,0}+ n_{t,1}+ \lambda .(s_0 - s_1)(n_{t,0} - n_{t,1})$. (5)

   Where, λ takes the value 0.02 so as to keep the distortion level low. Then find the smallest r_t among all 2^8 by,

   υ=arg(minr_t). (6)
10. Then modify l_υ bits in cover sequence to make it same as C_υ and change $s_0 = s_0+ n_{\upsilon,0}$ and $s_1 = s_1+ n_{\upsilon,1}$.

After this, we get a new cover sequence with the data embedded in it. Then compare the new cover sequence with the locations in PCRM having its value *x* and *x+1*. If there is a change in the new cover sequence from the PCRM value, ie, original value in PCRM was *x* and was changed to *x+1* in the new sequence which implies that the corresponding pixel location has become *x* times greater than 10 in the original video but after embedding data it have its value *x+1* times greater than 10, then change the corresponding pixel in any frame to make its difference frame value greater than or less than 10.

Repeat this process for all the changed bits in the new cover sequence. Thus we get the stego video. The value *k*, candidate vector lengths l_t and value of α should be embedded using any steganographic methods and send to the decoder.

B. *Data Extraction Method:*

The video is converted into frames and each frame is made gray. Using these gray frames generate PCRM and the histogram, as explained earlier and determine the peak value. Generate a binary cover sequence from the PCRM by using the peak value of the histogram.

Steps of extraction

1. Assign Y=$2^{(k+8)}$ and X=0.
2. Calculate

   T=max[1,round(Y.α)]. (7)
3. Take a bit in the stego sequence, if the bit is 0, update value of Y as Y=T
   Otherwise update values of Y and X as Y=Y-T and X=X+T respectively.
4. If Y>1 goto step 2, otherwise convert X into a binary value of (*k*+8) bits.

   R(k)=$\left\lfloor X/2^{(k-1)} \right\rfloor$mod2 (8)

   where, k=1,2,.....,(*k*+8)

   To calculate the secret bits, generate a matrix H such that

   H=[$I_K Q^T$], (9)

   where, Q is the stego-key.
5. To get the secret bits do the calculation

   s=H.R^T (10)

   Repeat the above steps until all bits in the stego sequence are processed.

6. Collect all calculated secret bits and concatenate to get the binary secret message sequence. Convert the sequence into the string.

IV. RESULTS

We implemented the hiding and extraction algorithms on an uncompressed video having frame size 240X320. The method was applied on two frames and it was found to hide a maximum of 2520 bits. The maximum Peak Signal to Noise Ratio (PSNR) was found to be 61 dB and the minimum value was about 39 dB. The degree of complexity was found to be less and the time of execution was found to be less than two minutes.

The histogram distortion was found by the equation

$$H = \sum_{i=1}^{2} |h'_i - h_i| \qquad (11)$$

It was found that the distortion of histogram is less than any other steganographic methods used.

TABLE I. TIME MEASUREMENT FOR EMDEDDING DIFFERENT BITS OF DATA

No. of bits embedded	Time for data hiding	Time for data extraction	PSNR
24	10.87s	12.15s	61.09dB
48	14.05s	12.00s	56.77dB
96	16.00s	12.01s	53.03dB
144	20.83s	11.93s	51.44dB
576	32.34s	11.69s	44.97dB
1152	63.19s	11.12s	42.20dB
2496	97.64s	6.75s	39.32dB

TABLE II. HISTOGRAM DISTORTION Vs BITS EMBEDDED.

No. Of Bits Embedded	Histogram Distortion	PSNR
24	104	61.08
48	88	56.77
96	108	53.03
144	204	51.44
576	168	42.20
1152	82	41.24
2496	678	39.32

V. CONCLUSION

We proposed a new data hiding method using motion histogram if a video. Unlike most data hiding methods in video that rely on motion vector, we chose a different approach that does pixel level motion estimation.

A motion histogram is developed from the difference frames and the histogram data is used as the cover sequence for hiding. The embedding and extraction algorithms are implemented and the results are evaluated. The proposed method is found to be less complex and maintains the steganographic distortion within the desired level.

The method was implemented by using only two frames. It was found that the histogram distortion is less than any other steganographic methods. Future work will be directed towards performing the method on more number of frames and also on compressed video.

REFERENCES

1. Haoran, Deepu, Liang-Tien, *"A New Motion Histogram to index motion content in video segments"*, Elsevier Pattern Recognition Letters 26, 2005.
2. Xingpeng, Shuozhong, *"Efficient data hiding with histogram preserving property",* Springer Telecommunication system, 2010.
3. F.A.P. Petitcolas, R. J. Anderson and M. G. Kuhn, "*Information hiding- A survey",* Proc. IEEE, vol. 87, no. 7, pp. 1062-1078, Jul. 1999.
4. X. Zhang and S. Wang, "*Dynamical Running Coding in Digital Steganography",* IEEE signal processing letter, vol. 13, no. 3, March 2006.
5. Hussein A. Aly, "*Data Hiding in Motion Vectors of compressed Video Based on their Associated Prediction Error",* IEEE Transaction on information forensics and security, vol. 6, no. 1, March 2011.

DENOISING OF IMAGES AND PERFORMING COMPRESSION USING ADAPTIVE ARITHMETIC CODING

ANCY M K[1] & ROSHNI V S[2]

[1]Department of Electronics And Communication Engineering, Amaljyothi College of Engineering, Kanjirapally,Kottayam,India
[2]ER and DCI Institute of Technology, Trivandrum, India

Abstract—This paper proposes a new algorithm for efficient storage and transmission of images particularly in Picture Archiving and Communication Systems (PACS). The algorithm contains two parts. First, involves denoising an image corrupted by impulse noise using Directional Weighted Median (DWM) filtering. Second involves the compression of the denoised image by using improved Adaptive Arithmetic Coding(AAC). It is observed that denoising an image and performing compression, the compression ratio attained is much larger. The ease of storing and transmission of digital images is a boon to many applications.

Index Terms*—Adaptive Arithmetic Coding, Directional Weighted Median Filter, Impulse noise detector,*

I. INTRODUCTION

In a Picture Archiving and Communication Systems (PACS) network and also in digital radiology, it is desirable to use a nondestructive image compression technique in order to minimize the storage space required and also to improve the transmission speed [1].The PACS system has to store large number of images. Large amount of data can adversely affect the performance of PACS systems. Hence it becomes important to perform compression on the original acquired image. Compression mainly aims to reduce the amount of data required to represent an image. The amount of compression in an image depends on the similarity between the pixels. The important reason for dissimilarity is the presence of noise within an image. Thus image denoising becomes important. The compression attained on the denoised image is better than the compression performed on the original image. Compression methods can be reversible or irreversible [2]-[3]. A reversible or error free compression can attain higher compression ratio. Better denoising means higher is the compression ratio. In the irreversible compression higher compression ratio can be attained at the expense of data loss.

Two important type of noise are Gaussian noise and impulse noise [4].. Here in the proposed work we are considering the images corrupted by impulse noise.

Impulse noise is of two types they are salt and pepper noise and also random valued noise. Impulse noise can be removed by proper nonlinear

or order static filtering particularly median filters are used. Limitation regarding median filtering is that they tend to blur or degrade the edge structures like corners which exist in almost all images [5]-[9].

The denoised image can be subjected to a lossless compression. Here coding redundancy with in an image is utilized [10]. There exist mainly two different coding techniques. They are the fixed length coding and variable length coding. In fixed length coding each of the unique symbols or the unique pixel intensities would be given code words of fixed length. In the proposed work we are utilizing variable length coding that assigns fewer bits to most probable intensity values than to less probable ones. The coding techniques used earlier were Run length coding [11] where an image can be represented as run length pairs, where it specifies the start of a new intensity and the number of consecutive pixels that have that intensity. The compression ratio attained was not that much better hence another coding called Huffman coding was used [12]. Here each unique source symbols that is, the image intensities were coded one at a time. This is considered as an optimal coding technique. Another important coding technique is arithmetic coding [13]. Here entire sequences of source symbols or intensities are coded and the sequence of message can be represented by a value between 0 and 1.Arithmetic coding is slower than Huffman coding but can attain higher compression ratio.

In the proposed work firstly, we perform noise detection by checking each and every pixel to have impulse noise or not. If a pixel is corrupted by impulse noise we replace the noisy pixel by using the information of the four directions to weight the pixels in the window. The filter used is directional weighted median (DWM) filter [14]. Secondly we perform compression on the denoised image using Adaptive Arithmetic Coding (AAC).Normal Static Arithmetic Coding (SAC) uses fixed probabilities for the entire pixel while AAC [15] dynamically estimates the probability of each pixel based on the previously encoded symbols.

The paper is organized into four sections. SectionII explains the procedures in the work. Section III gives

the experimental results followed by conclusion in section IV.

II. PROCEDURES IN THE PROPOSED WORK

A. Block Diagram of the Work

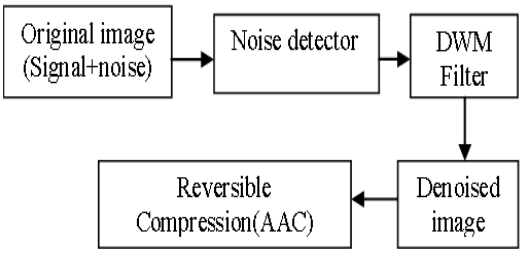

Fig 1. Complete block diagram of the proposed work

The original acquired image would be consisting of signal part and noise part. The noise detector checks each and every center pixel in a 5x5 window to be noisy or not. If the selected pixel is noisy proper directional weighted median filtering is done. Next we perform reversible compression on the denoised image.

B. Noise Detector

Here we consider a 5x5 window that moves along each and every pixel. The center pixel of a 5x5 window is taken. The center pixel would be associated with four sets of pixels in the four directions-horizontal, vertical and the two diagonal directions. Calculate the direction index along the four directions. The four set of pixel can be identified by their coordinate position. Consider the center pixel under consideration in a 5x5 window is centered at coordinate *(i,j)*

Let S_k(k=1to4) denote the four directions.

S_1(Diagonal D1)={*(i-2,j-2),(i-1,1),(i+1,j+1),(i+2,j+2)*}

S_2(Horizontal) = {*(i,j-2),(i,j-1),(i,j+1)(i.j+2)*}

S_3(Vertical)={*(i-2,j),(i-1,j),(i+1,j)(i+2,j)* }

S_4(Diagonal D2)={*(i-2,j+2),(i-1,j+1),(i+1,j-1)(i+2,j-2)*}

In general the coordinate can be represented as (*i*+*s*, *j*+*t*)

Algorithm for noise detection

1) Select the pixel which is to be checked

2) Calculate the direction index $d_{i,j}^{(k)}$ along all the four directions. Direction index along any direction is the sum of absolute difference of gray level values between center pixel and four pixels in that direction.

$$d_{i,j}^{(k)} = \sum_{(s,t)\in S_k} w_{s,t} \left| y_{i+s,j+t} - y_{i,j} \right| , 1 \le k \le 4$$

where

$$w_{s,t} = \begin{cases} 2, & (s,t)\ \epsilon\ \Omega^3 \\ 1, & otherwise \end{cases}$$

$$\Omega^3 = \{(s,t): -1 \le s,t \le 1\}$$

3)Among the four direction index associated with a pixel identify the minimum one.

$$r_{i,j} = \min\left\{ d_{i,j}^{(k)} : 1 \le k \le 4 \right\}$$

4) Compare the minimum direction index$r_{i,j}$ with a threshold. If the direction index is less than the threshold then it is not noisy else it is noisy

5)If noisy perform directional weighted median filtering

C. Directional Weighted Median Filtering

After impulse noise detection we would replace the noisy pixel based on the information in the four directions.

Algorithm

1) Calculate the standard deviation in the horizontal, vertical and the two diagonal directions.

2) Identify the pixel set in the direction which corresponds to minimum standard deviation. Minimum standard deviation means that the center pixel would be more similar to the pixel values in that direction

3) Assign weights to these set of pixel and can restore the noisy pixel as

$$m_{i,j} = median\{wm_{s,t} * y_{i+s,j+t}\}$$

Where

$wm_{s,t}$=

$$\begin{cases} 2\ , for\ pixels\ where\ \ deviation\ is\ minimum \\ 1, otherwise \end{cases}$$

the output of the DWM filter as

$$u_{i,j} = \alpha_{i,j} y_{i,j} + (1 - \alpha_{i.j}) m_{i,j}$$

$$\alpha_{i,j} \begin{cases} 0\ r_{i,j} > T \\ 1\ r_{i,j} \le T \end{cases}$$

D. Results Of Denoising

In this section we are comparing DWM filter with the normal existing median filter in the removal of random valued impulse noise. We are evaluating the Peak Signal to Noise Ratio (PSNR) of the image obtained by DWM and median filtered image. PSNR can be calculated from Mean Square Error (MSE).

$$MSE = \frac{1}{MN} \sum_{y=1}^{M} \sum_{x=1}^{N} [I(x,y) - I'(x,y)]^2$$

$I(x,y)$ =originalnoisy image

$I'(x,y)$=Filtered image

M,N dimensions of the image

PSNR=20*log 10(255/sqrt(MSE))

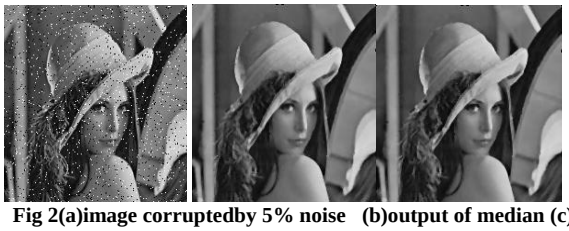

Fig 2(a)image corruptedby 5% noise (b)output of median (c) output of DWM

E. Compression of images

In this section we deal with compression of denoised image by Static Arithmetic Coding (SAC) and also Adaptive Arithmetic Coding (AAC).Arithmetic coding is an important compression technique in which an image can be represented by less number of bits than needed actually. In arithmetic coding a sequence of symbol could be encoded by providing a value between zero and one. Here we can say that the image can be represented by a value between zero and one. We using binary code to represent this value .Compression Ratio (CR) can be represented as,

$$CR = \frac{\text{number of bits needed to represent original image}}{\text{numbers of bits needed to represent the code}}$$

How Static Arithmetic Coding is performed

The algorithm for encoding an image is explained below

1) Identify the unique pixel intensity in an image.
2) We begin with the current interval [L,H) initialized to [0,1).
3) The current interval would be divided into subinterval on the basis of probability of the unique intensity present in an image.
4) The first intensity in the image is identified. The subinterval corresponding to that intensity would again be divided into smaller sub interval on the basis of probability. The number of sub intervals is same as the number of unique intensity in the image.
5) Identify the next intensity and their corresponding subinterval obtained from step 3.The sub interval obtained from step 3 is again divided on basis of probability.
6) Repeat the step 4 until the entire image can be represented by a value between zero and one.

Adaptive Arithmetic Coding(AAC)

AAC is an efficient method that allows updating the probabilities in the static arithmetic coding process in order to reduce the data size. AAC dynamically calculates the probability of the current pixel based on the entirepixel that precedes it. Here it involves two steps. In the first step the true probabilities are calculated whereas in the second step the AAC encode the input image and update the probabilities dynamically when finding the last occurrence of the current pixel.

Overview of the proposed method

Let *X* be an image of *m* pixels. Instead of coding X with a fixed probability distribution, a dynamic probability table is used. Therefore, while encoding the image pixels, we check whether we have encoded the last occurrence of current pixel. If this is the case we must subtract the frequency of corresponding pixel from the image size, and hence the probability table must be recomputed to encode the remaining pixels. It is seen that if we have a message of n symbols, we have at most updated the probability table n-1 times. Fig 2 shows how the encoding algorithm works.

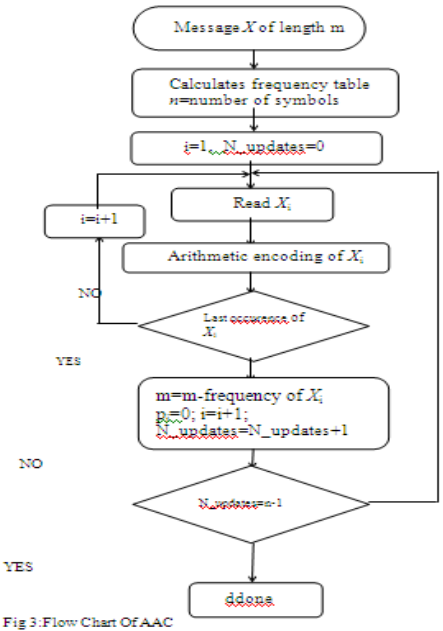

Fig 3:Flow Chart Of AAC

III. RESULT AND OBSERVATIONS

In this section we show the experimental results to evaluate the performance of the denoising technique and also the proposed coding technique. Peak Signal to Noise Ratio(PSNR) of images corrupted by different noise percentage was evaluated. PSNR obtained by directional weighted median filtered image is compared with median filtered image and graphs were ploted.

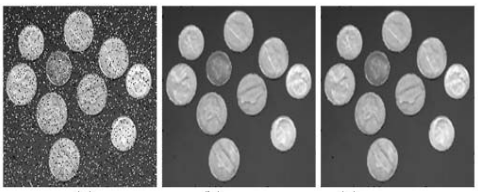

(a) (b) (c)

Fig 4: (a)image coins with 10% noise (b)output of median (c)output of DWM

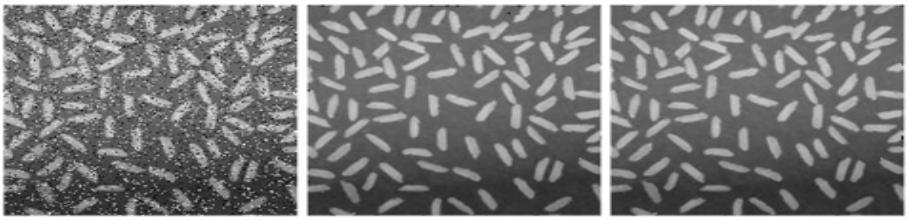

(a) (b) (c)

Fig.5 (a) image rice with 10% noise (b)output of median (c)output of DWM

Image Name	Noise Percentage / Filter Type	PEAK SIGNAL TO NOISE RATIO(PSNR)					
		5%	10%	15%	20%	25%	30%
Lena	Median	41.00	38.57	36.92	35.01	33.93	29.47
	DWM	44.05	40.62	38.97	37.06	35.63	30.95
Coins	Median	48.61	41.98	39.28	37.01	33.55	30.41
	DWM	55.91	48.56	45.18	42.57	38.59	34.98
Rice	Median	48.02	45.95	42.21	39.06	35.06	31.76
	DWM	49.94	47.87	44.18	41.03	36.47	33.04

Table 1: PSNR obtained by median filtering and DWM filtering on different Images for different noise percentage

Figure 4 and 5 shows the resulting images obtained as a result of median and DWM filters. The output of DWM is slightly better than median. From table 1 it is clear that PSNR value is better for DWM filtered image than the normal median. Larger PSNR means proper denoising. The above table shows that there wasa5% , 15%,and 4% improvement in PSNR values of Lena, coins and rice images while DWM filters were used .

The denoised image is then subjected to compression by using Static Arithmetic Coding (SAC) and also by Adaptive Arithmetic Coding (AAC).

Image Name	Noise percentage	Compression Ratio(CR)			
		SAC		AAC	
		Median	DWM	Median	DWM
Lena	5%	1.0601	1.0604	2.1872	2.1874
	10%	1.057	1.0592	2.1270	2.1273
	15%	1.054	1.058	2.1134	2.1205
	20%	1.055	1.056	2.0319	2.0369
	25%	1.050	1.0511	2.0692	2.0706
	30%	1.048	1.049	1.9811	2.0207

Table 2: Comparison of CR obtained by SAC and AAC on coins

Image Name	Noise percentage	Compression Ratio(CR)			
		SAC		AAC	
		Median	DWM	Median	DWM
Lena	5%	1.0601	1.0604	2.1872	2.1874
	10%	1.057	1.0592	2.1270	2.1273
	15%	1.054	1.058	2.1134	2.1205
	20%	1.055	1.056	2.0319	2.0369
	25%	1.050	1.0511	2.0692	2.0706
	30%	1.048	1.049	1.9811	2.0207

Table 3: Comparison of CR obtained by SAC and AAC on lena

Table 2and 3 shows that the compression ratio attained by AAC is better than SAC. Consider the case in which originally 100 bits were needed to represent the image. From table 4 the CR attained by AAC is almost 5 and by SAC it is about 1.27.According to definition of CR that is the ratio of number of bits needed to represent the original image

to that needed to represent the code, it can be verified that for SAC it requires about 78 bits to represent the image while in case of AAC it requires only 20 bits to represent the same image. So less number of bits required to be transmitted in case of AAC than SAC.

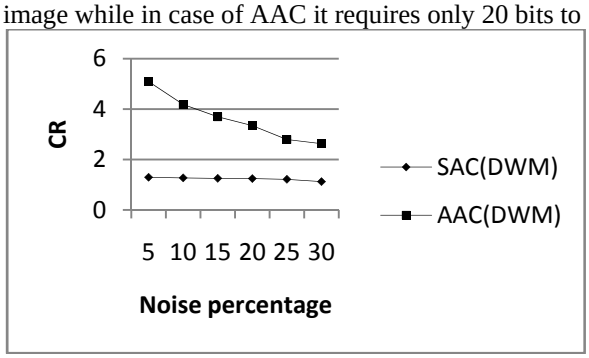

Fig 6. Graph showing Noise percentage versus CR for image coins

The above graph shows that the CR obtained by AAC is better than SAC. As noise percentage increases CR gets decreased due to greater dissimilarity in pixel values

Noise percentage	TIME ELAPSED(seconds)	
	SAC	AAC
5%	126.135	3.487
10%	132.260	3.528
15%	136.315	4.470

Table 4: Comparison of time elapsed by SAC and AAC for image coins.

Above table shows that time elapsed by AAC is lesser compared with SAC. Also as the noise percentage increases the time taken for coding also increases since the number of dissimilar pixel is greater for large noise content.

IV. CONCLUSION

From the experimental results obtained from the above section we can conclude that the extend of compression depends on the similarity among the pixels in an image. Lesser the noise content more is the similarity among the pixels at the same time the Peak Signal to Noise Ratio (PSNR) attained is also large. By proper denoising filters noise present in the original acquired image can be removed. Here by Directional Weighted Median (DWM) filtering noise was used and there was 5%,4% and 15% improvement in the PSNR values of Lena, coins and rice images respectively while using DWM in comparison with the median.

Then compression is performed on the denoised image. The compression ratio attained by output of DWM is slightly better than the output attained by median filter. Compression reduces the number of bits needed to represent the image that is greater compression means storage space required is less. Here compression is performed by SAC and AAC. AAC is highly advantageous due to two reasons mainly. Firstly the storage space required for storing the image is less as it can attain higher CR. Secondly the time taken for transmission would also be less. Thus the two important aspects of any Picture Archiving and Communication System (PACS) that is storage space and transmission time is reduced by the new Adaptive Arithmetic Coding

REFERENCES

[1] G. Q. Macquire, Jr., M. E. Noz, A. Bakker, K. Bijl, H. Didden, and J. P. J. de Valk, "Introduction to PACS for those interested in image processing,"*Information Processing in Medical Imaging*, pp. 315-323, 1988

[2] Tzong-Jer Chen, and Keh-Shih Chuang,"A Pseudo Lossless Image Compression Method,"*Third International Congress on Image and Signal Processing"*,pp.610-615, 2010

[3] M.Rabbani, and P.W.Jones, "Digital Image Compression Techniques,"SPIE press,1991

[4] Yiqiu Dong,RaymondH,andShufangXu,"A detection statistic for random-valued impulse noise,"*IEEE Trans. On Image Processing*,vol16,no. 4, pp.1112-1120, April 2007.

[5] T. Chen and H. R. Wu, "Space variant median filters for the restorationof impulse noise corrupted images,"*IEEE Trans. Circuits Syst. II*, vol.48, no. 8, pp. 784–789, Aug. 2001.

[6] R. H. Chan, C.-W. Ho, and M. Nikolova, "Salt-and-pepper noise re-moval by median-type noise detectors and detail-preserving regular-ization,"*IEEE Trans. Image Process*., vol. 14, no. 10, pp. 1479–1485,Oct. 2005

[7] W. Luo, "A new efficient impulse detection algorithm for the removal of impulse noise,"*IEICE Trans. Fundam.*, vol. E88-A, no. 10, pp.2579–2586, Oct. 2005

[8] E. Abreu, M. Lightstone, S. K. Mitra, and K. Arakawa,"A new efficient approach for the removal of impulse noise from highly corruptedimages," *IEEE Trans. Image Process*., vol. 5, no. 6, pp.1012–1025,Jun. 1996.

[9] Mukesh C Motwani,Mukesh C Gadiya,andRakhi C Motwani,"Survey of image denoising techniques,"unpublished.

[10] Sonal, and Dinesh Kumar,"A study of various image compression techniques,"unpublished.

[11] C.Tu, J.Liang, and T. D. Tran,"Adaptiverunlengthcoding,"*IEEE Signal Processing Letters*, vol 10,pp. 61-64,Mar.2003. 301].

[12] Sharma.M,"Compression Using Huffman Coding," *International Journal of Computer Science and Network Security*, VOL.10 No.5, May 2010,"

[13] P. G. Howard and J. S. Vitter, "Analysis of Arithmetic Coding for Data Compression," *Information Processing and Management*, 28, no. 6, pp. 749-763, 1992.

[14] Yiqiu Dong, and ShufangXu,"A new directional weighted median filter for removal of random-valued impulse noise,"*IEEE Signal Processing Letters*, vol. 14,no.3,pp.193-196, March 2007

[15] AtefMasmoudi, William Puech, and Mohamed SalimBouhlel,"Efficient adaptive arithmetic coding based on updated probability distribution for lossless image compression," *Journal of Electronic Imaging*,vol.19,no.2,pp. 023014-1-6, April-June2010

Ancy M K received the B-Tech degree in Electronics and Communication Engineering from Mahatma Gandhi University, Kerala, India in 2010. She is pursuing M.Tech degree Communication Engineering at AmalJyothi College of Engineering, Kanjirapilly,Kerala,India. Her areas of interests are Communication Engineering and Mat lab.

DETECTION OF EPILEPSY USING HEART RATE VARIABILITY

MITHIN.R[1], ELIZABETH THOMAS T[2] & ABU BECKER[3]

[1,2&3]Dept. of ECE, AJCE, Kottayam, Kerala

Abstract— To investigate whether epileptic seizures could be predicted or detected by means of heart rate variability. Patients with temporal lobe epilepsy participated in the prospective study while enrolled for video/EEG monitoring. ECG was continuously monitored and 30 min seizure sessions and non seizure sessions were chosen for analysis. Mean, standard deviation and RMSSD of the RR time interval were recorded and observed. Low frequency, high frequencies and reciprocal HF power were determined using FFT spectral analysis. All of the analyzed and extracted features depicted a minimum variation in the heart rate variability indicating a pre-seizure onset characteristics. Specifically high reciprocal HF power peaks suggest suppressed parasympathetic around seizure onset time. Seizure detection using HRV analysis seems to be a promising method for non-invasive seizure detection in the early phase of the clinical event..

Index Terms— *Heart rate variability, seizure-onsite detection, temporal lobe epilepsy, FFT spectral analysis, reciprocal HF-power*

I. INTRODUCTION

Epileptic seizures are often thought to have a well-defined onset time determined with EEG and clinical signs. However some persons suffering from epilepsy can sense the seizures coming before it is registered on the EEG indicating that physiological changes happen in the pre-ictal period before the seizures arise. Seizure alert dogs have also been shown to predict seizures several minutes before they occur for some epilepsy patients, but the specific signals by which the dogs sense the seizure coming are still unknown. Cortical function changes might occur at some stage in the pre-ictal period, but also autonomic changes have been hypothesized to occur before seizure onset, although no reliable marker of this has been found. A non invasive technique of measuring changes in the autonomic nervous system is by means of Heart Rate Variability(HRV) analysis. It has been demonstrated that specific frequency bands of HRV are associated with specific physiological parameters. Thus the high- frequency band(HF) (0.15-0.40 Hz) defining the respiratory frequency in an HRV analysis is said to represent the parasympathetic tonus and the low frequency(LF)(0.04-0.15 Hz) defining the non-respiratory frequency in an HRV analysis is believed to be a mixture of sympathetic and parasympathetic tonus.

HRV studies of frontal lobe epilepsy have shown a lower inter-ictal HF, which indicates a reduction of the parasympathetic tonus and it is postulated to generate the relative high number of "Sudden Unexpected Death" in this epileptic group. Patients with generalized tonic clonic seizure history have significant lower HF and higher LF in comparison with a normal population. On the contrary temporal lobe epilepsy(TLE) patients have found a general lower LF compared with matching healthy individuals. The general conviction however is that TLE have an overall lower HRV power than matching healthy individuals.

Many of the studies involving HRV analysis of epileptic patients have been made with a view to investigate the reason why epilepsy patients have been made with a view to investigate the reason why epilepsy patients have increased risk for Sudden Unexpected Dead(SUDEP). These studies therefore concentrate on the inter-ictal time period, often with 24 hours HRV analysis, where seizures do not occur. Consequently these studies do not consider the faster evolving chances that might occur in the pre-ictal and ictal period, where a seizure prediction or detection might be possible. However a few studies have been made in consideration to these aspects reports of an increase in the HRV powers in the pre-ictal period of both HF and LF, where the HF power reach maximum 30 sec pre-seizure onset followed by a sudden and drastic decrease, while the LF power reach maximum at seizure onset followed by a sudden and drastic decrease, while the LF power reach maximum at seizure onset. There has been found tendencies of reduced HRV-powers pre-ictal by means of power spectrum analysis, although no significant difference in LF, HF powers were established compared with a similar period just before the pre-ictal state.

The purpose of this study is to assess whether epileptic seizures could be predicted or detected by means of Heart Rate Variability analysis on patient with temporal lobe epilepsy.

II. QRS DETECTION

Heart rate variability signals describe either the time period elapsed between successive heartbeats or the

"instantaneous heart rate" on each beat instant. Thus the first step of HRV analysis is the detection of the heartbeat time instants. The most precise way of doing that is through QRS detection.

A typical QRS detector consists of a preprocessing part followed by a decision rule. Several different QRS detectors have been proposed within last decades. The preprocessing of the ECG usually includes at least bandpass filtering to reduce power line noise, baseline wander, muscle noise, and other interference components. The passband can be set to approximately 5–30 Hz which covers most of the frequency content of QRS complex. In addition, preprocessing can include differentiation and/or squaring of the samples. After preprocessing, the decision rules are applied to determine whether or not a QRS complex has occurred. The decision rule usually includes an amplitude threshold which is adjusted adaptively as the detection progresses. In addition, the average heart beat period is often used in the decision. The fiducial point is generally selected to be the R-wave and the corresponding time instants are given as the output of the detector.

The accuracy of the R-wave occurrence time estimates is often required to be 1–2 ms and, thus, the sampling frequency of the ECG should be at least 400 Hz . If the sampling frequency of the ECG is less than 400 Hz, the errors in R-wave occurrence times can cause critical distortion to HRV analysis results, especially to spectrum estimates. The distortion of the spectrum is even bigger if the overall variability in heart rate is small. The estimation accuracy can however be improved by interpolating the QRS complex e.g. by using a cubic spline interpolation or some model based approach. It should be, however, noted that when the SA-node impulses are of interest there is an unavoidable estimation error of approximately 3 ms due to fluctuations in the AV-nodal conduction time.

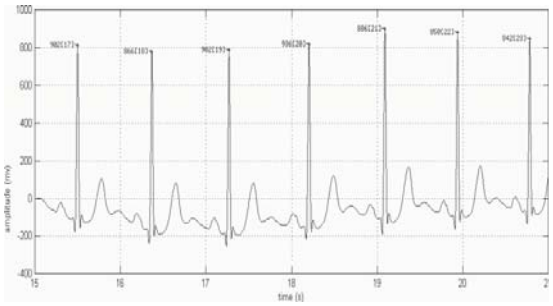

Fig.1. Result of QRS detection. The dots indicate the detected peak of each R wave. The detection instants are used to generate the RR interval series. The numbers outside the brackets are the calculated RR interval values in milliseconds and the ones inside the brackets are the indexes of the intervals

III. TIME DOMAIN ANALYSIS MODULE

In this module, the time series of RR intervals obtained on the previous module is evaluated. Importing RR interval series from previously typed ASCII files is also possible. The user will get the HP signal graph and the following statistics of the time series: total number of intervals; maximum amplitude value, minimum amplitude value and dynamic range; average amplitude, standard deviation and variance coefficient; pNN50 and rMSSD. The time-domain methods are the simplest to perform since they are applied straight to the series of successive RR interval values. The most evident such measure is the mean value of RR intervals (RR) or, correspondingly, the mean HR (HR).

IV. FREQUENCY DOMAIN ANALYSIS MODULE

In this module, ECG Lab presents a power spectrum density (PSD) graph of the HRV signal, as well as some spectral parameters. The user defines three frequency bands: very low frequency (VLF), low frequency (LF) and high frequency (HF). Then the following parameters are calculated: absolute energy in each band and the total energy; normalized energy in each band (as a percentage of the total energy); relative energy in the LF and HF bands (in comparison to the total energy in both bands); LF/HF ratio.

Due to uneven sampling and ectopic beats, the user can choose one of three different techniques: removal of ectopic beats from the time series; replacement of ectopic beats with normal intervals; removal of ectopic beats and interpolation of the HRV signal using cubic splines. The user can also use the heart rate signal (HR) instead of the heart period signal (HP). There are three different methods available for PSD estimation: Fast Fourier Transform (FFT), auto-regressive model (AR) and Lomb-Scargle periodogram.

V. PATIENTS AND METHODS

A. Patients

Adult patients with TLE, who already have been diagnosed and referred to Video/EEG monitoring for either presurgical evaluation or assessment of seizure frequency at Neurophysiologic Department of SCT hospital, Trivandrum were eligible for inclusion in the study. Patients with a history of coronary heart disease, diabetes or any other known disease that might affect the autonomic nervous system were excluded, as were pregnant or nursing female patients.

Data were obtained from patient during their 2-4 days of 24 h Video/EEG monitoring.

B. Methods

ECG was retrieved by a wireless Nexus 10 device with a sample rate of 400Hz, using adhesive recording electrodes. Data was obtained by the Nexus 10 software program and saved in raw ASCII format for further data processing.

The seizures were identified and their timing was noted based on the analysis of EEG recordings.

Seizures without EEG- correlation were excluded as well as seizures arising within 2 hours of previous seizures. ECG data sessions from 25-30 min pre-seizure onset to 30 sec-5min post seizure onset were chosen for further HRV calculation and analysis.

A custom computer program was created using matlab for retrieval of the tachogram(R-R intervals)from the ECG data. The program firstly removed the artifacts and the line noise artifacts using simple band pass filter specifications and secondly found out the R peaks by simple detection. A manual R peak plotting program was also created in order to ensure that the retrieved tachogram was correct in spite of automatically faultily plotted R-peaks and or missed R peak.

The HRV parameters were extracted using the time domain analysis to detect the amount variations in the heart rate and were later retrieved using the Fast Fourier Transformation power spectral density of the RR interval tachogram. This ensured that a new analysis could be made for every heart beats and maximizing the possibility of detecting any fast involving fluctuations. The delta frequency of 0.015625Hz determined the boundaries of the Low Frequency and High Frequency bands making the LF band power representing powers of frequencies from 0.046875 Hz to 0.140625Hz and the HF power band representing powers of frequencies from 0.15625Hz to 0.390625Hz. As extraordinary HF power drops were repeatedly seen just about seizure onset a reciprocal HF power graph was created and maximum peak value and peak time were found for every session.

VI. RESULTS

Three patients (2 female, 1 male) had seizure(s) with EEG-correlate during their hospitalization, resulting in 6 recorded and analyzed seizures (1 secondary generalized tonic-clonic seizure (GTCS), 4 complex partial seizures (CPS) and 1 simple partial seizures (SPS)) and 6 non-seizure sessions for comparison (3 day + 3 night).

No significant LF-power peaks or drops were found for any of the seizure sessions compared with non-seizure sessions. LF/HF-ratio graphs showed peak tendencies in the region of seizure onset for most of the analyzed seizures, but peaks with equal or higher amplitude were also seen at non-seizure session for one patient (Patient 3). The peak tendencies for LF/HF-ratio at seizure onset were highly due to, and caused by substantial HF-power drops at same time. This was most evident when computing the HF-power data as reciprocal HF-power, where unique high peak values were seen just around seizure onset time for all 3 seizures. Figures 1-3 show the reciprocal HF- power graphs 5 min pre-seizure for all 3 seizures.

Reciprocal HF-power peaks were clearly manifesting just around seizure-onset for all seizures. Unfortunately movement artifacts made the EKG retrieval impossible only seconds after seizure-onset for patient 3, seizure 2. Thus it could be argued that even higher reciprocal HF-power peaks would have been reached for these seizures if more EKG-data were available.

The reciprocal HF-power peaks maximum were evident between 10 sec pre seizure-onset and 24 sec post onset with peaks amplitudes 2.96-93.63 times higher than the respective patient's non-seizure reciprocal HF-power peak(Table 1).

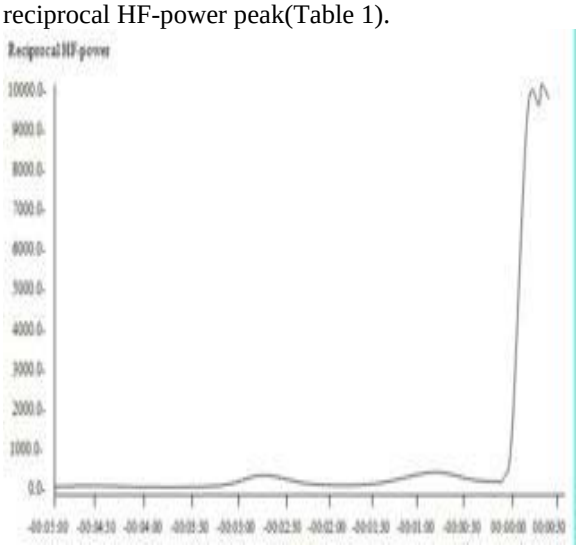

Fig.1. Patient 1, seizure 1. Reciprocal HF-power graph, 5 min pre-seizure onset to 30 sec post seizure onset. Maximum peak time at 00:00:09. Y-axis in 1/(s2/Hz). X-axis in tt:mm:ss. 00:00:00 = seizure onset

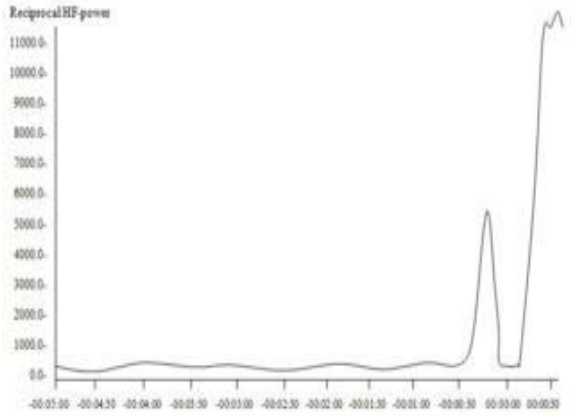

Fig.2. Patient 2, seizure 1. Reciprocal HF-power graph, 5 min pre-seizure onset to 30 sec post seizure onset. Maximum peak time at 00:00:24. Y-axis in 1/(s2/Hz). X-axis in tt:mm:ss. 00:00:00 = seizure onset

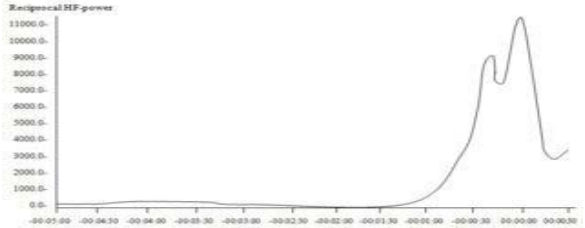

Fig.3. Patient 3, seizure 1. Reciprocal HF-power graph, 5 min pre-seizure onset to 30 sec post seizure onset. Maximum peak time at -00:00:10. Y-axis in 1/(s2/Hz). X-axis in tt:mm:ss. 00:00:00 = seizure onset

Table 1

	Type of seizure	Reciprocal HF-power peak amplitude seizure in ($1/s^2$/Hz))	Reciprocal HF-power peak amplitude non-seizure in ($1/s^2$/Hz))	Ratio (Peak amplitude Seizure / Peak non-seizure)	Peak time vs. Seizure-onset time
Patient 1	GTCS	9957	1376	7.24	9 sec after
Patient 2	CPS	11825	4000	2.96	24 sec after*
Patient 3	CPS	11472	199	57.65	10 sec after

GTCS = Secondary Generalized Tonic-Clonic Seizure, CPS = Complex Partial Seizure, SPS = Simple Partial Seizure. (*) At patient 2's seizure two peaks were recorded, the first manifested 10 sec before seizure with and amplitude at app. 5500 ($1/s^2$/Hz)

Although some maximum peak amplitudes did not manifest until post seizure-onset the reciprocal HF-power amplitude exceeded non-seizure maximum for all seizures between 30 sec pre seizure-onset and seizure onset time.

VII. DISCUSSION

The main purpose of this study was to measure HRV on a short time basis and thus search for specific changes in the different HRV-parameters before seizure-onset. Focus was set on individual analysis of every seizure. This (and the low number of recruited patients) naturally diminishes the opportunity to make statistical analysis, but also enhances the possibility of discovering new findings in regard to individual and group specific changes in HRV-parameters on the short term basis. As mentioned earlier most scientific studies regarding HRV-analysis of epileptic patients has been done with long term analysis inter-ictal (often 24 hours) in regard to control to estimate general HRV differences for example on the topic of sudden unexplained death (SUDEP). Some research however has also been done in consideration of the pre-ictal period with short term HRV-analysis. Novak et al. found that both LF and HF power amplitude and rising minutes before seizure –onset with HF power peak about 30 sec pre-seizure-onset followed by a rapid decline and minimum each during seizure for TLE with complex partial seizures. Also a more recent study by Malarvili and Masbah concerning seizure detection of new-born children found a HF-power drops during seizure. Although the HF-power drops during seizure have been stats in these previous studies it has not been quantified. The reciprocal HF power calculation is an easy way of doing this, but to the best of our knowledge the method has not been used in any study previous to this study.

The result of this study show a clear tendency towards an extreme and unique HF-power drop and no thereby a reciprocal HF-power peak just around the time of seizure onset. This indicates an almost total absence of parasympathetic tonus during the early stages of seizure activity. Even though some of the reciprocal HF-power peak did not occur until after seizure-onset, all of the 3 seizures had reciprocal HF-power values exceeding the maximum non-seizure amplitude (patient specific) just before or at time of seizure onset. This indicates that a parasympathetic suppression happens few seconds before seizure onset, which opens the possibility of predicting the seizure seconds before seizure-onset.

A number of studies shown that mechanical stimulation of the vagal tonus, which produce parasympathetic stimulation with Vagus Nerve Stimulation (VNS), have reduces seizure frequency for several epileptic patient . It has also been established that the LF/HF ratio is decreased during stimulation , as LF power diminish and HF power increased, which indicates an elevated parasympathetic tonus during stimulation. Combined with the trend of drastic HF power decline around seizure-onset seen in this study, speculation could be made, that the VNS ensures that drastic parasympathetic suppression and thereby HF-power decline never occurs and seizures consequently are prevented.

Although VNS stimulates the vagal tonus, no effect have been proven on the HF power in long term time intervals (24 hours), before and after implantation of VNS . However , one study showed tendencies of nocturnal decline in HF-power 3 years after implantation Barone et al. argue that the lack of detectable HF-power increased at 3-mouths follow up could be that the stimulation creates adaption, which counter balances the direct effect of the vagus stimulation. This seems plausible, as VNS often is set to stimulate for 30 sec period followed by 5 min non-stimulating period which result in more than 2 hours stimulation a day. To erase any adaption effect it would be of great interest if the VNS only stimulated when necessary.

Morris found a reduction of seizure frequency and seizure diminution for epileptic patients with "on-demand " VNS initiated by the patient, when sensing a seizure coming. An "on-demand" VNS could be argued to diminish the adaption of constant long-term VNS stimulation, which may well suggest that vagus nerve stimulation would have a more efficient effect, when only applied "on-demand". If this thesis is combined with the findings in this study of a future aspect could be: A HF power detector signaling when VNS-stimulation should occur, where by the HF-power fails to reach critical low value and seizure consequently terminates.

This scenario of course still depends on the ability of predicting seizure by reciprocal HF-power peaks and doing so in time to terminate arising seizures with VNS. All 3 seizures in this study manifested the

reciprocal HF-power peaks around seizure-onset (10sec pre-24 sec post), but all the seizure also had reciprocal HF-power above non-seizure maximum before or at time of seizure –onset, which suggest that a prediction of seizure could be made. We have to admit that method by which the timeline is created in this study argues against an online (i.e., real-time) prediction of seizures, because every FFT-power density spectrum analysis consist of 32 R-R intervals before and 32 R-R intervals after the given time on the time axis. Thus a detection of extensive reciprocal HF-power amplitude is not accessible until 32 heart beats after a given time. This obviously limits the possibility of seizure prediction with the method used in this study, but a possible way to overcome this limitation could be to either use a different method than a FFT in retrieving the power density spectrum or to down scale the window length to for example 32 R-R intervals.

Although prediction of seizures with HRV analysis seems unsure, a seizure detection alarm itself could be an important tool for many people suffering with epilepsy. The result of this study strongly indicates that seizure detection is possible with HRV-analysis, but as this is only a pilot study further large scale studies needs to be done for significant standardized analysis.

VIII. CONCLUSION

During epileptic seizures we demonstrated reciprocal HF-power peaks multiple times higher than maximum non-seizure periods day and night (patient-specific) just around seizure onset (10sec pre-24sec post). Data suggests that seizure detection using HRV seems very likely, and prediction a few seconds before seizure-onset could be possible. If seizure-prediction could be made by means of HF-power measurement seconds before seizure-onset, possibility of automatic seizure-termination with a combined VNS could be a future aspect. Further studies, with larger patient-samples and control periods are needed for evaluation of the clinical usefulness of our method.

ACKNOWLEDGMENT

Thanks to all the staff at Neurophysiologic Department of SCT Hospital, Trivandrum and CDAC for their assistance and providing all the necessary equipment for realizing the measurements.

REFERENCES

[1] S.W.Brown and V.Strong, The use of seizure-alert dogs, *Seizure* 1 (Jan 2001)

[2] D.J.Dalziel, B.M.Uthman, S.P.Megorray and R.L.Reep, Seizure-alert dogs: a review and preliminary study, Seizure 2 (Dec 2003), 115-120

[3] D.H.Karem and A.B.Geva, Forecasting epilepsy from the heart rate signal, *Med Biol Eng Comput* 43 (Mar 2005), 230-239

[4] V.V.Novak, L.A.Reeves, P.Novak, A.P.Low and W.F.Sharbough, Time-frequency mapping of R-R interval during complex partial seizures of temporal lobe origin, *JAuton Nerv Syst* 77 (Sep 1999), 195-202.

EFFICIENT QUANTIZATION OF PARALLEL FIR FILTER USING NUS AND MAD ALGORITHMS

MERLIN MATHEW[1], NISHA THOMAS[2] & GEEVARGHESE TITUS[3]

[1]Department of ECE, ER and DCI Institute of Technology
[2]Department of ECE, Amal Jyothi College of Engineering, Trivandrum, India
[3]Amal Jyothi College of Engineering, Kottayam, India

Abstract— Parallel (or block) FIR digital filters can be used either for high-speed or low-power (with reduced supply voltage) applications. Traditional parallel filter implementations cause linear increase in the hardware cost with respect to the block size. Recently, an efficient parallel FIR filter implementation technique requiring a less-than linear increase in the hardware cost was proposed. The use of the appropriate fast FIR filter structures and the proposed quantization scheme can result in reduction in the number of binary adders. This paper makes two contributions for quantization. First, the coefficients are quantized using NUS (National University of Singapore) algorithm and then MAD (Maximum Absolute Difference) quantization algorithm. Quantization is done in a new method of SPT (Signed Power of Two) term allocation. The coefficient values are not allocated with the same number of SPT terms. Coefficient values with larger magnitudes are allocated with more SPT terms than those with smaller magnitudes. MAD quantization algorithm is considered more efficient for the implementation of parallel filters than NUS algorithm.

I. INTRODUCTION

Low complexity FIR filter implementation has been given extensive consideration. However, most of the past efforts have been directed towards multiplier less implementation with coefficients expressed as sums of signed power-of-two terms (SPT)**.** Furthermore, very little work has been done that deals directly with reducing the hardware complexity of parallel FIR filters.

Traditionally, the application of parallel processing to an FIR filter involves the replication of the hardware units that exist in the original filter. If the area required by the original circuit is A, then the L-parallel circuit requires an area of L x A**.** Recently, an efficient parallel FIR filter implementation technique requiring a less-than linear increase in the hardware cost was proposed using FFAs (Fast FIR Algorithms) **.** The hardware cost can be reduced further by exploiting the frequency spectrum characteristics. This is achieved by selecting appropriate FFA structures out of many possible FFA structures all of whom have similar hardware complexity at the word-level. However, their complexity can differ significantly at the bit-level.

In order to implement a digital filter in hardware, the ideal filter coefficients must first be quantized. Traditionally, the quantization process consists of a direct binary conversion of the coefficients in conjunction with a truncation or rounding scheme. This quantization method is straightforward and time-efficient. However, the quantized filter coefficients contain large number of nonzero bits.

It is well known that if each coefficient value of a digital filter is a sum of signed power-of-two (SPT) terms, the filter can be implemented without using multipliers. In the past decade, several methods have been developed for the design of filters whose coefficient values are sums of SPT terms. Most of these methods are for the design of filters where all the coefficient values have the same number of SPT terms. It has also been demonstrated recently that significant advantage can be achieved if the coefficient values are allocated with different number of SPT terms while keeping the total number of SPT terms for the filter fixed. Some method allows the number of SPT terms for each coefficient to vary subject to the number of SPT terms for the entire filter. This provides the possibility of finding a better filter without increasing the number of adders, which determines the realization cost for a given filter length. The increase in the freedom of selecting the SPT terms will reduce the quantization error of the coefficients.

II. QUANTIZATION ALGORITHMS

Consider the general formulation of a length-N FIR filter,

$$Y_n = \sum_{i=0}^{N-1} h_i x_{n-i}, \quad n=0, 1, 2, ..., \infty$$

where $\{x_i\}$ is an infinite length input sequence and $\{h_i\}$ are the length N FIR filter coefficients.Quantization is done using these filter coefficients. Here we will discuss about NUS (National University of Singapore) and MAD (Maximum Absolute Difference) quantization algorithm.

A. NUS Algorithm

If the filter coefficients are first scaled before the quantization process is performed, the resulting filter will have much better frequency-space characteristics. The NUS algorithm employs a scalable quantization process. To begin the process, the ideal filter is normalized so that the largest coefficient has an absolute value of 1. The normalized ideal filter is then multiplied by a variable scale factor (VSF). The VSF steps through the range of numbers from 0.4375 to 1.13 with a step size of 2^ (-W), where W is the coefficient word-length. Signed power-of-two (SPT) terms are then allocated to the quantized filter coefficient that represents the largest absolute difference between the scaled ideal filter and the quantized filter. The NUS algorithm iteratively allocates SPT terms until the desired number of SPT terms has been allocated or until the desired NPR specification is met. Once the allocation of terms has stopped, the normalized peak ripple (NPR) is calculated. The process is then repeated for a new scale factor. The quantized filter leading to the minimum NPR is chosen.

NUS algorithm is described by the following pseudocode:

Normalize the set of filter coefficients so that the magnitude of the largest coefficient is 1;
For VSF=Lower Scale: Step Size: Upper Scale,
{
Scale normalized filter coefficients with VSF;
Quantize the scaled coefficients using SPT term allocation scheme in NUS algorithm ;
Calculate NPR of the quantized filter;
}
Choose the quantized coefficient that leads to the minimum NPR.

Normalized Peak Ripple (NPR) can be calculated using the equation

$$NPR = \delta / g$$

where δ is the pass band ripple (in dB) and g is the pass band gain (in dB)

The parameter δ is chosen during the filter design, and g is calculated by:

$$g = (Pmax + Pmin) / 2$$

where Pmax and Pmin are the maximum and minimum pass band frequencies.

SPT Term Allocation: If each coefficient value of a digital filter is a sum of signed power-of-two (SPT) terms, the filter can be implemented without using multipliers. Most of the methods are for the design of filters where all the coefficient values have the same number of SPT terms. It has been demonstrated recently that significant advantage can be achieved if the coefficient values are allocated with different number of SPT terms while keeping the total number of SPT terms for the filter fixed. The number of SPT terms allocated to a coefficient is determined by the statistical quantization step-size of that coefficient and the sensitivity of the frequency response of the filter to that coefficient. Coefficient values with larger magnitudes are allocated with more SPT terms than those with smaller magnitudes. Comparing with the allocation scheme where all the coefficient values are allocated with the same number of SPT terms, this new allocation scheme produces designs with significantly smaller normalized peak ripple magnitude.

DESIGN EXAMPLE: Consider an ideal filter section with the following parameters: pass band ripple=3dB, stop band ripple=60dB, pass band frequency=3000Hz, stop band frequency=3300Hz, sampling frequency=8000Hz.Frequency responses are shown below: From fig. 1 and 2, ripples of the NUS quantized filter increases compared to Ideal filter.

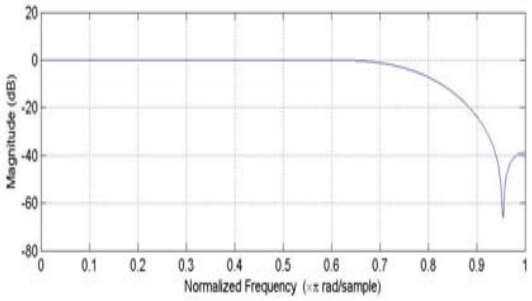

Fig. 1. Frequency response of Ideal filter

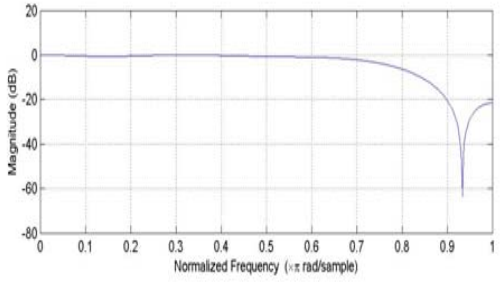

Fig. 2. Frequency response of NUS Quantized filter

B. Look-Ahead MAD Quantization

In parallel FIR filters, the NPR cannot be used as a selection criterion for choosing the best quantized filter since pass band/stop band ripples cannot be defined for the set of filters obtained by the application of FFAs. It is shown that the maximum absolute difference (MAD) between the frequency responses of the ideal filter and the quantized filter can be used as an efficient selection criterion for parallel filters.

The parameter used for Look-ahead MAD quantization algorithm instead of using Normalized Peak Ripple in NUS algorithm, is Maximum Absolute Difference between the frequency responses of ideal filter and quantized filter.

When the quantized filter is implemented, a post-processing scale factor (PPSF) is used to properly rescale the magnitude of the resulting data stream. The value of the PPSF is determined as follows:

PPSF=Max [Abs (Ideal Filter Coeffs.)] / VSF

Essentially, the PPSF reverses the normalization and scaling is introduced in the quantization process. While the scaling process changes the magnitude of the filter response, it should be noted that it does not change the functionality of the filter.

MAD algorithm is described by the following pseudocode:

For each filter section in the parallel FIR filter,
{Normalize the set of filter coefficients so that the magnitude of the largest coefficient is 1;
For VSF = Lower scale: Step size: Upper scale,
{Compute PPSF by (11);
Convert PPSF into Canonic Signed Digit form;
If (No. of nonzero bits in PPSF) < prespecified value,
{Scale normalized coefficients with VSF;
Quantize the scaled coefficients using SPT term
allocation scheme in NUS algorithm;
Calculate MAD between the frequency responses
of the ideal and quantized filters;
}
}
Choose the quantized coefficient that leads to the minimum MAD;
}

CSD Algorithm:

An algorithm for computing the CSD format of a W bit number is represented here. Denote the two's complement representation of the number A as

$A=a_{w-1}.a_{w-2}.....a_1a_0$ and its CSD representation

$A= a_{w-1}.a_{w-2}.....a_1a_0$. The conversion is illustrated using the following iterative algorithm:

$a_{-1}=0$
$\gamma_{-1}=0$
$a_w= a_{w-1}$
for (i=0 to W-1)
{
$\square_i=(a_i)\ xor(a_{i-1})$
$\gamma_i= inv(\gamma_{i-1})*\square_i$
$a_i=(1-2a_{i+1})*\gamma_i$
}

DESIGN EXAMPLE: Consider an ideal filter section with the following parameters: pass band ripple=3dB, stop band ripple=60dB, pass band frequency=3000Hz, stop band frequency=3300Hz, sampling frequency=8000Hz.Frequency responses are shown below:

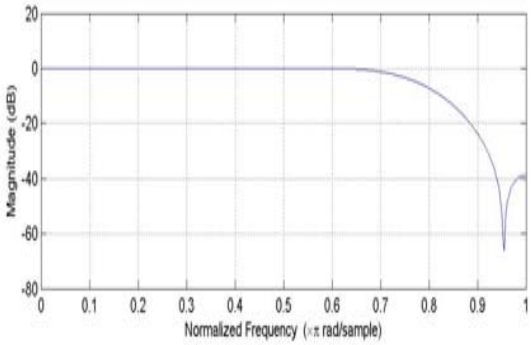

Fig. 3. Frequency response of Ideal filter

From fig. 3 and 4, ripples of the MAD quantized filter increases compared to Ideal filter.

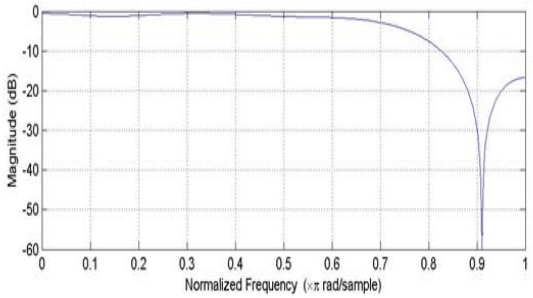

Fig. 3. Frequency response of MAD Quantized filter

III. CONCLUSION

It has been shown that the proposed NUS and look-ahead MAD quantization algorithms were shown to be very efficient for the implementation of parallel filters.

REFERENCES

[1] Jin-Gyun Chung, Yong-Bae Kim, Hang- Geun Jeong, Keshab K. Parhi, Zhongfeng Wang, "Efficient parallel FIR filter implementations using frequency spectrum characteristics" in Proceedings of IEEE ISCAS, (Monterey, CA),vol.5, pp. 354-358, June 1998.

[2] D. Li, J. Song, and Y. C. Lim, "A polynomial-time algorithm for designing digital filters with power-of-two coefficients," in Proceedings of 1993 IEEE ISCAS, (Chicago, IL), pp. 84-87, May 1993.

[3] C. L. Chen, K. Y. Khoo, and A. N. Willson, Jr., "An improved polynomial- time algorithm for designing digital filters with power-of- two coefficients," in Proceedings of 1995 IEEE ISCAS, (Seattle, WA), pp. 223-226, May 1995.

[4] Yong Ching Lim, Rui Yang, Dongning Li, and Jianjian Song, "Signed Power-of-Two Term Allocation Scheme for the Design of Digital Filters" IEEE Trans. Circuits Syst., vol.46, NO. 5, MAY 1999.

[5] D. A. Parker and K. K. Parhi, "Low-area/power parallel FIR digital filter implementations," Journal of VLSI Signal Processing, vol. 17, pp. 75-92, Sept. 1997.

[6] Zhi Shen, "Improving FIR Filter Coefficient Precision", Signal Processing Magazine, IEEE,vol.27, pp. 120-124, July 2010.

[7] Ajoy Kumar Dey, Susmita Saha, Avijit Saha, Shibani Ghosh, "A Method of Genetic Algorithm (GA) for FIR Filter Construction: Design and Development with Newer Approaches in Neural Network Platform", in proceedings of IJACSA, ol. 1, No. 6, December 2010.

[8] J. H. Satyanarayana and K. K. Parhi, "HEAT : Hierarchical EnergyAnalysis Tool," in *33rd ACM/IEEE Design Automation Conf.,* (L a Vega, NA), pp. 9-14, June 1996.

[9] Y. C. Lim, "Design of discrete-coefficient-value linear phase FIR filterswith optimum normalized peak ripple magnitude," *IEEE Trans. Circuits Syst.,* vol. 37, pp. 1480–1486, Dec. 1990.

[10] Y. C. Lim and S. R. Parker, "FIR filter design over a discrete power-of two coefficient space," *IEEE Trans. Acoust. Speech, Signal* vol *Processing*. ASSP-31, pp. 583–591, June 1983.

[11] Y. C. Lim, S. R. Parker, and A. G. Constantinides, "Finite wordlength FIR filter design using integer programming over a discrete coefficient space," *IEEE Trans. Acoust. Speech, Signal Processing,* vol. ASSP-30, pp. 661–664, Aug. 1982.

[12] Q. Zhao and Y. Tadokoro, "A simple design of FIR filters with powerof- two coefficients," *IEEE Trans. Circuits Syst.,* vol. 35, pp. 566–570 May 1988.

[13] S. Sriranganathan, D. R. Bull, and D. W. Redmill, "Low complexity twodimensional digital filters using unconstrained SPT term allocation," in *Proc. 1996 Int. Symp. Circuits Syst.,* 1996, pp. 762–764.

BRAIN TUMOR DETECTION USING ADAPTIVE K-MEANS CLUSTERING ALGORITHM

ANU V.S[1] & ROSHNI V.S[2]

[1]Department of Electronics and Communication, Amaljyothi College of engineering, Kanjirapally ,Kottayam, India
[2]Er and DCI Institute of Technology, Trivandrum, India

Abstract— Segmentation is an important process in medical image analysis. K-means clustering is a pixel based Method of segmentation which is simple and has relatively low computational complexity compared to other Segmentation methods. Here we propose a color based image segmentation method based on adaptive K- means Clustering and histogram based clustering for detection of tumor in Mr images. By using adaptive clustering high Performance and efficiency is obtained. In this segmentation algorithm, the Mr image is first converted to RGB color space and then to CIE lab color space. Then the k-means clustering is applied on both the A* space and b* space of CIE lab color space. Histogram clustering is done for the removal of unwanted pixels using the L* space of CIE lab color image and the cluster containing tumor objects in the Mr image is separated. The k-means clustering is suitable For biomedical image segmentation because number of Clusters is usually known for images of particular regions of The human anatomy. Adaptive k-means clustering can Provide better segmentation performance compared to Standard k-means algorithm and the speed of execution is Improved.

Index Terms—*Histogram Clustering, K-Means Clustering, Segmentation*

I. INTRODUCTION

Segmentation is the process .of dividing a digital image into multiple segments. The goal of segmentation is to simplify or change the representation of an image into something that is more meaningful and easier to analyze. In medical imaging, an image is captured, digitized and processed for doing segmentation and for extracting important information. Segmentation is an important process in medical image analysis and classification for radiological evaluation or computer aided analysis.

Image segmentation refers to the task of dividing an input image into regions of pixels that "belong together". Segmentation methods are classified into three categories:

1. Region based methods, 2. Pixel based methods, and 3.Edge based methods.

One way to approach image segmentation is to extract a suitable set of features from the image and apply a clustering algorithm to them. The clusters output by the algorithm can then be regarded as the image segments. The k-means clustering method is a pixel based segmentation method which is simple and computational complexity is less compared to other methods [1]. It is suitable for biomedical image segmentation as number of clusters k is usually known for particular regions of human anatomy.MR image of head consist of regions representing the bone, soft tissue, fat and back ground. Here the value

of k is chosen as 3. Each cluster is characterized by a constant intensity. But in practice the images are usually noise contaminated versions of reflected density function and the image intensity of the same class may change due to many reasons [3]. Different clusters at different locations may have similar intensity due to inhomogeneous nature of the imaging media. Therefore the ability of being adaptive to the local intensity distribution will be required for a clustering algorithm to obtain correct results. In this paper an adaptive method for k-means clustering is applied for getting better segmented output with improved speed of execution. Many researches have been done in improving k mean clustering but they require more computational complexity and software functionality. In this proposed work we are using color space transformation which is a fundamental operation in many image processing techniques. The algorithm of k-means is made adaptive for better results [2]. Therefore the use of color based segmentation with adaptive k-means clustering to gray MR images will help the pathologists to identify exact lesion size and shape in a much less execution time.

The paper is organized as follows. Section II gives a study of k-means clustering and histogram clustering followed by the study of adaptive k-means clustering in. Section III gives an idea about the color transformation operations. Section IV presents the proposed method. Experimental results and figures are given in section V followed by the conclusion.

II. STUDY OF HISTOGRAM CLUSTERING AND K-MEANS CLUSTERING

The term histogram clustering refers to grouping methods the input features of which are histograms. Histogram statistics is also a pixel based method which defines single or multiple thresholds to classify an image pixel by pixel. In this work the gray threshold value T is obtained by analyzing the histogram for peak values and then find the lowest

point which will be located between two consecutive peaks in histogram. By using this threshold T a pixel can be classified into one or more classes. Consider an image f(x,y) which is segmented into two classes using a threshold T

$$g(x,y)=\begin{cases}1 \text{ if } f(x,y) > T\\ 0 \text{ if } f(x,y) < T\end{cases}$$

Here g(x,y) is the segmented image and T is the threshold assigned to the lowest point, which is located between two peak values of the histogram.

Cluster analysis or clustering is the task of assigning a set of objects into groups called clusters so that the objects in the same cluster are more similar to each other than to those in other clusters. K-means clustering is a method of cluster analysis which aims to partition *n* observations into *k* clusters in which each observation belongs to the cluster with the nearest mean. K-means is a widely used clustering algorithm to partition data into k clusters. Clustering is the process for grouping data points with similar feature vectors into a single cluster and for grouping data points with dissimilar feature vectors into different clusters. The K-means algorithm and its development algorithms are in the family of center base clustering algorithms. Here an iterative technique that is used to partition an image into *K* clusters. The general clustering algorithm is:

1. Pick *K* cluster centers, either randomly or based on some heuristic
2. Assign each pixel in the image to the cluster that minimizes the distance between the pixel and the cluster center
3. For each center, recompute the new center from all data points belonging to this center.
4. Repeat steps 2 and 3 until convergence is attained that is no pixels change clusters

The quality of the solution depends on the initial set of clusters and the value of *K*. Let the feature vectors derived from l clustered data be $X = \{xi / i= 1,2,\ldots,l\}$. The generalized algorithm initiates k cluster centroids $C = \{c j/ j = 1,2,\ldots,k\}$ by randomly selecting k feature vectors from X. Later, the feature vectors are grouped into k clusters using a selected distance measure such as Euclidean distance so that $d = \| xi - c j \|$.

In the next step we will recompute the clustercentroids based on their group members and then regroup the feature vectors according to the new cluster centroids. The clustering procedure stops only when all cluster centroids tend to converge. Since the algorithm is extremely fast, a common method is to run the algorithm several times and return the best clustering found.

III. COLOR SPACE TRANSFORMATION

In this method the original MR Image is rendered as a gray level image but as this is insufficient for supporting fine features we will pseudo color map it to RGB color space. This provides more useful features and enhances visual density. Here each gray value is mapped to R, G and B values. But for retrieving the important features to benefit the clustering process, this is further converted to a uniform CIElab color model (L*a*b*). The CIElab color space is a perceptually uniform color space. The change of same amount in a color value should produce a change of about the same visual importance[4]. Color acceptability decision making is simplified by the transformation of RGB values to a uniform color space, in which the distance between points is directly proportional to perceived color difference. Here color values could be easily compared. The L* space gives the luminosity values, a* space and b* space gives the color information. The positive a* value represents red and negative green.

The positive b* is yellow and negative blue.

The translation formulas from RGB to Lab color space is given below

$$L^*=116(h(Y/Yn)) - 16,$$

$$a^*=200(h(X/Xn) - h(Y/Yn)),$$

(1)

$$b^*=200(h(Y/Yn) - h(Y/Yn)),$$

$$h(p)=\begin{cases}\sqrt[3]{p} & p>0.008856\\ 7.787p + 16/116 & p\le 0.008856\end{cases}$$

Where Yn, Xn and Zn are the standard tristimulus values. Here D65 white point reference is used.

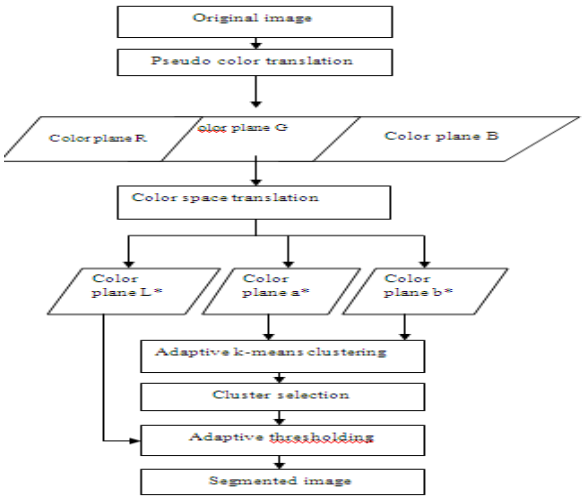

Fig 1 Flow chart of method

IV. PROPOSED METHOD

In this method we are combining the adaptive k-means clustering and adaptive thresholding method for segmentation. Here the adaptive k-means

clustering is applied in the a* and b* space of CIE lab color space. The flow chart of method is shown in Figure 1.For improving the speed and efficiency of clustering some additional steps are included in the convergence of k-means clustering method. This method can reduce the complexity and can detect targets in a dataset. The additional steps are included for recalculating the new centers in k-means algorithm. These steps are as follows

1. After recomputing the clusters, then calculate the mean for new centers.
2. Then find the absolute value between the current center and the next center, if the absolute value is greater than the mean in the previous step, then keep this center as the new center, otherwise the new center will be equal to the average of the current center and the next center.
3. Repeat these steps till the end of the cluster number.

Rest of the algorithm is similar to k-means clustering. The flow chart for this method is shown in figure2.

After clustering process cluster containing an area of interest is selected as primary segment and to eliminate pixels which are not related to the interested area adaptive thresholding is applied and final segment is obtained. The results are then combined to form a common clustered output. From this the cluster containing tumor is selected. Then adaptive thresholding is done on this image

In adaptive thresholding for each pixel in the image, a threshold has to be calculated. If the pixel value is below the threshold it is set to the background value, otherwise it assumes the foreground value. The assumption behind the method is that smaller image regions are more likely to have approximately uniform illumination, thus being more suitable for thresholding. Here we find the local threshold to statistically examine the intensity values of the local neighborhood of each pixel. The statistic which is most appropriate depends largely on the input image. Simple and fast functions include the *mean* of the *local* intensity distribution

T= mean

The *median* value,

T= median

The size of the neighborhood has to be large enough to cover sufficient foreground and background pixels, otherwise a poor threshold is chosen. On the other hand, choosing regions which are too large can violate the assumption of approximately uniform illumination.

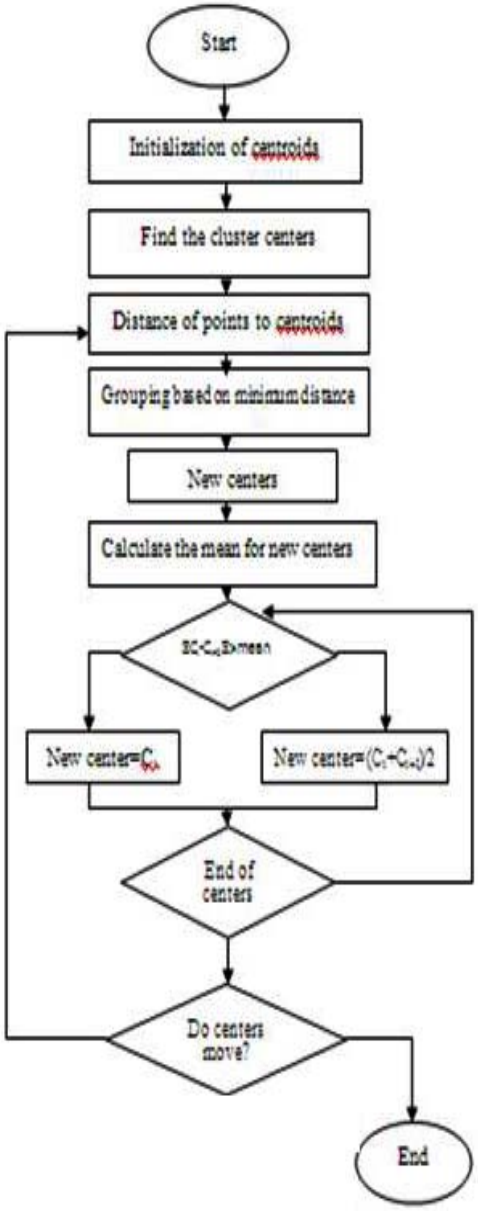

Fig 2 Flow chart of adaptive k-means clustering

V. EXPERIMENTAL RESULTS

Here a 289×252 gray MR image is taken. It is color mapped to RGB color space and then to CIE lab color space. Then k-means clustering is applied on both a* and b* space. The resulting common clusters are found. From these clusters the interested cluster containing tumor is selected. Then by applying histogram thresholding interested segment is obtained. Initially clustering is done by using standard k-means algorithm and then adaptive k-means is done. Generally an MR Image consist of regions representing bone, soft tissue, fat and back ground. Visual judgment from gray and color test images

suggest the value of k should be 3. Figure 3 shows the image labeled by cluster indices. Here we are separating the clusters by giving gray, white and black colors. The final segmented outputs of normal and adaptive methods are shown in figure 3 and 4. Figures obtained for different window sizes for thresholding is also shown in figure 5.Segmentation results obtained from proposed method are more efficient and fast compared to k-means clustering. The time taken for normal and adaptive methods is shown in the table1.

TABLE 1
EXECUTION TIME FOR CLUSTERING

METHOD	EXECUTION TIME(IN SECONDS)
K-MEANS CLUSTERING	175.758005
ADAPTIVE K-MEANS CLUSTERING	34.171739

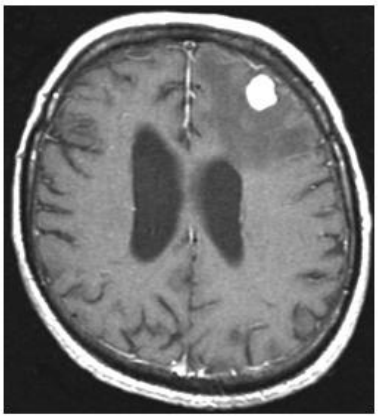

a) Gray level MR Image

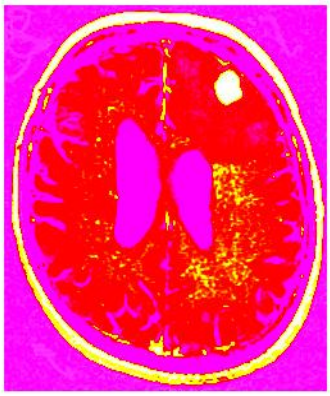

b) CIE lab image

Fig 3 MR Brain images

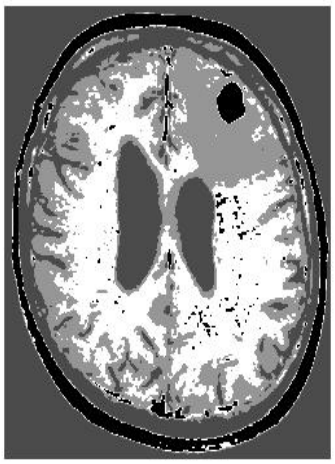

a) Combined k-means cluster output

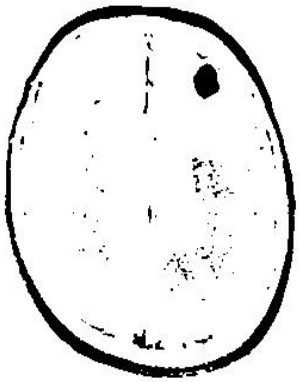

b) Cluster containing tumor

Fig 3 Result of k-means clustering

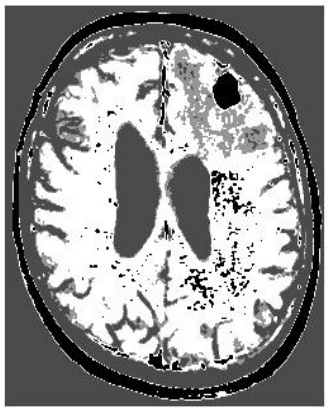

a) Combined adaptive k-means clustering output

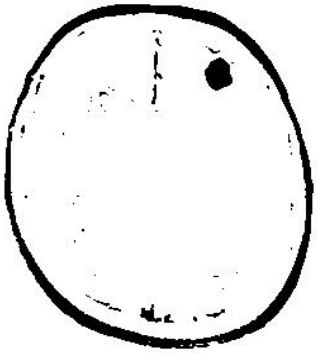

b) Cluster containing tumor

Fig 4 Result of adaptive k-means clustering

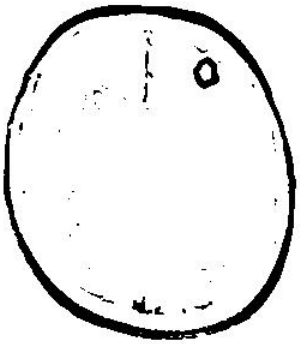

a) 10x10 window

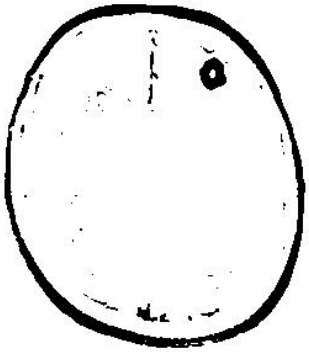

b) 14x14 window

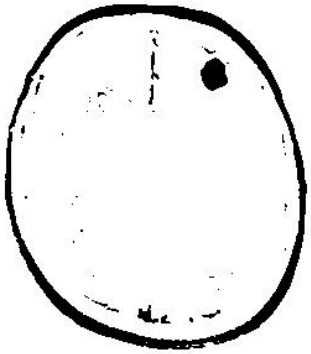

c) 18x18 window

Fig 5 Output for different window size in adaptive thresholding

VI. CONCLUSION

In this work a color based adaptive k-means clustering and adaptive thresholding is proposed. Using this method a faster and efficient detection of the cluster containing tumor is possible. The execution time for adaptive k-means clustering is less compared to that of normal k-means clustering. The methods used are simple and less complex.

REFERENCES

[1] Ming-Ni Wu,Chia-Chen Lin,Chin-Chen Chang, "*Brain Tumor Detection Using Color-Based K-Means Clustering Segmentation*" Third International Conference on Intelligent Information Hiding and Multimedia Signal Processing, 2007. IIHMSP 2007.pp 245-250

[2] Ali Salem Bin Samma,Rosalina Abdul Salam " *Adaptation of K-Means Algorithm for Image Segmentation* ", World Academy of Science, Engineering and Technology 50 2009

[3] Chen, C. W, Luo, J., Parker, K. J., "*Image Segmentationvia Adaptive K-mean Clustering and Knowledge-based Morphological Operations with Biomedical Applications*," *IEEE Transactions on Image Processing*, Vol. 7, No, 12, Dec. 1998, pp. 1673-1683.

[4] Christine,C.,Thomas,F., "*A study of Efficiency and Accuracy in the Transformation from RGB to CIELAB Color space*," IEEE Transactions on Image on Image Processing,Vol.6,No,7,July.1997,pp.1046-1048

[5] Chen,C W, Luo,J.,Parker,K.J, " *Medical Image Segmentation Using K-Means Clustering And Improved Watershed Algorithm* "IEEE transactions on Image Processing,Vol.7,No,12,Dec.1998,pp.1673-1683.

[6] Gonzalez,R.C,Woods,R.E.,Digital Image Processing,2nd ed.,Prentice Hall,Englewood Cliffs,NJ,2002

IMPLEMENTATION OF AREA EFFICIENT FIR FLITER WITH SYMMETRIC COEFFICIENTS BASED ON FFA

GEETHU GOPAN[1], NISHA THOMAS[2] & GEEVARGHESE TITUS[3]

[1,3]Department of ECE ,AJCE, Kanjirappally
[2]ER & DCI, Thiruvanthapuram

Abstract—This paper describes the design an area efficient parallel FIR filter structure by utilizing the property of symmetricity of the filter coefficients based on Fast FIR Algorithms (FFA). Using this method the number of multipliers required for the filter structure can be tremendously decreased by slightly increasing the number of adders in the system. The increase in the number of adders can be neglected since the size required for an adder is negligible to that for a multiplier. An important criterion is that the number of taps must be a multiple of 3 or 2.

Index Terms — *Digital Signal Processing, Parallel FIR Filters, Fast FIR algorithms, Symmetric Property.*

I. NTRODUCTION

As the technology advances the need and demand for highly power efficient and area reduced structures are increasing in the Digital Signal Processing systems. FIR filters is one of the fundamental building blocks of a DSP system. FIR filters have a wide variety of applications ranging from video and image processing to wireless communication applications. The major drawback of FIR filters is their increased need of computational power and also the size. This lead to the pipeline and parallel filter structures. Development of these two structures lead to the reduced area, reduced power consuming filter structures in the DSP systems.

Traditionally, the parallel processing involves the replication of the hardware units that exists in the original filter. If the original filter has a size A, then its parallel filter structure requires a size of L X A. In many design situations, the hardware overhead incurred due to the parallel processing cannot be tolerated due to the design area. Therefore, it is important to limit the silicon area required for the parallel filter structure.

A large number of works have been done on the basis of reduction of complexity of parallel FIR filter structures. In this paper, parallel processing is being utilized. A few papers are present on the task of reducing the complexity of the filter structures. In [1], by utilizing polyphase decomposition, larger sized blocks is generated using iterated smaller sized blocks.

Fast FIR Algorithms used in [1] – [3] shows the implementation of L sized parallel filter using (2L-1) parallel blocks of size N/L. In [4] – [5], iterative short convolution methods are utilized for reducing the required size of the filter structure.

In all the above discussed works, the scope of symmetricity of the filter coefficients is not at all considered. By taking advantage of symmetricity, a large number of multipliers can be eliminated from the hardware structure. The proposed work offers a new filter structure based on FFA that utilizes the symmetric property. The paper is organized in the following way. In section II, the basic FFA structure is being explained briefly. Then in section III, the proposed work is explained in detail and in section IV, the results obtained and comparisons are performed.

II. FAST FIR ALGORITHMS

The basic expression of an N tap filter can be expressed as

$$y(n) = \sum_{i=0}^{N-1} h(i)x(n-i); \qquad n = 0,1,2 \ldots \infty \tag{1}$$

where {x(n)} is the infinite length input sequence and {h(i)} is the N-length filter tap coefficients. A traditional L - parallel filter can be obtained using the polyphase decomposition using the following equation [3]

$$\sum_{p=0}^{L-1} Yp(Z^L)z^{-p} = \sum_{q=0}^{L-1} X_q(z^L)z^{-q} \sum_{r=0}^{L-1} Hr(z^L)z^{-r} \tag{2}$$

where p, q, r = 0,1,2,…L-1. For this filter structure design it requires L^2 sub filter blocks of length N/L.

A. 2 X 2 FFA structure(L = 2)

According to the equation (2), a two-parallel structure can be expressed as

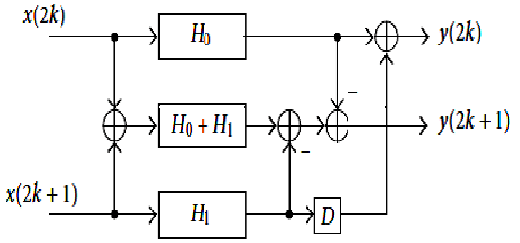

Fig. 1 Two parallel FIR filter structure using FFA.

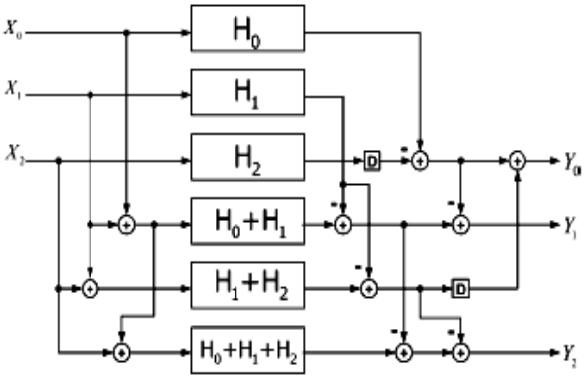

Fig. 2 Three parallel FIR filter implementation using FFA

$$Y_0 + z^{-1}Y_1 = (H_0 + z^{-1}H_1)(X_0 + z^{-1}X_1)$$
$$= H_0X_0 + z^{-1}(H_0X_1 - H_1X_0) + z^{-2}H_1X_1 \quad (3)$$

which shows that

$$Y_0 = H_0X_0 + z^{-2}H_1X_1$$
$$Y_1 = H_0X_1 + H_1X_0 \quad (4)$$

The equation (4) shows the traditional parallel filter structure with N/L as the length of the subfilter block with 2N multipliers and (2N – 2) adders.

The equation (4) can be rearranged and can be written as

$$Y_0 = H_0X_0 + z^{-2}H_1X_1$$
$$Y_1 = (H_0 + H_1)(X_0 + X_1) - H_0X_0 - H_1X_1 \quad (5)$$

The structure implemented using the above equation requires threes subfilter blocks of length N/2 and 3N/3 multipliers and 3(N/2 - -1) adders which results in the reduction of area when compared to the traditional parallel filters. The structure resulting from the equation (5) is shown in Fig. 1.

B. 3 X 3FFA (L = 3)

Similarly, a three parallel filter structure can also be developed and can be expressed as

$$Y_0 = H_0X_0 - z^{-3}H_2X_2 + z^{-3}[(H_1 + H_2)(X_1 + X_2) - H_1X_1]$$
$$Y_1 = (H_0 + H_1)(X_0 + X_1) - H_1X_1 - H_0X_0 - z^{-3}H_2X_2$$
$$Y_2 = (H_0 + H_1 + H_2)(X_0 + X_1 + X_2) - [(H_0 + H_1)(X_0 + X_1) - H_1X_1][(H_1 - H_2)(X_1 + X_2) - H_1X_1]. \quad (6)$$

The hardware structure utilizing the equation (6) requires 3N multipliers and 2N + 4 adders which will in turn reduces the complexity when compared to the traditional parallel filter structures. The structure according to the equation (6) is shown in Fig. 2.

III. PROPOSED STRUTURE BASED ON FFA UTILIZING SYMMETRIC PROPERTY

The equation (4), (5) and (6) represents structures which will slightly reduce the required multipliers than the traditional parallel filter structures. In all these structures the properties of symmetricity of filter taps have never been considered. By slightly manipulating the polyphase structure according to the FFA so as to utilize the symmetric property, large number of multipliers can be reduced by slightly increasing the number of adder required for the structure. Variation in the structure must be done in such a way that half number of multiplier can be avoided from repetition. So, for an N-tap filter the amount of multipliers saved wilt the number of subfilter block with symmetric coefficients times half the number of multiplications in each subfilter block.

A. PROPOSED 2 X 2 FFA (L =2)

From the basic equation of traditional filter (4), the proposed equation can be written as

$$Y_0 = \frac{1}{2}[(H_0 + H_1)(X_0 + X_1) + (H_0 - H_1)(X_0 - X_1)] - H_1X_1 - z^{-2}H_1X_1,$$
$$Y_1 = \frac{1}{2}[(H_0 + H_1)(X_0 + X_1) - (H_0 - H_1)(X_0 - X_1)] \quad (7)$$

Equation (7) can be used to implement two parallel structure with less multiplier.

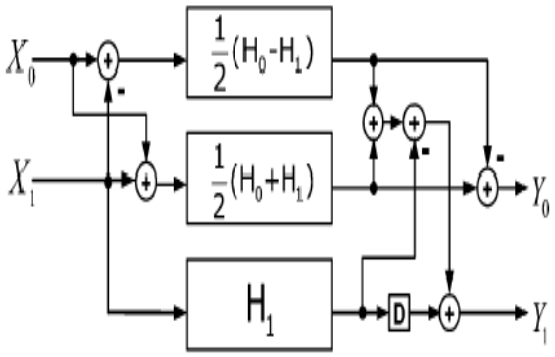

Fig. 3 proposed two parallel structure using FFA

Example I: Consider an 8-tapfilter with symmetric coefficients being applied the proposed system. The filter coefficients can be expressed as

{ h(0), h(1), h(2), h(3), h(4),….h(7) } .

In the filter taps the symmetricity is in such a way that

h(0) = h(7) h(1) = h(6)
h(2) = h(5) h(3) = h(4)

In such a way, we can conclude that

$$H_0 \pm H_1 = \{ h(0) \pm h(1), h(2) \pm h(3), h(4) \pm h(5) \; h(6) \pm h(7) \}$$

which represents the first two subfilter blocks of proposed two parallel structure, where

$$h(0) \pm h(1) = \pm(h(6) \pm h(7))$$

$$h(2) \pm h(3) = \pm(h(4) \pm h(5))$$

Thus it is clear from the example that half the number of multipliers can be reduced in the proposed parallel structure when compared to the traditional structure and also the FFA structure. Each output of the multipliers responds to two taps. Compared to the existing FFA two parallel FIR filter structure, the proposed FA structure leads to one more subfilter block which contains symmetric coefficients. It will lead to the increase in the amount of adders in the blocks. In this case, it will result in an increase of 2 adders.

The 8 tap filter structure according to the proposed FFA is shown in Fig. 4.

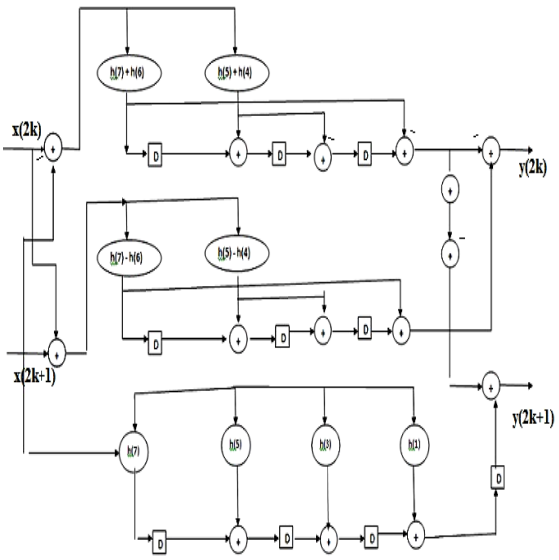

Fig. 4 Proposed 8 tap filter structure

IV. RESULTS AND COMPARISONS

The proposed FFA structure has been applied on AN 8 tap FIR filter with symmetric coefficients and the hardware level implementation is shown in Fig. 5.

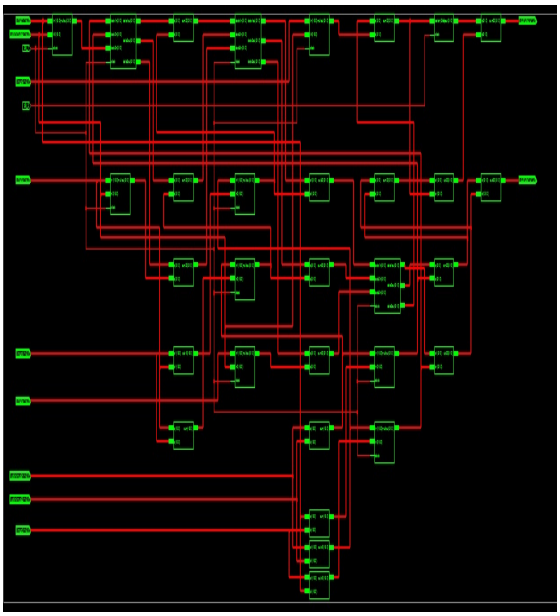

Fig. 5 Proposed 8 tap FIR filter implementation.

The FIR filter structure based on the basic equation (4) is shown in Fig. 6

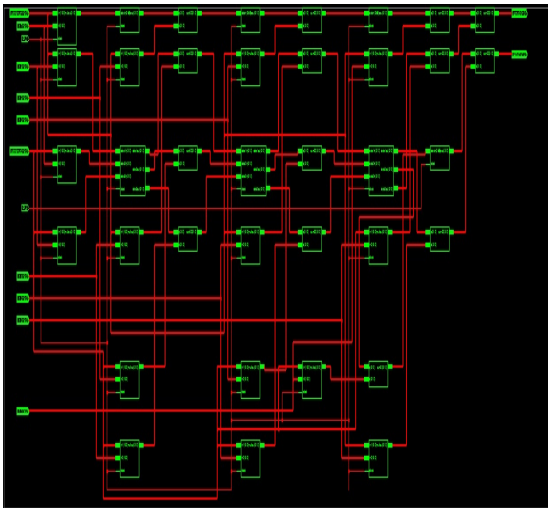

Fig. 6 Basic 8 tap filter implementation.

From the Fig. 5 and Fig. 6, its evident that the hardware requirement of the proposed structure is less when compared to the normal filter structure.

A few more comparisons based on different length filter taps are shown in Fig.7

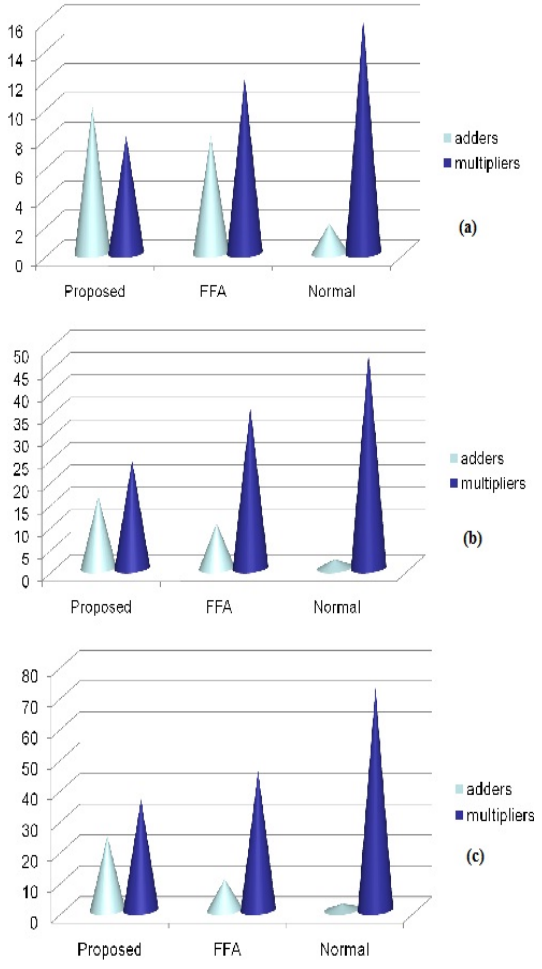

Fig. 7 (a) Comparison of 8 tap filter structures
(b) comparison of 24 tap filter structures
(c) comparison of 36 tap filter structures.

TABLE OF COMPARISON BETWEEN DIFFERENT LENGTH TAP FILTER STRUCTURES.

Order of filter	Utilization properties	PROPOSED FFA	Basic structure.
8-tap filter	Number of multipliers	8	16
	Number of adders used	10	2
	Delay	4.93ns	4.73ns
24-tap filter	Number of multipliers	24	47
	Number of adders used	7	1
	Delay	4.94ns	4.94ns

The proposed FIR filter structure with tap lengths 8,24 and 36 are obtained using the tool VHDL all which are done in integer base. The ideal filter coefficients are obtained using MATLAB for all the 8, 24 and 36 filters.

V. CONCLUSION

In this paper, a new parallel FIR filter structures, which are beneficial to symmetric convolutions when the number of taps is the multiple of 2 or 3. Multipliers are the major portions in hardware consumption for the parallel FIR filter implementation. The proposed new structure exploits the nature of even symmetric coefficients and save a significant amount of multipliers at the expense of additional adders. Since multipliers outweigh adders in hardware cost, it is profitable to exchange multipliers with adders. Moreover, the number of increased adders stays still when the length of FIR filter becomes large, whereas the number of reduced

multipliers increases along with the length of FIR filter. Consequently, the larger the length of FIR filters is, the more the proposed structures can save from the existing FFA structures, with respect to the hardware cost.

REFERENCES

[1] D. A. Parker and K. K. Parhi, "Low-area/power parallel FIR digital filter implementations," *J. VLSI Signal Process. Syst.*, vol. 17, no. 1, pp. 75–92, 1997.

[2] J. G. Chung and K. K. Parhi, "Frequency-spectrum-based low-area low-power parallel FIR filter design," *EURASIP J. Appl. Signal Process.*, vol. 2002, no. 9, pp. 444–453, 2002.

[3] K. K. Parhi, *VLSI Digital Signal Processing Systems: Design and Implementation*. New York: Wiley, 1999.

[4] Z.-J. Mou and P. Duhamel, "Short-length FIR filters and their use in fast non recursive filtering," *IEEE Trans. Signal Process.*, vol. 39, no.6, pp. 1322–1332, Jun. 1991.

[5] C. Cheng and K. K. Parhi, "Hardware efficient fast parallel FIR filter structures based on iterated short convolution," *IEEE Trans. Circuits Syst. I, Reg. Papers*, vol. 51, no. 8, pp. 1492–1500, Aug. 2004.

[6] C. Cheng and K. K. Parhi, "Furthur complexity reduction of parallel FIR filters," in *Proc. IEEE Int. Symp. Circuits Syst. (ISCAS 2005)*, Kobe, Japan, May 2005.

[7] C. Cheng and K. K. Parhi, "Low-cost parallel FIR structures with 2-stage parallelism," *IEEE Trans. Circuits Syst. I, Reg. Papers*, vol. 54, no. 2, pp. 280–290, Feb. 2007.

[8] Yu-Chi Tsao and Ken Choi, "Area-Efficient Parallel FIR Digital Filter Structures for Symmetric Convolutions Based on Fast FIR Algorithm", in IEEE Trans ON VERY LARGE SCALE INTEGRATION (VLSI) SYSTEMS, vol. 20, no. 2, February 2012.

A HIGH BANDWIDTH RECTANGULAR MICRO STRIP ANTENNA FOR AIRCRAFT APPLICATIONS

YAMUNA THERESE MAHESH[1] & MIDHUN JOY[2]

[1,2]Department of Electronics, Amal Jyothi College of Engineering, Kottayam, India

Abstract*:* **In** this paper, a high bandwidth rectangular micro strip patch antenna has been designed to use in aircraft applications including GPS service and L-band communication services. Micro strip antennas consist of a planar resonant radiating element parallel to, but separated, from a ground plane by a thin dielectric substrate. The purpose of this work is to obtain a small, efficient and economical integrated antenna that can work effectively for various applications. The operating frequency ranges from 1525MHz to 1660MHz with a bandwidth of 135MHz.the polarization used in the antenna is RHCP. Good impedance and axial ratio characteristics have been obtained.

Index Terms*—circular polarization, axial ratio, impedance matching, returns loss.*

I. INTRODUCTION

An antenna is a transducer that transmits or receives electromagnetic waves. A micro strip antenna consists of a metallic pattern on one side of a dielectric substrate and ground plane on the other side of the substrate. Micro strip antennas are becoming more and more popular every day. Some of the advantages of micro strip antennas are light weight, low volume and easy integration with microwave integrated circuits (MIC).

We propose a high bandwidth rectangular micro strip antenna with a wide range of applications. This antenna can be used for L-band communication services in aircraft. Since the GPS frequency is 1575MHz, this antenna can effectively provide GPS services. The axial ratio of the proposed antenna is very small ensuring a perfect circular polarization. To excite the antenna co-axial feed method is used so that radiation effects are minimized.

II. THEORY

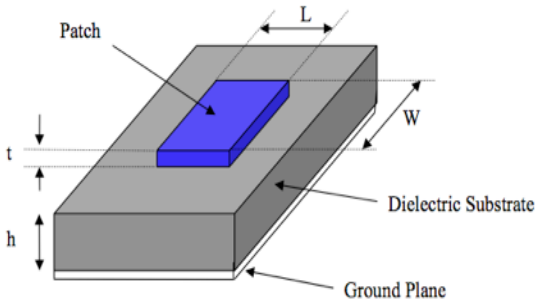

Fig 1 rectangular micro strip antenna

The standard equations used in the design are
The width (w) is

$$W = \frac{c}{2 \cdot f_c \cdot \sqrt{\frac{\varepsilon_r + 1}{2}}}$$

Where

C is the speed of light, f is the frequency and € is the dielectric constant of the substrate.

The length extension (ΔL)

$$\Delta L = 0.412 \cdot h \cdot \frac{\left(\varepsilon_{reff} + 0.3\right)\left(\frac{W}{h} + 0.264\right)}{\left(\varepsilon_{reff} - 0.258\right)\left(\frac{W}{h} + 0.8\right)}$$

Where h is the height of the substrate

The effective length is

$$L_{eff} = \frac{c}{2 \cdot f_c \cdot \sqrt{\varepsilon_{reff}}}$$

The actual length (L) is

$$L = L_{eff} - 2 \cdot \Delta L$$

Width of the ground plane is

$$W_g = 6 \cdot h + W$$

Length of the ground plane is

$$L_g = 6 \cdot h + L$$

The dielectric substrate in the antenna is duroid (dielectric constant is 2.2).
The excitation to the antenna is given by co-axial feed method.

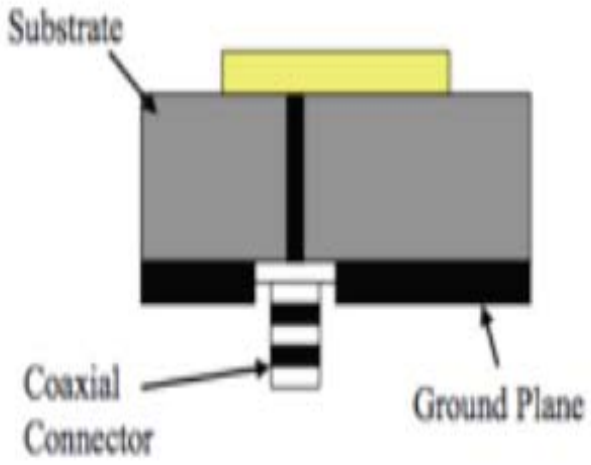

Fig 2 co-axial feeding method

By using co-axial feeding, the radiation effects are minimized.

III. DESIGN DETAILS

The antenna design software is HFSS (high frequency structure simulator). The general steps in the design are

Draw the geometric model-create the objects that make up the antenna model and assign materials to the objects

Setup the problem-setup boundary conditions and excitations

Generate a solution-to define the designed range of frequency and to obtain the results

Analyze the solution results

Photo lithographic fabrication method is used, which is a cost effective method

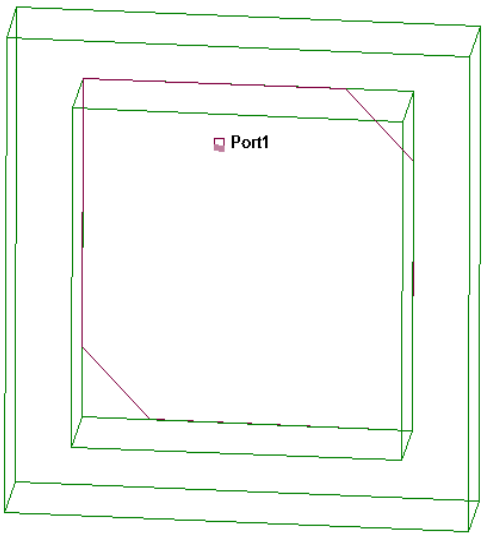

Fig 3 designed 3D structure

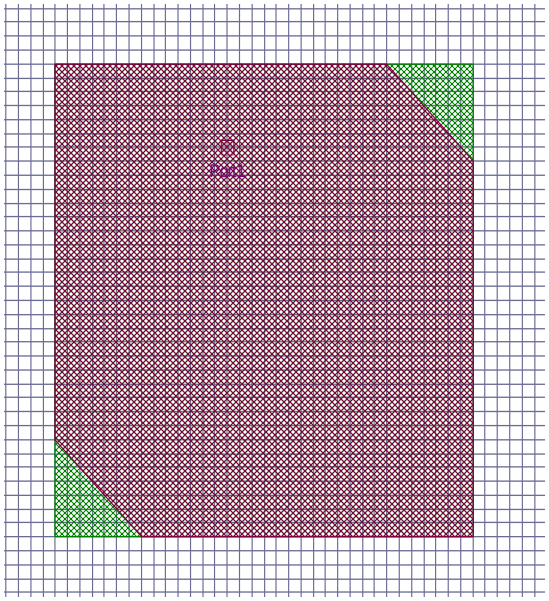

Fig 4 designed planar structure

IV. RESULTS AND DISCUSSION

We analyze the HFSS plots for VSWR, return loss, axial ratio and RHCP gain pattern. For a good antenna the VSWR (voltage standing wave ratio) must range from one to two. Return loss indicate the power which is reflected back to the source. At the desired frequency of operation the return loss should be a minimum. In a circularly polarized antenna the axial ratio will be near to 0db. By analyzing the results we can see that the proposed antenna meet all the conditions

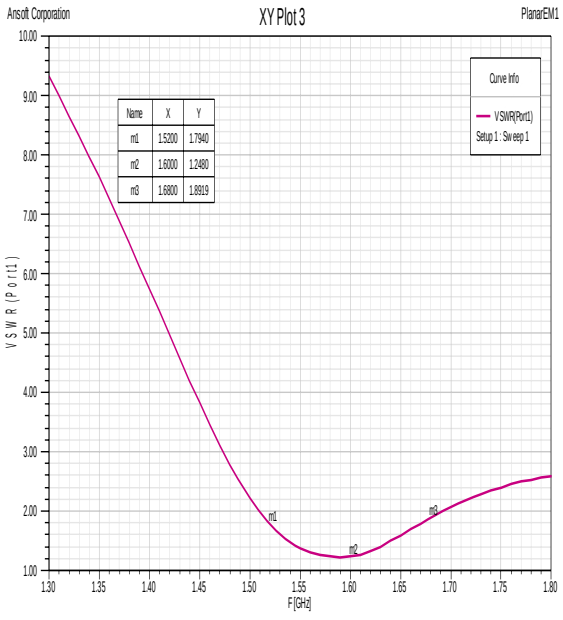

Fig 5 VSWR plot

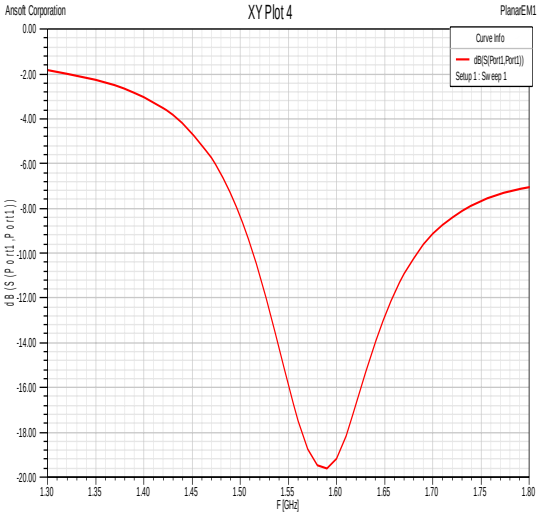

Fig 6 return loss plot

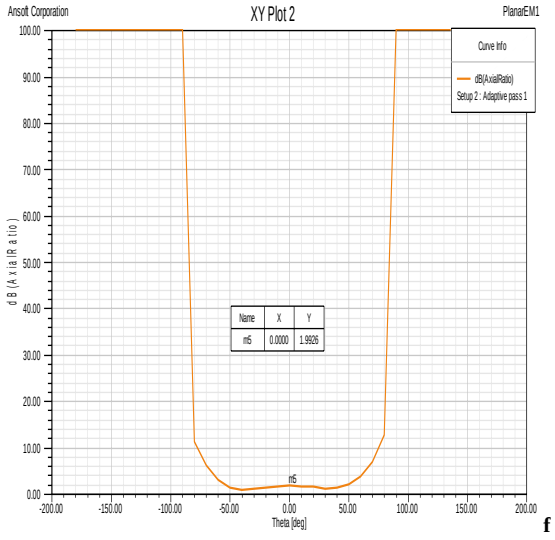

Fig 7 axial ratio plot

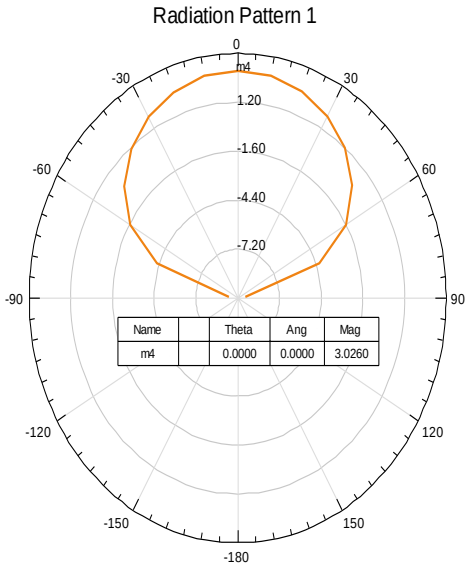

Fig 8 RHCP Gain

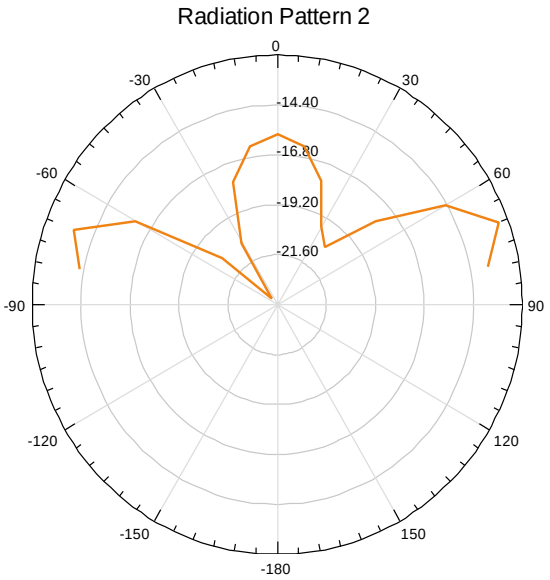

Fig 9 LHCP gain

In a circularly polarized antenna,the electric field components are having same magnitude with different phase.RHCP and LHCP are the two types of circular polarization.it is a RHCP circularly polarized antenna.so the RHCP gain should be a high value and LHCP gain should be a low value.

SL NO	PARAMETER	DIMENSIONS
1	Patch W*L	70*55
2	thickness	9.6mm
3	material	RT duroid/6006

Table 1 antenna dimensions

SL NO	PARAMETER	OBTAINED VALUE
1	frequency	1525MHz to 1660MHz
2	bandwidth	135MHz
3	polarization	RHCP
4	VSWR	1.8
5	RHCP gain	6db
6	Axial ratio	1.9db

Table 2 antenna results

V. CONCLUSION

A high bandwidth small size rectangular micro strip antenna is proposed. It exhibits a high bandwidth without compromising the gain. The fabrication method used is photo lithographic method. It can effectively provide L-band communication services and GPS services.

REFERENCES

1. Micro strip-Fed Circularly Polarized Square-Ring Patch

   Antenna for GPS Applications IEEE TRANSACTIONS ON ANTENNAS AND PROPAGATION, VOL. 57, NO. 4, APRIL 2009

2. Design of Small Integrated Antenna for Peer to Peer Wireless Communication, International Journal of Mobile Network Communications & Telematics (IJMNCT) Vol.2, No.3, June 2012

3. H. M. Chen and K. L. Wong, "On the circular polarization operation of annular-ring micro strip antennas," IEEE Trans. Antennas Propagate.,

   vol. 47, no. 8, pp. 1289–1292, Aug. 1999.

4. A. K. Bhattacharyya and L. Shafai, "A wider band micro strip antenna for circular polarization," *IEEE Trans. Antennas Propagate.*, vol. 36, no. 1, pp. 157–163, Jan. 1988.

5. J. R. James and P. S. Hall, Handbook of Micro strip Antenna. London, U.K.: Peter Peregrinus Ltd., 1989, vol. 1

A DUAL-BAND MINIATURE MICROSTRIP ANTENNA FOR PRECISE GPS APPLICATIONS

JAYACHANDRAN R2[1], K.G. SATHEESHKUMAR[2] & BINOSHI SAMUAL[3]

[1,2]Department of ECE, Amal Jyothi College of Engineering, Kanjirapally, Kottayam, India
[3]Department of ECE,AJCE

Abstract- A dual-band circularly polarized stacked microstrip antenna for precise global positioning system (GPS) applications is proposed and experimentally studied. By stacking two different corner-truncated square patches in a dielectric substrate layer, the microstrip antenna for dual-frequency circular polarization (CP) can be achieved without an air layer between the two stacked patches. The top patch has a pair of truncated square corners, and the bottom patch has a pair of truncated isosceles triangular corners. A fabrication and cost effective antenna design for dual-band GPS at 1575 MHz and 1227 MHz is demonstrated here. Details of the obtained dual-band CP performances are presented and discussed.

***Index Terms**: Microstrip antenna, Circular polarization, Dual band, GPS.*

I. INTRODUCTION

A circularly polarized microstrip antenna is widely used for global positioning system (GPS) applications owing to its advantages of low cost, low profile, and broad receiving pattern [1]. The antenna for circular polarization (CP) can be used to reduce the multi-path effect around a GPS receiver [2]. Furthermore, the antenna having broad receiving pattern in the upper hemispherical coverage is beneficial to receive the GPS signals from satellites [3]. Recently, the dual-frequency microstrip antenna with two shorted elliptical annular patches separated by an air layer [4] has been demonstrated for high-precision GPS applications. In order to achieve precise triangulation, both L1 (1575 MHz) and L2 (1227 MHz) frequencies are required at the GPS receiver to correct ionospheric delay in signal propagation. Because the above two CP operating frequencies are close each other (the ratio of the two frequencies is 1.28), the dual-band CP design using stacked microstrip patches is considered to be a good antenna solution to the precise GPS application [5]. Single-feed stacked microstrip antennas, such as the antenna structures with an air layer [5] or two different dielectric substrate layers [6], have also been reported. Either the air layer or the two different dielectric substrate layers can help the antennas carry out the dual-band CP operation, especially achieving good impedance matching at the above two CP operating frequencies. However, the air layer leads to an increase in the antenna thickness and fabrication complexity, and the two specific substrate materials limit the flexibility in the antenna design and fabrication. A dual-band circularly polarized stub loaded microstrip patch antenna for GPS applications [7] has presented. But its fabrication is complex due to large size and short circuit stub loading.

In this article, a probe-fed circularly polarized microstrip antenna with two stacked corner-truncated patches for dual-band GPS applications is presented. The proposed antenna has the advantage of not requiring an air layer between the two stacked patches. Moreover, only one substrate material is needed in the proposed antenna structure. Typical designs of the proposed antenna are described in the next section. Experimental results of the obtained CP performance for the proposed antenna are presented and discussed.

II. ANTENA DESIGN

Figure 1 illustrates the geometry of the proposed dual-band circularly polarized microstrip antenna with two stacked patches, where Rogers TMM4 substrate of thickness 2h = 6.4 mm and relative permittivity εr = 4.5 is used. The top patch with side length W1 has a pair of truncated square corners with the dimension of D1 ×D1 , and the bottom patch with side length W2 has a pair of truncated isosceles triangular corners with the dimension of D2 × D2 . Cutting of a pair of corners in the square patch allows the excitation of the two near-degenerate orthogonal modes (TM10 and TM01 modes) along the diagonal of the patch [8]. Besides, the probe at proper feed position can excite these two modes with 90o phase difference and equal amplitude to produce CP. As shown in Fig. 1, the microstrip antenna fed at a point in the x axis can produce left-hand circularly polarized radiation, while the antenna fed at a point in the y axis radiates right-hand circularly polarized wave. It should be mentioned that the side lengths (D1 and D2) of truncated corners dominate the axial ratio of CP and the feed position determines the impedance matching of the antenna.

In the proposed antenna design, the top patch is used as a resonant radiator for 1575 MHz, and the bottom patch for 1227 MHz Due to different truncated corner shapes in the two patches, the current distribution of the top patch differs from that of the bottom patch. It is expected to have less coupling effect between the top and bottom patches

when the proposed antenna is excited at 1227 MHz or 1575 MHz Then, the required CP performances of the proposed antenna without an air layer between the two patches can be more easily achieved at both 1227 MHz and 1575 MHz CP frequencies.

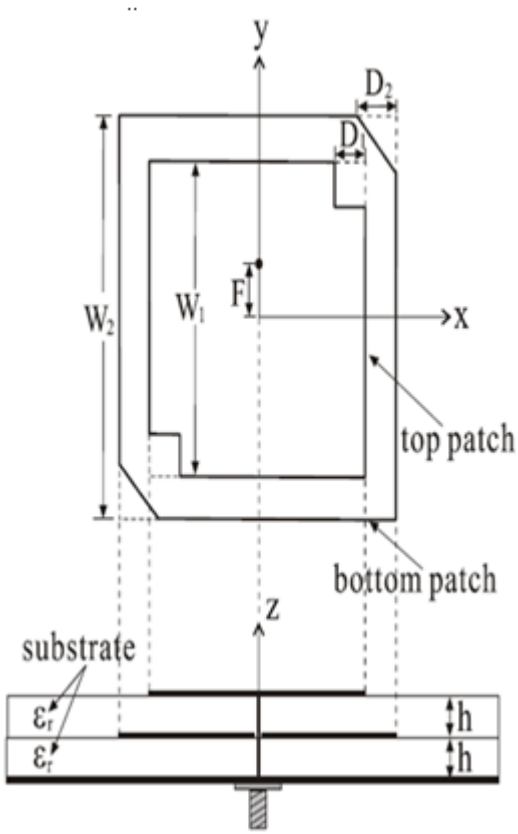

(Fig.1: Geometry of a probe-fed dual-band circularly polarized microstrip antenna with two stacked patches.)

III. EXPERIMENTAL RESULTS AND DISCUSSIONS.

To produce dual-band CP at 1227 MHz and 1575 MHz, the side lengths of the top and bottom patches studied here are fixed to be 43.4 mm and 51.6 mm, respectively. Figure 2 shows simulated results of the return loss for the proposed dual-band microstrip antenna in HFSS. By choosing the proper feed position (F = 17 mm) in the y axis, L1 and L2 GPS bands of the proposed single-feed antenna can both be excited with good impedance matching. The obtained impedance bandwidths of 10-dB return loss for the L1 and L2 bands are 90 MHz (or 5.7%) and 35 MHz (or 2.8%), respectively. It is also observed that the size of the antenna is reduced than the previous design with an air layer [5]. This is due to the fact that the air layer lowers the effective relative permittivity of the substrate and makes the resonant electric length longer.

The measured axial ratio in the broadside direction is presented in Figure 3. The CP bandwidths of 3-dB axial ratio for the L1 and L2 bands are 11 MHz (or 0.95%) and 12 MHz (or 0.98%), respectively. Figure 4 plots the simulated far field radiation pattern at Φ=0º and θ=0º plane.

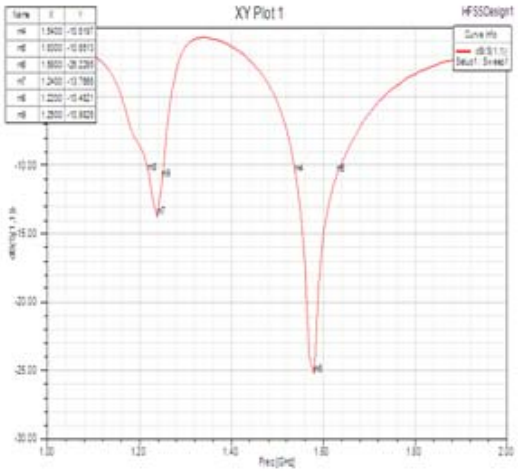

(Fig. 2: Simulated return loss for the proposed dual-band antenna; εr = 4.5, h = 6.4 mm, W1 = 51.6 mm, D1 = 6 mm, W2 = 43.4 mm, D2 = 4 mm, F = 17 mm.)

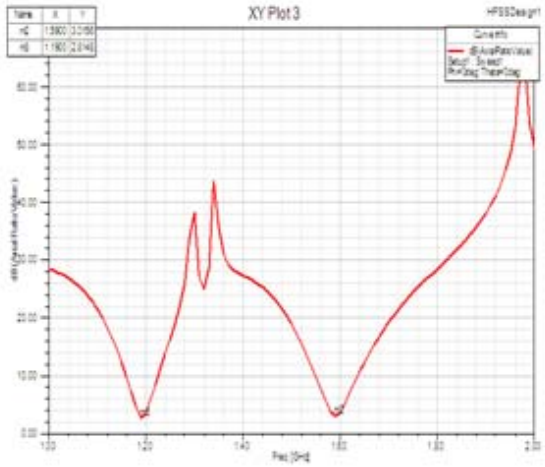

(Fig. 3: Simulated axial ratio against frequency; antenna parameters are given in Figure 2.)

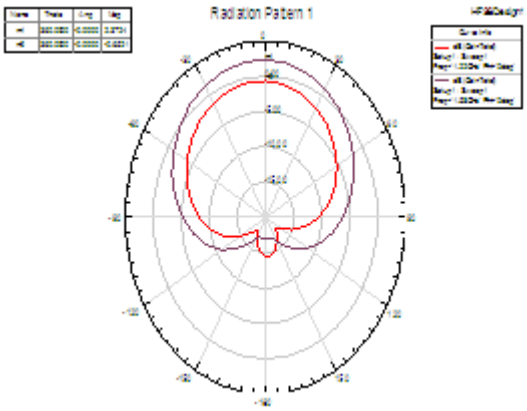

(Fig. 4: simulated far field radiation pattern at Φ=0º and θ=0º plane; antenna parameters are given in Figure 2.)

IV. CONCLUSION

A single-feed dual-band stacked microstrip antenna for precise GPS operations at 1227 and 1575 MHz has been presented and investigated. In the proposed antenna design, the dual-frequency CP operation is achieved by using two stacked patches with truncated square corners or isosceles triangular corners. Compared with the conventional dual-band stacked microstrip antennas with an air layer [5] or two substrate materials [6], the present proposed antenna has advantages of low cost, small size and easy fabrication. In this study, dual-frequency CP performances of the proposed antenna, such as impedance bandwidths, axial ratio, and radiation patterns, are demonstrated.

REFERENCES

[1]. M. S. Braasch and A. J. Van Dierendonck, "GPS Receiver Architectures and Measurements," *Proc. IEEE,* vol. 87, no. 1, pp. 48-64, Jan. 1999.

[2]. N. Padros, J. I. Ortigosa, J. Baker, M. F. Iskander, and B. Thornberg "Comparative study of high-performance GPS receiving antenna designs," *IEEE Trans. Antennas Propag.,* vol. 45, no. 4, pp. 698-706, Apr. 1997.

[3]. J. M. Tranquilla and S. R. Best, "A study of the quadrifilar helix antenna for global positioning system (GPS) applications," *IEEE Trans. Antennas Propag.,* vol. 38, no. 10, pp. 1545-1550, Oct. 1990.

[4]. L. Boccia, G. Amendola, and G. Di Massa, "A dual frequency microstrip patch antenna for high-precision GPSapplications," *IEEE Antennas Wireless Propag. Lett.*, vol. 3, pp. 157-160, 2004.

[5]. C. M. Su and K. L. Wong, "A dual-band GPS microstrip antenna," *Microw. Opt. Technol. Lett.*, vol. 33, no. 4, pp. 238-240, May 2002.

[6]. X. F. Peng, S. S. Zhong, S. Q. Xu, and Q. Wu, "Compact dual-band GPS microstrip antenna," *Microw. Opt. Technol. Lett.*, vol. 44, no. 1, pp. 58-61, Jan. 2005.

[7]. A. Heidari, M. Heyrani, and M. Nakhkash, "A dual-band circularly polarized stub loaded microstrip patch antenna for GPS applications" Progress In Electromagnetics Research, PIER 92, 195–208, 2009

[8]. S. Y. Ke, "Single-feed microstrip antenna with two-layer substrate for circular polarization," in *Proc. International Symposium on Communication*, paper no. 212, Nov. 2005. 1599-1604, October 1990.

COLOR VIDEO RANDOM IMPULSE NOISE REMOVAL USING FUZZY FILTER

FATHIMA MAJEED[1], SUHAIL AHMED[2] & G.V.SRIDHAR[3]

1,3Department Of ECE, Al-Ameer College Of Engg.&IT – Visakhapatnam,A.P
[2]Department Of CSE, GITAM University, –Visakhapatnam,A.P

Abstract—In this paper, a new fuzzy filter for the removal of random impulse noise in color video is presented. By working with different successive filtering steps, a very good tradeoff between detail preservation and noise removal is obtained. One strong fil- tering step that should remove all noise at once would inevitably also remove a considerable amount of detail. Therefore, the noise is filtered step by step. In each step, noisy pixels are detected by the help of fuzzy rules, which are very useful for the processing of human knowledge where linguistic variables are used. Pixels that are detected as noisy are filtered, the others remain unchanged. Fil- tering of detected pixels is done by blockmatching based on a noise adaptive mean absolute difference. The experiments show that the proposed method outperforms other state-of-the-art filters both visually and in terms of objective quality measures such as the mean absolute error (MAE), the peak-signal-to-noise ratio (PSNR) and the normalized color difference (NCD).

Index Terms*—Circuits and systems, computers and information processing, computational and artificial intelligence, filtering, fil- ters, fuzzy logic, image denoising, logic, nonlinear filters.*

I. INTRODUCTION

IMAGES and VIDEOS belong to the most significant & vital For an illustration of the effectiveness of fuzzy set theory in image processing, we refer to, e.g., [20]. Most filters in literature, that are developed for video, are intended for sequences corrupted by additive Gaussian noise (e.g., [3]-[7]). Only few video filters for the impulse noise case can be found (e.g., [19]-[20], [13], [3], [4], [6]). However, several impulse noise filters for still images exist. The best known among them are the median based rank-order filters (e.g., [8]-[10], [12], [14]-[17], [18]. But also some fuzzy tech- niques can be found [11]-[18], [13], [1]. Such 2-D filters could be used to filter each of the frames of a video successively. Color images impulse noise have been removed with the use of fuzzy filter by following the fuzzy rules. Similarly,using the fuzzy rules for the fuzzy filter Color Videos random impulse noise has been removed. The videos which are used for noise removal can be found in the above mentioned reference numbers in parenthesis[ ]. information in today's world (e.g., traffic observations, However, temporal inconsistencies will arise due to the neglec- surveillance systems, autonomous navigation, etc.). However, the images are likely to be corrupted by noise due to bad acquisi- tion, transmission or recording. Such degradation negatively in- fluences the performance of many image processing techniques and a preprocessing module to filter the images is often required. Among those filters, more and more fuzzy techniques start to appear in literature [7], [11]-[18], [22], [4], [3], [14]-[17], [9], [12], [13]. Fuzzy set theory was introduced by Zadeh in 1965 [14] and is a generalization of classical set theory. A clas- sical crisp set over a universe X can be modelled by a X – {0,1} mapping (characteristic function): an element x € X belongs to the set or does not belong to it. Fuzzy sets are now modelled as X - [0,1] mappings (membership functions). So the character- istic function is extended to a membership function where also membership degrees between zero and one are allowed. An el- ement can now also belong to some degree to the set, which allows a more gradual transition between belonging to and not belonging to. Such gradual transition makes fuzzy sets very useful for the processing of human knowledge in terms of linguistic variables (e.g., large, small, etc.). There is for example no need to use a threshold to decide whether a difference in color component value between two pixels is large or not. Two differ- ences that differ only one unit (which is not noticeable by the human eye) could then be respectively large and not large. For a larger difference, this degree will be higher than that of a smaller difference. tion of the temporal correlation between successive frames. A better alternative would be to use 3-D filtering windows, in which also pixels from neighboring frames are taken into account [19]-[20], [3], [13], [5], [6]. The main problem in using neighboring frames is motion between them. In the method proposed in this paper, we will therefore only in non-moving areas assign a temporal impulse between two corresponding spatial positions to noise (detection phase) and for the replacement of a noisy pixel (filtering phase) motion compensation will be applied to find the most reliable pixel in the previous frame. Analogously, a distinction between filters intended for greyscale images and for color images needs to be made. Filters for greyscale images could be used for color images by applying them on each of the color bands of the image separately. In this
paper, we consider the images to be modeled in the RGB color space. However, such approach will

generally introduce many color artefacts, especially in textured areas, due to the neglection of the correlation between the different color bands. To incorpo- rate this correlation, vector-based methods were introduced. The output for a given color pixel is then the pixel in the window around the given pixel, that has the smallest accumulated distance (Euclidean distance, angular distance, etc.) to all other vectors in the window [12], [14]-[18], [3], [15], [4], [6], [14], [2], [4], [5], or which is the most similar to all window Pixels[4],[13].To avoid blurring due to the filtering of noise-free pixels, this filtering framework has been further refined by weighted filtering techniques [18], [10], [20] and switching schemes where the filter is only used for detected noisy pixels [1], [12], [14], [19], [4], [8], [3], [5], [3], [15], [14], [19]. The drawback of vector-based methods, however, is that their performance is highly reduced for higher noise levels. Consider for example a neighborhood, in which all pixels have one noisy component, and the other components are noise-free. It would be better to filter the color bands separately, but by using information from the other color bands. However, not much alternatives for the vector-based approach can be found in literature. Some examples developed for still images are, e.g., [12], [13]. In this paper, we present a filter for the removal of random im- pulse noise in color image sequences, in which each of the color components is filtered separately based on fuzzy rules, in which information from the other color bands is integrated. To preserve the details as much as possible, the noise is removed by three successive filtering steps. Only pixels that have been detected to be noisy are filtered. This filtering is done by blockmatching, a technique used for video compression that has already been adopted in video filters for the removal of Gaussian noise (e.g., [4]-[6]). The correspondence between blocks is usually calcu- lated by a mean absolute difference (MAD), that is heavily sub- ject to noisy impulses. Therefore, we introduce a MAD measure that is adaptive to detected noisy pixels components. To benefit as much as possible from the spatial and temporal information available in the sequence, the search region for corresponding blocks contains pixel blocks both from the previous and current frame. The experiments show that the proposed method outper- forms other state-of-the-art filters both visually and in terms of objective quality measures such as the MAE, PSNR and NCD. The paper is structured as follows. The successive filtering steps of the proposed filter are discussed in Section II. In Section III, values for the used parameters are determined and a comparison to other state-of-the-art filters is carried out. The paper is concluded in Section IV.

II. THE PROPOSED ALGORITHM

The filtering framework presented in this paper is intended for color video corrupted by random impulse noise. If we respec- tively denote the original (noise-free) sequence by , the th frame of that sequence by and the red, green and blue com- ponent of the color of the pixel at the th row and th column in that frame by and (i.e.,), then the noisy sequence is determined as follows [1], [2]:

$$I_o \quad t$$

$$I_o(t)$$

$$I_o(x,y,t) \qquad x \qquad y$$

$$I_o^R(x,y,t),\ I_o^G(x,y,t) \qquad I_o^B(x,y,t)$$

$$I_o(x,y,t) = (I_o^R(x,y,t), I_o^G(x,y,t), I_o^B(x,y,t))$$

$$I_o$$

$$I_n^c(x,y,t) = \begin{cases} I_o^c(x,y,t), & \text{with probability } 1-p, \\ \eta^c(x,y,t), & \text{with probability } p, \end{cases}$$

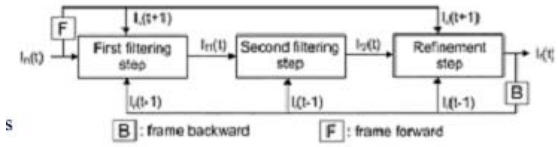

Fig. 1. Overview of the different steps in the proposed algorithm

where $c \in \{R,G,B\}$ and $p \in [0,1]$ denotes the probability that a pixel component value is corrupted and replaced by a identically distributed independent random noise value $\eta^c(x,y,t)$ coming from a uniform distribution on the interval of possible color component values. For the color videos used in the experiments of this paper, 8 bits are used for the storage of the color component values and we work with a uniform distribution on the interval [0, 255]. Further, the probability that a given color component value is corrupted is independent on whether the neighboring values or the values in the other color components are corrupted or not.

The proposed filtering framework consists of three successive filtering steps as depicted in Fig. 1. By removing the noise step by step, the details can be preserved as much as possible. Indeed, if a considerable part of the noise has already been removed in a previous step, and more noise-free neighbors to compare to are available, it will be easier to distinguish noise from small details. In the first step (Section II-A) (with output denoted by), we calculate for each pixel component a degree to which it is considered noise-free and a degree to which it is considered noisy. If the noisy degree is larger than the noise-free degree, the pixel component is filtered, otherwise it remains unchanged. The determination of both degrees is mainly based on temporal information (comparison to the corresponding pixel component in the previous frame). Note, however, that only in non-moving areas can large temporal differences be assigned to noise. In areas where there is motion, such differences might also be caused by that motion. As a consequence, and as can be seen in Fig. 2, impulses in moving areas will not always be detected in this step. They can, however, be detected in the second step (Section II-B) (output). Analogously as to the first step, again a noise-free degree and a noisy degree are calculated. However, the detection is now mainly based on color information. A pixel component can be seen as noisy if there is no similarity to its (spatio-temporal) neighbors in the given color, while there is in the other color bands. The third step (Section II-C) (output), finally, removes the remaining noise and refines the result by using as well temporal as spatial and color information.

For example, homogeneous areas can be refined by removing small impulses that are relatively large in that region, but are not large enough to be detected in detailed regions and that thus have not been detected yet by the previous general detection steps. The results of the different successive filtering steps are illus- trated for the 20th frame of the "Salesman" sequence in Fig. 2. A. First Filtering Step

1) Detection: In this detection step, we calculate for ach of the components of each pixel a degree to which it is considered noise-free and a degree to which it is thought to be noisy. A

Fig. 2. The original 20th frame of the "Salesman" sequence (a), the frame corrupted by 20% random impulse noise (b) (PSNR = 15.05 dB) and the result after the first (c) (PSNR = 23.72 dB), second (d) (PSNR = 29.42 dB) and refinement step (e) (PSNR = 36.78 dB) respectively.

component for which the noisy degree is larger than the noise-free degree, i.e., that is more likely to be noisy than noise-free, will be filtered. Other pixel components will remain unchanged. The noise-free degree and the noisy degree are determined by fuzzy rules as follows.

We consider a pixel component to be noise-free if it is similar to the corresponding component of the pixel at the same spatial location in the previous or next frame and to the corresponding component of two neighboring pixels in the same frame. In the case of motion, the pixels in the previous frames can not be used to determine whether a pixel component in the current frame is noise-free. Therefore, more confirmation (more similar neighbors or also similar in the other color components) is wanted instead. For the noise-free degree of the red component (and analogously for the other components), this is achieved by the following fuzzy rule.

Fuzzy Rule 1: IF(($|I_n^R(x,y,t) - I_f^R(x,y,t-1)|$ is NOT LARGE POSITIVE OR $|I_n^R(x,y,t) - I_n^R(x,y,t+1)|$ is NOT LARGE POSITIVE) AND there are two neighbors $(x+k, y+l, t)$ $(-2 \le k,l \le 2$ and $(k,l) \ne (0,0))$ for which $|I_n^R(x,y,t) - I_n^R(x+k,y+l,t)|$ is NOT LARGE POSITIVE) OR (there are four neighbors $(x+k, y+l, t)$ $(-2 \le k,l \le 2$ and $(k,l) \ne (0,0))$ for which $|I_n^R(x,y,t) - I_n^R(x+k,y+l,t)|$ is NOT LARGE POSITIVE OR (there are two neighbors $(x+k, y+l, t)$ $(-2 \le k,l \le 2$ and $(k,l) \ne (0,0))$ for which $|I_n^R(x,y,t) - I_n^R(x+k,y+l,t)|$ is NOT LARGE POSITIVE AND ($|I_n^G(x,y,t) - I_n^G(x+k,y+l,t)|$ OR $|I_n^B(x,y,t) - I_n^B(x+k,y+l,t)|$ are NOT LARGE POSITIVE)) THEN the red component $I_n^R(x,y,t)$ is considered NOISE-FREE.

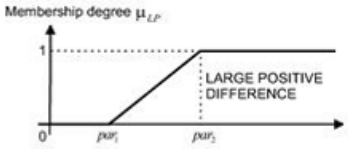

Fig. 3. The membership function μ_{LP} of the fuzzy set *large positive*.

To represent the linguistic value *large positive* in the above rule, a fuzzy set is used, with a membership function as μ_{LP} depicted in Fig. 3 (see Section III-A for the determination of the parameters). For the conjunctions (AND), disjunctions (OR) and negations (NOT) in fuzzy logic, triangular norms, triangular conorms and involutive negators [16] are used. In this paper, we will use the minimum operator, the maximum operator and the standard negator $(N_s(x) = 1 - x, \forall x \in [0,1])$ respectively. Those operators are simple in use and yielded the best results, but the difference compared to the results for another choice of operators is neglectible. The outcome of the rule, i.e., the degree to which the red component of the pixel at position (x,y,t) is considered noise-free, is determined as the degree to which the antecedent in the fuzzy rule is true:

$$\mu^R_{\text{noise-free}}(x,y,t) = \max(\min(\max(\alpha_1(x,y,t), \alpha_2(x,y,t)), M_2(x,y,t)), \max(M_4(x,y,t), M_{2b}(x,y,t)))$$

where

$$\alpha_1(x,y,t) = (1 - \mu_{LP}(|I_n^R(x,y,t) - I_f^R(x,y,t-1)|)),$$
$$\alpha_2(x,y,t) = (1 - \mu_{LP}(|I_n^R(x,y,t) - I_n^R(x,y,t+1)|)),$$

and where $M_2(x,y,t)$ and $M_4(x,y,t)$ respectively denote the degree to which there are two (respectively four) neighbors for which the absolute difference in the red component value is not large positive, that is determined as the second (respectively fourth) largest element in the set

$$\{1 - \mu_{LP}(|I_n^R(x,y,t) - I_n^R(x+k,y+l,t)|) \| -2 \le k,l \le 2 \text{ and } (k,l) \ne (0,0)\}$$

and $M_{2b}(x,y,t)$ denotes the degree to which there are two neighbors for which the absolute differences in the red component and one of the two color components are not large positive, determined as the second largest element in the set

$$\{\min(1 - \mu_{LP}(|I_n^R(x,y,t) - I_n^R(x+k,y+l,t)|), \max(1 - \mu_{LP}(|I_n^G(x,y,t) - I_n^G(x+k,y+l,t)|), 1 - \mu_{LP}(|I_n^B(x,y,t) - I_n^B(x+k,y+l,t)|))) \| -2 \le k,l \le 2 \text{ and } (k,l) \ne (0,0)\}.$$

Analogously, a degree to which the component of a pixel is considered noisy is calculated. In this step, we consider a pixel component to be noisy if the absolute difference in that compo- nent is large positive compared to the pixel at the same spatial location in the previous frame and if not for five of its neighbors the absolute difference in this component and one of the other two color bands is large positive compared to the pixel at the same spatial location in the previous frame (which means that the difference is not caused by motion). Further, we also want a

confirmation either by the fact that in this color band, there is a direction in which the differences between the considered pixel and the two respective neighbors in this direction are both large positive or large negative and if the absolute difference between those two neighbors is not large positive (i.e., there is an impulse between two pixels that are expected to belong to the same ob- ject) or by the fact that there is no large difference between the considered pixel and the pixel at the same spatial location in the previous frame in one of the other two color bands. For the red component (and analogously the other components) this leads to the following fuzzy rule.

Fuzzy Rule 2: IF($|I_n^R(x,y,t) - I_f^R(x,y,t-1)|$ is LARGE POSITIVE AND NOT (for five neighbors $(x+k, y+l, t)$ $(-2 \le k,l \le 2$ and $(k,l) \neq (0,0))$ $|I_n^R(x+k,y+l,t) - I_f^R(x+k,y+l,t-1)|$ is LARGE POSITIVE AND($|I_n^G(x+k,y+l,t) - I_f^G(x+k,y+l,t-1)|$ OR $|I_n^B(x+k,y+l,t) - I_f^B(x+k,y+l,t-1)|$ is LARGE POSITIVE)))

AND ((in one of the four directions (the differences $I_n^R(x,y,t) - I_n^R(x+k,y+l,t)$ AND $I_n^R(x,y,t) - I_n^R(x-k,y-l,t)$ $((k,l) \in \{(-1,-1),(-1,0),(-1,1),(0,1)\}$, are both LARGE POSITIVE OR both LARGE NEGATIVE) AND the absolute difference $|I_n^R(x+k,y+l,t) - I_n^R(x-k,y-l,t)|$ is NOT LARGE POSITIVE) OR ($|I_n^G(x,y,t) - I_f^G(x,y,t-1)|$ is NOT LARGE POSITIVE OR $|I_n^B(x,y,t) - I_f^B(x,y,t-1)|$ is NOT LARGE POSITIVE))

THEN the red component $I_n^R(x,y,t)$ is considered noisy.

Analogously to the linguistic term *large positive*, also *large negative* is represented by a fuzzy set, characterized by the membership function given in Fig. 4 (see Section III-A for the determination of the parameters). The degree to which for five neighbors the absolute differences in the red component and one of the other two components are large positive compared to the corresponding pixels in the previous frame, denoted by $t_{\text{pos}}(x,y,t)$, is determined as the fifth largest value in the set

$$\{\min(\mu_{\text{LP}}(|I_n^R(x+k,y+l,t) - I_f^R(x+k,y+l,t-1)|),\ \max(\mu_{\text{LP}}(|I_n^G(x+k,y+l,t) - I_f^G(x+k,y+l,t-1)|),\ \mu_{\text{LP}}(|I_n^B(x+k,y+l,t) - I_f^B(x+k,y+l,t-1)|)))\ |\ 2 \le k,l \le 2 \text{ and } (k,l) \neq (0,0)\}.$$

The degree to which the absolute difference between the pixel at position (x,y,t) and the corresponding pixel in the previous

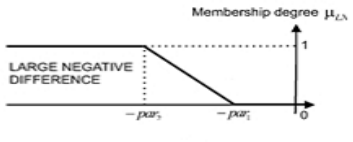

Fig. 4. The membership function μ_{LN} of the fuzzy set *large negative*.

frame is large positive and five of its neighbors do not show motion, is then given by

$$\beta(x,y,t) = \min(\mu_{\text{LP}}(|I_n^R(x,y,t) - I_f^R(x,y,t-1)|), 1 - t_{\text{pos}}(x,y,t)).$$

Further, the degree to which there is no large difference between the considered pixel and the pixel at the same spatial location in the previous frame in one of the other two color bands is given by

$$\delta(x,y,t) = \max(1 - \mu_{\text{LP}}(|I_n^G(x,y,t) - I_f^G(x,y,t-1)|), 1 - \mu_{\text{LP}}(|I_n^B(x,y,t) - I_f^B(x,y,t-1)|)).$$

Finally, the degree to which there is a direction in which the pixel at position (x,y,t) is an impulse, denoted by $\gamma(x,y,t)$, is determined as the maximum value in the set

$$\{\min(\max(\epsilon_{(k,l)}^1(x,y,t), \epsilon_{(k,l)}^2(x,y,t)), \epsilon_{(k,l)}^3(x,y,t)) \mid (k,l) \in \{(1,1),(1,0),(1,-1),(0,1)\}\}$$

where

$$\epsilon_{(k,l)}^1(x,y,t) = \min(\mu_{\text{LP}}(I_n^R(x,y,t) - I_n^R(x+k,y+l,t)), \mu_{\text{LP}}(I_n^R(x,y,t) - I_n^R(x-k,y-l,t))),$$

$$\epsilon_{(k,l)}^2(x,y,t) = \min(\mu_{\text{LN}}(I_n^R(x,y,t) - I_n^R(x+k,y+l,t)), \mu_{\text{LN}}(I_n^R(x,y,t) - I_n^R(x-k,y-l,t))),$$

$$\epsilon_{(k,l)}^3(x,y,t) = 1 - \mu_{\text{LP}}(|I_n^R(x+k,y+l,t) - I_n^R(x-k,y-l,t)|).$$

Combining the above, we get

$$\mu_{\text{noisy}}^R(x,y,t) = \min(\beta(x,y,t), \delta(x,y,t), \gamma(x,y,t)).$$

2) Filtering: In this subsection, we discuss the filtering for the red color band. The filtering of the other color bands is analogous. We decide to filter all red pixel components that are considered more likely to be noisy than noise-free, i.e., for which $\mu_{\text{noisy}}^R(x,y,t) > \mu_{\text{noisefree}}^R(x,y,t)$. The red components of the other pixels remain unchanged to avoid the filtering of noise-free pixels (that might have been uncorrectly assigned a low noisy degree, but for which the high noise-free degree assures us that it is noise-free) and thus detail loss. On the other hand, noisy pixel components might remain unfiltered due to an uncorrect high noise-free degree, but those pixels can still be detected in the next filtering step.

$$\mu_{\text{unch}}^R(x,y,t) = \begin{cases} 0, & \text{if } \mu_{\text{noisy}}^R(x,y,t) > \mu_{\text{noisefree}}^R(x,y,t) \\ 1, & \text{else.} \end{cases}$$

$\mu_{\text{unch}}(x,y,t) = (\mu_{\text{unch}}^R(x,y,t), \mu_{\text{unch}}^G(x,y,t), \mu_{\text{unch}}^B(x,y,t))$ is thus a vector that gives information on whether the respective color component of the color pixel $I_n(x,y,t)$ should be filtered. Analogously as $I_n(t)$ denotes the tth frame of I_n, $\mu_{\text{unch}}(t)$ denotes the 2-D array of vectors that gives information about the pixel components of the tth frame of the sequence I_n. To exploit the spatial and temporal information in the sequence as much as possible, the filtering is performed by blockmatching. To do this, a noise-adaptive mean absolute difference (MAD) is used to calculate the correspondence between the color components of two $(2 \cdot W + 1) \times (2 \cdot W + 1)$ blocks of image pixels (where W is a general parameter that determines the block size):

$${}^R\text{MAD}_{I_n}^{I_n}(x,y,r,s,W) = \frac{\sum_{k=-W}^{+W} \sum_{l=-W}^{+W} \nu(x,y,k,l,r,s)\phi(x,y,k,l,r,s)}{\sum_{k=-W}^{+W} \sum_{l=-W}^{+W} \nu(x,y,k,l,r,s)}$$

with

$$v(x,y,k,l,r,s) = \mu^R(x+k,y+l) \cdot \bar{\mu}^R(x+k+r,y+l+s)$$

and

$$\phi(x,y,k,l,r,s) = |I^R(x+k,y+l) - \bar{I}^R(x+k+r,y+l+s)|.$$

In the above equations, I and $\bar{I}$ are the two frames (2-D color images), to which the blocks belong, x and y indicate the spatial coordinates of the central pixel of the considered block in I, and r and s respectively stand for the vertical and horizontal coordinates of the displacement vector, i.e., the block that is considered in $\bar{I}$ has $(x+r, y+s)$ as the central pixel. The binary functions μ^c and $\bar{\mu}^c$ ($c \in \{R,G,B\}$) indicate whether the pixel components $I^c(x,y)$ and $\bar{I}^c(x,y)$ are reliable and should be used ($\mu^c(x,y) = 1$, respectively $\bar{\mu}^c(x,y) = 1$) or not ($\mu^c(x,y) = 0$, respectively $\bar{\mu}^c(x,y) = 0$). Using only noise-free pixel components allows us to calculate a more reliable measure to estimate whether two blocks would correspond in the red component if they were both noise-free. If $\sum_{k=-W}^{+W}\sum_{l=-W}^{+W} \mu^R(x+k,y+l)\cdot\bar{\mu}^R(x+k+r,y+l+s) = 0$, the noise adaptive MAD is assigned the value $+\infty$. Further, the noise adaptive MAD is not considered reliable if not for at least half of the positions in the $(2\cdot W+1)\times(2\cdot W+1)$ blocks, both compared values are reliable ($\mu^R(x+k,y+l) = 1$ and $\bar{\mu}^R(x+k+r,y+l+s) = 1$) or not for half of the reliable positions the absolute difference $|I^R(x+k,y+l) - \bar{I}^R(x+k+r,y+l+s)|$ is not large positive (i.e., $\mu_{LP}(|I^R(x+k,y+l) - \bar{I}^R(x+k+r,y+l+s)|) = 0$). It is also not considered reliable if both the green and blue component of the central pixels are reliable (i.e., $\mu^G(x,y) = 1$, $\mu^G(x+r,y+s) = 1$, $\mu^B(x,y) = 1$ and $\mu^B(x+r,y+s) = 1$) and their absolute difference is large positive (i.e., $\mu_{LP}(|I^G(x,y) - \bar{I}^G(x+r,y+s)|) = 1$ and $\mu_{LP}(|I^B(x,y) - \bar{I}^B(x+r,y+s)|) = 1$). In these cases, the noise-adaptive MAD is changed to the value $+\infty$, such that the block will not be used for the filtering.

For the filtering of a red component $I_n^R(x,y,t)$ in this first step of our algorithm, we determine the displacement vectors $(\underline{u}(x,y,t), \underline{v}(x,y,t))$ and $(\bar{u}(x,y,t), \bar{v}(x,y,t))$ for the best matching $(2\cdot W_1+1)\times(2\cdot W_1+1)$ block in a search region of size $(2\cdot W_2+1)\times(2\cdot W_2+1)$ in respectively the previous frame $I_f(t-1)$ and the current frame $I_n(t)$ (due to large motion, sometimes no corresponding block might be found in the previous frame, but the region around the given pixel in the current frame might be similar) as follows (for the optimization of the parameters W_1 and W_2, refer to Section III-A):

$$(\underline{u}(x,y,t), \underline{v}(x,y,t)) = \arg \min_{-W_2\le r,s\le W_2} {}^R\mathrm{MAD}^{I_n(t),\mu_{\mathrm{unch}}(t)}_{I_f(t-1),Id}(x,y,r,s,W_1).$$

The minimum value itself is denoted by $\underline{\mathrm{mmad}}(x,y,t)$. We have used the identity function Id for the binary function corresponding to the previous frame, since this frame has already been filtered and should be noise-free.

$$(\bar{u}(x,y,t), \bar{v}(x,y,t)) = \arg \min_{-W_2\le r,s\le W_2,(r,s)\neq(0,0)} {}^R\mathrm{MAD}^{I_n(t),\mu_{\mathrm{unch}}(t)}_{I_n(t),\mu_{\mathrm{unch}}}(x,y,r,s,W_1).$$

The minimum value itself is denoted by $\overline{\mathrm{mmad}}(x,y,t)$. We have restricted ourselves here to pixels $(x+r, y+s, t)$, for which $\mu^R_{\mathrm{unch}}(x+r,y+s,t) = 1$, since only noise-free pixels should be used to replace the noisy pixel component $I_n^R(x,y,t)$.

A pixel component $I_n^R(x,y,t)$, for which $\mu^R_{\mathrm{unch}}(x,y,t) = 0$, is then filtered as the noise-free center of the best corresponding block in the search region, if it exists ($\min(\underline{\mathrm{mmad}}(x,y,t), \overline{\mathrm{mmad}}(x,y,t)) < +\infty$). Otherwise, a spatial filtering is performed. If $\mu^R_{\mathrm{unch}}(x,y,t) = 1$, the pixel component remains unchanged in this step. Summarized, the output of this first step for the red component $I_n^R(x,y,t)$ is given as follows.

If $\mu^R_{\mathrm{unch}}(x,y,t) = 1$, then

$$I^R_{f_1}(x,y,t) = I^R_n(x,y,t),$$

else if $\mu^R_{\mathrm{unch}}(x,y,t) = 0$, then

$$I^R_{f_1}(x,y,t) = \mathrm{FILT}^{I^R_n(t),\mu^R_{\mathrm{unch}}(t),}_{I^R_f(t-1)}(x,y,\underline{u}(x,y,t), \underline{v}(x,y,t), u(x,y,t), v(x,y,t), \underline{\mathrm{mmad}}(x,y,t), \overline{\mathrm{mmad}}(x,y,t)),$$

with (in a general notation)

$$\mathrm{FILT}^{I,\mu}_{\tilde{I}}(x,y,u,v,\tilde{u},\tilde{v},m,\tilde{m}) = \begin{cases} I(x+u,y+v) & \text{if } m = \min(m,\tilde{m}) < +\infty \\ \tilde{I}(x+\tilde{u},y+\tilde{v}) & \text{if } \tilde{m} = \min(m,\tilde{m}) < +\infty \\ \mathrm{SF}^I_\mu(x,y,W_1) & \text{if } m = \tilde{m} = +\infty \end{cases}$$

where the spatial filtering framework is given by

$$\mathrm{SF}^I_\mu(x,y,W) = \frac{\sum_{k=-W}^{+W}\sum_{l=-W}^{+W}\mu(x+k,y+l)\cdot I(x+k,y+l)}{\sum_{k=-W}^{+W}\sum_{l=-W}^{+W}\mu(x+k,y+l)}.$$

If $\sum_{k=-W}^{+W}\sum_{l=-W}^{+W}\mu(x+k,y+l) = 0$, which is unlikely to happen in practical situations, then the output is given by $\mathrm{SF}^I_\mu(x,y,W) = \mathrm{median}\{I(x+k,y+l) \mid -W \le k,l \le W\}$

B. Second Filtering Step

In our aim to preserve the details as much as possible, the noise is removed in successive steps. In this step, the noise is detected based on the output of the previous step (I_{f_1}). Also in this second filtering step, a degree to which a pixel component is expected to be noise-free and a degree to which a pixel component is expected to be noisy, is calculated. In the calculation of those degrees, we now take into account information from the other color bands.

A color component of a pixel is considered noise-free if the difference between that pixel and the corresponding pixel in the previous frame is not large in the given component and also not large in one of the other two color components. It is also considered noise-free if there are two neighbors for which the difference in the given component and one of the other two components are not large. So, the other color bands are used here as a confirmation for the observations in the considered color band to make those more reliable.

For the red component (and analogously the other color components), this gives the following fuzzy rule.

Fuzzy Rule 3: IF($|I^R_{f_1}(x,y,t) - I^R_f(x,y,t-1)|$ is NOT LARGE POSITIVE AND($|I^G_{f_1}(x,y,t) - I^G_f(x,y,t-1)|$ is NOT LARGE POSITIVE OR $|I^B_{f_1}(x,y,t) - I^B_f(x,y,t-1)|$ is NOT LARGE POSITIVE)

OR(for two neighbors $(x+k,y+l,t)$ $(-1 \le k,l \le 1$ and $(k,l) \neq (0,0))$ $|I^R_{f_1}(x,y,t) - I^R_f(x+k,y+l,t)|$ is NOT LARGE POSITIVE AND($|I^G_{f_1}(x,y,t) - I^G_f(x+k,y+l,t)|$ is NOT LARGE POSITIVE OR $|I^B_{f_1}(x,y,t) - I^B_f(x+k,y+l,t)|$ is NOT LARGE POSITIVE))

THEN the red component $I_{f_1}^R(x,y,t)$ is considered NOISE-FREE.

The degree to which the red component of the pixel at position (x,y,t) is considered noise-free, is then given by

$$\mu_{2,\text{noisefree}}^R(x,y,t) = \max\{\zeta(x,y,t), \eta(x,y,t)\}$$

where

$$\begin{aligned}\zeta(x,y,t) &= \min(1-\mu_{\text{LP}}(|I_{f_1}^R(x,y,t) - I_f^R(x,y,t-1)|),\\ &\quad \max(1-\mu_{\text{LP}}(|I_{f_1}^G(x,y,t) - I_f^G(x,y,t-1)|),\\ &\quad 1-\mu_{\text{LP}}(|I_{f_1}^B(x,y,t) - I_f^B(x,y,t-1)|)))\end{aligned}$$

and $\eta(x,y,t)$ is the second largest element in the set

$$\begin{aligned}\{&\min(1-\mu_{\text{LP}}(|I_{f_1}^R(x,y,t) - I_f^R(x+k,y+l,t)|),\\ &\max(1-\mu_{\text{LP}}(|I_{f_1}^G(x,y,t) - I_f^G(x+k,y+l,t)|),\\ &1-\mu_{\text{LP}}(|I_{f_1}^B(x,y,t) - I_f^B(x+k,y+l,t)|)))\\ &\| -1 \le k,l \le 1 \text{ and } (k,l) \neq (0,0)\}.\end{aligned}$$

A pixel component is considered noisy if there are three neighbors that differ largely in that component, but are similar (not a large difference) in the other two components. It is also considered noisy if in the considered color band, its value is larger or smaller than the component values of all its neighbors, and this is not the case in both of the other color bands.

For the red component of a pixel (and analogously for the other components), this corresponds to the following fuzzy rule.

Fuzzy Rule 4: IF (for three neighbors $(x+k,y+l,t)$ ($-1 \le k,l \le 1$ and $(k,l) \neq (0,0)$) $|I_{f_1}^R(x,y,t) - I_f^R(x+k,y+l,t)|$ is LARGE POSITIVE AND $|I_{f_1}^G(x,y,t) - I_f^G(x+k,y+l,t)|$ is NOT LARGE POSITIVE AND $|I_{f_1}^B(x,y,t) - I_f^B(x+k,y+l,t)|$ is NOT LARGE POSITIVE) OR (((for all neighbors $(x+k,y+l,t)$ ($-1 \le k,l \le 1$ and $(k,l) \neq (0,0)$) $I_{f_1}^R(x,y,t) - I_f^R(x+k,y+l,t)$ is LARGE POSITIVE) OR (for all neighbors $(x+k,y+l,t)$ ($-1 \le k,l \le 1$ and $(k,l) \neq (0,0)$) $I_{f_1}^R(x,y,t) - I_f^R(x+k,y+l,t)$ is LARGE NEGATIVE)) AND NOT (((for all neighbors $(x+k,y+l,t)$ $(-1 \le k,l \le 1$ and $(k,l) \neq (0,0))$ $I_{f_1}^G(x,y,t) - I_f^G(x+k,y+l,t)$ is LARGE POSITIVE) OR (for all neighbors $(x+k,y+l,t)$ $(-1 \le k,l \le 1$ and $(k,l) \neq (0,0))$ $I_{f_1}^G(x,y,t) - I_f^G(x+k,y+l,t)$ is LARGE NEGATIVE)) AND ((for all neighbors $(x+k,y+l,t)$ ($-1 \le k,l \le 1$ and $(k,l) \neq (0,0)$) $I_{f_1}^B(x,y,t) - I_f^B(x+k,y+l,t)$ is LARGE POSITIVE) OR (for all neighbors $(x+k,y+l,t)$ $(-1 \le k,l \le 1$ and $(k,l) \neq (0,0))$ $I_{f_1}^B(x,y,t) - I_f^B(x+k,y+l,t)$ is LARGE NEGATIVE))))

THEN the red component $I_{f_1}^R(x,y,t)$ is considered NOISY.

The noisy degree for the red component of the pixel at position (x,y,t) is then calculated as follows:

$$\mu_{2,\text{noisy}}^R(x,y,t) = \max(\theta(x,y,t), \kappa(x,y,t))$$

where $\theta(x,y,t)$ is the third largest element in the set

$$\begin{aligned}\{&\min(\mu_{\text{LP}}(|I_{f_1}^R(x,y,t) - I_f^R(x+k,y+l,t)|),\\ &\min(1-\mu_{\text{LP}}(|I_{f_1}^G(x,y,t) - I_f^G(x+k,y+l,t)|),\\ &1-\mu_{\text{LP}}(|I_{f_1}^B(x,y,t) - I_f^B(x+k,y+l,t)|)))\\ &\| -1 \le k,l \le 1 \text{ and } (k,l) \neq (0,0)\}\end{aligned}$$

and

$$\begin{aligned}\kappa(x,y,t) = \min(&\max(m_1^R(x,y,t), m_2^R(x,y,t)),\\ &\min(\max(m_1^G(x,y,t), m_2^G(x,y,t)),\\ &\max(m_1^B(x,y,t), m_2^B(x,y,t))))\end{aligned}$$

where

$$\begin{aligned}m_1^c(x,y,t) = \min\{&\mu_{\text{LP}}(|I_{f_1}^R(x,y,t) - I_f^R(x+k,y+l,t)|)\\ &\| -1 \le k,l \le 1 \text{ and } (k,l) \neq (0,0)\},\end{aligned}$$

$$\begin{aligned}m_2^c(x,y,t) = \min\{&\mu_{\text{LN}}(|I_{f_1}^R(x,y,t) - I_f^R(x+k,y+l,t)|)\\ &\| -1 \le k,l \le 1 \text{ and } (k,l) \neq (0,0)\},\end{aligned}$$

with $c \in \{R,G,B\}$

All red (and analogously green and blue) components for which $\mu_{2,\text{noisy}}^R(x,y,t) > \mu_{2,\text{noisefree}}^R(x,y,t)$ are filtered ($\mu_{2,\text{unch}}^R(x,y,t) = 0$), the other red components remain unchanged ($\mu_{2,\text{unch}}^R(x,y,t) = 1$):

$$\mu_{2,\text{unch}}^R(x,y,t) = \begin{cases} 0, & \text{if } \mu_{2,\text{noisy}}^R(x,y,t) > \mu_{2,\text{noise free}}^R(x,y,t) \\ 1, & \text{else.}\end{cases}$$

Analogously to the first step, for the filtering of the red components (and analogously the green and blue components) for which $\mu_{2,\text{unch}}^R(x,y,t) = 0$, we search for the noise-free center of the best corresponding block in the search region in the current and previous frame.

$$\begin{aligned}&(\underline{u}'(x,y,t), \underline{v}'(x,y,t))\\ &\quad = \arg \min_{W_2 \le r,s \le W_2} {}^R\text{MAD}_{I_f(t-1),fd}^{I_{f_1}(t),\mu_{2,\text{unch}}(t)}(x,y,r,s,W_1).\end{aligned}$$

The minimum value itself is denoted by $\underline{\text{mmad}}'(x,y,t)$.

$$\begin{aligned}&(\bar{u}'(x,y,t), \bar{v}'(x,y,t))\\ &\quad = \arg \min_{\substack{W_2 \le r,s \le W_2,(r,s) \neq (0,0),\\ \mu_{2,\text{unch}}^R(x+r,y+s,t)=1}} {}^R\text{MAD}_{I_{f_1}(t),\mu_{2,\text{unch}}(t)}^{I_{f_1}(t),\mu_{2,\text{unch}}(t)}\\ &\qquad \times (x,y,r,s,W_1).\end{aligned}$$

The minimum value itself is denoted by $\overline{\text{mmad}}'(x,y,t)$.

If $\mu_{2,\text{unch}}^R(x,y,t) = 0$, the $I_{f_1}^R(x,y,t)$ is filtered as

$$\begin{aligned}I_{f_2}^R(x,y,t) = \text{FILT}_{I_f^R(t-1)}^{I_{f_1}^R(t),\mu_{2,\text{unch}}^R(t)}&(x,y,\underline{u}'(x,y,t),\underline{v}'(x,y,t),\\ &\bar{u}'(x,y,t),\bar{v}'(x,y,t),\underline{\text{mmad}}'(x,y,t),\overline{\text{mmad}}'(x,y,t)).\end{aligned}$$

Red pixel components that are considered noise-free ($\mu_{2,\text{unch}}^R(x,y,t) = 1$) remain unchanged:

$$I_{f_2}(x,y,t) = I_{f_1}(x,y,t).$$

C. Third Filtering Step

The result from the previous steps is further refined based on temporal, spatial and color information. Namely, the red component (and analogously the green and blue component) of a pixel is refined in the following cases:

- In non-moving areas, pixels will correspond to the pixels in the previous frame, which allows us to detect remaining isolated noisy pixels. If (x,y,t) lies in a non-moving 3×3 neighborhood, i.e., (with $\Delta(x,y,t) = |I_{f_2}^c(x,y,t) - I_f^c(x,y,t-1)|$)

$$\frac{\sum_{k=-1}^{1}\sum_{l=-1}^{1}\sum_{c\in\{R,G,B\}}\Delta(x+k,y+l,t)}{24} - \frac{\sum_{c\in\{R,G,B\}}\Delta(x,y,t)}{24} < \text{par}_1$$

and if $|I^R_{f_2}(x,y,t) - I^R_f(x,y,t-1)| > \mathrm{par}_2$ and $|I^R_f(x,y,t-1) - I^R_n(x,y,t+1)| < \mathrm{par}_1$, then the red component $I^R_{f_2}(x,y,t)$ is considered to be noisy $(\mu^R_{3,\mathrm{unch}}(x,y,t) = 0)$. The last check is to prevent noise propagation in the case that the pixel in the previous frame would not have been filtered correctly.

- Very small impulses might not have been detected by the algorithm. In homogeneous areas however, such impulses might be relatively large and can be detected more easily. Let $L^R_2(x,y,t)$ and $S^R_2(x,y,t)$ respectively denote the second largest and second smallest red component value among the eight neighbors in a 3×3 neighborhood around $I^R_{f_2}(x,y,t)$. If $L^R_2(x,y,t) - S^R_2(x,y,t) < \mathrm{par}_2$ (homogeneous neighborhood) and further also $I^R_{f_2}(x,y,t) - L^R_2(x,y,t) > I^R_2(x,y,t) - S^R_2(x,y,t)$ or $S^R_2(x,y,t) - I^R_{f_2}(x,y,t) > L^R_2(x,y,t) - S^R_2(x,y,t)$ (the red component is clearly larger or smaller than the neighborhood), then the red component $I^R_{f_2}(x,y,t)$ is considered to be noisy $(\mu^R_{3,\mathrm{unch}}(x,y,t) = 0)$
- Based on color information, the red component $I^R_{f_2}(x,y,t)$ is considered to be noisy $(\mu^R_{3,\mathrm{unch}}(x,y,t) = 0)$, if in a 3×3 neighborhood two neighbors $I^R_{f_2}(x+k, y+l, t)$ $(-1 \le k,l \le 1, (k,l) \ne (0,0))$ can be found for which $|I^R_{f_2}(x,y,t) - I^R_{f_2}(x+k,y+l,t)| > \mathrm{par}_2$ and $|I^R_{f_2}(x,y,t) - I^R_{f_2}(x+k,y+l,t)| > |I^G_{f_2}(x,y,t) - I^G_{f_2}(x+k,y+l,t)| + |I^B_{f_2}(x,y,t) - I^B_{f_2}(x+k,y+l,t)|$

In all other cases the red component value is considered to be noise-free and should not be adapted anymore $(\mu^R_{3,\mathrm{unch}}(x,y,t) = 1)$

Analogously as in the previous steps, for the filtering of the red components for which $\mu^R_{3,\mathrm{unch}}(x,y,t) = 0$, we search for the noise-free center of the best corresponding block in the search region in the current and previous frame.

$$(\underline{u}''(x,y,t), \underline{v}''(x,y,t)) = \arg \min_{-W_2 \le r,s \le W_2} {}^R\mathrm{MAD}^{I_{f_2}(t),\mu_{3,\mathrm{unch}}(t)}_{I_f(t-1),Id}(x,y,r,s,W_1).$$

The minimum value itself is denoted by $\underline{\mathrm{mmad}}''(x,y,t)$

$$(u''(x,y,t), v''(x,y,t)) = \arg \min_{\substack{W_2 \le r,s \le W_2,(r,s) \ne (0,0),\\ \mu^R_{3,\mathrm{unch}}(x+r,y+s,t-1)=1}} {}^R\mathrm{MAD}^{I_{f_2}(t),\mu_{3,\mathrm{unch}}(t)}_{I_{f_2}(t),\mu_{3,\mathrm{unch}}(t)} \times (x,y,r,s,W_1).$$

The minimum value itself is denoted by $\overline{\mathrm{mmad}}''(x,y,t)$

A red component $I^R_{f_2}(x,y,t)$ for which $\mu^R_{3,\mathrm{unch}}(x,y,t) = 0$, is filtered as

$$I_f(x,y,t) = \mathrm{FILT}^{I_{f_2}(t),\mu^{''}_{3,\mathrm{unch}}(t)}_{I_f(t-1)}(x,y,\underline{u}''(x,y,t), \underline{v}''(x,y,t), u''(x,y,t), v''(x,y,t), \underline{\mathrm{mmad}}''(x,y,t), \overline{\mathrm{mmad}}''(x,y,t)).$$

Otherwise $(\mu^R_{3,\mathrm{unch}}(x,y,t) = 1)$, it remains unchanged:

$$I^R_f(x,y,t) = I^R_{f_2}(x,y,t).$$

III. EXPERIMENTAL RESULTS

To be able to judge the performance of the proposed method, we will use the mean absolute error (MAE), the peak-signal-to-noise ratio (PSNR) and the normalized color difference (NCD) as objective measures of similarity and dissimilarity between a filtered frame $I_f(t)$ and the original one $I_o(t)$, each containing m rows and n columns of pixels.

The MAE is given by

$$\mathrm{MAE}(I_o(t), I_f(t)) = \frac{\sum_{c \in \{R,G,B\}} \sum_{x=1}^{m} \sum_{y=1}^{n} |I^c_o(x,y,t) - I^c_f(x,y,t)|}{3 \cdot n \cdot m}.$$

The lower the MAE, the more similar (less dissimilar) the images.

The PSNR value is defined as

$$\mathrm{MSE}(I_o(t), I_f(t)) = \frac{\sum_{c \in \{R,G,B\}} \sum_{x=1}^{m} \sum_{y=1}^{n} (I^c_o(x,y,t) - I^c_f(x,y,t))^2}{3 \cdot n \cdot m},$$

$$\mathrm{PSNR}(I_o(t), I_f(t)) = 10 \cdot \log_{10} \frac{S^2}{\mathrm{MSE}(I_o(t), I_f(t))},$$

where S denotes the maximum possible value of a pixel component (here $S = 255$). The higher the PSNR value, the more similar (less dissimilar) the images.

Finally, the NCD, between an original and a filtered frame, is calculated as

$$\mathrm{NCD}(I_o(t), I_f(t)) = \frac{\sum_{x=1}^{m} \sum_{y=1}^{n} \left\| I^{\mathrm{LAB}}_o(x,y,t) - I^{\mathrm{LAB}}_f(x,y,t) \right\|}{\sum_{x=1}^{m} \sum_{y=1}^{n} \left\| I^{\mathrm{LAB}}_o(x,y,t) \right\|}$$

where $\| \cdot \|$ is the Euclidean norm and $I^{\mathrm{LAB}}_o(x,y,t)$ and $I^{\mathrm{LAB}}_f(x,y,t)$ respectively denote the $L^*a^*b^*$-transform [42] of the original and the filtered frame. The lower the NCD value, the more similar (less dissimilar) the images.

The remainder of this section is structured as follows. The parameter values for the membership functions and the window sizes are determined in Section III-A. The proposed filtering framework is compared to other state-of-the-art noise reduction methods in Section III-B. Some notes on the complexity are discussed in Section III-C.

A. Parameter Selection

First the parameters par_1 and par_2 that determine the membership functions μ_{LP} and μ_{LN} in Figs. 3 and 4 are determined. To do this, we have fixed the window sizes W_1 and W_2 of the pixel neighborhood and the search region in the filtering as $W_1 = 2$ (5×5 neighborhood) and $W_2 = 5$ (11×11 search region) and we have let the parameters par_1 and par_2 run over a

TABLE I
DETERMINATION OF THE PARAMETERS par_1 AND par_2 (ARITHMETIC MEAN OF THE AVERAGE PSNR (dB) VALUES AROUND THE MAXIMUM)

$par_1 \backslash par_2$	29	30	31	32	33
18	32.38	32.39	32.40	32.38	32.37
19	32.39	32.41	32.41	32.40	32.39
20	32.39	32.41	32.42	32.40	32.39
21	32.39	32.40	32.41	32.40	32.39
22	32.39	32.40	32.41	32.40	32.39

TABLE II
DETERMINATION OF THE PARAMETERS W_1 AND W_2 (ARITHMETIC MEAN OF THE AVERAGE PSNR (dB) VALUES)

$W_1 \backslash W_2$	5	6	7	8	9	10	11
1	31.42	31.42	31.41	31.38	31.33	31.31	31.27
2	32.42	32.49	32.57	32.57	32.55	32.55	32.54
3	32.45	32.54	32.63	32.64	32.64	32.64	32.64
4	32.46	32.56	32.65	32.67	32.67	32.67	32.67
5	32.35	32.45	32.55	32.57	32.57	32.58	32.58

range of possible values. The parameter values were then determined as the couple $(\mathrm{par}_1, \mathrm{par}_2)$, for which the arithmetic mean of the PSNR result of the nine sequences "Salesman", "Bus" and "Tennis", each corrupted with respectively 5%, 15% and 25% random impulse noise in each of the color bands, reached its maximum. The obtained values, which we will also use in the remaining experiments, are $(\mathrm{par}_1, \mathrm{par}_2) = (20, 31)$ (Table I).

Next, the window sizes W_1 and W_2 are set. For the above selected parameter values for par_1 and par_2, we now let the parameters W_1 and W_2 run over a range of possible values. As can be seen in Table II, from the couple $(W_1, W_2) = (2, 7)$ on, the arithmetic mean of the PSNR values of the nine test sequences hardly increases. Although we have focused in this paper on the noise filtering capability of the filter and not on its complexity, it should be mentioned that most of the computation time needed by the method goes to the filtering of detected pixels, i.e., the search for the best matching block. The size of a block (the number of pixels that has to be handled for each block) and the size of the search region (the number of blocks to which a given block should be compared) increases quadratic with respect to respectively W_1 and W_2. Therefore, we have decided to use the couple $(W_1, W_2) = (2, 7)$ for the remaining experiments.

Comparison to Other State-of-the-Art Filters

In this subsection, the performance of the proposed method is compared to that of the adaptive vector median filter (AVMF) from [31] and [32], the video adaptive vector directional median filter (VAVDMF) with 3-D filtering window from [30] and the 2-D fuzzy impulse noise reduction method for color images (INRC) from [33].

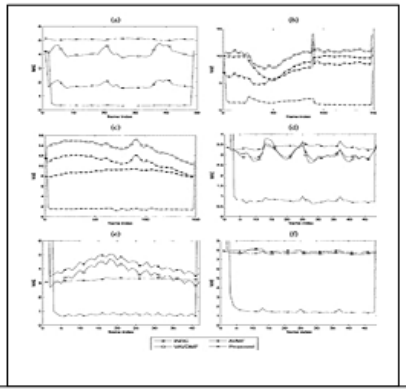

Fig. 5. MAE results for the different methods applied on (a) "Salesman" (p =5%) , (b) "Tennis" (p = 10 %) , (c) "Bus" (p = 15 %) , (d) "Foreman" (p = 20%) , (e) "Chair" (p = 25 %) and (f) "Deadline" (p = 30 %)

In the video adaptive vector directional median filter [30], the vectors are first ordered based on increasing angular distance. If the absolute distance between the central pixel in the window and the mean of a given number of vectors that have the lowest accumulated angular distance, is greater than a given threshold, then the central pixel is filtered as the pixel with the lowest accumulated absolute distance (magnitude), otherwise, it remains unchanged.To show that the proposed filter takes real advantage from the temporal information, we have also compared the proposed filter to the 2-D fuzzy impulse noise reduction method for color images. Further, this filter is also a representative of a non-vector-based filter, in which the color bands are filtered separately. However, in the detection of noisy pixel components, also information from the other components is used. All methods have been processed on the "Salesman", "Bus" and other four sequences, for random impulse noise levels (in each color band) ranging from p=5% to p=30%. The results of these experiments in terms of MAE, PSNR and NCD are respectively presented in Figs. 5 and 7, from which it is can be concluded that the proposed method outperforms all other methods.

Fig8:110th frame of tennis

Fig9:20th frame of Deadline .

Figs. 8 and 9 respectively show for the 110th frame of the "Tennis" sequence and the 20th frame of the "Deadline"sequence, the original frame, the noisy frame and the result obtained by the different compared methods.

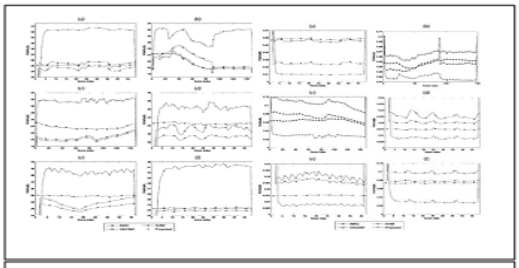

Fig. 6&7. PSNR & NCD results for the different methods applied on (a) "Salesman" (p =5%) , (b) "Tennis" (p = 10%) , (c) "Bus" (p = 15 %) , (d) "Foreman" (p = 20%) , (e) "Chair" (p = 25 %) and (f) "Deadline" (p = 30 %)

We see that the VAVDMF removes the noise very well. The filter also performs less well in the case of motion (e.g., "Salesman" (arms), "Tennis" (ball), "Chair", "Bus"), due to the fact that the pixels in the filtering window from the previous and next frame will then not always correspond to the same object.

Next, the INRC results in very good noise removal, even for high noise levels. At the cost of this, however, too much detail gets lost (e.g., side lines on the table in "Tennis") and the images become a little blurry. This is no surprise, since the 2-D filter does not benefit from the available extra temporal information in such non-moving areas. Finally, the proposed fuzzy filter combines very good detail preservation to very good noise removal and clearly out performs all compared filters. The filter benefits very well from the extra information coming from similar regions in a spatio-temporal neighborhood.

The algorithm was implemented inMatlab in combination with the mex-function and executed on an Intel® Xeon® CPU X3360 @ 2.83 GHz.

TABLE III
AVERAGE RUNNING TIME (SECONDS PER FRAME) FOR THE PROCESSING OF THE "SALESMAN" SEQUENCE

	% random impulse noise						
	0	5	10	15	20	25	30
INRC	0.65	0.67	0.69	0.71	0.73	0.75	0.76
VAVDMF	7.77	7.72	7.67	7.65	7.65	7.59	7.57
AVMF	1.21	1.21	1.22	1.21	1.21	1.22	1.22
Proposed	2.54	4.76	6.92	8.98	10.95	12.90	14.84

IV. CONCLUSION

In this paper, we have presented a new filtering framework for color videos corrupted with random valued impulse noise. In order to preserve the details as much as possible, the noise is removed step by step. The detection of noisy color components is based on fuzzy rules in which information from spatial and temporal neighbors as well as from the other color bands is used. Detected noisy components are filtered based on blockmatching where a noise adaptive mean absolute difference is used and where the search region contains pixels blocks from both the previous and current frame. The experiments showed that the proposed method outperforms other state-of-the-art methods both in terms of objective measures such as MAE, PSNR and NCD and visually.

REFERENCES

[1] E. Abreu, M. Lightstone, S. K. Mitra, and K. Arakawa, "A new efficient approach for the removal of impulse noise from highly corrupted images," IEEE Trans. Image Process., vol. 5, no. 6, pp. 1012-1025,1996.

[2] R. H. Chan, C. Hu, and M. Nikolova, "An iterative procedure for removing random-valued impulse noise," IEEE Signal Process. Lett., vol.11, no. 12, pp. 921-924, 2004.

[3] S. M. M. Rahman, M. O. Ahmad, and M. N. S. Swamy, "Video denoising based on inter-frame statistical modelling of wavelet coefficients," IEEE Trans. Circuits Syst. Video Technol., vol. 17, no. 2, pp.187-198, 2007.

[4] L. Jovanov, A. Pizurica, V. Zlokolica, S. Schulte, P. Schelkens, A.Munteanu, E. E. Kerre, and W. Philips, "Combined wavelet-domain and motion-compensated video denoising based on video codec motion estimation methods," IEEE Trans. Circuits Syst. Video Technol.,vol. 19, no. 3, pp. 417-421, 2009.

[5] H. B. Yin, X. Z. Fang, Z. Wei, and X. K. Yang, "An improved motion-compensated 3-D LLMMSE filter with spatio-temporal adaptive filtering support," IEEE Trans. Circuits Syst. Video Technol., vol. 17no. 12, pp. 1714-1727, 2007.

[6] L. Guo, O. C. Au, M. Ma, and Z. Liang, "Temporal video denoising based on multihypothesis motion compensation," IEEE Trans. Circuits Syst. Video Technol, vol. 17, no. 10, pp. 1423-1429, 2007.

[7] T. Mélange, M. Nachtegael, E. E. Kerre, V. Zlokolica, S. chulte, V. DeWitte, A. Pizurica, and W. Philips, "Video denoising by fuzzy motion and detail adaptive averaging," J. Electron. Imaging, vol. 17, no. 4, pp.043005-, 2008.

[8] T. Chen, K. K. Ma, and L. H. Chen, "Tri-state median filter for image denoising," IEEE Trans. Image Process., vol. 8, pp. 1834-1838, 1999.

[9] R. C. Hardie and C. G. Boncelet, "LUM filters: A class of rank-order-based filters for smoothing and sharpening," IEEE Trans.Signal Process., vol. 41, pp. 1061-1076, 1993.

[10] S. J. Ko and Y. H. Lee, "Center weighted median filters and their applications to image enhancement," IEEE Trans. Circuits Syst., vol. 38,pp. 984-993, 1991.

[11] S. M. Guo, C. S. Lee, and C. Y. Hsu, "An intelligent image agent based on soft-computing techniques for color image processing," Expert Systems With Appl., vol. 28, pp. 483-494, 2005.

[12] S. Schulte, V. De Witte, M. Nachtegael, D. Van der Weken, and E. E.Kerre, "Fuzzy random impulse noise reduction method," Fuzzy SetsSyst., vol. 158, pp. 270-283, 2007.

[13] S. Schulte, M. Nachtegael, V. De Witte, D. Van der Weken, and E. E.Kerre, "A fuzzy impulse noise detection and reduction method," IEEE Trans. Image Process., vol. 15, no. 5, pp. 1153-1162, 2006.

[14] F. Russo, "Fire operators for image processing," Fuzzy Sets Syst., vol.103, no. 2, pp. 265-275, 1999.

[15] F. Russo, "Hybrid neuro-fuzzy filter for impulse noise removal," Pattern Recognit., vol. 32, pp. 1843-1855, 1999.

[16] H. K. Kwan, "Fuzzy filters for noise reduction in images," in Fuzzy Filters for Image Processing, M. Nachtegael, D. Van der Weken, D.Van De Ville, and E. E. Kerre, Eds. Heidelberg, Germany: Springer,2003, pp. 54-71.

[17] J. H. Wang, W. J. Liu, and L. D. Lin, "An histogram-based fuzzy filter for image restoration," IEEE Trans. Syst. Man Cybern. B, Bern., vol.32, no. 2, pp. 230-238, 2002.

[18] H. Xu, G. Zhu, H. Peng, and D. Wang, "Adaptive fuzzy switching filter for images corrupted by impulse noise," Pattern Recognit. Lett., vol. 25,pp. 1657-1663, 2004.

[19] F. Cocchia, S. Carrato, and G. Ramponi, "Design and real-time implementation of a 3-D rational filter for edge preserving smoothing," IEEE Trans. Consum. Electron., vol. 43, no. 4, pp. 1291-1300, 1997.

[20] J.-S. Kim and H. W. Park, "Adaptive 3-D median filtering for restoration of an image sequence corrupted by impulse noise," SignalProcess.: Image Commun., vol. 16, pp. 657-668, 2001.

POWER CONTROL OF HYBRID ACTIVE WIND GENERATOR FOR DISTRIBUTED POWER GENERATION BY USING IGCT BASED UPFC.

ADCY ALEX[1] & R .SENTHIL KUMAR[2]

[1,2]Department of Electrical and Electronics Eng. ,SNS college of Tech., Coimbatore

Abstract –Now a days renewable energy resources has much attention than non-renewable energy sources. Among them wind energy plays an important role because it is a clean source of energy and it is perennially available. The output of the wind generator, normally fluctuates greatly due to wind speed variations and thus the output fluctuations can have a serious influence on the power system operation. In the proposed system, a variable speed wind generator and HHOG (High purity hydrogen & oxygen generator) system is combined inorder to maintain a constant power output to the grid. HHOG is to provide active power compensation, while reactive power compensation is done by using IGCT based UPFC. The performance of the proposed system is evaluated by simulation analysis, in which simulation are performed by using MATLAB/Simulink.

IndexTerms- *High purity Hydrogen and Oxygen Generator(HHOG);Integrated gate commutated thyristor(IGCT);Unified power flow controller(UPFC).*

I. INTRODUCTION

In recent years , there has been a growing interest in wind energy power systems because of the environmental benefits and the economic benefits of fuel savings .However ,since wind energy is not constant and the windmill output is proportional to the cube of wind speed ,the generated power of wind turbine generator(WTG) fluctuates. If the capacity ratio of the power source for WTG is very small , the power source doesnot cause the frequency to fluctuate by output fluctuations. However , if the ratio of WTG capacity is large ,frequency fluctuation of the power system will increase .

In this paper a combination system of variable speed wind generator and HHOG is proposed inorder to maintain a constant output power to the grid .HHOG is to provide active power compensation, while reactive power compensation is done string current exists[2]-[4]. To minimize the string current, string current diverter should be used[2]. The proposed system should decrease the draw done by using IGCT based UPFC .There has been growing interest in the use of FACTS controllers in power transmission applications .One FACTS controller in particular ,the UPFC, is capable of concurrently or selectively controlling transmission line power flows. Voltage magnitudes and phase angles in a power system. Hence, it is expected that its use and control applications will grow, particularly in new deregulated markets where simultaneous independent and fast controls of active and reactive power flows are an asset. The UPFC controller brings major benefits in steady state operation of power system as well as in emergency situations, where it will be possible to rapidly and effectively redirect power flows and/or damp power oscillations.

The UPFC is conceptually a synchronous voltage source (SVS) which generates the adjustable voltage on the ac side .the voltage source exchanges both active power and reactive power with the transmission system. The UPFC consists of two voltage source converters, one in series and one in shunt in a transmission line. The performance of the proposed system is evaluated by using MATLAB/Simulink.

II. OPERATING PRINCIPLE OF UPFC

The UPFC is the most versatile and complex of the FACTS devices ,combining the features of the STATCOM and SSSC. The main reason behind the wide spreads of UPFC are its ability to pass the real power flow bi-directionally, maintaining well regulated DC voltage, workability in the wide range of operating conditions etc. The basic components of the UPFC are two voltage source inverters(VSIs) sharing a common dc storage capacitor and connected to the power system through coupling transformer .One VSI is connected to in shunt to the transmission system via a shunt transformer ,while the other one is connected in series through a series transformer. The DC terminals of the two VSCS are coupled and this creates a path for active power exchange between converters .Thus the active supplied to the line by line by the series converter can be supplied by the series converter can be supplied to the line by the series converter can be supplied by the shunt converter. Therefore a different range of control options is available compared to STATCOM/SSSC. The UPFC can be used to control the flow of active and reactive power through the transmission line and to conrol the amount of reactive power supplied to the transmission line and to control the amount of reactive power supplied to the transmission line at the poin the of installation. The series inverter is controlled to inject

a symmetrical 3 phase voltage system of controllable magnitude and phase angle in series with the line to control active and reactive power flows on the transmission line So ,this inverter will exchange active and creative power with the line. The reactive power is electronically provided by the series inverter, and the active power is transmitted to the dc terminals. The shunt inverter is operated in such a way as to demand this dc terminal power from the line keeping voltage across the storage capacitor Vdc constant .So the net real power absorbed from the line by the UPFC is equal only to the losses of the inverter and their transformers .The remaining capacity of the shunt inverter can be used to exchange reactive power with the line so to provide a voltage regulation at the connection point

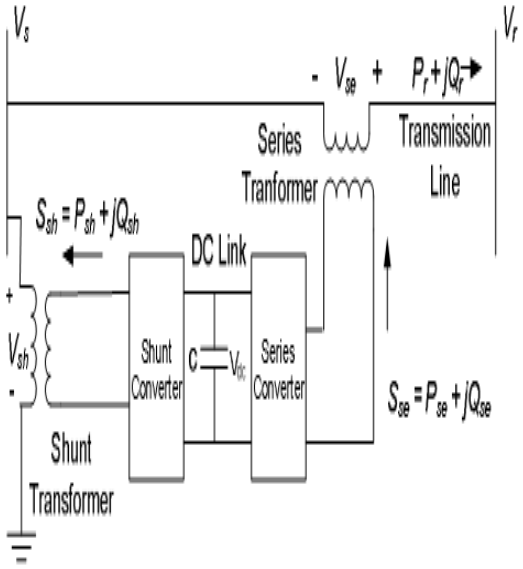

Figure 1.BASIC CIRCUIT ARRANGEMENT OF UPFC

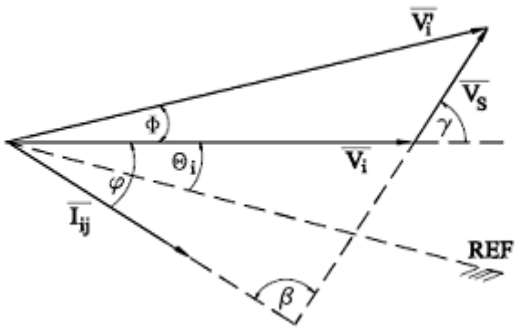

Fig 2. PHASOR DIAGRAM OF UPFC

Active and Reactive powerflows in a transmiossion line can be expressed by

Skm=Vk*Ikm=Vk[(Vk+Vb-Vm/Zkm+jXb)+(Vk-Ve/jXe)] (1)

Smk=Vm*Imk=Vm[(Vm-Vb-Vk/Zkm+jXb)] (2)

Where Xb,Xe & Zkm are transmission line impedance, parallel and series source impedances

III. PROPOSED SYSTEM

In the proposed system we are combining a fuel system with the wind turbine system for active power compensation. The entire system shown below

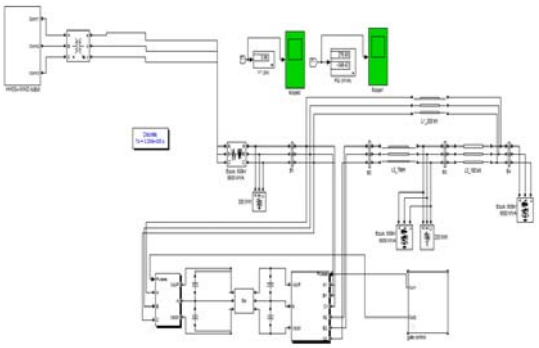

Figure 3.SYSTEM WITH UPFC

The smoothing of the power can be obtained by using the energy storage devices.The figure 4 ,5,6 show the design of fuel cell and its output

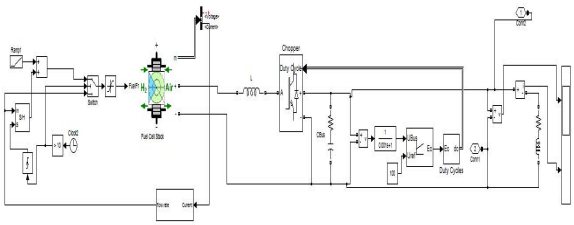

Figure 4. DESIGN OF FUEL CELL Voltage(V)

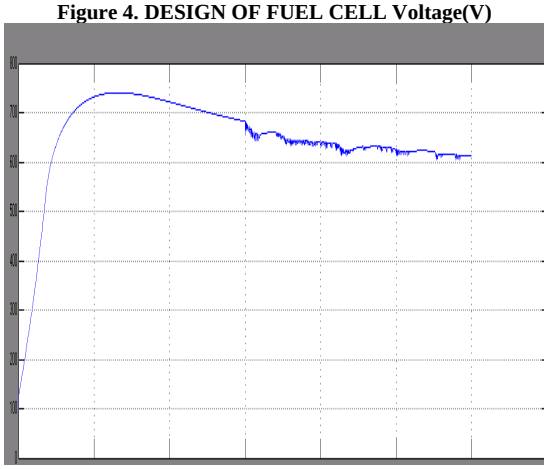

Figure 5.OUTPUT VOLTAGE WAVE FORM Current(I)

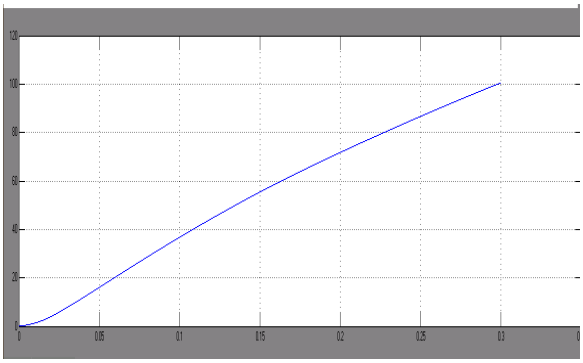

Figure 6.OUTPUT CURRENT WAVEFORM

In this paper the wind energy is given to AC-DC-AC PWM converter and after that it is connected to the grid. The following figure shows the combination circuit.

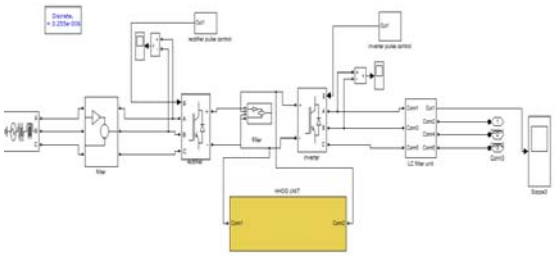

Figure 7.CONVERTER DESIGN WITH FUELCELL

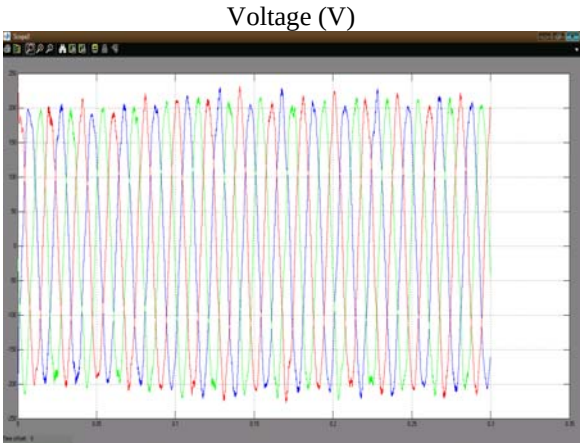

Figure 8.OUTPUT WAVEFORM OF COMBINED SYSTEM

The reactive power is the latest soul of a power transmission system.It is very precious in keeping the system voltage stable.It is evident that sufficient reactive power reserve is required to maintain terminal voltage at the load bus.The voltage control should be carried out on line against a possible disturbance,particularly in a heavily loaded system.Such control should be fast for online application flexible for changing system conditions and easy to comply with operators decision making logic.

Inorder to maintain constant voltage profile on various conditions of load and system configuration changes,power system are equipped with a lot of voltage controlling device,such as capacitor UPFC for supplying reactive power.The objective of reactive power control in a power station is to minimize the real power loss which will reduce the operating cost and improve the voltage profile.

Following figure shows the UPFC output i.e, the voltage stability ,real and reactive power compensation.

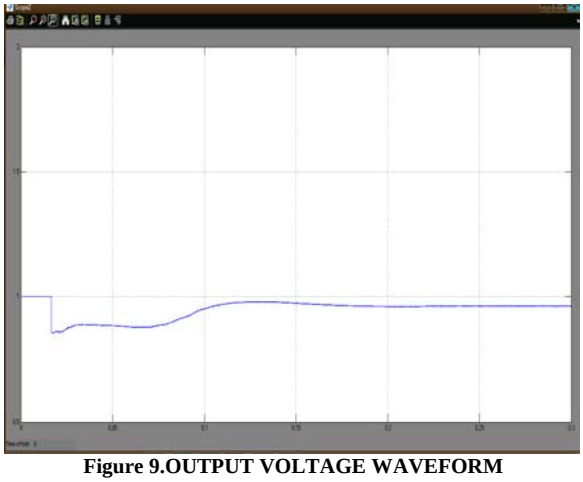

Figure 9.OUTPUT VOLTAGE WAVEFORM

Figure 10.OUTPUT WAVEFORM FOR REAL & REACTIVE POWER COMPENSATION

IV. CONCLUSION

In recent years ,wind energy operation to generate electrical power has had a great improve.Transmissions study and using wind energy in electrical grids and connection of windfarm to grid is function of power system topology.Using FACTS devices inorder to transmit maximum windfarm generated power by keeping their stability under various system conditions is considered .In this paper UPFC in wind farms generated maximum transmission power is generated.

REFERENCES

[1]R.Takahashi,H.Kinoshiita,T.Murata,J.Tamura,M.Sugimasa,A.Komura,M.Futami,M.Ichinosse,and K.Ide," A co-operative control method for output power smoothing and hydrogen production by using variable speed wind generator," in *proceedings .EPE-PEMC,2008,page.2337-2342*

[2] F.Barbir,"PEM electrolysis for production of hydrogen from renew able energy sources," *solarEnerg*, volume. 78, no. 5, page. 661–669, May. 2005

[3] G.O.Cimuca, C.Saudemont ,B.Robyns, and M.M Radulescu, "Control and performance evaluation of a flywheel energy storage system associated to a variable speed wind generator," *IEEE Transaction. Industrial.Electronics.*, volume. 53, no. 4, pp. 1074–1085,June. 2006.

[4] R.Takahashi,J.Tamura,M.Futami,and K.Ide, "Wind farm stabilization by doubly-fed synchronous wind generator ," *in proceeding.PEDS*, 2005, page. 1572–1577.

5] S.M.Muyeen,J.Tamura and T.Murata, "Stability augmentation of a grid connected windfarm,london,Unitied Kingdom.: Springer-verlag,october 2008.

[[6] N.Tambey,M.L.Kothari, "Damping of power system oscillations with UPFC," *IEEE proc. Transaction.Distribution.* , volume. 150, Number., march 2003.

[7] C.T. Chang, Y .Y. Husu , "Design of UPFC controllers and supplementary damping controller for power transmission control and stability enhancement of a longitudinal power system," *IEEE proceeding, Generation., Distribution..*, volume. 149, NO. 4, July 2002.

[8]Z.J.Meng,P.L.So, "A current injection UPFC model for enhancing power system dynamic performance," *IEEE Transaction. on Power system* 2000.

[9] "Understanding,Concept and Technology of FACTS"-N.G.Hingorani,Gyugyi,IEEE Press 2000

[10] T. Zhou, B. Francois, M. el Hadi Lebbal, and S. Lecoeuche, "Real time emulation of a hydrogen-production process for assessment of an active wind-energy conversion system," *IEEE Transaction. Industrial Electron., volume 56*, no. 3, pp. 737–746, March. 2009.

CLASSIFICATION OF FACES USING COMPLEX-WT FACE AND EIGEN FACES

NIMMI RAMADAS V[1] & KUMARI ROSHNI V S[2]

AmalJyothiCollege of Engineering
ER&DCI

Abstract—In this work, a face recognition algorithm based on a combination of Dual tree complex wavelet transform (DTCWT) and Principal component analysis (PCA) is proposed. DTCWT is used to extract the facial features and PCA is used as a dimension reduction technique. Face classification is compared using five different distance measures. Experiments on ORL database shows that our proposed work works well on Cityblock distance measure.

Index Terms—*Dual Tree Complex Wavelet Transform, PCA, Distance measure, face recognition*

I. INTRODUCTION

Biometrics or biometric recognition is an automated recognition method that allows verification of true individual identity of a person based on their physiological or behavioral characteristics [1]. A physiological biometric would identify a person based on ones voice, DNA, fingerprint or behavior. Behavioral biometrics refers to the behavior of a person including gait, voice, etc. The purpose of such systems is to provide better control of access to physical facilities and to increase the efficiency of access to services and their utilization [2].

Face recognition is one of the personal identification methods that have the merits of both physiological as well as behavioral biometric methods. Although reliable methods of biometric personal identification systems exist,these methods rely on the cooperation of theparticipants whereas personal identification system such as face recognition does not require the consent of the test subject.

Face recognition is the process of capturing a face and matching it against a trained database. Facial recognition algorithms often identify faces by extracting features from a facial image. These features are then used to search in the database for images with matching features.

Several studies have been devoted to represent face image in low dimensional feature space by some subspace analysis technique for dimensionality reduction, eg., PrincipalComponent Analysis (PCA), Fisher Discriminant Analysis (FDA) [3]or to represent face image by multiple feature fusion [4]. One of the classical methods for dimension reduction is the PCA [5]. Although the method is simple to implement PCA requires the 2D face image matrix to be transformed to 1D image vectors. 2D PCA can extract facial features more efficiently and obtains a higher recognition rate
than PCA. Another kind of studiesaims to extract facial features robust against environmental variations. Some of them utilize wavelet analysis to detect facial geometrical structure eg. Discrete Wavelet Transform (DWT) [6], Gabor Wavelet Transform (GWT) [7]. However the lack of shift invariance and poor directional selectivity makes DWT difficult to extract geometrical features such as ridges and edges in facial images. GWT has much redundant information and burdens with heavy computational cost.

In this paper a novel face recognition algorithm is proposed. In face recognition techniques the first step is to extract the facial features. Features must be independent of the size, orientation and location of the pattern. Here complex- WT is used to extract facial features. This wavelet transform decomposes each face image into six band pass sub images that are strongly oriented at six different angles and two low pass sub images. Then we connect these eight sub images to form a feature vector and use PCA for dimension reduction purposes. Here distance measures are used as the classifiers.

The paper is organized as follows: Section II gives an introduction on Complex-WT face. Section III presents an introduction on eigenfaces. A brief on distance measures is given on section IV. The proposed method is explained in section V. the experimental results are presented on section VI followed by conclusion on VII

II. COMPLEX-WT FACE

A facial feature representation based on DTCWT is commonly referred to as Complex-WT face [8]. The dual tree complex wavelet transform (DTCWT) calculates the complex transform of a signal using two separate DWT decompositions. The structure of DTCWT [9] is shown in Figure 1.The DTCWT employs two real DWTs. Tree *a*corresponds to the real part of the wavelet transform and tree *b* corresponds to the imaginary part of the wavelet transform.The two real DWTs uses two different set of filters,witheach set satisfying the perfect

reconstruction conditions.Since the filter used in one are designed to be different from those in the other, it is possible for one DWT to produce the real coefficients and the other the imaginary coefficients

Let $h_0(n),h_1(n)$ denote low pass/high pass filter pair for the upper filter bank and $g_0(n),g_1(n)$ denote the low pass/high pass filter pair for the lower filter bank. Let the wavelet associated with each of the two real wavelet transforms be denoted as $\psi_h(t)$and $\psi_g(t)$. The filters are designed so that the complex wavelet

$$\psi(t) = \psi_h(t) + j\,\psi_g(t)$$

is approximately analytic. Also the filters are designed such that $\psi_g(t)$ is approximately the Hilbert transform of $\psi_h(t)$.

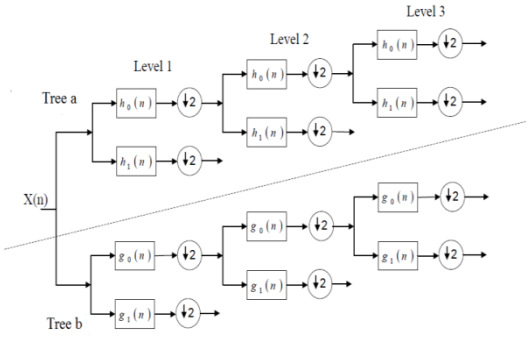

Fig 1.Structure of DTCWT [9]

The DTCWT does not appear to be complex. Since the outputs from the two trees can be interpreted as real and imaginary parts of complex coefficients the wavelet transform effectively becomes complex. At each level, the DTCWT decomposes an image into six bandpass subbands that are oriented at six different angles of $-75^0,-45^0,-15^0,15^0,45^0,75^0$ respectively as shown in the Figure.2

Fig 2 Two dimensional dual tree complex wavelets in spatial domain oriented at $-75^0,-45^0,-15^0,15^0,45^0,75^0$ respectively [10].

The advantages of DTCWT over DWT are its approximate shift invariance and good orientation selectivity i.e., the squared magnitude of a given complex wavelet coefficient provides an accurate measure of spectral energy at a particular location in space,scale and orientation. This means that the CWT based algorithms will be almost shift invariant, thus reducing many of the disadvantages of the critically sampled DWT.A shift invariant transform has the property that the signal path through any single subband of the transform and its inverse may be characterized by a unique z transfer function which is unaffected by the down and up sampling within the transform [10], [11].

III. EIGENFACE

The approach of using eigenfaces for recognition was developed by Sirovich and Kirby and used by Matthew Turk and Alex Pentland in face classification. A set of eigenfaces can be generated by performing a mathematical process called Principal Component Analysis (PCA) on a larger set of human faces.In PCA, uncorrelated principal components are extracted by linear transformation of the original variable so that the first few principal components contain most of the variations in the original dataset. The extracted uncorrelated components are called principal components (PC) and are estimated from the data covariance matrix. PCA can be done by eigenvalue decomposition of a data covariance matrix or singular value decomposition of a data matrix. PCA is the simplest of the true eigen vector based multivariate analyses[12].

Given an M dimensional human face with feature vector $X=[x_1, x_2, x_3, ..x_M]^T$ Let its mean be denoted by E[X]. The covariance matrix C is denoted by

$$C=E[(X-E[X])(X-E[X])^T] \quad (1)$$

Now we can calculate the eigen values $\lambda_1,\lambda_2,\lambda_3,\ldots\lambda_M$ and correspondingeigen vectors $v_1,v_2,v_3,\ldots v_M$ from the covariance matrix.

$$C\,v_i=\lambda_i v_i,\ i=1,2,..M \quad (2)$$

The eigenvalue measures the amount of variation explained by each principal component. The first principal component will be having a higher eigenvalue and the subsequent principal components will be having a smaller eigenvalue, The eigenvectors provides the weights to compute the uncorrelated principal component, which are the linear combination of the original variables

Dimension reduction by PCA can be achieved by letting those eigenvectors with large eigenvalues to represent the face vector. Since the eigenvectors associated with the first few eigenvalues look like face images PCA is also referred to as the use of eigenfaces. The objective of PCA is to reduce dimensionality by extracting the first few principal componentsthat contain the most variations in the dataset and to summarize the data with little loss of information [13].

Given the eigenfaces, every human face in the database can be represented as a vector of weights. The weights are obtained by projecting the image into eigenface components. When a new test image is given,the new image is also represented by its vector of weights. The identification of the test image is done by locating the image in the database whose weights are closest to that of the test image.

IV. DISTANCE MEASURES

Distance measure simply gives the distance between the test image and the training image in the database.The classification is done by setting a threshold based on the distance obtained. Let *X, Y* be the feature vectors of length *n* obtained by the face recognition algorithms. Let X represents the weight of test image and Y represents the weight of the training image. The five distance measures used in this paper are the following.

Euclidean distance:

$$d(X,Y) = \|X - Y\| = \sqrt{\sum_{i-1}^{n} (x_i - y_i)^2} \quad (3)$$

Squared norm:

$$d(X,Y) = \|X - Y\|^2 \quad (4)$$

Cosine Distance:

$$d(X,Y) = -cos(X,Y) = \frac{-\sum_{i-1}^{n} x_i y_i}{\sqrt{\sum_{i=1}^{n} x_i^2}\sqrt{\sum_{i=1}^{n} y_i^2}} \quad (5)$$

Manhattan Distance (City block distance):

$$d(X,Y) = \sum_{i=1}^{n} |x_i - y_i| \quad (6)$$

Correlation Distance:

$$d(X,Y) = \frac{n\sum_{i=1}^{n} x_i y_i - \sum_{i=1}^{n} x_i \sum_{i=1}^{n} y_i}{\sqrt{(n\sum_{i=1}^{n} x_i^2 - (\sum_{i=1}^{n} x_i)^2)(n\sum_{i=1}^{n} y_i^2 - (\sum_{i=1}^{n} y_i)^2)}} \quad (7)$$

V. PROCEDURE FOR THE PROPOSED WORK

The algorithm for the proposed work is givenby the following steps:

*Step1:*Extend the facial image with original size n_r x n_c to n_r x $n_c$ie, $([n_r/2^L]+1)*2^L$ x$([n_c/2^L]+1)*2^L$.

*Step2:*The 2D DTCWT is performed on the extended facial image

Step3: Compute the magnitude of its complex coefficients and normalize them as shown in figure (3(a)).

*Step4:*A clip method is used to reduce the effects of abrupt mutation as shown in figure (3(b)).

(a) (b)

Fig 3: (a) -Normalized subimages (b) - Clipped subimages

*Step5:*Each clipped subimage is reshaped into $([n_r/2^L]+1)([n_c/2^L]+1)$ x1 vector and all these vectors are joined to form a large vector of size$8([n_r/2^L]+1)([n_c/2^L]+1)$ x1.

*Step6:*The face vector is given to the eigenface approach which generates the set of eigenfaces.

*Step7:*The weights corresponding to each of the eigenface for a particular human face is then calculated.

Step8: Then distance measure is used for face classification.

FACE CLASSIFICATION

When a test image is given, the weights corresponding to the eigenfaces is calculated. Then the distance, d between the test image and the images in the database are then calculated.

Face classification is done by checking if the input image is below a certain threshold, T1 then the input image is said to be a known face. If the input face is above the certain threshold, T1 and below a second threshold, T2 the input image is said to be an unknown face. If the image is above the second threshold, T2 then the input image is said to be NOT a face. The flow chart for face classification is shown in figure 4

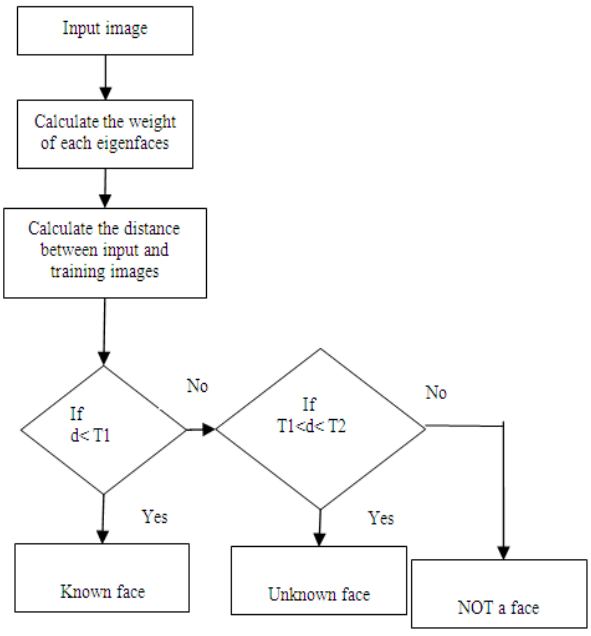

Fig 4: Flow Chart for Face Classification

VI. EXPERIMENTS

The face database from AT & T(Olivetti) Research laboratories Cambridge(ORL) were used for the experiments.

Fig 5: Sample images in ORL database

The ORL database contains ten different images of 40 individuals. The database contains a set o face images taken between April 1992 and April 1994 at the lab. The images of some subjects were taken at different times, varying light, with different facial expressions such as open/closed eyes, smiling/not smiling and facial details such as glasses/no glasses. The images were taken with the subject in an upright frontal position against a dark background. The size of each image is 92*112 pixels. A sample of ORL database [14] is shown in figure 5.

EXPERIMENTAL RESULTS

The experimental results were done by resizing the input facial images to a critical size. Some of natural images were also taken for face classification along with the face database. Here level 4 decomposition is used. The work has also presented a brief study on the variations on the recognition rates when the level of decomposition changes. Figures 6(a) and 6(b) shows the variations of recognition rates with respect to percentage of eigenfaces in case of PCA and this work respectively.

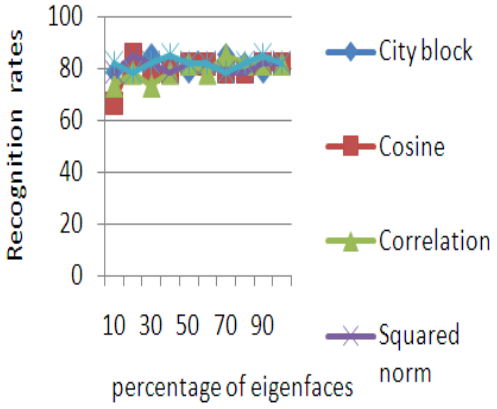

(a)

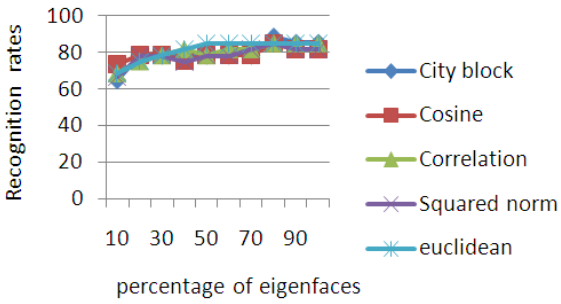

(b)

Fig 6: (a)-PCA approach
(b)-this work

Figure 7(a) and 7(b) shows the variations of recognition rates as the levels of decomposition changes in the case of
DT-CWT and this work respectively.

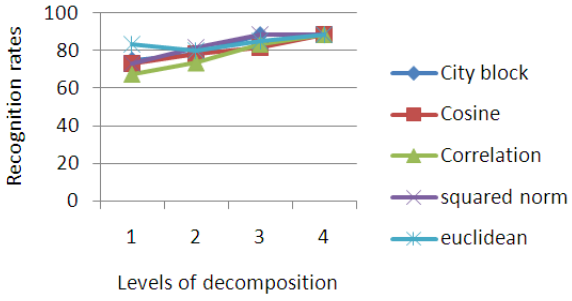

(a)

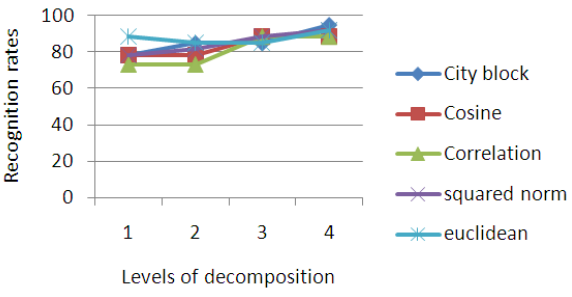

(b)

Fig 7: (a)-DT-CWT approach
(b)-this work

VII. CONCLUSION

In this work, a new scheme of combining complex-WT face and eigenfaces approaches is presented. Owing to the properties of DT-CWT such as good directional selectivity and shift invariance, the complex –WT face approach will provide us with facial features robust to variations of illumination and facial expression. The proposed method suggests that 80% of eigenfaces gives the best result. It has been also studied that level 4 decomposition performs the best among all the distance measures. The City block distance measure has been obtained as the best distance measure method for this work. Neural networks can be incorporated to obtain a higher recognition rate

REFERENCES

[1] A. K. Jain, A. Ross, and S. Prabhakar,"An introduction to biometric recognition," *IEEE Trans.Circuits Syst.Video Technol*., vol. 14,no. 1,pp. 4-20, 2004

[2] Shang-Hung Lin ,"An introduction to face recognition technology,"

[3] P. L. Belhumeur, J. P. Hespanha, and D. J. Kriegman, "Eigenfaces versus fisherfaces: Recognition using class specific linear projection," *IEEE Trans. Pattern Anal. Mach. Intel.,* vol. 19,no. 7,pp. 711-720,Jul. 1997

[4] Y. Fu, L. L. Cao, G. D. Guo, and T. S. Huang,"Multiple feature fusion by subspace learning," in *Proc. ACM Int. Conf. Image and Video Retrieval*, 2008, pp. 127-134.

[5] M. Turk, A. P.Pentland,"Face recognition using eigenfaces,"in *IEEE Conference on Computer Vision and Pattern Recognition*, 1991, pp. 586-591

[6] H. K. Ekenel and B. Sankur,"Multiresolution face recognition," *Image Vis. Comput*., vol. 23,pp. 469-477,2005

[7] C. J. Liu and H. Wechsler,"Gabor feature based classification using the enhanced fisher linear discriminant model for face recognition," *IEEE Trans. Image Process*., vol. 11,no. 4,pp. 467-476,Apr. 2002

[8] C. C.Liu and D. Q. Dai,"Face recognition using dual-tree complex wavelet features," *IEEE Trans. Image Process*., vol. 18,no. 11,Nov.2009

[9] G. Serbes, and N. Aydin," Denoising Embolic Doppler Ultrasound Signals using Dual tree complex discrete wavelet transform," 32nd Annual international conference of the IEEE EMBS Buenos Aires, Argentina.2010

[10] W. Selesnick, R. G. Baraniuk, and N, G.Kingsburg,"The dual-tree complex wavelet transform-a coherent framework for multiscale signal and image processing," *IEEE Signal Process. Mag*., vol. 22, no. 6,pp. 123-151,Nov. 2005

[11] K Jaya Priya, R S Rajesh, "Dual Tree Complex Wavelet Transform based Face Recognition with Single View," The International Conference on Computing, Communications and Information Technology, vol.5, 2010.

[12] M. Turk and A. Pentland,"Eigenfaces for recognition," *Journal of Cognitive Neuroscience*. vol.3. no.1

[13] F. Song, Z. Guo and D. Mei," Feature selection using principal component analysis," International Conference on System Science, Engineering Design and Manufacturing Informatization,2010

[14] http://www.cl.cam.ac.uk/research/dtg/attarchive/facedatabase.html

OPTIMIZATION OF LINK-BASED NON-TREE CLOCK NETWORK USING AN EFFICIENT ALGORITHM

ASWATHY VIJAYAN[1] & A.SRIDEVI[2]

[1,2]SNS College of Technology, Coimbatore

Abstract Clock network is a vulnerable victim of variations as well as a main power consumer in many integrated circuits. Clock skew is becoming increasingly difficult to control due to variations. Recently, link-based non-tree clock network[1] attracts people's attention due to its appealing tradeoff between variation tolerance and power overhead. Link based non-tree clock distribution is a cost-effective technique for reducing clock skew variations. Existing non-tree clock routing methods[1] have a few drawbacks. The length of the link is long, link distribution is uneven and is also very complex to design. In this paper, a new MST based algorithm is proposed to overcome these drawbacks. The effects of the link insertion on clock skew variability are analyzed. The algorithm is implemented in VHDL language using Altera Quartus II and its effectiveness is validated using SPICE based simulation. Experimental results show that the new algorithm is able to achieve same or better skew reduction with an average of 5% wire length increase when compared to 15% wire length increase of the existing algorithms.

Keywords — Clock network, clock skew, variations, link, non-tree clock distribution

I. INTRODUCTION

In synchronous VLSI designs, the quality of clock network is vitally important, since almost every data transfer are coordinated by clock signal. The clock network suffers from two simultaneous challenges: variability and power. Clock skew, which is the difference between clock signal delays, is very sensitive to variations. Clock network is also a large power consumer because of its large fan out size and high switching frequency. To address these problems, several solutions like variation aware clock tree routing, buffer/wire sizing, non-tree clock distribution have been proposed. The most effective among these methods is non-tree clock routing because of the existence of multiple paths from clock source to the sinks, which makes the delay in the sinks correlated, resulting in reduced skew variation.

There are several types of non-tree clock distribution network methodologies that have been proposed. These non-tree networks are classified mainly as 1-dimensional and 2-dimensional structures. In a 1-dimensional approach, several clock sinks are attached to single piece of connection. This connection will be driven at multiple points from a binary tree and so skew between any two sinks attached to
this interconnect will be small. An example of 1-dimensional non-tree clock network[8,9] is given in Fig.1(a). A key limitation of the 1-dimensional structure is that it does not handle the skew variation between different 1-dimensional regions.

The 2-dimensional non-tree structure[10-12] is also called mesh. Depending upon the location of mesh, from clock source to sink, the mesh structure can be further classified as leaf level, top level and multi level mesh. In leaf level (Fig. 1(b)), the mesh is close to clock sinks. In top level (Fig. 1(c)), the mesh is close to clock source and in multi level (Fig. 1(d)), several meshes are at different levels. In the leaf level mesh approach, a metal wire mesh is overlaid on the entire chip area and driven at multiple points directly from the clock source or through a routing tree. Each clock sink is connected to the nearest point on the mesh. This technique is very effective in suppressing skew variations in microprocessor designs. A leaf-level mesh[10,11] normally consumes enormous wire resources and also consumes larger power. It is also hard to integrate with clock gating, which is a common low-power technique. Therefore, its application is restricted to high-end products such as microprocessors. In contrast, a top-level mesh[12] may consume less wire and power. In the top-level mesh approach, the clock source drives a coarse mesh directly and clock sub-trees are attached to the mesh. The mesh structure is having negligible skew variations, but skew variations within each sub-tree still exist. Most recently, a multilevel mesh[13] approach is also proposed. But this mesh structure is also having larger wire/power overhead.

Recently, a link-based non-tree algorithm has been proposed in which cross links are added in an existing clock tree. By suitably choosing the correct locations of the links, significant reduction in skew variability can be achieved with very small increase in wire length when compared to the original clock tree. A link-based non-tree is shown in Fig. 2. The vital aspect of the link-based methodology is to

determine the proper location of the cross links, for which some algorithms were proposed. While these algorithms are highly effective, they suffer from several drawbacks. Some of these are: high complexity, lengthy links that might cause routing problems and uneven distribution of links across all regions of the clock tree that might limit skew variability reduction.

In this paper, MST based routing algorithm is used to insert cross links between two nodes in an existing clock tree. This algorithm can overcome the drawbacks of existing algorithm. The algorithm is implemented in VHDL language using Altera Quartus II and its effectiveness is vaidated using SPICE based simulation. Experimental results show that the new algorithm is able to achieve same or better skew reduction with an average of 5% wire length increase

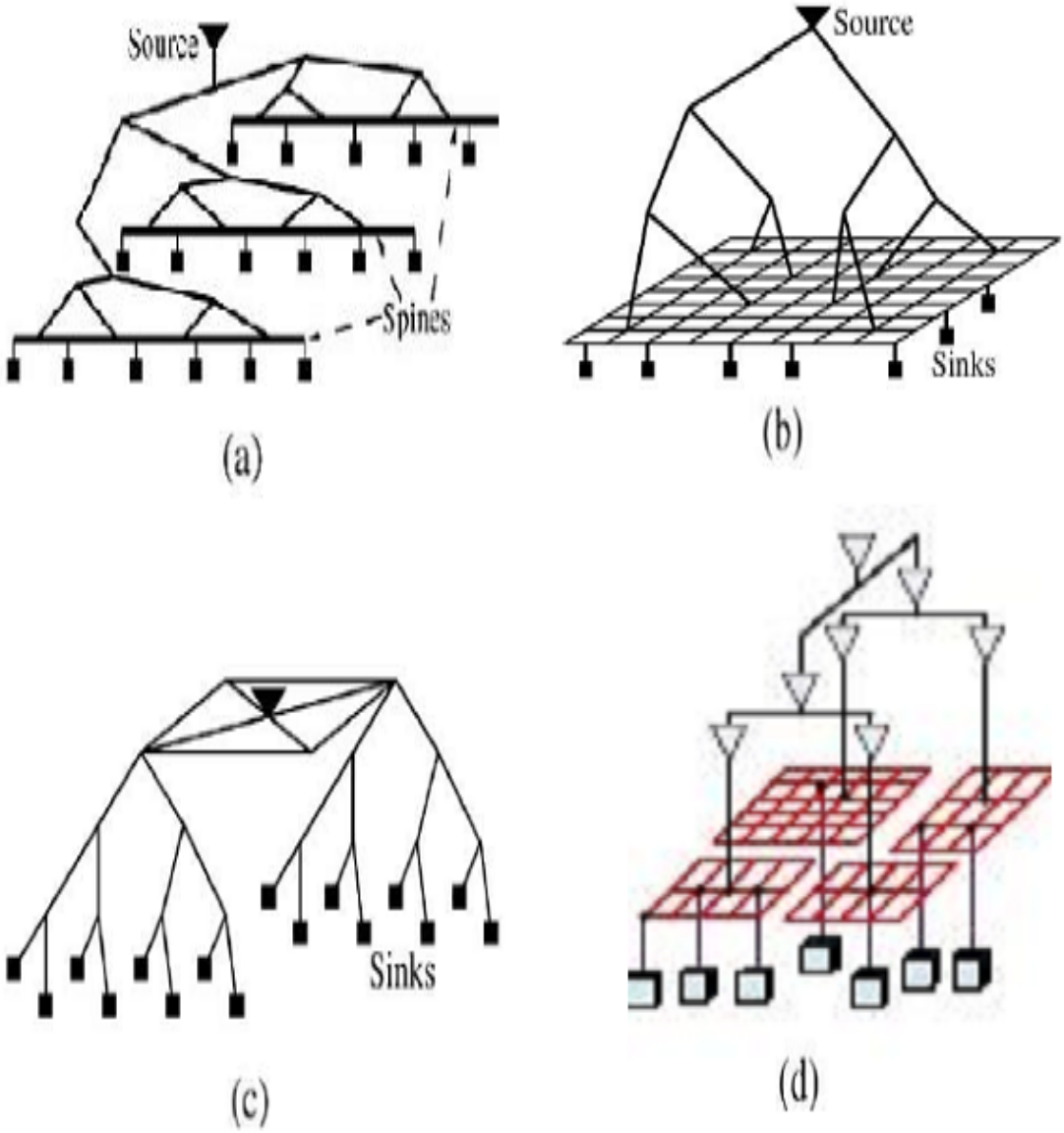

Fig.1. Non-Tree Clock Distribution Network: (a) 1-Dimensional; (b)Leaf Level Mesh; (c)Top Level Mesh; (d)Multi Level Mesh.

when compared to 15% wire length increase of the existing algorithms

II. EFFECT OF LINK INSERSION

In this section, we will review a link-based non-tree clock distribution network. Delay and skew variation of a non-tree *RC* network will be analyzed. An Elmore delay model is employed because of its high fidelity[14] and ease of computation.

A. Delay in RC Network

A non-tree *RC* network can be represented by a graph *G*=(*V,E*). The graph *G* consists of a node set *V* composed of a source node, several sinks and internal nodes. In an *RC* network, the Elmore delay at node *i* is given by

$$t_i = \sum_j R_{i,j} C_j \qquad (1)$$

where C_j is the ground capacitance at a node *j* in *V* . The transfer resistance $R_{i,j}$, is equal to the voltage at node *i* when 1A current is injected into node *j* and all other node capacitors are zero. The *RC* network can be decomposed to a spanning tree *T,* where *T*= (*V,*E_T), having a set of link edges *El* such that *E* = E_T E_l. As an alternative approach which is easier for analysis, the delay from the source node to each node can be evaluated by starting with delays in the tree *T* and then incrementally inserting every link edge in E_l.

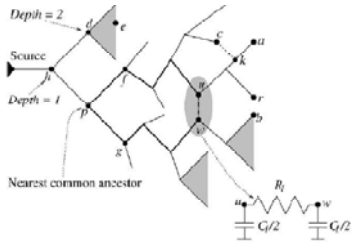

Fig.2. Crosslink Insertion

In Fig. 2, a network is indicated by the solid lines and a crosslink is inserted between node *u* and *w*. If the link has a wire resistance of R_l and wire capacitance of C_l, the link insertion can be decomposed by inserting a resistor of R_l between *u* and *w* and adding a capacitor $C_l/2$ of at node *u* and *w*. Adding link capacitors will not change the network topology and so, its effect can be estimated easily. If the Elmore delay before the link insertion, from the source to any sink *i* is t_i; then the delay $\widetilde{t_i}$ after only adding the link capacitors is given by

$$\widetilde{t_i} = t_i + \frac{C_l}{2}\left(R_{i,u} + R_{i,w}\right) \qquad (2)$$

The impact of the link resistance *Rl* can be analyzed by using the technique by Chan and Karplus. The delay at node *i* is changed from $\widetilde{t_i}$ to $\widehat{t_i}$ given by

$$\widehat{t_i} = \widetilde{t_i} - \frac{\widetilde{t_u} - \widetilde{t_w}}{R_l + r_u - r_w} r_i \qquad (3)$$

where r_i, r_u and r_w are equal to the Elmore delay at *i*, *u*, and *w*, respectively, when C_u= 1, C_w = −1 and the other node capacitances are zero.

B. Skew Variability Between Link Endpoints

If a link is inserted between nodes *u* and *w*, then according to, the skew between *u* and *w* after link insertion is given by:

$$\widehat{q_{u,w}} = \frac{R_l}{R_l + r_u + r_w}\left(q_{u,w} + \frac{Cl}{2}(R_{u,u} - R_{w,w})\right) \quad (4)$$

where, $q_{u,w} = t_u - t_w$ is the original skew between nodes *u* and *w*, $\widehat{q_{u,w}}$ is the final skew after the link insertion, C_l is the link capacitance, R_l the link resistance, $R_{u,u}$ and $R_{w,w}$ the transfer resistances of nodes *u* and *w*. Since the effect of capacitance can be easily estimated and removed , equation (4) gets reduced to:

$$\widehat{q_{u,w}} = \frac{R_l}{R_l + r_u + r_w} q_{u,w} \qquad (5)$$

Thus, from equation (5), we can see that the final skew is a scaled value of the original skew with the scaling factor of $\frac{R_l}{R_l + r_u + r_w}$. The scaling factor is always less than 1, therefore, the skew between nodes *u* and *w* is always reduced as a result of link insertion. It has also been proved that inserting a link as close to sink nodes as possible is better in terms of skew variability reduction. For example, in Fig.2, when we want to reduce the skew between nodes *r* and *b*, then it is better for the link to be closer to the nodes *r* and *b* as possible.

III. ALGORITHM OVERVIEW

A. Link Insertion Algorithm Overview

Our objective is to design a clock routing algorithm that can achieve a low skew variability and low wire consumption. The approach taken towards building a non-tree clock distribution network is an incremental approach. The different steps in the approach are explained below:

1. From any of the available clock tree routing algorithms, obtain the initial clock tree.

2. From the given the clock tree, select node pairs where cross links has to be inserted, in such a way that the insertion of cross links should minimize the skew variability.
3. The addition of link capacitance might change the original skew of the clock tree, so we need to tune the nodes of the clock tree in such a way that the original skew is not altered. The effect of link capacitance must be considered only on the link end points and the nodes are tuned in a bottom-up fashion so as to obtain the original skew after the addition of link capacitance.
4. Finally, the links are inserted to the selected node pairs. The effect of link capacitance has been removed already by bottom-up tuning; so only the effect of link resistances will be present, which will reduce the skew variability.

In the above procedure, step 2 is the main step and has a tremendous influence on the quality of the final non tree since selecting the wrong node pairs might result in worse skew variability.

B. Selecting node pairs for link insertion

The requirements of a good node pair selection algorithm are:

1. The algorithm must support an efficient distribution of the links across the clock network. Failure of the algorithm ,might lead to high skew for the sinks in the region where links are not added.
2. It must have a very low complexity in terms of the number of links added. The increase in runtime with increase in the number of links must be less.
3. The algorithm must avoid lengthy links and so the total wire length is reduced.
4. Asymmetric clock tree networks should also be handled by this algorithm

Two algorithms have been proposed earlier for node pair selection. They are "Rule based" link pair selection algorithm and "min-matching based" node pair selection algorithm. Though both algorithms are able to reduce the skew variability significantly when compared to the original clock tree with little wire consumption, they do not satisfy some of the above mentioned requirements.

In this paper, a "MST based algorithm with Rule Based Deletion" is proposed, in which the drawbacks of the existing algorithms are addressed.

c. Rule Based Selection Scheme

The rule based approach is derived directly from the equation (4). In this method, two main rules are defined for node pair selection called α, β and γ rules, which are given below:

α rule: The α value of any link is defined as $\alpha = \frac{R_l}{R_{loop}} \leq \alpha_{max}$, where is the total resistance $R_{loop} = R_l + r_u - r_w$ along the loop of $p \rightarrow u \rightarrow w \rightarrow p$. The lower the value of α, the lower the scaling of the original skew and the better the link for skew reduction.

β rule: The β value of any line is defined as $\beta = \left|(\frac{C_l}{2}(R_{u,u} - R_{w,w}))\right| \leq \beta_{max}$. The β value determines the extra skew introduced into the original clock tree due to the link capacitance. If the value of β is lower, then the tuning required in the original tree is lesser.

γ rule: The γ rule is intended to make sure that the links added does not worsen the skew variation between any two pairs in the clock network significantly. The Nearest Common Ancestor (NCA) node for a sink pair has certain depth in the original tree. We call this depth as the level of the node pair and denote it using γ of the link pair.

In this method, the α, β, γ values of any link is less than the maximum value set by the user will be added to the tree. The lesser the value of α, β and γ, the better the effectiveness of the link in skew variation reduction. But choosing too low values for these variables will result in very less number of links, thereby reducing the effectiveness of link insertion.

D. Minimum Weight Matching Based Selection

The min-matching based link insertion algorithm uses the bipartite min-matching algorithm for selecting the node pairs for link insertion. In this method, the clock network is divided into several regions, in such a way that links are added to every region. The clock network is first divided into two subtrees - the left subtree and the right subtree. Each subtree is again divided into *n* number of sub-subtrees. The clock network is represented by a bipartite graph with the two main subtrees as the two sides and the sub-subtrees on either side as the nodes of the bipartite graph with total of *2n* nodes. The edge weight between any two nodes in the bipartite graph is fixed as the minimum rectilinear distance between any two pairs of sinks of those sub-subtrees.

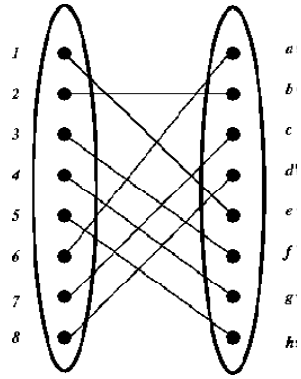

Fig 3: A bipartite graph model for selecting node pairs between two subtrees using min--matching based link insertion algorithm

For example, in Fig3, The shortest rectilinear distance between any two pairs of sinks of the sub-subtrees 2 and *b* is the edge weight between nodes 2 and *b*. This bipartite graph will have *n* links with minimum total wire length. This gives an idea that every sub-subtree in the clock network is linked to another by a cross link. This idea is illustrated in Figure 3.

E. MST Based Link Insertion Algorithm with Rule Based Deletion

The rule based approach [1] is derived directly from the equation (4). In this method, two main rules are defined for node pair selection called α and β rules, which are given below:

α rule: The α value of any link is defined as $\alpha = \frac{R_l}{R_{loop}} \leq \alpha_{max}$, where is the total resistance $R_{loop} = R_l + r_u - r_w$ along the loop of $p \rightarrow u \rightarrow w \rightarrow p$. The lower the value of α, the lower the scaling of the original skew and the better the link for skew reduction.

β **rule**: The β value of any line is defined as $\beta = \left|(\frac{C_l}{2}(R_{u,u} - R_{w,w}))\right| \leq \beta_{max}$. The β value determines the extra skew introduced into the original clock tree due to the link capacitance. If the value of β is lower, then the tuning required in the original tree is lesser.

One of the key demerits of the existing algorithm like min matching algorithm [1] is that the addition of lengthy links. One way to avoid the addition of lengthy links is to allow a given node to be connected to more than one node on the opposite side of the bipartite graph. More than one link should not be allowed between any given pair of nodes to avoid crowding of links. These two conditions has to be satisfied, then the selected links will not be too lengthy and all the sub-subtrees will be linked. This is illustrated in Fig.3. in which there are no extremely lengthy links.

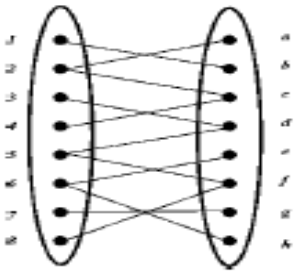

Fig.3. The Bipartite Graph for MST based Algorithm

In order to satisfy both these conditions, a MST is constructed in the complete bipartite graph. The edge weight between any two nodes in the bipartite graph is given as the minimum rectilinear distance between any two pairs of sinks of those two sub-subtrees in the clock network. By constructing a MST in the complete bipartite graph, few nodes in the graph will have multiple links. Crowding of links between any two nodes can also be avoided. One problem which is possible in constructing a complete MST is that the total wire length might become very high. To avoid this problem, we remove links from the selected MST edges based on α and β rules used in the rule based node pair selection algorithms.

The MST based algorithm with Rule based deletion includes the following steps:

1. Decompose the clock tree network into left and right sub treesT_l, T_r.
2. For every pair $(T_{l,i}, T_{r,j})$, find out the weight. Weight= minimum rectilinear distance between leaf pairs.
3. Selectively remove those edges that have α and β values higher than the set limits of α_{max} and β_{max}
4. Select the node pairs between which the link has to be inserted.

F. Merits

The advantages of MST based algorithm for the selection of link pairs are:

- In MST based method, the clock network is divided into sub-trees, so it gives a good and even distribution of links across all the regions of the clock network.
- The overall complexity of the algorithm is *O*(*nlogn*), in terms of number of nodes and in terms of the number of links to be inserted. This is much better than the *O*(*n*3) complexity of the min-matching algorithm.
- In MST algorithm multiple links are allowed to be connected to a given node in the bipartite graph, therefore the chances of adding a lengthy link is greatly reduced when compared to the min-matching algorithm.

- The MST based algorithm will work well in an unbalanced clock tree than the min-matching based algorithm. This is because, when the two sides of the bipartite graph have unequal number of nodes, then some nodes will not be linked while using the min-matching algorithm. But in MST algorithm, all the nodes are connected to at least one node on the opposite side of the bipartite graph.
- Because of the use of rule based deletion, all the physical characteristics of the links are taken into account before the addition of the link. This means that bad links are not get added to the clock network. We can also effectively control the total wire length consumption by carefully selecting the values of α_{max} and β_{max}values for rule based deletion.

Thus, the MST based algorithm with rule based deletion has all the required features of a good algorithm.

IV. EXPERIMENTAL RESULTS

The algorithm is implemented in VHDL language using Altera Quartus II and the effectiveness of the algorithm is
validated using SPICE based simulation. The tree network can be either considered as an array or as a matrix. Each elements of the matrix can be considered as nodes of the tree network. The resistance and capacitance values (R_l, C_l) of the link are given as inputs. All the delay values are also given.

The VHDL file can be made from Altera Quartus II and in which the minimum rectilinear distance between each and every node is calculated. The minimum rectilinear distance represents the edge weight. The weights that are within the range of α and β are considered and others are discarded. The cross links has to be inserted between those selected nodes.

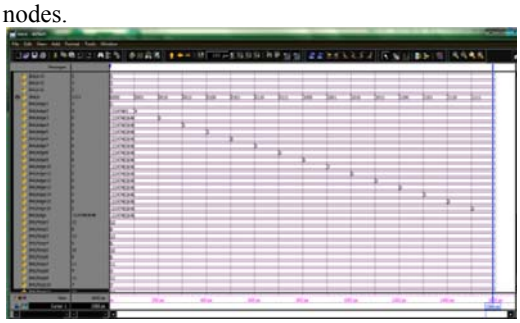

Fig. 4. . Output Waveform for the Selection of Nodes Pairs

The algorithm implemented in Altera Quartus II is simulated in Modelsim. Fig. 4 shows the output waveform for the selection of node pairs. Here comparison of each edge weight values is shown. The positive edge values are taken, that is the cross links can be inserted between those node pairs that gives a positive weight. The RTL schematic for the algorithm is shown in Fig.5.

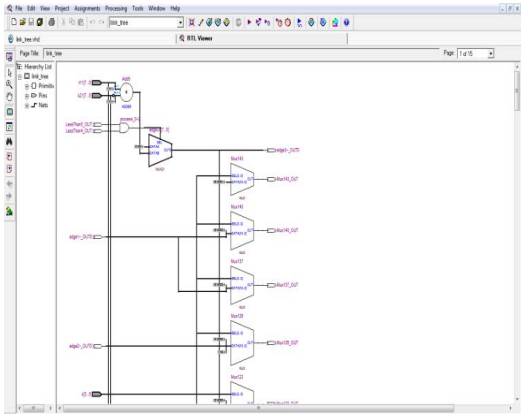

Fig. 5. RTL Schematic for the algorithm

After finding the nodes, the cross links are inserted. The cross links are a resistor with two capacitors. The clock tree network is simulated in SPICE. The experimental results shows that the clock tree network with link insertion is having lesser delay and wire length when compared with the clock network without link.

The Table I below shows, the effect of link insertion on standard deviation, wire length, skew variation and CPU usage for different link insertion techniques like Mesh-S(Sparse leaf mesh), Mesh-D(Dense leaf mesh), Link-R(Rule Delta), Link-M(Min Matching), Link-MST(MST based algorithm).

TABLE I
STANDARD DEVIATION,WIRE LENGTH, SKEW VARIATION AND CPU USAGE FOR DIFFERENT LINK INSERTION TECHNIQUE

Method	Standard Deviation	Wire length	Skew variation	CPU(s)
Mesh-S	0.03	77%	0.92	0.045
Mesh-D	0.02	142%	0.72	0.045
Link-R	0.50	15%	0.08	0.069
Link-M	0.46	10%	0.09	0.007
Link-MST	0.20	5%	0.068	0.047

V. CONCLUSION

An efficient MST based link insertion algorithm is used for inserting cross links in a clock tree network. It can overcome the drawbacks of the existing algorithm of lengthy links. The effectiveness of the entire algorithm is validated using VHDL in Quartus ll. The new algorithm is able to achieve comparable or better skew variability reduction with significantly lower wire length and power. The results shows that the links added by the proposed algorithm

are shorter on average and thereby making the non tree routable.

REFERENCES

[1] Rajaram, J. Hu, and R. Mahapatra. "Reducing clock skew variability via cross links," in *Proceedings of the ACM/IEEE DAC*, San Diego, CA, June 2004, pages 18–23.

[2] S. R. Nassif, "Modeling and analysis of manufacturing variations," in *Proceedings of the IEEE CICC*, San Diego, CA, May 2001, pp. 223–228.

[3] R. Saleh, S. Z. Hussain, S. Rochel, and D. Overhauser, "Clock skew verification in the presence of IR-drop in the power distribution network," in *IEEE Transactions on CAD*, vol.19, no.6, pp.635–644, June 2000.

[4] W.-C. D. Lam, C.-K. Koh, and C.-W. A. Tsao, "Power supply noise suppression via clock skew scheduling," in *Proceedings of the IEEE ISQED*, San Jose, CA, March 2002, pp. 355–360.

[5] B. Lu, J. Hu, G. Ellis, H. Su, "Process variation aware clock tree routing," in *Proceedings of the ISPD*, Monterey, CA, April 2003, pp. 174–181.

[6] J. Chung and C.K. Cheng, "Optimal Buffered Clock Tree Synthesis," in *IEEE ASIC conference*, Austin, TX, Sept. 1994, pp. 130–133.

[7] S. Pullela, N. Menezes, and L. T. Pillage, "Reliable non-zero skew clock trees using wire width optimization," in *Proceedings of the ACM/IEEE DAC*, Dallas, TX, June 1993, pp. 165–170.

[8] S. Lin and C. K. Wong, "Process-variation-tolerant clock skew minimization," in *Proceedings of the IEEE/ACM ICCAD*, San Jose, CA, November 1994, pp. 284–288.

[9] N. A. Kurd, J. S. Barkatullah, R. O. Dizon, T. D. Fletcher, and P. D. Madland, "A multigigahertz clocking scheme for the Pentium 4 microprocessor," in *IEEE Journal of SSC*, vol.36, no.11, pp. 1647–1653, November 2001.

[10] M. P. Desai, R. Cvijetic, and J. Jensen, "Sizing of clock distribution networks for high performance CPU chips," in *Proceedings of the ACM/IEEE DAC*, Las Vegas, NV, June 1996, pp. 389–394.

[11] P. J. Restle, T. G. McNamara, D. A. Webber, P. J. Camporese, K. F. Eng, K. A. Jenkins, D. H. Allen, M. J. Rohn, M. P. Quaranta, D. W. Boerstler, C. J. Alpert, C. A. Carter, R. N. Bailey, J. G. Petrovick, B. L. Krauter, and B. D. McCredie, "A clock distribution network for microprocessors," *IEEE Journal of SSC*, vol.36, no.5, pp. 792–799, May 2001.

[12] H. Su and S. S. Sapatnekar, "Hybrid structured clock network construction," in *Proceedings of the IEEE/ACM ICCAD*, San Jose, CA, November 2001, pp. 333–336.

[13] M. Mori, H. Chen, B. Yao and C.-K. Cheng, "A multilevel network approach for clock skew minimization with process variations," in *Proceeding of the Conference on ASP-DAC*, Yokohama, Japan, January 2004, pp. 263268.

[14] K. D. Boese, A. B. Kahng, B. A. McCoy, and G. Robins, "Near-optimal critical sink routing tree constructions," in *IEEE Transactions on CAD*, vol.14, no.12, pp. 1417–1436, December 1995.

[15] P. K. Chan and K. Karplus, "Computing signal delay in general RC networks by tree/link partitioning," in *IEEE Transactions on CAD*, vol.9, no.8, pp. 898–902, August 1990.

[16] T. Xue and E. S. Kuh. "Post routing performance optimization via multi-link insertion and non-uniform wiresizing," in *Proceedings of the IEEE/ACM ICCAD*, San Jose, CA,November 1995, pp. 575–580.

[17] C.-W. A. Tsao and C.-K. Koh, "UST/DME: a clock tree router for general skew constraints," in *Proceedings of the IEEE/ACM ICCAD*, San Jose, CA, November 2000, pp. 400–405.

[18] T.-H. Chao, Y.-C. Hsu, J.-M. Ho, K. D. Boese, and A. B. Kahng. "Zero skew clock routing with minimum wirelength," in *IEEE Transactions on CS-ADSP*, vol.39, no.11, pp.799–814, November 1992.

[19] R.-S. Tsay, "Exact zero skew," in *Proceedings of the IEEE/ACM ICCAD*, Santa Clara, CA, November 1991, pp.M 336–339.

[20] J. Cong, A. B. Kahng, C.-K. Koh, and C.-W. A. Tsao. "Bounded-skew clock and Steiner routing," in *ACM Transactions on DAES*, 3(3):341–388, July 1998.

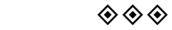

DESIGN OF CARRY SELECT ADDER WITH AREA AND POWER EFFICIENCY

ANJU S1[1] & P.GOWTHAM[2]

[1]PG Scholar, Department of ECE, SNS College of Tech, Coimbatore
[2]Assistant Professor, Department of ECE, SNS College of Tech, Coimbatore

Abstract-Adder is one of the most common used digital component in the design of digital integrated circuit. Carry select adder provide a good compromise between cost and performance in carry propagation adder design. From the structure of carry select adder there is still a scope of reducing the area and power consumption with slight increase in delay. In this paper the modification at gate level is introduced. The modified architecture is applied for 16-, 32-, 64-bit and compare the delay, power and area with the regular carry select adder.

Keywords-*Regular carry select adder, Modified carry select adder, ripple carry select adder, BEC*

I. INTRODUCTION

Addition is the fundamental and most often used arithmetic operation in Microprocessors Digital Signal Processors and digital processing application specific integrated circuits. Therefore Binary Adders are the building block in VLSI circuits. In Ripple Carry Adder (RCA), it takes longer time to propagate the carry from one stage to the next stage. So this adder will introduce the overall delay in the circuit. To avoid this problem carry save adder came into the role and had sort out this delay problem up to some extent. The carry look ahead adder [1] computes group generate signals as well as group propagate signal to avoid waiting for the ripple. In rapidly growing mobile industries, the faster units are not the only concern but also smaller area and less power become major concerns for design of digital circuits [2]. The speed of addition in digital adders is determined by time required to propagate the carry through the adder. In the case of elementary adder for each bit position the sum is generated sequentially only after the previous bit position has been summed and a carry propagated into the next position [3]. Among various adders, the CSA is intermediate regarding speed and area [4]-[7].In this paper we proposed Modified Carry Select Adder (MCSA) architecture to reduce area and power with minimum speed penalty. The basic idea of this work is to achieve area and power reduction [8]-[11]. The Modified Carry Select Adder is designed by using single Ripple Carry Adder (RCA) and Binary to excess one converter (BEC) instead of using dual converter. The remaining paper is organized as follows. Section II deals with area and delay analysis of basic adder block. Section III describes the Regular carry select adder and section IV describes the delay and area evaluation of it. Section V, VI, VII presents the Modified carry select adder, binary to excess one converter and delay and area evaluation methodology respectively. Section VIII Include the comparison result and Section IX give the simulation result.

II. CALCULATIONOF AREA AND DELAY OF BASIC

ADDER BLOCK

The basic block of carry select adder consists of elements like XOR gate, Full Adder, Half Adder and Multiplexer. The delay and area evaluation methodology considers the entire gate to be made up of AND, OR, INVERTER each having delay equal to 1 unit and area equal to 1 unit. The XOR gate, Multiplexer, Half Adder has the same delay of 3 unit. The Full Adder has delay of 6 unit. The full adder, half adder, XOR gate and multiplexer requires area of 13, 6, 5 and 4 respectively.

III. REGULARCARRY SELECT ADDER

The structure of Regular Carry Select Adder is partitioned into a number of groups. Each group consists of two copies of Ripple Carry Adder. One copy Evaluate the sum and carry for Cin=0 and other copy evaluate the sum and carry for Cin=1.The sums and carry corresponds to Cin=0 and Cin=1 is fed to multiplexer. Depending on the carry out of the previous group the corresponding sum and carry is selected.

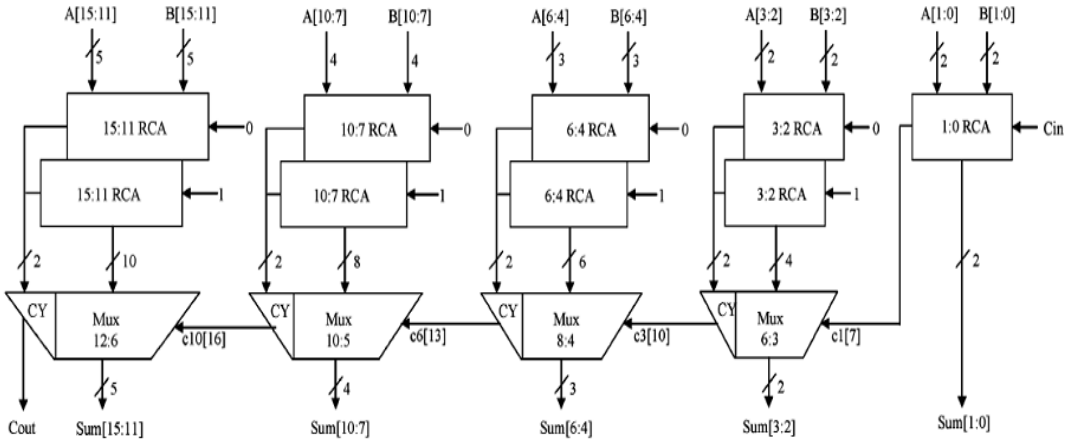

Fig.1. Regular Carry Select Adder

IV. DELAY AND AREA EVALUATION OF REGULAR CARRY SELECT ADDER

The structure of 16-bit Regular Carry Select Adder have five groups of different size Ripple Carry Adder(RCA).The group1 is a ripple carry adder with carry input(Cin).The steps leading to the area and delay evaluation is as follows: 1) The group2 has two sets of 2-bit RCA. Based on the consideration of delay value of the basic building blocks of adder, the arrival time of C1[time(t)=7] of 6:3 Mux is earlier than S3[t=8] and later than S2[t=6].Thus Sum3[t=11] is the summation of S3 and mux[t=3] and sum2[t=10] is the summation of C1 and Mux.

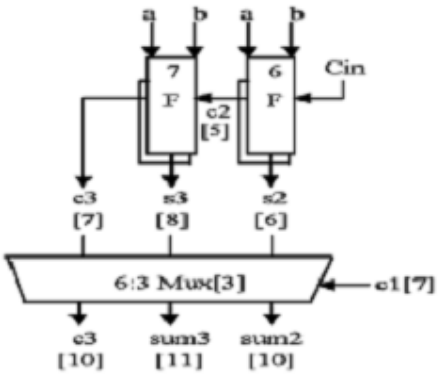

Fig. 2. Group 2

2) For group 3 to 5, the arrival time of mux selection input is always greater than the arrival time of the data outputs from the RCA's. Therefore from group3 to group5 the delay can be determined respectively as follows:

{c6,sum[6:4]}=c3[t=10]+ mux

{c10,sum[10:7]}=c6[t=13]+ mux

{cout,sum[15:11]}=c10[t=16]+ mux

3) The delay and area count of different groups is listed in Table I.

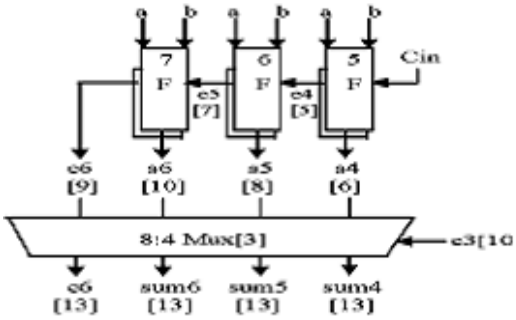

Fig. 3. Group 3

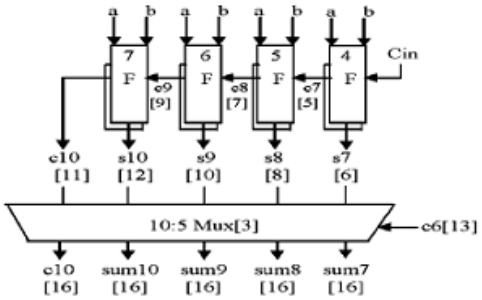

Fig. 4. Group 4

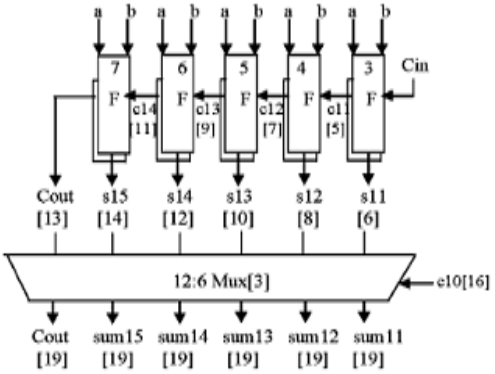

Fig. 5. Group 5

V. MODIFIED CARRY SELECT ADDER

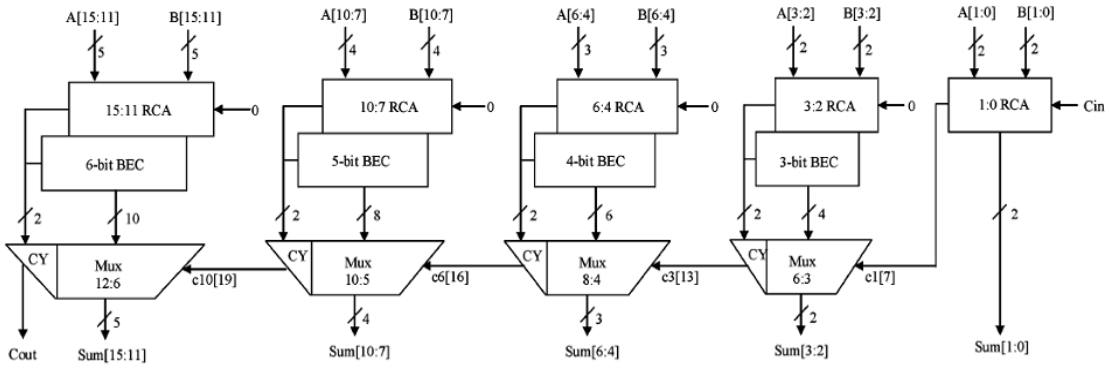

Fig. 6. Modified Carry Select Adder

A modified carry select adder make use of single RCA and Binary to Excess One converter (BEC) instead of using RCA to reduce area and power consumption with speed penalty. The number of logic gates used in the modified carry select adder is less as compared to the Regular carry select adder. The Modified carry select adder replaces RCA with Cin=1 with Binary to Excess One Converter so that number of gates can be reduced. The architecture of modified carry select adder for 16-bit is also divided into five groups. The importance of BEC comes from large silicon area reduction when designing modified carry select adder for larger bits.

VI. BINARY TO EXCESS ONE CONVERTER

The logic diagram of 4-bit Binary to Excess One Converter is shown in Figure 6.The Boolean expression depicting Binary to Excess One Converter are listed below

X0=~B0

X1=B1^B2

X2=B2^(B1&B0)

X3=B3^(B0&B1&B2)

The main idea of this project is to replace RCA ith Cin=1 with Binary to Excess One Converter. For n-bit RCA n+1 bit BEC is required. With BEC we can reduce the area and power consumption .

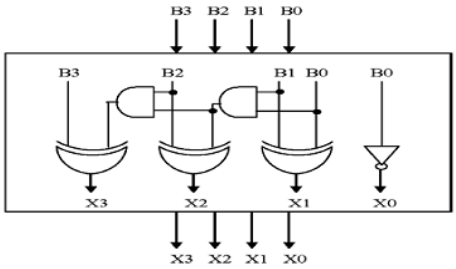

Fig. 7. Binary to Excess One

A 4-bit BEC with 8:4 mux is shown in Figure 7.The output of RCA with Cin=0 and the output of BEC is given to the multiplexer. Depending on the selection line the corresponding sum and carry is selected.

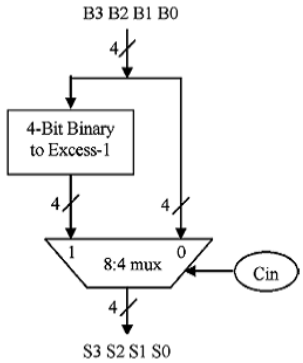

Fig. 8. 4-bit BEC with 8:4 Mux

VII. DELAY AND AREA EVALUATION OF MODIFIED CARRY SELECT ADDER

. Similar to that of Regular Carry Select Adder, Modified carry select adder also has five groups.

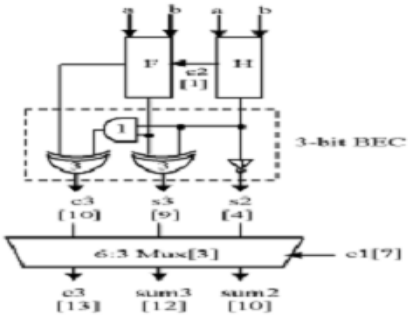

Fig. 9. Group 2

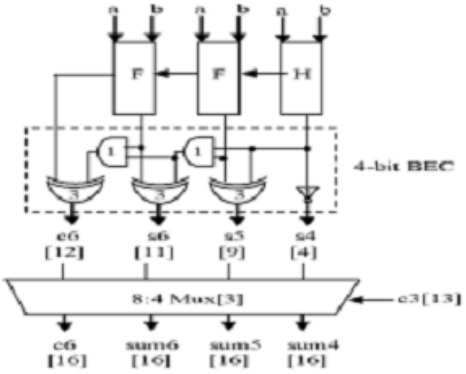

Fig. 10. Group 3

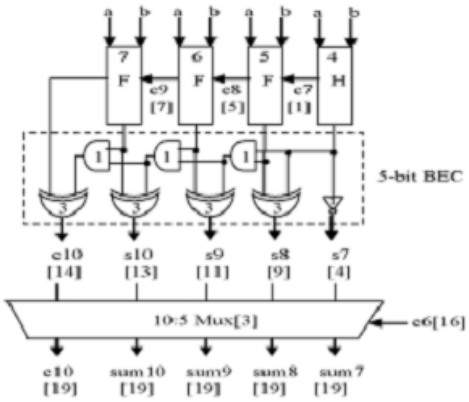

Fig. 11. Group 4

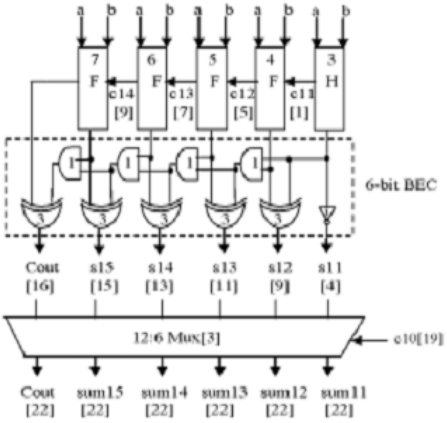

Fig.12. Group 5

1) The group2 has one 2-bit RCA. Instead of another RCA with Cin=1 a 3=bit BEC is used. The selection input C1[time(t)=7] of 6:3 mux arrive earlier than S3[t=9] and C3[t=10] later than S2[t=4]. Thus sum3 and final C3 (output from mux) are depending on S3 and mux and partial C3 and mux respectively.

2) The arrival time of mux selection input is always greater than the arrival time of data output from the Ripple Carry Adders for group3 to group 5.

3) The delay and area count of group2 to 5 is listed in Table I

TABLE I
DELAY AND AREA ANALYSIS OF REGULAR AND MODIFIED CARRY SELECT ADDER

Group	Delay		Area	
	Regular	Modified	Regular	Modified
Group 2	11	13	57	43
Group 3	13	16	83	61
Group 4	16	19	117	84
Group 5	19	22	147	107

VIII. RESULT ANALYSIS

The comparison result of Regular and Modified Carry Select Adder is listed in Table II

TABLE II
COMPARISON RESULTS OF REGULAR AND MODIFIED CARRY SELECT ADDER

Word Size	Adder	No of LUT	No of slices	Delay (ns)	Power (mW)
16 bit	RCSA	45	30	18.842	408.14
	MCSA	43	25	21.935	407.44
32 bit	RCSA	102	55	22.788	409.52
	MCSA	97	55	26.884	409.28
64 bit	RCSA	219	118	34.549	433.20
	MCSA	213	121	37.734	432.48

IX. SIMULATION RESULTS

Regular and modified carry select adder is designed and synthesized in Verilog HDL .Result showed that modified carry select adder has reduced area and power consumption as compared to the regular carry select adder with speed penalty.

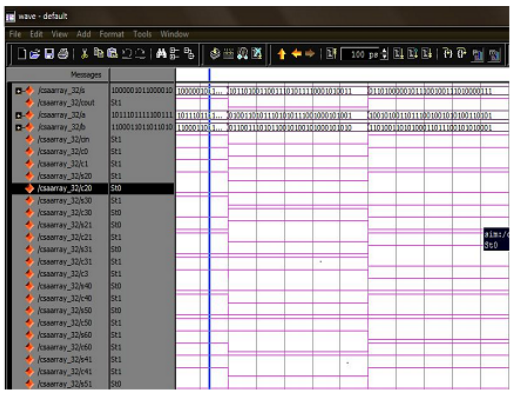

Fig. 13. Simulation results for 16 bit Regular Carry Select Adder

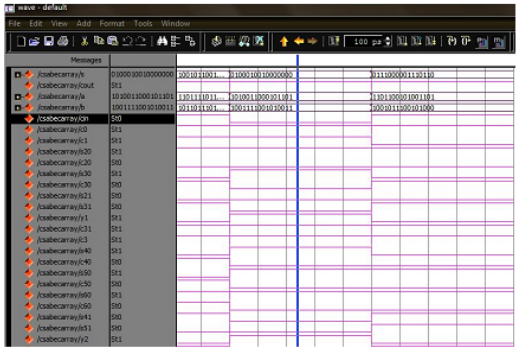

Fig 14. Simulation result for Modified 16 bit Carry Select Adder

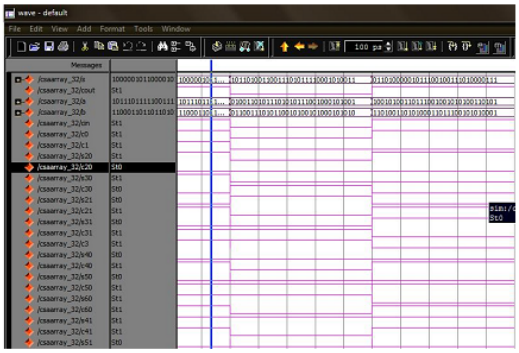

Fig 15. Simulation result for Regular 32 bit Carry Select Adder

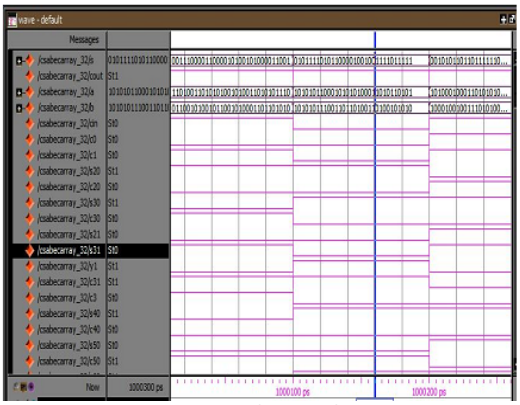

Fig. 16. Simulation result for Modified 32 bit Carry Select Adder

X. CONCLUSION

In this paper an area and power efficient carry elect adder is proposed. Replacing the RCA for Cin=1 in regular the regular carry select adder by the proposed Binary to Excess One Converter the number of gates can be reduced. The reduced number of gates result in reduced area and power consumption. The compared result showed that modified carry select adder ha slight increase in delay, but the area and power consumption is significantly reduced.

XI. ACKNOWLEDGEMENT

We thank to Dr.P.Rmamoorthi, Prof.S.Arumugam, Prof. B.Devi of the VLSI Division, SNS College of Technology, Coimbatore, for their contribution of this work.

XII. REFERENCE

[1] [1]Weinberger; J.L. Smith, "A Logic for High-Speed Addition", National Bureau of Standards, Circulation 591, pp. 3-12, 1958.

[2] O. J. Bedrij, "Carry-Select Adder", IRE transactions on Electronics Computers, vol.EC-11, pp. 340-346, June1962.

[3] Youngjoon Kim and Lee-Sup Kim, "64-bit carry-select adder with reduced area", Electronics Letters, vol.37, issue 10, pp.614-615, May 2001.

[4] B.Ramkumar, Harish M Kittur and P.Mahesh Kannan, "ASIC implementation of Modified Faster Carry Save Adder", European Journal of Scientific Research, vol.42, pp.53-58, 2010.

[5] Kuldeep Rawat, Tarek Darwish. and Magdy Bayoumi, "A low power and reduced area Carry Select Adder", 45th Midwest Symposium on Circuits and Systems, vol.1, pp. 467-470,March 2002.

[6] Akhilesh Tyagi, "A Reduced Area Scheme for Carry-Select Adders", IEEE International Conference on Computer design, pp.255-258, Sept 1990

[7] I.Chyn Wey, Cheng-Chen Ho, Yi- Sheng Lin and Chien-Chang Peng,"An area efficient carry select adder Design by sharing the common Boolean Logic term",International Multiconference of Engineers and Computer Scientists vol II ,Hong Kong,2012.

[8] Y. Kim and L.-S. Kim, "64-bit carry-select adder with reduced area,"Electron. Lett., vol. 37, no. 10, pp. 614–615, May 2001.

[9] J. M. Rabaey, Digtal Integrated Circuits—A Design Perspective.Upper Saddle River, NJ: Prentice-Hall, 2001.

[10] Y. He, C. H. Chang, and J. Gu, "An area efficient 64-bit square root carry-select adder for low power applications," in Proc. IEEE Int. Symp.Circuits Syst., 2005, vol. 4, pp. 4082–4085.

[11] T.-Y. Chang and M.-J. Hsiao,"Carry-Select Adder using single Ripple-Carry Adder", Electronics letters, vol.34, pp.2101-2103, October 1990.

BINDING AFFINITIES OF BENZOPYRAZINES WITH CYCLIN DEPENDENT KINASES

ARUN KUMAR V.A[1] & KESHAV MOHAN[2]

[1]Department of S&H (Computer Applications), Sathyabama University, Chennai, India

Abstract -1KE8 is a Cyclin-dependent kinase (CDK) that belongs to a family of protein kinases. CDKs are considered a potential target for anti-cancer medication. Benzopyrazines and its derivatives are an important class of fused heterocyclic displaying a broad spectrum of biological activities which have made them privileged structures in pharmacologically active compounds. Modification in their structure has offered a high degree of diversity that has proven useful for the development of new therapeutic agents having improved potency and lesser toxicity. In the present work, attempts were made to identify leading quinoxaline moieties as candidate drugs against 1KE8 by carrying out docking experiments with 46 analogues and assigning docking scores.

Key words: *Benzopyrazine, CDK, Quinoxaline, Anti Cancer drugs, Glide*

I. INTRODUCTION

Cancer, medically known as malignant neoplasm, is a broad group of disease, involving different cell types in the human body with unregulated cell growth. In cancer, cells divide and grow uncontrollably forming tumors and invade near by cells and organs. There are over 200 different known neoplasm's that affect human cell type.
Common treatment protocol for cancer involved surgery, radiation and chemotherapy. Clinical trials are studies in which people volunteer to take part in tests of new drugs of medical procedures. Clinical trials are used to develop new medical regimes for cancer. It is estimated that about 9 million new cancer cases are diagnosed every year and over 4.5 million people die from cancer each year in the world.

Drug design is the inventive process of finding new drug molecule based on the knowledge of a biological target. In contrast to traditional methods of drug discovery, computer aided drug design begins with a hypothesis that modulation of a specific biological target may have therapeutic value. Ligand based drug design depends on the knowledge of the molecules that bind to the biological target, where as structure based drug design relies on the knowledge of the three dimensional structure of the biological target. The most fundamental goal is to predict whether a given molecule will bind to a target protein and if so how strongly.

II. MATERIALS AND METHODS

1KE8, a cyclin dependent kinase is selected for this study and docking exercises carried out for identifying 1KE8 inhibitor. 1KE8 belongs to a family of protein kinases which regulate the cell cycle. It is also involved in regulating transcription, mRNA processing, and the differentiation of nerve cells. CDKs are considered a potential target for anti-cancer medication. If it is possible to selectively interrupt the cell cycle regulation in cancer cells by interfering with CDK action, the cell will die. A CDK inhibitor is a chemical that inhibits the function of CDKs.

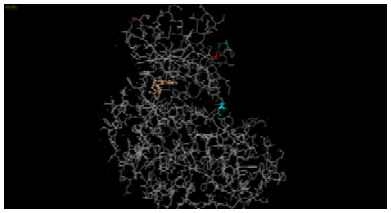

Fig.1. 3D structure of 1KE8

The receptor protein was downloaded from Protein Data Bank [PDB] and refined using protein wizard of Schrodinger suit 2012[7-9]. A typical PDB structure file consists only of heavy atoms and may include a cocrystallized ligand, water molecules, metal ions, and cofactors. Some structures are multimeric, and may need to be reduced to a single unit. It is therefore needed to prepare proteins in a form that is suitable for modeling calculations. The tools of Schrodinger suite 2012 is used for the purpose. The refining process involves fixing structures first, then deleting unwanted chains and waters, then fixing or deleting het groups, and finally performing some optimization of the fixed structure.

Analogues of benzopyrazines are an important class of heterocyclic displaying a broad spectrum of biological activities which have made them privileged structures in pharmacologically active compounds. Benzopyrazine has been considered as a wonder nucleus which posses almost all types of biological activities[6]. This diversity in the biological response profile has attracted the attention of many researchers to explore this skeleton to its multiple potential

against several activities. They are clinically effective as antibacterial, antifungal, anti-inflammatory, anticancer, anti-tubercular and antineoplastic agents. Interestingly, it also shows anti-HIV and anti-proliferative activity. Modification in their structure has offered a high degree of diversity that has proven useful for the development of new therapeutic agents having improved potency and lesser toxicity.

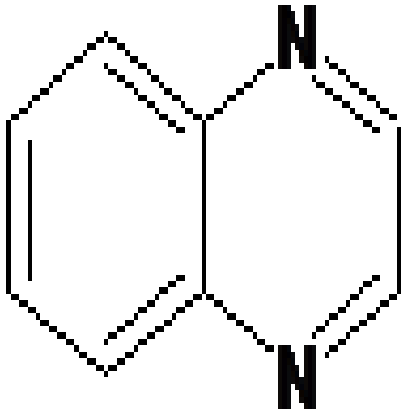

Fig.2. Structure of Quinoxaline

The docking experiments provide with structure which can bind the protein with least energy. Such a structure is considered as drug candidate. In this case all docking calculations were carried out with Schrodinger Glide 2012. This program performs a hierarchical search of ligand conformations undergoing a filtering procedure and finally minimizes in the field of the receptor using the OPLS-AA force fields in conjunction with a distance-dependent dielectric model. Glide uses two concentric boxes to generate the potential grids and define the binding site.

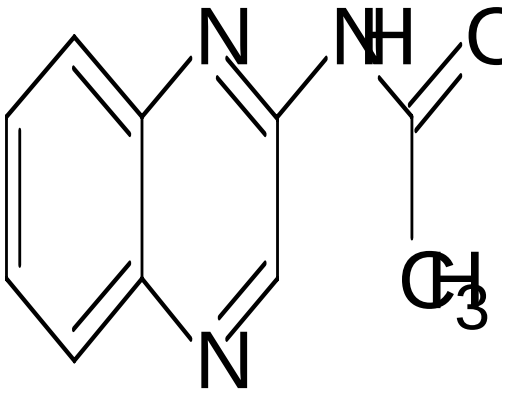

Fig.3. Structure of q22 (N-(quinoxaline-2-yl)acetamide)

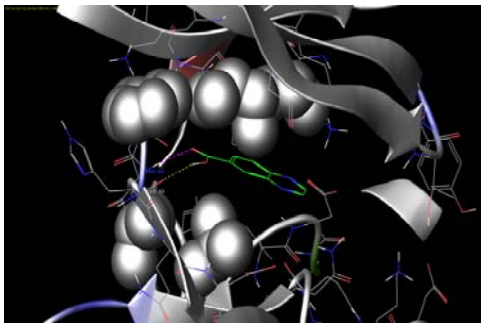

Fig.4. The Optimal docking of q22 with 1KE8

Default input parameters were used in all computations (no scaling factor for the van der Waals radii of non-polar protein atoms and a scaling factor of 0.8 for non-polar ligand atoms). All compounds were docked and scored using the Glide standard-precision (SP) mode[1,3,4]. Upon completion of each docking calculation, 30 poses per ligand were saved. The best-docked structures were ranked using a model energy score (Emodel) derived from a combination of Glide Score (Gscore, a modified and extended version of the empirically based ChemScore function), Coulombic, and van der Waals energies, and the strain energy of the ligands. The top- ranked compounds obtained in this way were docked and scored again with the Glide extra-precision (XP) mode, and the best of 10 XP-docked structures was finally selected as final docking solution[7,8,9].

III. RESULTS AND DISCUSSIONS

The results of docking experiments of the first 10 lead drug candidates are tabulated below in the order of decreasing Glide score.

From docking scores in Table.1, the following conclusions can be drawn. N-(quinoxaline-2-yl)acetamide (q22) shows the maximum glide score value of -6.69. The nearest two ligands i.e. (Quinoxaline-6ylcarbonyl)sodium (q45) and (Quinoxaline-6ylcarbonyl)potassium (q46) give the value of -6.14. q22 gives the Lipophillic van der Waal's energy of -3.24 where as the nearest ligands (q45 and q46) give the energy value of -2.72. Hydrophobic enclosure reward is the cumulative hydrophobic interaction between the ligand and the receptor atom[2]. The ligand q22 gives the maximum value of the hydrophobic enclosure reward (-0.82). This shows that N-(quinoxaline-2-yl)acetamide (q22) is the best suitable ligand which is well placed in the pocket of the receptor atom[5]. This best fit is depicted in Fig.5.

In the case of hydrogen bond energy released, q22 releases less compared with q45 and q46. They show the value of -0.75. The electrostatic energy of q22 is -0.19, which is higher than the other two ligands.

Table I. Docking score for 10 selected ligands (1- GScore, 2- LipophilicEvdW, 3- PhobEn, 4- Hbond, 5- Electro)

Ligands	1	2	3	4	5
N-(quinoxalin-2-yl)acetamide (q22)	-6.69	-3.24	-0.82	-0.61	-0.19
(Quinoxaline-6-ylcorbonyl)sodium (q45)	-6.14	-2.72	-0.75	-0.7	-0.15
(Quinoxaline-6ylcarbonyl)potassium (q46)	-6.14	-2.72	-0.75	-0.7	-0.15
[Hydroxy(quinoxaline-2-yl)phophoryl]sodium(q33)	-5.68	-2.58	-0.57	-0.7	-0.32
[Hydroxy(quinoxaline2yl)phophoryl]potassium(q32)	-5.65	-2.57	-0.57	-0.7	-0.3
Quinoxaline -2-ylsulfamic acid (q18)	-5.39	-2.04	-0.2	-1.3	-1.06
Quinoxaline 6-ylphosphoramidic acid (q23)	-5.38	-1.72	0	-2.34	-0.96
Quinoxaline -2-ylphosphoramidic acid (q19)	-5.89	-1.48	0	-1.42	-2.49
Quinoxaline 6-yl-sulfamic acid (q24)	-5.21	-2.03	0	-1.32	-1.08
2,3,6,7 tetrachloroquinoxaline (q9)	-5.11	-3.54	-1.05	0	-0.08

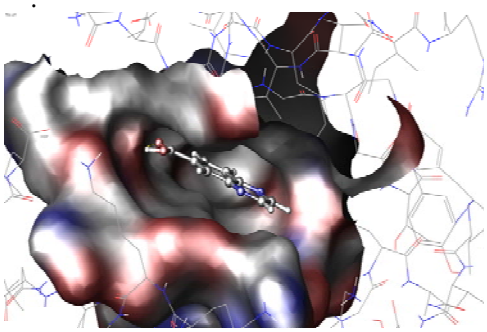

Fig.5. Display showing 1KE8 – q22 best fit

So we can conclude that the ligand q22 i.e. N-(quinoxalin-2-yl)acetamide is the best ligand among the other 46 ligands docked against the inhibitor, 1KE8.

IV. CONCLUSION

N-(quinoxaline-2-yl)acetamide (q22) binds effectively at the active site of 1KE8 with binding energy -6.69 (Kcal/mol). There is no extensive study carried out in the ligand, N-(quinoxaline-2-yl)acetamide. So this result of the *in silico* studies reveal that the molecule is potential candidate for drug, which needs to undergo wet lab trials. Bioavailability, metabolic half life and lack of side effects etc are to be optimized before making it a safe and efficacious drug.

REFERENCES

[1] Friesner, R. A.; Banks, J. L.; Murphy, R. B.; Halgren, T. A.; Klicic, J. J.; Mainz, D. T.; Repasky, M. P.; Knoll, E. H.; Shelley, M.; Perry, J. K.; Shaw, D. E.; Francis, P.; Shenkin, P. S., 2004, Glide: A new approach for rapid, accurate docking and scoring. 1. Method and assessment of docking accuracy. J. Med. Chem. 47 (7), 1739-1749.

[2] Friesner, R. A.; Murphy, R. B.; Repasky, M. P.; Frye, L. L.; Greenwood, J. R.; Halgren, T. A.; Sanschagrin, P. C.; Mainz, D.T., 2006, Extra precision glide: Docking and scoring incorporating a model of hydrophobic enclosure for protein-ligand complexes. J. Med. Chem., 49 (21), 6177-6196.

[3] Krovat, E. M.; Steindl, T.; Langer, T., 2005, Recent Advances in Docking and Scoring. Curr. Comput.-Aided Drug Des., 1, 93-102.

[4] Kontoyianni, M.; McClellan, L. M.; Sokol, G. S., 2004, Evaluation of Docking Performance: Comparative Data on Docking Algorithms. J. Med. Chem., 47, 558-565.

[5] Sherman, W.; Day, T.; Jacobson, M. P.; Friesner, R. A.; Farid, R., 2006, Novel Procedure for Modeling Ligand/Receptor Induced Fit Effects. J. Med. Chem., 49, 534.

[6] Prasad et al., 2011, Anti Inflammatory Activity of Some New Thio-Ether Derivatives of Quinoxaline. Pharmacologyonline 1: 1023-1030.

[7] MOE, Version 2008.10, Chemical Computing Group, Inc., www.chemcomp.com.(2008)

[8] Maestro, Version 9.2, Schrödinger, LLC, New York, NY, (2012).

[9] Glide, Version 5.7, Schrödinger, LLC, New York, NY, (2012).

◈◈◈